学位論文

Physical Conditions of Molecular Gas in Nearby Merging Luminous Infrared Galaxies

(近傍高光度赤外線相互作用銀河の分子ガスの物理状態)

平成 28 年 12 月 博士 (理学) 申請

東京大学大学院理学系研究科

天文学専攻

斉藤　俊貴

Abstract

Gravitational interactions between gas-rich galaxies are thought to play an important role in the formation and evolution of galaxies. Such gas-rich galaxy mergers trigger burst of star formation and efficient accretion to the central supermassive black holes, leading them to dusty brighter populations, so-called (ultra-)luminous infrared galaxies (U/LIRGs). As a tracer of the fuel for the IR engines hidden behind large column of dust, molecular line emissions at longer wavelengths (millimeter, submillimeter, and far-IR) are suitable to investigate U/LIRG activities directly. In this Thesis, we investigate physical conditions of molecular gas in two nearby merging LIRGs, NGC 1614 and VV 114, through high angular resolution and high sensitivity observations of multiple molecular diagnostic lines; (1) CO (four transitions), (2) CH_3OH (two blended transitions), and (3) HCN (three transitions) and HCO^+ (three transitions) rotational lines supplemented with other lines and continuum emission with Atacama Large Millimeter/submillimeter Array (ALMA) and Very Large Array.

NGC 1614 is one of the nearby LIRGs. Since this system is thought to be a remnant stage of a gas-rich galaxy merger without any heavily obscured AGN or bright AGN activity, we can use this galaxy as a template of starburst-dominated galaxies. The another target, a nearby mid-stage merging LIRG VV 114, is known to have a characteristic dust and gaseous filament ($\sim$ 6 kpc length) across the progenitor's galaxies. The filament harbors three distinctive regions; a hard X-ray detected AGN, starbursting clumps, and Overlap region at the collision front. Taking advantage that these three regions can be observed simultaneously by small fields of view of submillimeter interferometers, we can test molecular diagnostics.

High-resolution, high-sensitivity, and uv-matched ALMA observations allow us to solve excitation conditions of these molecules under local thermodynamical equilibrium (LTE) or non-LTE assumptions in order to parameterize and differentiate thermal and chemical properties of molecular gas. We found that (1) CO spectral line energy distribution up to $J_{\rm upp} = 6$ in NGC 1614 can be explained by two-phase molecular gas ISM (> 70 K and ~ 19 K), which is consistent with observed two-phase dust spectral energy distribution (~ 110 K and ~ 35 K). PDR is the main heating source for the cold ISM, while mechanical heating from supernovae or stellar winds is required for the warm ISM. (2) CH_3OH abundance ($X_{\rm CH_3OH}$) peaks at the extended (a few kpc) Overlap region, where is located between the progenitor's disks of VV 114. The abundance is almost an order of magnitude larger than the nuclear regions. This indicates that the presence of AGN and intense starburst activities suppress CH_3OH at the nuclear regions by strong photodissociation (i.e., efficient destruction) and/or desorption of the precursor molecule CO (i.e., inefficient production), and merger-induced shocks enhance CH_3OH at the Overlap region. The extended, bright CH_3OH emission cannot be explained by hot-core environments. (3) Surface density of star formation rate ($\Sigma_{\rm SFR}$) strongly correlates with the excitation conditions and flux densities of HCN and HCO^+, indicating that star formation activity may govern the physical properties of dense gas ISM in the filament of VV 114, although the putative AGN position doesn't fit to this scenario. The AGN, which shows relatively low $\Sigma_{\rm SFR}$, has the highest excitation ratios (i.e., high T) and HCN/HCO^+ ratios (i.e., high $X_{\rm HCN}$), showing completely different thermal and chemical properties from star-forming regions. In addition, we found that the tstar formation efficiency doesn't simply correlate with the dense gas fraction. By adopting the turbulence-regulated star formation model, we suggest that the Overlap region has diffuser and more turbulent dense gas properties relative to dense gas at the eastern nucleus. This is consistent with the shock interpretation of the CH_3OH enhancement at the Overlap region.

Our studies succeeded in distinguishing and interpreting molecular gas properties affected by AGN, star formation, and merger-induced shocks took place in nearby merging LIRGs.

Acknowledgements

I would like to express my sincere gratitude to my supervisor, Ryohei Kawabe. He provided me this precious opportunity to study at the University of Tokyo and National Astronomical Observatory of Japan. I especially would like to express my deepest appreciation to my advisor, Daisuke Iono. He provided me a lot with elaborated advice, guidance, assistance, and encouragement in researches throughout the course of this work together with Ryohei Kawabe. Their suggestions are always a lighthouse for me to overcome various problems. Mere words could never express my gratitude to them.

I would like to thank Kouichiro Nakanishi, Daniel Espada, Cong K. Xu, Hiroyuki Kaneko, Min S. Yun, Shuro Takano, Kazimierz Sliwa, Masatoshi Imanishi, Yoichi Tamura, Sabine König, Susanne Aalto, Kentaro Motohara, Hajime Sugai, Yoshiaki Hagiwara, and John E. Hibbard for useful advices and suggestive comments in researches. I gratefully appreciate it that Junko Ueda and Takuji Yamashita not only help me in my researches, but also encourage me every time as senior students and collaborators. I would like to thank Tetsuo Hasegawa, Satoru Iguchi, Kenichi Tatematsu, Masao Saito, Norikazu Mizuno, Masaaki Hiramatsu, Yoichi Matsuda, Hiroshi Nagai, Bunyo Hatsukade, Kazuya Saigo for participating in the seminars and teaching many things. I thank all staffs at Chile Observatory for successful observations.

I dare to thank Sinya Komugi, Cinthya Herrera, Joten Okamoto, Patricio Sanhueza, Kana Matsui-Morokuma, Quang Nguyen Luong, and Natsuko Izumi for playing together, frequently inviting me to go out, and discussing with me. I also thank previous and current students at Chile Observatory, Kazuhiro Kiyokane, Yuzo Otomo, Kosuke Fujii, Chihomi Hara, Ayumu Matsuzawa, Shin Koyamatsu, Satoshi

Ohashi, Kyoto Onishi, Yusuke Aso, Kapibara-san, Andrea Silva, Minju Lee, Yuta Kato, Tomonari Michiyama, Takuya Kurahashi, Kuwahara-san, Misaki Ando, Ippei Kurose, Masayuki Yamaguchi, Jinshi Sai, Hiroyuki Ishikawa, Akira Hosokawa, for playing together, eating out and drinking alcohol, which made my life at Mitaka fruitful. Thanks to them, I could really enjoy my student life.

I specially thank Hitomi Morikai for supporting my life. Without her help, I could not finish my Ph.D thesis. Thank you so much for being with me all the time.

I am in debt to and thank all the people who have not mentioned here but have supported me. I shall never forget their kind support. The last but not least, I would like to thank my mother, Akemi Saito, my grand parents, Shoji (Masani) Saito and Kazu Saito, and my granduncle, Masamitsu Sasaki, and all the relatives for their constant supports and encouragements for my student life.

Contents

List of Figures

List of Tables

Chapter 1

Introduction

1.1 Dusty Galaxies in the Universe

Observations at far-ultraviolet (FUV) and far-infrared (FIR) wavelengths have revealed that the cosmic history of star formation is peaked at z $\approx$ 2 (Madau & Dickinson 2014, for a review). Since FUV is thought to be mainly emitted by young massive stars, it can be used as a direct tracer of recent star formation. The FIR emission, contrary to FUV, is re-radiated from dust which absorbs the FUV radiation, and therefore it is a tracer of "obscured" star formation (e.g., Murphy et al. 2011; Kennicutt & Evans 2012). Considering these radiation mechanisms, it is clear that more than half of the star formation at z $\leq$ 2 are hidden behind a large column of dust (Figure 1.1a) (e.g., Takeuchi et al. 2005). Such dusty star formation activity is known to mainly take place in IR-bright galaxies, called luminous infrared galaxies (LIRGs; 10^{11} $L_{\odot} \leq L_{\rm IR} < 10^{12}$ $L_{\odot}$, where $L_{\rm IR}$ is the total infrared luminosity from 8 μm to 1000 μm) and ultraluminous infrared galaxies (ULIRGs; 10^{12} $L_{\odot} \leq L_{\rm IR} < 10^{13}$ $L_{\odot}$). They are the brightest and rarest galaxy populations in the local Universe (e.g., Soifer et al. 1987), although this is not the case with higher redshift galaxies. Goto et al. (2010) have shown that ULIRG and LIRG contribution to the total IR (TIR) luminosity function (LF) increases by a factor of 10 and 1.8 from z = 0.35 to 1.4, respectively (Figure 1.1b), suggesting that U/LIRGs are more common and important drivers of obscured star formation at higher redshift (see also Le Floc'h et

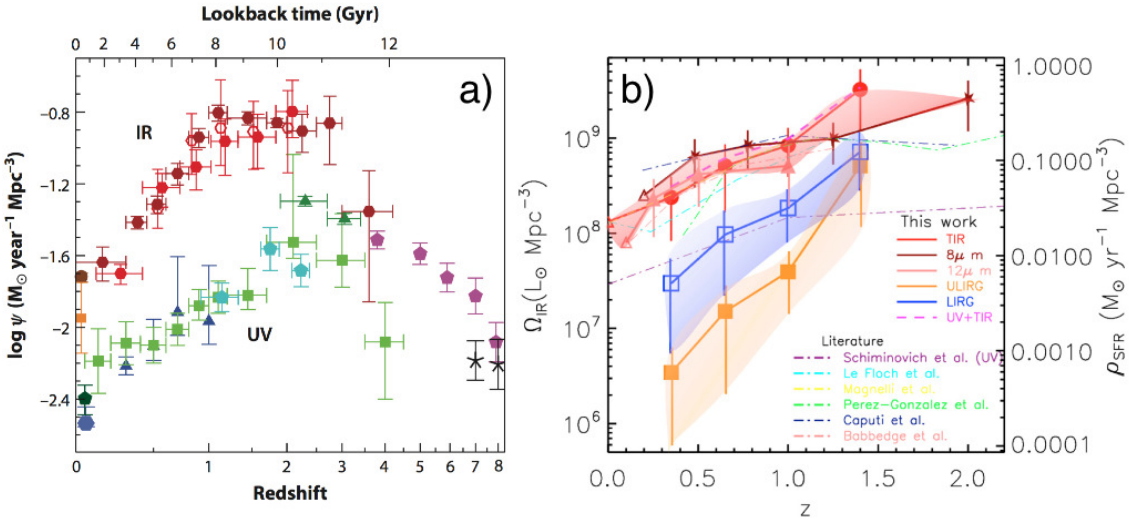

Figure 1.1. (a) Redshift evolution of star formation rate (SFR) densities in the FUV and FIR (Madau & Dickinson 2014). (b) Redshift evolution of total IR (TIR) luminosity density based on TIR LFs (red circles), 8 μm LFs (stars), and 12 μm LFs (filled triangles) (Goto et al. 2010). The blue open squares and orange filled squares are for only LIRGs and ULIRGs, also based on TIR LFs.

al. 2005).

The redshift evolution of dusty star-forming galaxies becomes clearer when we plot TIR LFs for several redshift bins. Figure 1.2 shows the TIR LFs for four PACS Evolutionary Probe (PEP) fields in different redshift bins from z $\sim$ 0 to z $\sim$ 4 (Gruppioni et al. 2013). The PEP fields include four famous fields: the Cosmic Evolution Survey field (COSMOS field; 2 deg^2), the Extended Chandra Deep Field-South (ECDFS; $\sim$ 700 arcmin^2), the Great Observatories Origins Deep Survey field (GOODS-N field; $\sim$ 300 arcmin^2), and GOODS-S field ($\sim$ 300 arcmin^2) at 70, 100, 160, 250, 350 and 500 μm. They found a clear, strong evolution for the TIR LF, which is consistent with the redshift evolution of total star formation rate (SFR) densities and U/LIRG's LFs.

Those pictures are consistent with the redshift evolution of a recently established relation, "star formation main sequence", which is a nearly linear relation between stellar mass ($M_\star$) and SFR observed in multiple wavelengths (e.g., optical, IR, and

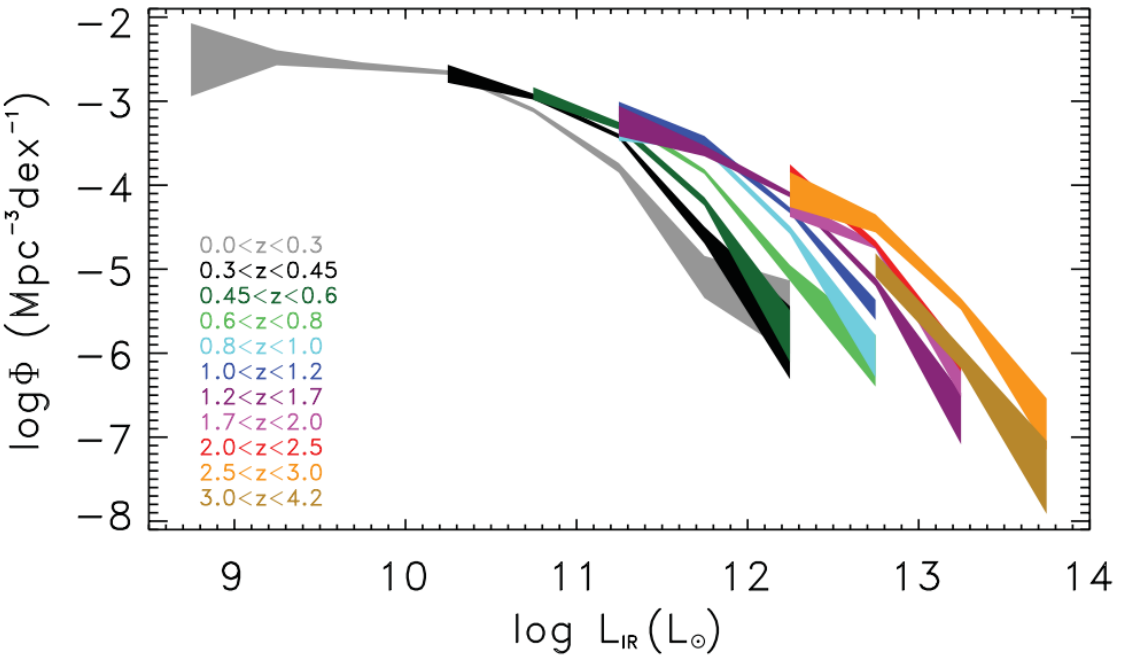

Figure 1.2. Total IR LF estimated by combining the data from the four PEP fields plotted in different redshift intervals from z $\sim$ 0 to z $\sim$ 4 (Gruppioni et al. 2013). The different color filled areas represent the $\pm 1\sigma$ uncertainty regions at different redshifts.

radio; Elbaz et al. 2011; Karim et al. 2011; Tasca et al. 2015) and reconstructed by numerical simulations (e.g., Sparre et al. 2015). The main sequence at z $\sim$ 1 and 2 are $\sim$ 7 and $\sim$ 20-30 times higher in SFR at given $M_\star$ than the local main sequence, respectively (e.g., Brinchmann et al. 2004; Daddi et al. 2007; Salim et al. 2007; Rodighiero et al. 2011; Wuyts et al. 2011; Whitaker et al. 2012), indicating that galaxies on the main sequence are forming more new stars in the higher-z Universe compared with today (Figure 1.3).

Both observational evidences of redshift evolution of star formation have strongly suggested that dusty star formation was dominantly taking place in U/LIRGs at the peak epoch of star formation, and thus U/LIRGs are one of the key populations to study cosmic star formation history, which is the fundamental aspect of galaxy formation and evolution. However, observations toward such high-z U/LIRGs are difficult due to their distances and instrumental limitations. Therefore, inspecting

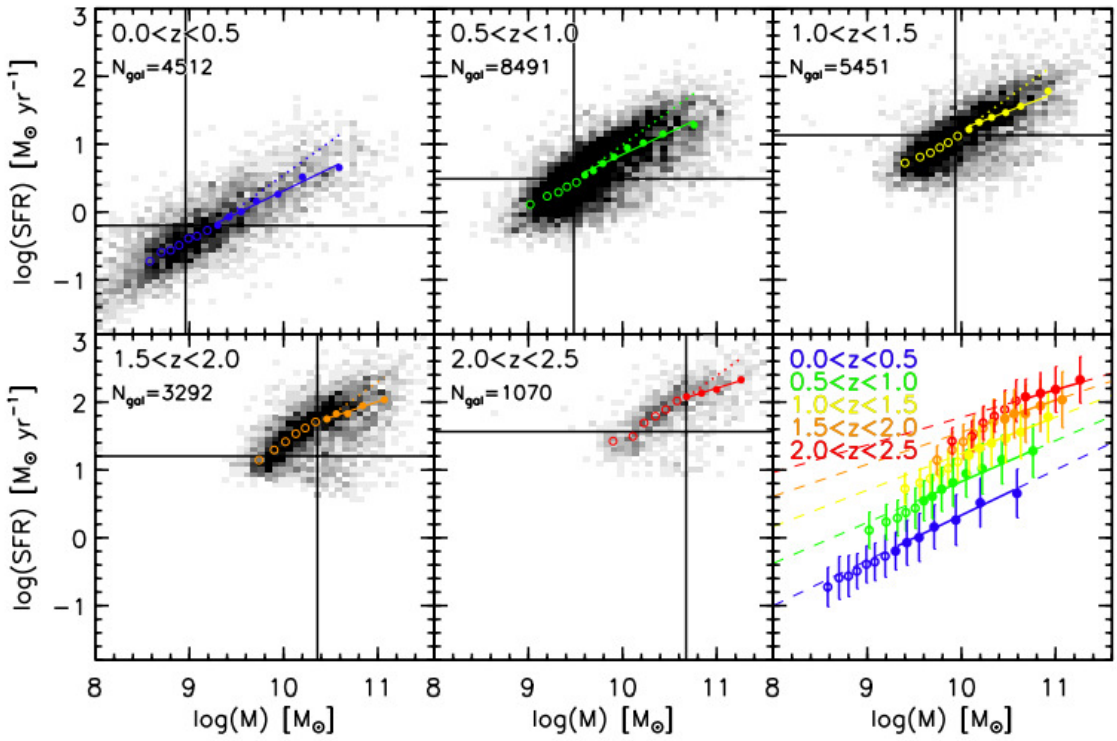

Figure 1.3. The star formation main sequence for star-forming galaxies at $0 < z < 2.5$ (Whitaker et al. 2012). The x-axis shows total stellar mass of galaxies. The medians and scatter are colorized by redshift.

local U/LIRGs is one of the first step to understand star-forming galaxies in the Universe.

1.2 U/LIRGs and Galaxy Mergers

1.2.1 Triggering U/LIRGs via Galaxy Merger

It is observationally known that U/LIRGs at low redshift are almost exclusively strongly interacting and merging systems (e.g., Kartaltepe et al. 2010, see Figure 1.4). Note that at high redshift, LIRGs are not necessarily mergers because "normal" isolated disk galaxies are rich enough in gas to reach LIRG-like activity (Daddi et al. 2010; Tacconi et al. 2010), but it remains true that the strongest starbursts (ULIRGs

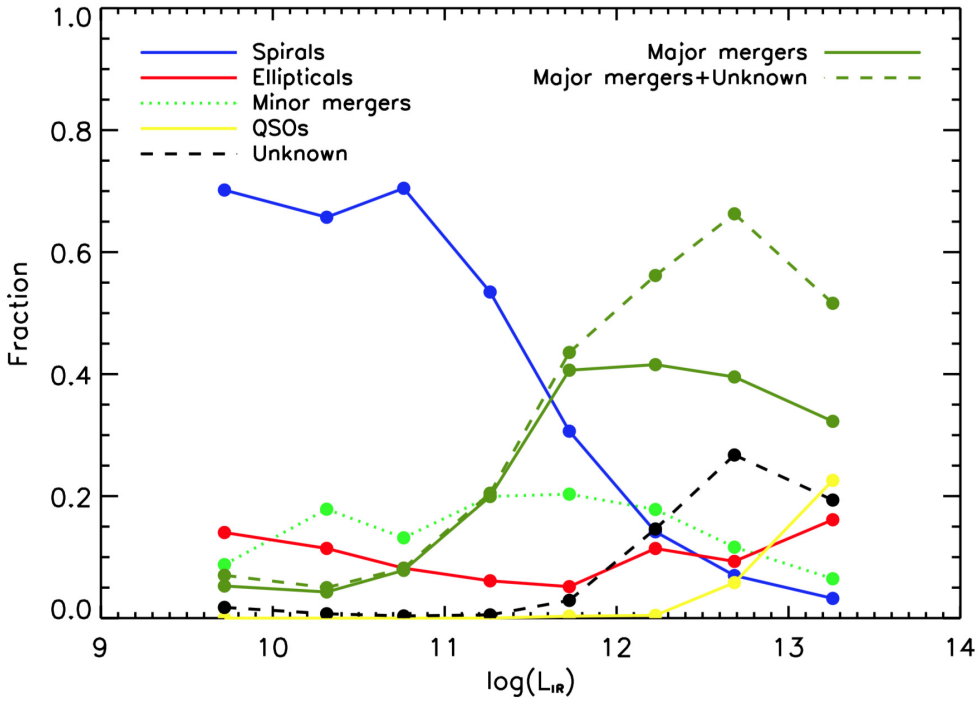

Figure 1.4. Fraction of 70 μm sources in the COSMOS field that are morphologically classified as spirals (blue solid), ellipticals (red solid), minor mergers (green dotted), major mergers (dark green solid), QSOs (yellow solid), unknown (black dashed), or major mergers+unknown (green dashed) as a function of $L_{\rm IR}$ (Kartaltepe et al. 2010).

and Hyperluminous infrared galaxies, HyLIRGs) are predominantly merging systems. Merger-induced star formation consists, for a large part, of nuclear starbursts taking place in the central 100 - 1000 pc. Nuclear activity in merger-induced starbursts has long been emphasized in studies of the merger-star formation connection (e.g., Soifer et al. 1984; Sanders et al. 1988; Duc et al. 1997). Nevertheless, the importance of nuclear starbursts among merger-induced star formation in general has long been overstated in the literature. This may be partly because theorists have long been able to explain only nuclear starbursts, or because of using infrared and/or Hα luminosities to trace star formation. Observed star formation is dependent on metallicity, dust properties, and threshold effect making them more sensitive to compact central starbursts than to spatially extended star formation with lower surface brightness density. In fact, there is a large fraction of systems in which merger-induced star

formation is spatially extended, taking place outside the central kpc, and in these system the extended star forming component is not just a relic from extended star formation in pre-merger spiral galaxies, but participates to the total starburst activity, even if there is also intense star formation in the nucleus. The relatively large spatial extent of star formation and the problem it poses for theoretical models was probably first recognized by Barnes (2004) in the Mice (NGC 4676A+B, see also Chien & Barnes (2010) in NGC 7252). A well-known example is the Antennae system (NGC 4038+4039), where a large fraction of the starburst activity takes place at several kpc from the nuclei in big "super star cluster" (SSCs) formed along spiral arms throughout the merging disks, and in the shocked overlap region between the two gas disks (Wang et al. 2004) - these star-forming components are more important than the dust-enshrouded nuclear star formation revealed in the infrared. There is to our knowledge no thorough census of the contributions of nuclear and extended star formation to merger-induced activity, probably because unveiling dust-enshrouded nuclear star formation and detecting spatially extended star formation at lower surface densities requires observations at high resolution facilities.

In a gas-rich interacting galaxy pair, the gas distribution becomes non-axisymmetric, which results in gravitational torquing of the gas. Gas initially inside the corotation radius (typically a radius of a few kpc) undergoes negative gravity torques and flows inwards in a more and more concentrated central component (inside the central kpc). Any model for star formation will then predict an increase of the star formation rate (global Kennicutt-Schmidt relation, models based on cloud-cloud collisions, etc), and thus the result is a centralized, nuclear starburst. As the driving process is gravitational torquing, early restricted three-body models could already describe the effect (Toomre & Toomre 1972). Later models have added extra physical ingredients leading to more accurate predictions on the star formation activity: e.g., self-gravity (Barnes & Hernquist 1991), hydrodynamics and feedback processes (Mihos & Hernquist 1996; Cox et al. 2008; Teyssier et al. 2010), shock-induced star formation (Saitoh et al. 2009; Matsui et al. 2012).

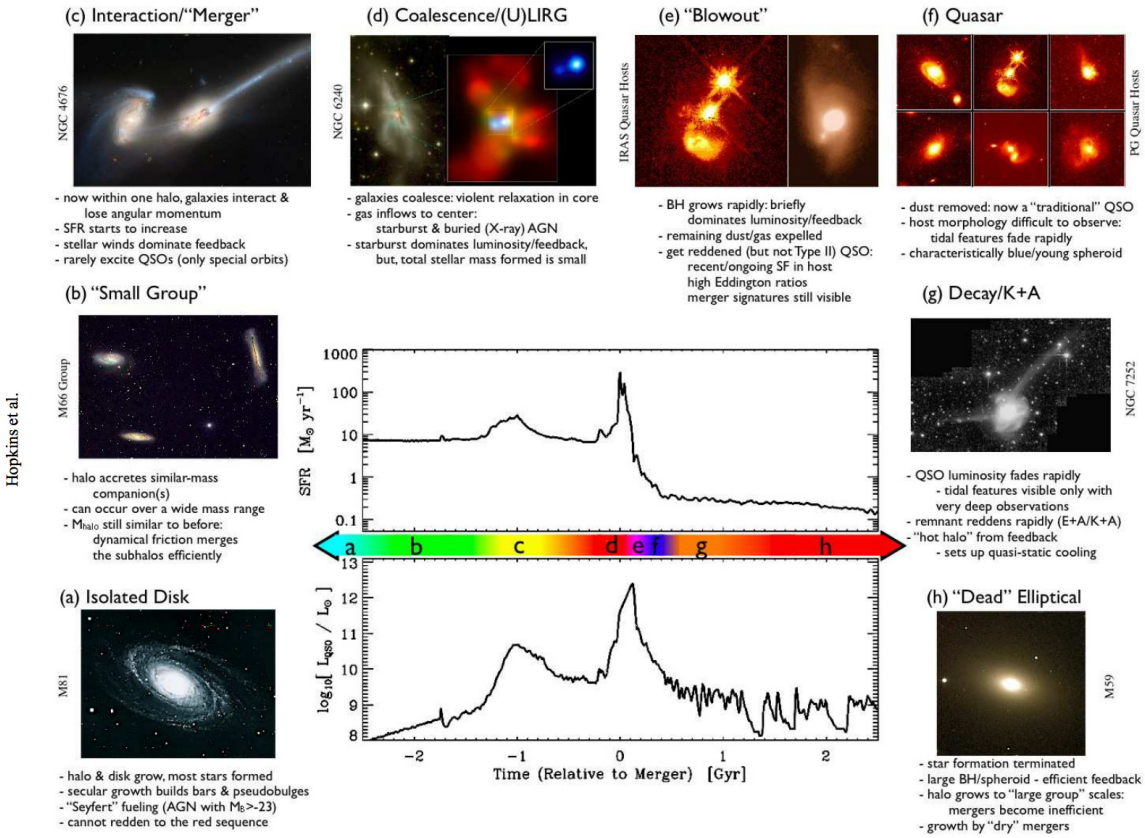

Figure 1.5. Schematic outline of the phases of growth in a "typical" galaxy undergoing a gas-rich major merger (Hopkins et al. 2008). The central panel shows a simulated history of SFR and central AGN luminosity ($L_{\rm QSO}$) during a major merger event.

1.2.2 The Role of Mergers in terms of Galaxy Evolution

Gravitational interactions between gas-rich galaxies do not only enhance their star formation activity, but change their apparent optical morphology and also trigger the growth of central supermassive black hole (active galactic nucleus, AGN), so, for a long time, galaxy mergers have been thought to play an important role for the formation and evolution of galaxies (e.g., Major mergers form most giant ellipticals; Toomre 1977). Considering that most local U/LIRGs are mergers (Figure 1.4), a proposal by Sanders et al. (1988), which suggested that U/LIRGs evolve into optical quasars, is highly relevant when discussing about galaxy evolution via mergers and

interactions. Hopkins et al. (2008) presented a single outline of the expected history of major merger of gas-rich galaxies as shown in Figure 1.5. In this outline, gas-rich major mergers pass through distinctive several phases for a few Gyr, and finally evolve into giant elliptical galaxies. A brief summary of the outline is as follows:

(a) Isolated Disk and (b) Small Group Spiral galaxies which evolve quiescently until the onset of a major merger.

(c) interaction/"Merger" Nuclear and extended star formation and accretion to AGN start to enhance during the early stages of the merger, but those are not so efficient. This phase is only robustly classified as merging/interacting galaxies by the presence of two nuclei. Their luminosities are expected not to reach at U/LIRG and quasar levels in general because of the moderate star formation and AGN, although there are exceptions (e.g., an early-stage merger NGC 232 with $L_{\rm IR} = 10^{11.44}\ L_{\odot}$; Armus et al. 2009).

(d) Coalescence/(U)LIRG During the coalescence, intense nuclear starburst and AGN activity are triggered by massive gas inflow, leading the host mergers to brighter phases which show comparable luminosities to U/LIRGs and submillimeter galaxies (SMGs). Since central growing black holes are largely embedded in molecular gas and dust (so they become brighter in IR), heavily obscured (or sometimes Compton-thick) multiple AGNs should frequently present during this phase (e.g., U/LIRGs NGC 6240, Mrk 273, and Mrk 231; Nakagawa et al. 1999).

(e) "Blowout" Most of molecular gas fallen into the merged nucleus are exhausted as the fuel for star formation and central AGN, and then the mature star-forming region, where supernova explosions frequently occur, and evolved AGN start to blow surrounding remaining gas and dust off. The early phase of this period is partially linked to observationally known dust-reddened quasars and/or IR-luminous quasars (also classified as HyLIRGs; Rowan-Robinson 2000; Farrah et al. 2002). Figure 1.6 shows the optical morphology of some dust-reddened quasars (Urrutia et al. 2008), clearly showing merging signatures ($\geq$ 75% of

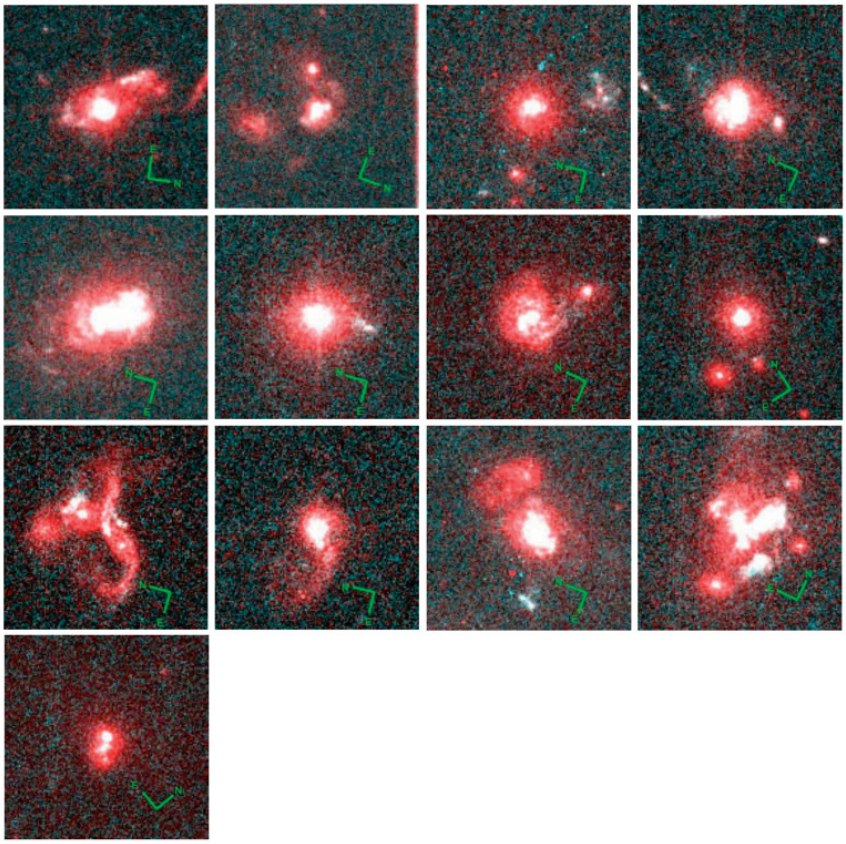

Figure 1.6. *HST* ACS (I and g-band composite) images of dust-reddened quasar host galaxies (Urrutia et al. 2008).

them are classified as mergers). They still show strong AGN and starburst activity (e.g., Kawakatu et al. 2006), so they are thought to have significant contribution to the brightest quasar population in the Universe.

(f) Quasar After removing dust, dust-reddened quasars will be visible in optical (i.e., "traditional" optical quasars).

(g) Decay/K+A Star formation and central quasar start to decline as the gas is consumed and dispersed, and most host galaxies have relaxed to resemble ellipticals. Sometimes, depending on merger properties and time, newly formed ellipticals may have a low-luminosity (decaying) AGN, or may be classified as a post-starburst (so-called E+A/K+A) galaxies.

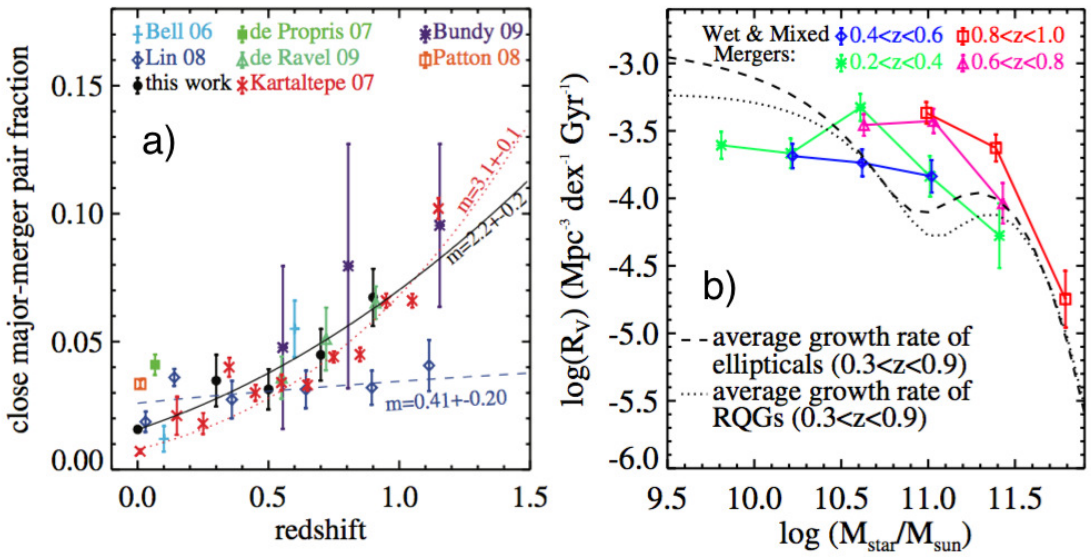

Figure 1.7. (a) Compiled observed major merger fractions at $0 < z < 1.5$ in the literature (Xu et al. 2012). Major merger is defined as the mass ratio less than 1:3. (b) Mass-depedent volute major merger rates of wet and mixed mergers (Xu et al. 2012). The dashed line is the average growth rate of ellipticals between z = 0.3-0.9 and dotted line that of red quiescent galaxies (Ilbert et al. 2010).

(h) "Dead" Elliptical After terminating star formation activity, they will become normal "Dead and red" ellipticals, who follows the observed correlations between black hole and spheroid properties (e.g., $M_{\rm BH}$ - σ relation; Kormendy & Ho 2013, for a review).

Furthermore, it is observationally known that galaxy pair fraction moderately increases as a function of redshift (e.g., Lotz et al. 2011; Xu et al. 2012). Figure 1.7a shows a plot compiled observed major merger fractions at $0 < z < 1.5$, showing increasing pair fraction proportional to $(1 + z)^{2.2}$ (see also Man et al. 2016, for higher redshifts). Quantitative analysis done by Xu et al. (2012) revealed that massive galaxies ($M_\star \sim 10^{10}$ - $10^{11.5}$ $M_\odot$) have undergone $\sim$ 0.5-1.5 major merger since z = 1 on average, which is consistent with the prediction from ΛCDM models (e.g., Stewart et al. 2009). They also showed that wet (i.e., gas-rich - gas-rich pair) and mixed (i.e., gas-rich - gas-poor pair) major mergers can fully account for the formation of ellipticals with $M_\star > 10^{10.5}$ $M_\odot$ (Figure 1.7b), which supports the argument shown in Figure 1.5.

Observational results shown here and Section 1.1 give us an idea that U/LIRGs are predominantly gas-rich mergers, which play a critical role in connecting starbursts, AGNs, red quasars, optical quasars, and ellipticals from early to current Universe (i.e., AGN-staburst connection, black hole-galaxy co-evolution; e.g., Ishibashi & Fabian 2016). But see Ueda et al. (2014) for a possible different evolutionary path from merging galaxies to disk galaxies.

1.3 U/LIRGs at (Sub-)millimeter Wavelengths

As shown in previous Sections, U/LIRGs may be a key population to understand the processes involved in formation and evolution of galaxies. However, inspecting the nature of U/LIRGs is not easy because observational studies suffer from heavy dust extinction. Longer wavelength observation is essential in order to investigate the obscured activities directly.

Although here we briefly summarize advantages and previous achievements of millimeter and submillimeter observations toward U/LIRGs, which are directly related to this Thesis, we note that a lot of useful diagnostics have been tested/investigated; e.g., X-ray (e.g., Nakagawa et al. 1999), hydrogen recombination lines at near-IR (e.g., Rich et al. 2015; Tateuchi et al. 2015), polycyclic aromatic hydrocarbon (PAH) (e.g., Ichikawa et al. 2014) and (ro-)vibrational transitions of H_2 at mid-IR (e.g., Stierwalt et al. 2014), OH, H_2O (e.g., Falstad et al. 2015) and atomic forbidden lines (e.g., Rosenberg et al. 2015) at far-IR, vibrationally-excited HCN (e.g., Aalto et al. 2015b), HCO^+ (e.g., Imanishi et al. 2016b), and HC_3N (e.g., Costagliola et al. 2015) rotational lines at submillimeter, and many.

1.3.1 Continuum Emission

In the radio to FIR regime, spectral energy distribution (SED) can be modeled with three components, non-thermal synchrotron, thermal bremsstrahlung (free-free), and thermal dust continuum emission (e.g., Condon 1992, see Figure 1.8). The synchrotron radiation in galaxies arises from relativistic electrons generated by shocks

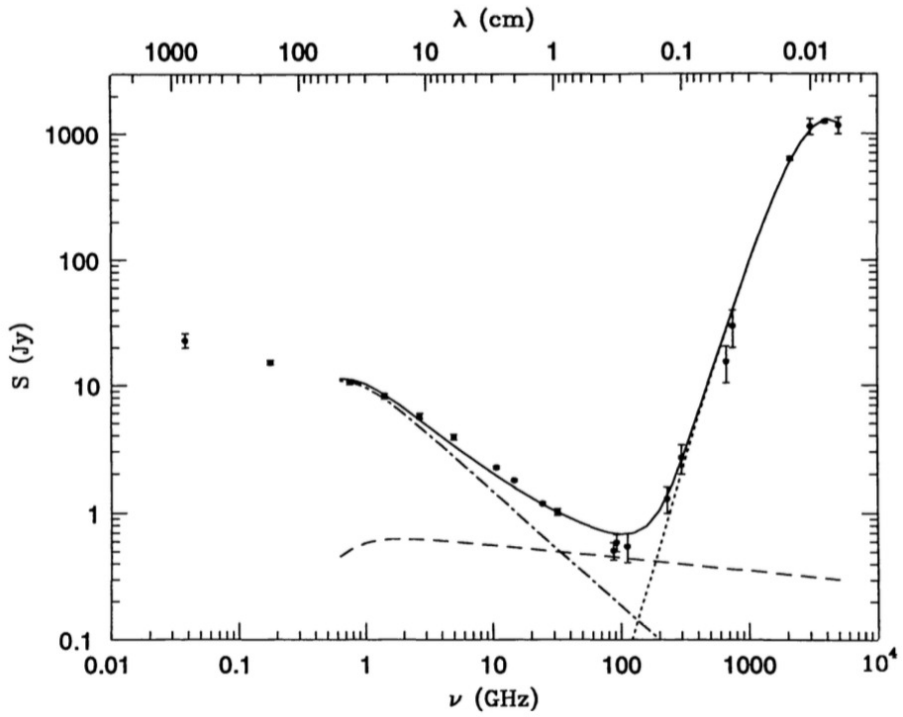

Figure 1.8. The observed radio-to-FIR SED of M82 (Condon 1992). Synchrotron (dot-dash line), free-free (dashed line), and dust (doted line) components are dominant at this wavelength.

mostly associated with supernova remnants. The free-free emission comes from H_{II} regions containing ionizing stars. The flux of the free-free emission is difficult to measure directly, because the flat spectrum (index $= -0.1$ in the optically thin regime) makes it weaker than the synchrotron emission (index ~ -0.8) below 30 GHz. The FIR continuum is represented by a modified blackbody spectrum which is emitted by interstellar dust grains heated by stars to temperatures between 20 - 200 K. High-resolution multi-wavelength observations are required to distinguish these three components. Past studies of the radio-to-FIR SED for U/LIRGs (e.g., U et al. 2012) had focused on the global properties (e.g., total SFR) due to the limited angular resolution at higher frequency (> 100 GHz). In this Thesis, we focus on the sub-kpc properties of the radio-to-FIR SED of the nearby starburst-dominated LIRG NGC 1614 using Atacama Large Millimeter/submillimeter Array (ALMA) and Very Large Array (VLA).

1.3.2 Rotational Transitions of CO

Recent single-dish and *Herschel* spectroscopic observations successfully detected bright high-J CO emission ($J = 4 - 3$ up to $30 - 29$; van der Werf et al. 2010; Rangwala et al. 2011; Rosenberg et al. 2012; Papadopoulos et al. 2012; Meijerink et al. 2013; Pellegrini et al. 2013; Kamenetzky et al. 2014; Lu et al. 2014; Schirm et al. 2014; Falstad et al. 2015; Mashian et al. 2015; Rosenberg et al. 2015) from nearby U/LIRGs, as well as lower-J CO lines (Michiyama et al. 2016, and references therein). The observational evidence of extreme CO excitation in U/LIRGs is explained by a combination of several heating models of interstellar medium (ISM) which consists of cosmic-ray dominated regions (CRDRs), photon dominated regions (PDRs), X-ray dominated regions (XDRs), and/or mechanically dominated regions, because coarse single-dish beams ($\sim$ 10 kpc) are not possible to distinguish many molecular conditions (Papadopoulos 2010; van der Werf et al. 2010; Bayet et al. 2011; Aalto 2013; Meijerink et al. 2013, see Figure 1.9). High-resolution imaging of various CO lines is an important way to investigate the multiple phases of the molecular ISM.

Interferometric studies of CO (6–5) transitions in nearby LIRGs showed that the distribution of the CO (6–5) emission is compact compared to the extended lower-J CO emission (Matsushita et al. 2009; Sliwa et al. 2013, 2014; Xu et al. 2014; Rangwala et al. 2015; Xu et al. 2015; Zhao et al. 2016), suggesting that CO (6–5) probes warmer and denser gas directly related to the nuclear activities. However, a direct comparison among distributions of multiple CO transitions is not straightforward as we are limited in angular resolution for the low-J lines, sensitivities and uv-coverages vary, and the high-J lines require good weather making observations scarce from the ground. In this Thesis, we present high-resolution, high-sensitivity, and uv-matched ALMA observations of the nearby starburst-dominated merging LIRG NGC 1614 in order to understand the distribution and kinematics of multiple CO lines and their excitation conditions in the nuclear region. We investigate lower-J CO lines up to $J_{\rm upp} = 6$, which are thought to be mainly excited by star-forming activities.

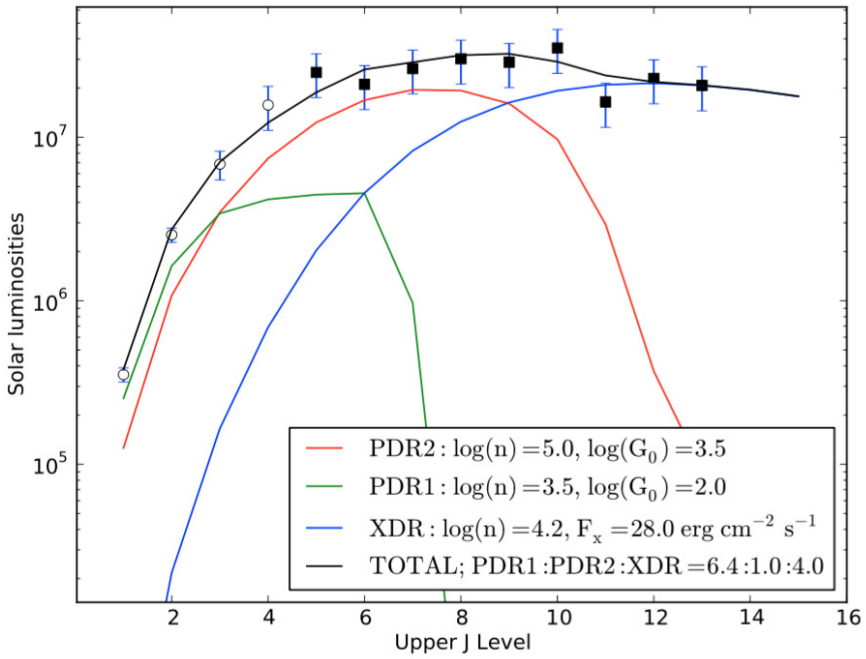

Figure 1.9. CO spectral line energy distribution (SLED) of the nearby ULIRG Mrk 231 (van der Werf et al. 2010). Colored lines indicate two model PDR components (red and green lines) and an XDR component (blue line).

1.3.3 Other Molecular Rotational Lines

Methanol

Bright thermal rotational transitions of methanol (CH_3OH) are often used as a tracer of extragalactic shocks, which are established by a large number of unbiased wide-band mm/sub-mm molecular line surveys toward galaxies over the last decade (Takano et al. 2014, and references therein). Extragalactic CH_3OH observations found that some of the galaxies have X_{CH_3OH} larger than $\sim 10^{-8}$ at the nuclei, arms, and bars with $\sim$ 100 pc resolution (e.g., IC 342; Meier & Turner 2005). Purely gas-phase chemistry cannot explain these observational evidences, because the formation process of CH_3OH in gas-phase is not efficient to produce X_{CH_3OH} greater than $\sim$ (1-3) $\times$ 10^{-9} (Lee et al. 1996). Alternatively, high CH_3OH abundance is believed to arise from a series of hydrogenations of CO on dust grain surfaces under a low-

temperature ($\sim$ 10 K) condition (Watanabe et al. 2003), because interstellar icy mantles are rich in CH_3OH ($\sim 10^{-6}$; e.g., Schutte et al. 1991). After the production on dust, it requires high temperature (i.e., hot-core chemistry; e.g., Garrod et al. 2008) or energetic heating (i.e., shock chemistry; e.g., Viti et al. 2011) mechanisms to heat the dust and then sublime CH_3OH into gas-phase. On the other hand, CH_3OH molecules are easily destroyed by UV radiation due to starburst or AGN without shielding (A_V $\sim$ 5; Martín et al. 2009). Thus, CH_3OH requires hot-core like or shocked ISM without strong UV radiation field to achieve an observable abundance. When hot-core like environment is excluded, CH_3OH lines become an excellent extragalactic shock tracer in molecular ISM.

However, most of the previous studies have so far mainly focused on nearby, bright galaxies or their nuclear regions (Henkel et al. 1987; Meier & Turner 2005; Martín et al. 2006a,b; Usero et al. 2006; García-Burillo et al. 2010; Aladro et al. 2011; Costagliola et al. 2011; Martín et al. 2011; Meier & Turner 2012; Davis et al. 2013; Meier et al. 2014; Takano et al. 2014; Watanabe et al. 2014; Aladro et al. 2015; Costagliola et al. 2015; Nakajima et al. 2015; Galametz et al. 2016; Nishimura et al. 2016). In this Thesis, we present multiple CH_3OH line observations toward the nearby merging LIRG VV 114, which are followup observations of our previous CH_3OH (2_K–1_K) detection at Overlap (Saito et al. 2015), in order to test kpc-scale shocks in molecular ISM due to a gas-rich galaxy-galaxy collision.

Dense Gas Tracers

Rotational transitions of HCN have high optically-thin critical densities ($n_{\rm crit}$) of $\sim 10^{5.5}$ cm^{-3}, $10^{7.0}$ cm^{-3}, and $10^{7.4}$ cm^{-3} at J = 1–0, 3–2, and 4–3, respectively, when assuming collisional excitation with H_2 and kinetic temperature ($T_{\rm kin}$) of 20 K. Since rotational transitions of HCO^+, a molecular ion, also have high optically-thin $n_{\rm crit}$ of $\sim 10^{4.7}$ cm^{-3}, $10^{6.1}$ cm^{-3}, and $10^{6.5}$ cm^{-3} at J = 1–0, 3–2, and 4–3, respectively, both HCN and HCO^+ are known to be excellent unbiased tracers of dense molecular ISM (e.g., Papadopoulos 2007; Shirley 2015). A tight linear correlation between log $L_{\rm FIR}$ (or star formation rate, SFR) and log $L'_{\rm dense}$ (or $M_{\rm dense}$) observed by HCN,

HCO^+, or other molecular species (e.g., Gao & Solomon 2004a,b; Graciá-Carpio et al. 2008; García-Burillo et al. 2012; Zhang et al. 2014; Privon et al. 2015; Usero et al. 2015; Stephens et al. 2016) was found in nearby spiral galaxies and U/LIRGs, suggesting that galaxies have a nearly constant (universal) SFR per dense gas mass (i.e., dense gas star formation efficiency; SFE_{dense}). This is consistent with the correlation observed by CO (3–2), which has a similar n_{crit} to HCO^+ (1–0), almost linearly correlates with log L_{FIR} (e.g., Iono et al. 2009; Leech et al. 2010; Mao et al. 2010; Wilson et al. 2012, but see also Michiyama et al. 2016 for a super-linear relation for gas-rich merging galaxies). Recent numerical simulations succeeded in reproducing such a linear correlation between log L_{FIR} and log L'_{dense} (e.g., Narayanan et al. 2008).

For multiple CO transitions in U/LIRGs, Greve et al. (2014) found a decreasing trend of the slope as J increases at least up to $J = 13$–12, which can be explained by a substantial contribution of additional warm and dense gas components to the higher-J line luminosities possibly (mechanically) heated by supernovae, stellar winds and/or AGN outflow (i.e., additional heating sources rather than radiation from star-forming regions are required) (see also Kamenetzky et al. 2016). On the other hand, relatively weak intensities of HCN and HCO^+ make it harder for us to study such J dependence of the slope of HCN and HCO^+ from galaxy to galaxy (or from region to region).

Contrary to excitation of a molecular species, molecular line intensity ratios between different species have been broadly studied for nearby starburst galaxies and U/LIRGs (Aalto 2013, and references therein). Some combination ratios of bright molecular lines have been proposed to be used to diagnose physical and chemical processes involved in starburst and accreting supermassive black hole (i.e., AGN) hidden inside their nuclear regions (e.g., $^{12}CO/^{13}CO$, HCN/CO, HCN/HCO^+, HCN/HNC, CN/HCN; Aalto et al. 1991; Sakamoto et al. 1997; Kohno et al. 2001; Aalto et al. 2002; Gao & Solomon 2004a,b; Meier & Turner 2005; Costagliola et al. 2013). Especially, HCN/HCO^+ line intensity ratios for given J are one of the established diagnostic tracers of AGN in mm and sub-mm wavelengths, and observational case studies of the ratios have been recently published for some bright galaxies (Kohno et al. 2001; Kohno 2005; Graciá-Carpio et al. 2006; Imanishi et al. 2007; Papadopoulos 2007;

Krips et al. 2008; Costagliola et al. 2011; Hsieh et al. 2012; Imanishi & Nakanishi 2013a,b; Iono, Saito et al. 2013; Izumi et al. 2013; García-Burillo et al. 2014; Imanishi & Nakanishi 2014; Aalto et al. 2015a; Aladro et al. 2015; Izumi et al. 2015; Martín et al. 2015; Saito et al. 2015; Imanishi et al. 2016a,b,c; Izumi et al. 2016; Privon et al. 2016), although a few observational and theoretical studies address the excitation state of both molecules (e.g., Krips et al. 2008; Izumi et al. 2013; Papadopoulos et al. 2014; Spilker et al. 2014; Kazandjian et al. 2015; Tunnard et al. 2015). Understanding excitation of dense molecular gas is a natural next step to establish a overall picture of dense molecular gas and its relation to star formation and AGN. U/LIRGs are ideal sources to study the excitation of the HCN and HCO^+ lines as the occurrence of high L_{FIR} suggests that the dense material is abundant near the nuclear region of these galaxies, and even the high-J transitions can be detected with relatively short observing time. Accordingly, we have been using ALMA in the past years to study the dense gas in a merging galaxy VV 114 (Iono, Saito et al. 2013; Saito et al. 2015, 2016b, but see also Yun et al. 1994; Iono et al. 2004b; Wilson et al. 2008; Sliwa et al. 2013). In this Thesis, we present spatially-resolved properties of the HCN and HCO^+ excitation toward VV 114.

1.4 Observation: Merging LIRGs

In order to test molecular line diagnostics listed in the previous Section using spatially-resolved observational data, we observed two nearby merging LIRGs, NGC 1614 and VV 114. Here we summarize the characteristics of these galaxies.

1.4.1 NGC 1614

NGC 1614 is one of the nearby (D_L = 68.6 Mpc; 1″= 330 pc) gas-rich LIRGs (log ($L_{IR}/L_\odot$) = 11.65; Armus et al. 2009) with merging signatures such as a tidal tail clearly seen in the HI (Figure 1.10a; Hibbard & Yun 1996) and optical images (Figure 1.10b; Alonso-Herrero et al. 2001). The total star formation rate (SFR) is $\sim$ 75 $M_\odot$ yr^{-1} based on the measurement of extinction-corrected Paschen α emission (Tateuchi

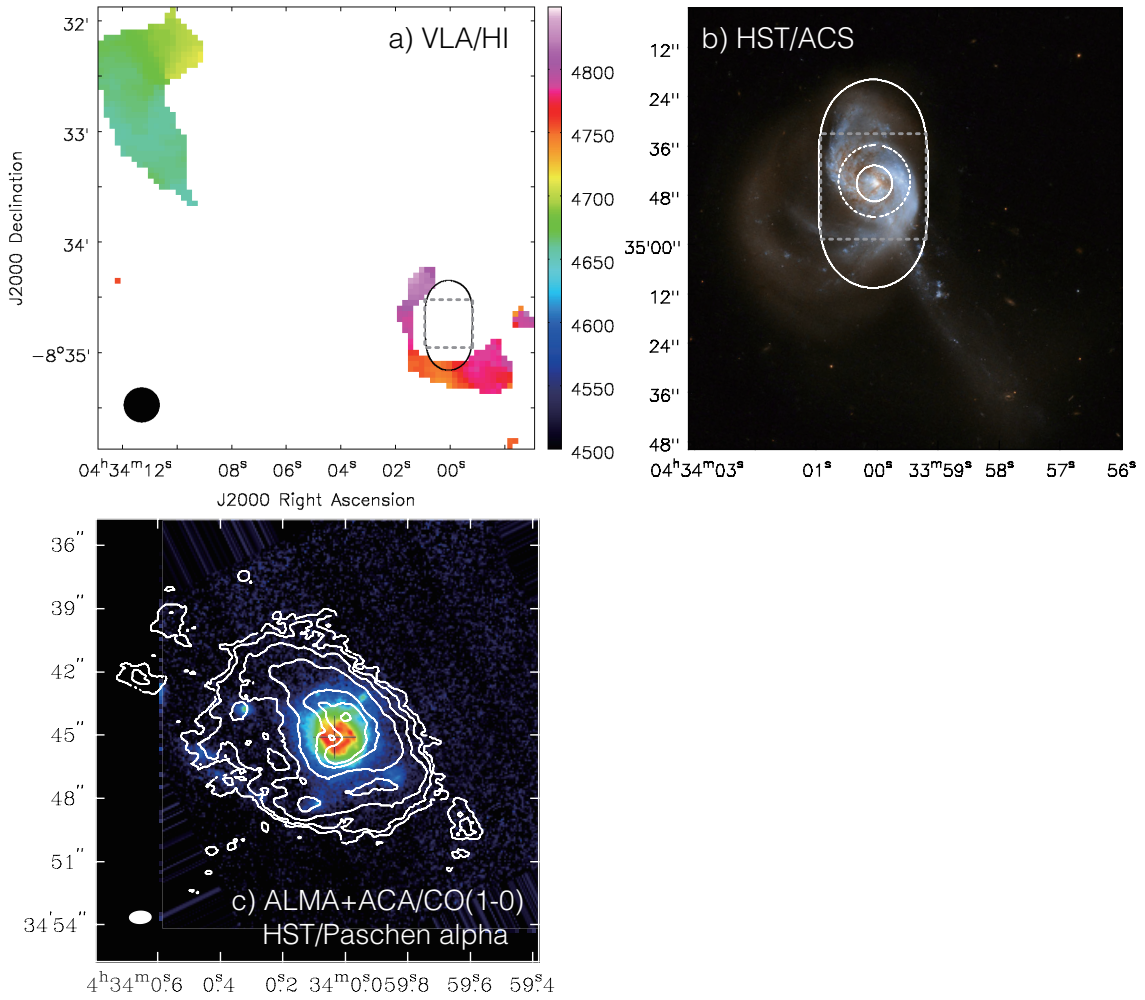

Figure 1.10. (a) HI image of NGC 1614 obtained by the Very Large Array (Hibbard & Yun 1996). The velocity field in color scale ranges from 4500 km s^{-1} to 4850 km s^{-1}. The black ellipse shows the field of view of the Band 6 observation. The dashed square corresponds to the imaging area of Figure 1.10c. (b) HST/ACS image of NGC 1614 [Credit: NASA, ESA, the Hubble Heritage Team (STScI/AURA)-ESA/Hubble Collaboration and A. Evans (University of Virginia, Charlottesville/NRAO/Stony Brook University)]. The white ellipse shows the field of view of the Band 6 observation. The dashed and solid circles show the field of view of the Band 7 and Band 9 observations, respectively. The field of view of the Band 3 observation is three times larger than that of the Band 7 observation. (c) ACA-combined CO (1–0) integrated intensity contour (see Section 3) overlaid on Paschen α image (Alonso-Herrero et al. 2001). The contours are 8.87 $\times$ (0.03, 0.06, 0.12, 0.24, 0.48, 0.64, and 0.96) Jy $beam^{-1}$ km s^{-1}. The black cross indicates the nucleus which is detected in Pa α and the radio continuum emission (Olsson et al. 2010; Herrero-Illana et al. 2014). The imaging area is same as CO images shown in Section 3.

et al. 2015). Numerical simulation by Väisänen et al. (2012) suggested that the galaxy is formed by a gas-rich minor merger with the mass ratio of $\sim$ 1/3-1/5. Low-J CO observations revealed that the system has a nuclear gas ring with an extended rotating gas disk and an arm-like structure (Olsson et al. 2010; König et al. 2013; Sliwa et al. 2014). Visually, NGC 1614 has been classified as a merger remnant because of no nearby companion (Rothberg & Joseph 2004), and is one of the remnants with a rotating molecular gas disk which possibly evolves into a late-type galaxy (Ueda et al. 2014). The starburst ring is detected in the 5 GHz and 8.4 GHz radio continuum, Paschen α (Figure 1.10c), PAH, and CO (6–5) emission (Alonso-Herrero et al. 2001; Olsson et al. 2010; Herrero-Illana et al. 2014; Xu et al. 2015), indicating a presence of strong SB along the ring (starburst ring). The radio and X-ray studies revealed little evidence for the presence of AGN (Herrero-Illana et al. 2014; Pereira-Santaella et al. 2015). This is consistent with the results from an AGN diagnostics using the HCN (4–3)/HCO^+ (4–3) line ratio (Costagliola et al. 2011; Imanishi & Nakanishi 2013a). In addition, Xu et al. (2015) argued that the non-detection of the nucleus in the ALMA 435 μm continuum image ruled out any significant AGN activity. We regard NGC 1614 as a starburst-dominated galaxy throughout this Thesis.

1.4.2 VV 114

VV 114 is one of the local luminous infrared galaxies ($D_{\rm L}$ = 87 Mpc, 1″= 400 pc, $L_{\rm IR} = 10^{11.69}\ L_{\odot}$; Armus et al. 2009). It is considered to be a mid-stage gas-rich major merger with the nuclear separation of $\sim$ 6 kpc (Figure 1.11). The system has a (molecular and ionized) gaseous and dust filamentary structure ($\sim$ 4 kpc) across the galaxy disks (Yun et al. 1994; Frayer et al. 1999; Iono et al. 2004b; Wilson et al. 2008; Rich et al. 2011; Iono, Saito et al. 2013; Sliwa et al. 2013; Saito et al. 2015; Tateuchi et al. 2015), which is not found in optical, FUV, and X-ray images (Scoville et al. 2000; Goldader et al. 2002; Grimes et al. 2006).

Our previous ALMA observations (Iono, Saito et al. 2013; Saito et al. 2015) revealed that the filament has multiple star-forming dense gas clumps at Overlap, one of which only has a CH_3OH (2_K–1_K) peak. In contrast, two massive clumps in the east-

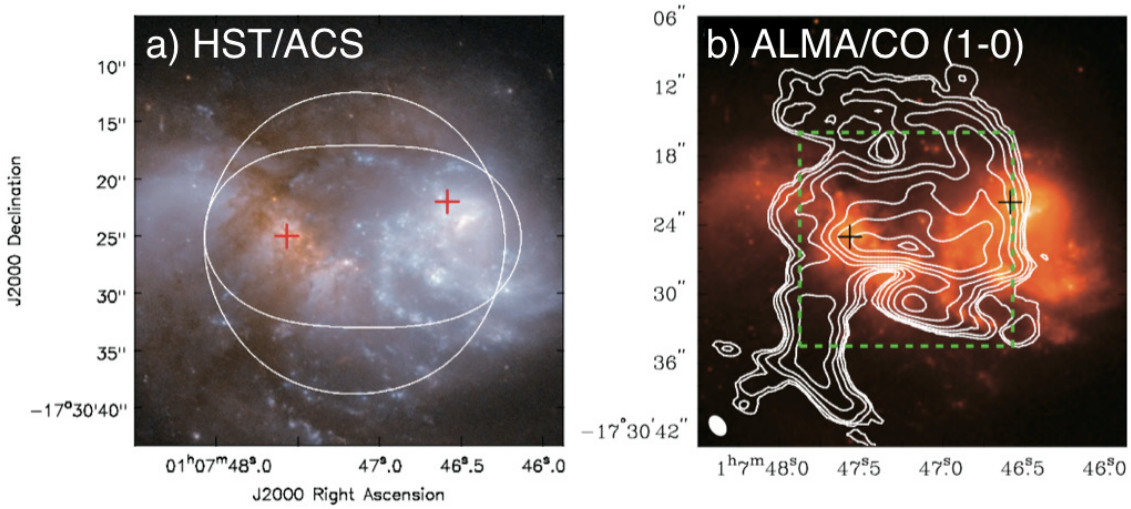

Figure 1.11. (a) HST/ACS image of VV 114 [Credit: NASA, ESA, the Hubble Heritage Team (STScI/AURA)-ESA/Hubble Collaboration and A. Evans (University of Virginia, Charlottesville/NRAO/Stony Brook University)]. The white circle and ellipse show the field of view of the Band 7 observation (Iono, Saito et al. 2013; Saito et al. 2015). The crosses show the K-band nuclei (Tateuchi et al. 2015). (b) ^{13}CO (1–0) integrated intensity image overlaid on the HST/ACS/F435W image of VV 114 (Saito et al. 2015).

ern nucleus, which harbor compact starburst ("SB") and putative hard X-ray AGN ("AGN"), are bright in CN, HCN, and HCO^+ lines. This indicates that VV 114 has kpc-scale chemical variations along the filament. However, since we were only able to observe ten molecular lines, the chemical composition in the filament is not fully understood, and thus we followed up VV 114 with ALMA spectral scan mode.

1.5 This Thesis

One of the problems of previous observational studies toward U/LIRGs at millimeter and submillimeter wavelengths is less or no spatial information. Even if some interferometric observations are available (e.g., Arp 220), the spatial resolutions, sensitivities, and missing flux effects do not match with each other, making it harder to discuss multiple molecular line and continuum emissions simultaneously. The only way to solve this problem is to observe with a uniform angular resolution, sensitiv-

ity, and *uv*-coverage. Obtaining such high-quality, uniform data at millimeter and submillimeter wavelength is very challenging, and now only achieved by the superb angular resolution and sensitivity capabilities of VLA and ALMA, respectively.

The main scope of this Thesis is to spatially resolve millimeter/submillimeter emission in U/LIRGs and to study physical properties of molecular gas and its relation to continuum sources. For this purpose, we made molecular line observations toward NGC 1614 and VV 114 with ALMA. We also used ALMA and VLA archival data in order to supplement our ALMA datasets.

This Thesis is organized as follows. We show the details of observations and data reduction, results, discussions, and a brief summary in each Chapter (Chapter 2-5) in order to clarify our achievements and future perspectives for each study. In Chapter 2, we study spatial properties of the radio-to-FIR SED for NGC 1614 by using ALMA and VLA data (Saito et al. 2016a). CO rotational transitions which were simultaneously observed with the SED were summarized in Chapter 3 (Saito et al. 2016c submitted). Next, we show the results related to ALMA spectral imaging scans toward VV 114 (Chapter 4 and 5). In Chapter 4, we show data including multiple rotational transitions of methanol (Saito et al. 2016b). Multiple rotational transitions of dense gas tracers (i.e., HCN and HCO^+) as well as HCN (1–0) and CS (7–6) lines are studied in Chapter 5 (Saito et al. 2017 in preparation). Finally, we summarize this Thesis and provide future development plans in Chapter 6.

We have adopted $H_0 = 70$ km s^{-1} Mpc^{-1}, $\Omega_{\rm m} = 0.3$, and $\Omega_\Lambda = 0.7$ throughout this Thesis.

Chapter 2

Spatially-resolved Radio-to-FIR SED of the Nearby LIRG NGC 1614

2.1 Abstract

In this Chapter, we present the results of ALMA 108, 233, 352, and 691 GHz continuum observations and VLA 4.81 and 8.36 GHz observations of the nearby luminous merger remnant NGC 1614. By analyzing the beam ($1\farcs0 \times 1\farcs0$) and uv ($\geq$ 45 kλ) matched ALMA and VLA maps, we find that the deconvolved source size of lower frequency emission ($\leq$ 108 GHz) is more compact (420 pc $\times$ 380 pc) compared to the higher frequency emission ($\geq$ 233 GHz) (560 pc $\times$ 390 pc), suggesting different physical origins for the continuum emission. Based on an SED model for a dusty starburst galaxy, it is found that the SED can be explained by three components, (1) non-thermal synchrotron emission (traced in the 4.81 and 8.36 GHz continuum), (2) thermal free-free emission (traced in the 108 GHz continuum), and (3) thermal dust emission (traced in the 352 and 691 GHz continuum). We also present the spatially-resolved (sub-kpc scale) Kennicutt-Schmidt relation of NGC 1614. The **result suggests** a systematically shorter molecular gas depletion time in NGC 1614 (average $\tau_{\rm gas}$ of 49 - 77 Myr and 70 - 226 Myr at the starburst ring and the outer region, respectively) than that of normal disk galaxies ($\sim$ 2 Gyr) and a mid-stage merger VV 114 (= 0.1 - 1 Gyr). This implies that the star formation activities in

U/LIRGs are efficiently enhanced as the merger stage proceeds, which is consistent with the results from high-resolution numerical merger simulations.

2.2 Observation and Data Reduction

2.2.1 ALMA Observations

Observations toward NGC 1614 were carried out as an ALMA cycle 2 program (ID = 2013.1.01172.S, PI: T. Saito) using thirty-five 12 m antennas. The band 3 and 6 receivers were tuned to the ^{12}CO (1–0) and ^{12}CO (2–1) line emission in the upper sideband. The band 3 data were obtained on August 30, 2014 (on-source time of $T_{\rm integ}$ = 16.9 min.) using the projected baseline lengths of 28 - 1060 m. The band 6 data were obtained on December 8, 2014 ($T_{\rm integ}$ = 22.0 min.) using the projected baseline lengths of 15 - 349 m. Each spectral window had a bandwidth of 1.875 GHz with 3840 channels, and two spectral windows were set to each sideband to achieve a total frequency coverage of $\sim$ 7.5 GHz. For the band 3 and 6 observations, J0423-0120 was used for the bandpass and phase calibrations, and Uranus was used for the flux calibration. The main target lines of the ALMA program were the ^{12}CO transitions (Section 3), and we subtracted all line features in the bandpass in order to obtain the continuum emission (Section 2.2.3).

2.2.2 Archival ALMA and VLA Data

NGC 1614 was observed using ALMA band 7 and band 9 as two cycle 0 programs (ID = 2011.0.00182.S, PI: C. K. Xu and 2011.0.00768.S, PI: A. Usero). We obtained the calibrated archival visibility data from the ALMA archive (see Sliwa et al. 2014 and Xu et al. 2015 for the details of the data). The band 7 data were obtained on July 31 and August 14, 2012 ($T_{\rm integ}$= 88.8 min.) with a projected baseline length of 18 - 1341 m. The band 9 data were obtained on August 13 and 28, 2012 ($T_{\rm integ}$ = 24.7 min.) with a projected baseline length of 20 - 394 m. J0423-0120 was used for the bandpass and phase calibrations for the band 9 observations. J0522-364 was used

for the bandpass calibration, while J0423-013 was used for the phase calibration for the band 7 observations. For the band 7 and 9 observations, Callisto and Ceres were used for the flux calibration, respectively.

NGC 1614 was observed using VLA C-band (4.89 GHz) and X-band (8.49 GHz). We use the archival calibrated visibility data (see Condon et al. 1990, Schmitt et al. 2006, Olsson et al. 2010, and Herrero-Illana et al. 2014 for the details of the data). The C-band observations were carried out using twenty-four to twenty-seven 25 m antennas. The C-band data were obtained on May 15, 1986 (A config.), August 10, 1986 (B config.), November 23, 1987 (B config.), June 17, 1994 (B config.), September 16, 1998 (B config.), and July 27, 1999 (A config.). The combined data has the projected baseline lengths of 137 - 36,605 m. The X-band observations were carried out using twenty-five to twenty-seven 25 m antennas. The X-band data were obtained on August 3, 1993 (C config.), July 27, 1999 (A config.), July 9, 2001 (C config.), July 8, 2003 (A config.), October 15, 2003 (B/A config.), and November 6, 2004 (A config.). The combined data has the projected baseline lengths of 32 - 36,620 m. For the C-band observations, 3C48, 3C138, J0134+329, and J0420-013 were used for the flux calibration, and J0019-000 and J0423-013 were used for the phase calibration. For the X-band observations, 3C48 and J0134+329 were used for the flux calibration, and J0423-013 was used for the phase calibration.

2.2.3 Data Reduction and Imaging

For analyses in this Section, we assume that the missing flux effect (i.e., absence of short spacings) is negligible because we only discuss the structure that is smaller than the "maximum recoverable scale" (MRS) of each observation. This is given by,

$$\mathrm{MRS} \approx 0.6 \times \frac{\lambda_{\mathrm{obs}}}{L_{min}} \tag{2.1}$$

where λ_{obs} is the observed wavelength and L_{min} is the minimum baseline in the array configuration (Lundgren 2013)[1]. The MRS is estimated from the minimum baseline length of the assigned configuration and the observed frequency. Since the minimum

[1]https://almascience.nao.ac.jp/documents-and-tools/cycle-2/alma-technical-handbook

Table 2.1. Imaging properties of continuum emission.

Telescope	Band	$\nu_{\rm rest}$ (GHz)	MRS ($''$)	uv-weight	Beam size ($''$)	S_ν (mJy)	Recovered flux (%)	Ref.
(1)	(2)	(3)	(4)	(5)	(6)	(7)	(8)	(9)
VLA	C	4.81	4.6	uniform	1.0 × 1.0	26.69 ± 0.13	42 ± 8	1, a
VLA	X	8.36	4.6	briggs	1.0 × 1.0	17.66 ± 0.07	...	b
ALMA	B3	108	4.6	briggs	1.0 × 1.0	6.39 ± 0.13	...	This work
ALMA	B6	233	4.6	uniform	1.0 × 1.0	8.02 ± 0.36	...	This work
ALMA	B7	352	4.6	briggs	1.0 × 1.0	29.23 ± 0.23	18 ± 4	2, c
ALMA	B9	691	4.6	briggs	1.0 × 1.0	222.3 ± 11.2	27 ± 4	3, d

Note. — Column 4: Maximum recoverable scale (MRS) of each observations. This is defined by $\sim 0.6\,\lambda_{\rm obs}$/(minimum baseline length), where $\lambda_{\rm obs}$ is the observed wavelength. Column 5: Visibility (uv-plane) weighting for imaging. "briggs" means Briggs weighting with `robust` = 0.5. Column 6: The synthesized beam size. The images are convolved into the same resolution. Column 7: Integrated flux density enclosed with the 3σ contour. We only consider the statistical error in this column. The systematic error of absolute flux calibration is estimated to be 3%, 3%, 5%, 10%, 10%, and 15% for VLA/C. VLA/X, ALMA/B3, ALMA/B6, ALMA/B7, and ALMA/B9, respectively. Column 8: The ALMA/VLA flux divided by the single-dish flux. We consider the statistical and systematic error. Column 9: Reference of the single-dish flux (1 = Bicay et al. (1995), 2 = Dunne et al. (2000), and 3 = Dunne & Eales (2001)) and the interferometric data (a = Olsson et al. (2010), b = Schmitt et al. (2006), c = Sliwa et al. (2014), and d = Xu et al. (2015)).

baseline of all data shown in this Section is clipped at 45 kλ (i.e., minimum baseline of the band 9 observation) before imaging processes, the produced images have a same MRS of $4\farcs6$ ($\simeq$ 1.5 kpc). The image properties (e.g., MRS, uv weighting, and beam size) are listed in Table 2.1.

We used the delivered calibrated uv data for the band 3 and 6 observations, and the calibrated archival uv data for the others. The data processing was accomplished using `CASA` (version 4.2.2; McMullin et al. 2007). We convolved all images into a same beam ($1\farcs0 \times 1\farcs0$). We subtracted all strong line emission features (e.g., CO and CN) before the imaging of continuum emission by masking the velocity range of $\pm$ 500 km s^{-1} centered on their rest frequencies. This velocity range is consistent with the velocity of a putative CO (1–0) outflow ($|v - v_{\rm sys}| < 420$ km s^{-1}; García-Burillo et al. 2015). The rms level of 4.81, 8.36, 108, 233, 352, and 691 GHz images (Figure 2.1)

are 32, 7.4, 51, 143, 68, and 736 μJy, respectively. The systematic errors of absolute flux calibration are estimated to be 3%, 3%, 5%, 10%, 10%, and 15% for 4.81, 8.36, 108, 233, 352, and 691 GHz, respectively. Throughout this Section, the pixel scales of all images are set to 0.″2/pixel. The absolute positional accuracy of the ALMA and VLA images are estimated to be less than 10% of the synthesized beam size. Since the synthesized beam sizes before convolving into the 1.″0 × 1.″0 resolution are smaller than 1.″0, the positional accuracy is better than 0.″1 which is smaller than the pixel size.

2.3 Results

2.3.1 4.81, 8.36, and 108 GHz Emission

The continuum images at 4.81, 8.36, and 108 GHz show a nearly circular (face-on) morphology (Figures 2.1a, 2.1b, and 2.1c) with a deconvolved major axis and minor axis of 1.″28 ± 0.″03 (∼ 420 pc) and 1.″15 ± 0.″05 (∼ 380 pc), respectively. The source size is derived by fitting a 2D gaussian in the image plane using `imfit` in `CASA` as shown in Figure 2.2. The fitting parameters are listed in Table 2.2. The strongest peaks coincide with each other, and the peaks are ∼ 0.″8 west of the nucleus identified from the high resolution 5 GHz continuum using Multi-Element Radio Linked Interferometer Network (synthesized beam of 0.″2; Olsson et al. 2010) and Paschen α image using *HST*/NICMOS (Alonso-Herrero et al. 2001). The offset arises due to the asymmetric starburst ring structure (Herrero-Illana et al. 2014; Xu et al. 2015). All of the residual images show a same strong negative peak at the nuclear position and a same positive ring-like structure, suggesting all continuum images contain a similar structure. This structure may be related to the presence of the starburst ring which is seen in all high-resolution multi-wavelength images (Alonso-Herrero et al. 2001; Olsson et al. 2010; König et al. 2013; Herrero-Illana et al. 2014; Xu et al. 2015).

A comparison of the 4.81 GHz flux observed by the VLA with the 4.83 GHz flux obtained by the Green Bank 91 m (GBT) telescope (Bicay et al. 1995) suggests that

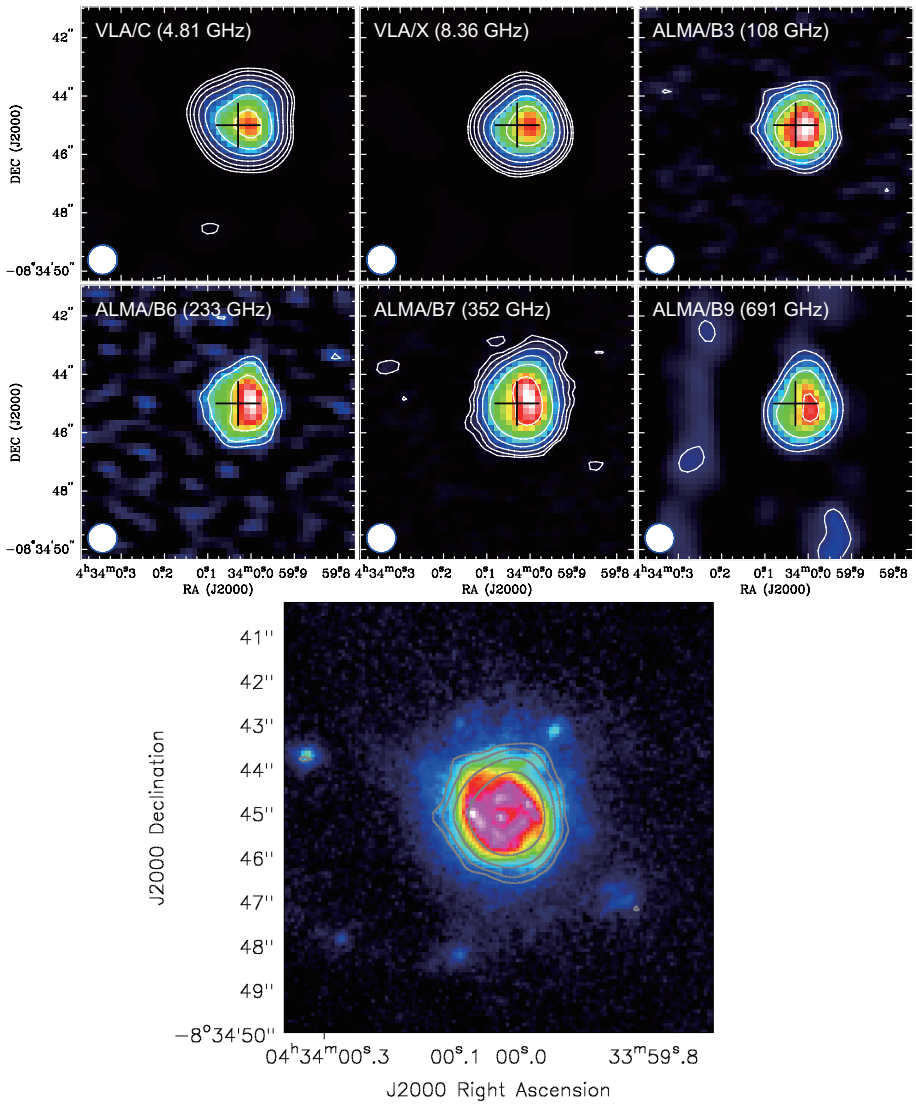

Figure 2.1. (top) The 4.81 GHz to 691 GHz continuum images of NGC 1614. The minimum uv ranges of all data are clipped at 45 $k\lambda$ to have the same MRS of 4.″6. The convolved beams (1.″0 × 1.″0) are shown in the lower left. The nth contours are at $3{\cdot}2^{n-1}\sigma$ except for the 691 GHz image ($2^n\sigma$) (n = 1, 2, 3 ...). The rms noise are 45, 25, 51, 143, 68, and 4800 μJy beam^{-1} for VLA/C, VLA/X, ALMA/B3, ALMA/B6, ALMA/B7, and ALMA/B9, respectively. The black cross indicates the peak position (nucleus) which is provided by the high-resolution image of the radio continuum (Olsson et al. 2010). (bottom) The 108 GHz contour image overlaid on the Paschen alpha color image.

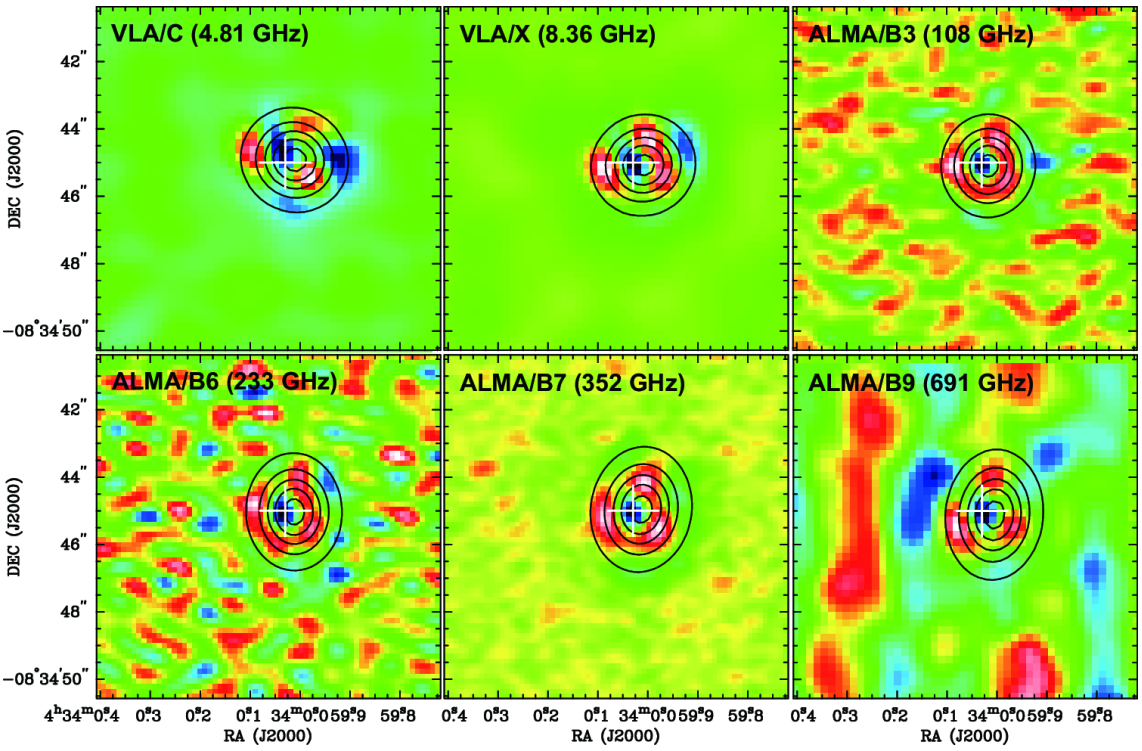

Figure 2.2. Model (contour) images and residual (color) images of the 2D Gaussian fitting. The contours are 10, 30, 50, 70, and 90% of the peak flux. The peak values are 14.3, 9.4, 2.6, 2.9, 9.1, and 95.6 mJy beam^{-1} for VLA/C, VLA/X, ALMA/B3, ALMA/B6, ALMA/B7, and ALMA/B9, respectively. The residual in color scale ranges from the minimum to maximum pixel value. The minimum values are -1.0, -1.0, -0.4, -0.6, -1.9, and -17.4 mJy beam^{-1} while the maximum values are 1.2, 0.7, 0.2, 0.5, 1.1, and 15.1 mJy beam^{-1} for VLA/C, VLA/X, ALMA/B3, ALMA/B6, ALMA/B7, and ALMA/B9, respectively. The white cross indicates the peak position (nucleus) which is provided by the high-resolution image of the radio continuum (Olsson et al. 2010).

the VLA data recovers 42 ± 8 % of the total emission (Table 2.1).

2.3.2 233, 352, and 691 GHz Emission

The continuum images at 233, 352, and 691 GHz show a slightly elongated elliptical morphology from the south to the north (Figures 2.1d, 2.1e, and 2.1f) with deconvolved major axes, minor axes, and position angles of 1.″70 ± 0.″09 (∼ 560 pc), 1.″18 ± 0.″13 (∼ 390 pc), and 176°.1 ± 2°.3, respectively (Figure 2.2 and Table 2.2).

Table 2.2. Results of the 2D gaussian fitting.

Band	R.A.	Decl.	$R_{\rm deconv}$*	P.A.	Axis ratio†	i‡
	(h m s)	(d m s)	($''$)	(°)		(°)
(1)	(2)	(3)	(4)	(5)	(6)	(7)
C	4:34:00.013	−8.34.44.918	1.279 ± 0.006	60.56 ± 0.49	0.918 ± 0.006	23.41 ± 0.04
X	4:34:00.012	−8.34.45.057	1.214 ± 0.006	115.49 ± 0.40	0.926 ± 0.007	22.16 ± 0.05
B3	4:34:00.017	−8.34.45.096	1.350 ± 0.026	176.2 ± 2.1	0.859 ± 0.027	30.85 ± 0.05
B6	4:34:00.013	−8.34.45.030	1.626 ± 0.058	1.4 ± 2.1	0.734 ± 0.048	42.75 ± 0.07
B7	4:34:00.014	−8.34.44.959	1.781 ± 0.015	171.88 ± 0.48	0.728 ± 0.011	43.26 ± 0.02
B9	4:34:00.006	−8.34.45.103	1.681 ± 0.063	174.89 ± 0.78	0.630 ± 0.050	50.95 ± 0.08

Note. — Column 4: Deconvolved source size which is defined as $[R_{\rm conv}$ - $(\theta_{\rm HPBW}/2)^2]^{0.5}$, where $R_{\rm conv}$ is the estimated major axis size of the gaussian fitting and $\theta_{\rm HPBW}$ is the synthesized beam size. Column 6: Value which the minor axis divided by the major axis. Column 7: Inclination with an assumption of a thin disk. See text.

The radial distribution of each emission (Figure 2.3a) suggests that the low frequency emission ($\leq$ 108 GHz) is systematically more compact relative to the high frequency emission ($\geq$ 233 GHz). The peak positions coincide with each other as well as the low frequency emission.

Assuming a circular disk geometry for simplicity, we estimate the inclination of the disk from the axial ratio (i.e., the minor axis divided by the major axis) using,

$$\cos i = \frac{a}{b} \tag{2.2}$$

where i is the inclination of the disk, a is the minor axis, and b is the major axis. The derived i is listed in Table 2.2. We found that 4.81, 8.36, and 108 GHz disks are nearly face-on (24.86 ± 0.02°on average), while those of 233, 352, and 691 GHz disks are slightly inclined (46.04 ± 0.16°on average) or more elongated toward the north-south direction.

The difference of the apparent morphology between the low frequency and the high frequency emission is caused by the differences of physics which produces the continuum emission. Assuming the higher frequency emission arises from the cold dust component and the lower frequency emission arises from the thermal bremsstrahlung

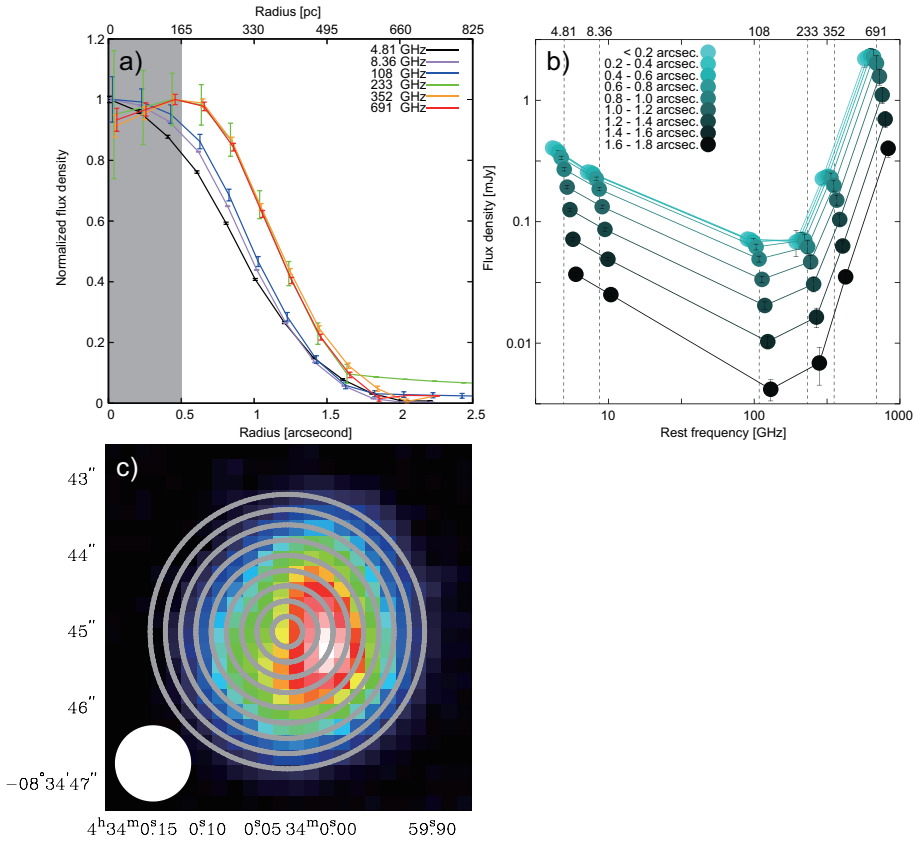

Figure 2.3. (a) Radial distribution of each emission. The shaded area indicates the convolved beam size. We only consider the statistical error in this plot because the y-axis is the normalized flux density. (b) Spatially-resolved SED. The color scale ranged from 0.″0 to 1.″8 indicates the radius of concentric rings which is shown in the right figure. (c) Concentric rings which are used for the photometry overlaid on the 691 GHz image. The grey solid rings indicate photometric regions where all the six continuum emission are detected. The convolved beam is shown in the bottom left corner.

and/or the non-thermal synchrotron which are associated with star-forming activities (see Section 2.4), the elongated higher frequency emission suggests that cold dust distribution is more extended toward the north-south direction and larger than the star forming regions. Deeper continuum observations with shorter baselines are necessary in order to trace more diffuse components.

The recovered fluxes at 352 and 691 GHz in the ALMA observations relative to those in the James Clerk Maxwell Telescope (JCMT; Dunne et al. 2000; Dunne &

Eales 2001) observations are 18 ± 4 and 27 ± 4 %, respectively. Large amounts of the 352 and 691 GHz emission are more extended than the MRS scale (∼ 1.5 kpc).

2.4 SED Modeling

2.4.1 Spatially-resolved Radio-to-FIR SED

We constructed the spatially-resolved SED of NGC 1614 (Figure 2.3b) from 4.81 to 691 GHz by measuring the flux densities contained in concentric rings defined by the width of 0.″2 (see Figure 2.3c). We note that the flux values between adjacent rings are not independent because the width of the ring is smaller than the convolved beam. However, since the continuum images are sufficiently resolved with the 1.″0 beam, this will not introduce any artificial bias in the discussion of the overall trend presented in the following sections. The shape of the SEDs are similar from region to region, while the total flux density systematically decreases as the ring radius increases. The most significant difference is the slope between the 108 and 233 GHz emission (i.e., the nuclear region shows a flatter spectrum). In order to understand the physical origins of the shape of the SED, we perform a simple SED fitting.

2.4.2 SED Formulation for Starburst-dominated Galaxies

We modeled the radio-to-FIR continuum emission by using the formulation described in Yun & Carilli (2002),

$$S(\nu_{\rm obs}) = (S_{\rm nth} + S_{\rm ff} + S_{\rm d})(1+z)\ {\rm Jy} \tag{2.3}$$

$$S_{\rm nth} = 25 f_{\rm nth} \nu_0^{-\alpha} \frac{\rm SFR}{M_\odot\ {\rm yr}^{-1}} D_{\rm L}^{-2} \tag{2.4}$$

$$S_{\rm ff} = 0.71 \nu_0^{-0.1} \frac{\rm SFR}{M_\odot\ {\rm yr}^{-1}} D_{\rm L}^{-2} \tag{2.5}$$

$$S_{\rm d} = 1.3 \times 10^{-6} \frac{\nu_0^3 \left[1 - e^{-(\nu_0/\nu_c)^\beta}\right]}{e^{(0.048\nu_0/T_d)} - 1} \frac{\rm SFR}{M_\odot\ {\rm yr}^{-1}} D_{\rm L}^{-2}, \tag{2.6}$$

where $S_{\rm nth}$, $S_{\rm ff}$, and $S_{\rm d}$ are the flux of non-thermal synchrotron, thermal bremsstrahlung (free-free), and thermal dust emission, respectively, ν_0 is the rest frequency in GHz, z

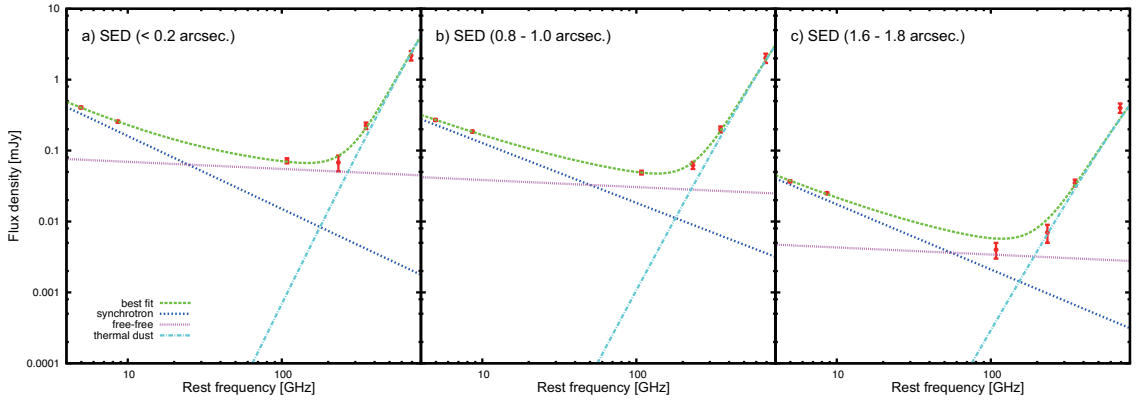

Figure 2.4. Results of the SED fitting for 3 photometric rings with the radius of (a) 0.″0 - 0.″2, (b) 0.″8 - 1.″0, and (c) 1.″6 - 1.″8. The blue, purple, and cyan lines show the best-fitted synchrotron, free-free, and dust continuum spectrum, respectively. The best-fitted spectrum is shown as the green line. Typical fitting error of the y-axis is 17%.

is the redshift, $f_{\rm nth}$ is the radio-FIR normalization term adopted by Condon (1992), α is the spectral index of non-thermal synchrotron emission, SFR is the star formation rate in $M_\odot$ yr^{-1}, $D_{\rm L}$ is the luminosity distance, ν_c is the critical frequency where the clouds become optically thick, β is the dust emissivity index, and T_d is the dust temperature.

This formulation is only valid for starburst-dominated galaxies (i.e., AGN contribution to the radio-to-FIR SED is negligible), because it is based on the assumption that all the three components are associated with massive star-forming activities (e.g., supernovae and their remnants, H II regions surrounding young stars, and dust particles heated by young massive stars). This assumption is applicable to NGC 1614 since multi-wavelength studies have so far found no significant evidence for an AGN (Alonso-Herrero et al. 2001; Imanishi & Nakanishi 2013a; Herrero-Illana et al. 2014; Xu et al. 2015). In order to minimize the number of free parameters, we fix z = 0.015938, $D_{\rm L}$ = 67.8 Mpc (Xu et al. 2015), ν_c = 2 THz (Yun & Carilli 2002), and $T_d = 35 \pm 2$ K (Xu et al. 2015) which is derived by using Spitzer/MIPS 24 μm and Herschel 70 - 500 μm data, in the fitting routine.

The results from the fit are listed in Table 2.3 and shown in Figure 2.4. The derived $f_{\rm nth}$ ranges between 0.43 - 1.45 (averaged $f_{\rm nth} = 0.66 \pm 0.13$). This is consistent with

Table 2.3. Results of the SED fitting.

Radius	$f_{\rm nth}$	α	β	$\log \Sigma_{\rm SFR}$ ($M_\odot$ yr^{-1} kpc^{-2})	$M_{\rm dust}$ ($\times 10^5$ $M_\odot$)	$\log \Sigma_{\rm H_2}$ ($M_\odot$ pc^{-2})	$\log \tau_{\rm gas}$ (yr)
(1)	(2)	(3)	(4)	(5)	(6)	(7)	(8)
0.″0 - 0.″2	0.56 ± 0.09	−1.03 ± 0.13	2.46 ± 0.16	$2.11^{+0.07}_{-0.08}$	3.3 ± 0.4	$3.80^{+0.11}_{-0.15}$	$7.69^{+0.19}_{-0.22}$
0.″2 - 0.″4	0.54 ± 0.09	−0.98 ± 0.15	2.40 ± 0.19	$2.08^{+0.08}_{-0.10}$	10.1 ± 1.3	$3.81^{+0.11}_{-0.15}$	$7.73^{+0.21}_{-0.23}$
0.″4 - 0.″6	0.51 ± 0.07	−0.92 ± 0.14	2.32 ± 0.19	$2.04^{+0.09}_{-0.11}$	17.1 ± 2.2	$3.82^{+0.11}_{-0.15}$	$7.78^{+0.22}_{-0.24}$
0.″6 - 0.″8	0.50 ± 0.07	−0.87 ± 0.11	2.22 ± 0.17	$1.97^{+0.08}_{-0.10}$	23.2 ± 2.9	$3.81^{+0.11}_{-0.15}$	$7.84^{+0.21}_{-0.23}$
0.″8 - 1.″0	0.52 ± 0.07	−0.84 ± 0.10	2.11 ± 0.16	$1.85^{+0.09}_{-0.11}$	25.9 ± 3.3	$3.74^{+0.11}_{-0.15}$	$7.89^{+0.22}_{-0.24}$
1.″0 - 1.″2	0.56 ± 0.08	−0.84 ± 0.10	2.02 ± 0.17	$1.68^{+0.09}_{-0.12}$	24.0 ± 3.0	$3.62^{+0.11}_{-0.15}$	$7.94^{+0.23}_{-0.24}$
1.″2 - 1.″4	0.70 ± 0.16	−0.87 ± 0.14	1.88 ± 0.26	$1.43^{+0.14}_{-0.21}$	19.6 ± 2.5	$3.46^{+0.11}_{-0.15}$	$8.03^{+0.32}_{-0.29}$
1.″4 - 1.″6	0.80 ± 0.40	−0.89 ± 0.22	1.80 ± 0.46	$1.15^{+0.22}_{-0.48}$	13.7 ± 1.7	$3.25^{+0.11}_{-0.15}$	$8.11^{+0.59}_{-0.37}$
1.″6 - 1.″8	0.76 ± 0.69	−0.92 ± 0.30	1.82 ± 0.72	$0.90^{+0.31}_{-0.90}$	8.7 ± 1.1	$2.99^{+0.11}_{-0.15}$	$8.09^{+1.01}_{-0.46}$

Note. — Column 1: Inside and outside radii of the concentric ring which are used for the photometry. Column 2: Multiplicative correction factor for non-thermal radio continuum emission. The $f_{\rm nth} = 1.0$ corresponds to the Galactic normalization adopted by Condon (1992). Column 3: The synchrotron spectral index. Column 4: Dust emissivity. Column 7: Molecular gas surface density assuming the gas-to-dust ratio of 264 ± 68. See text. Column 8: Gas depletion time which is defined by $\Sigma_{\rm SFR}/\Sigma_{\rm H_2}$ yr.

$f_{\rm nth}$ derived by global SED fitting, which typically shows the value of order unity (Yun & Carilli 2002). The synchrotron spectral index α shows a constant index of -0.9 within the error (Figure 2.5a). This is also consistent with global fitting values (e.g., Yun & Carilli 2002). The best-fit SFR surface density ($\Sigma_{\rm SFR}$) ranges between $10^{0.9}$ - $10^{2.1}$ $M_\odot$ yr^{-1} kpc^2 (Figure 2.5b), and this is similarly consistent with the $\Sigma_{\rm SFR}$ derived from the extinction-corrected Paschen α measurements (Herrero-Illana et al. 2014) and the thermal and non-thermal radio measurements decomposed using the 8.36 GHz continuum, near-IR extinction, and Paschen α equivalent width image (see Appendix A of Xu et al. 2015), when we take into account the missing flux of the radio-to-FIR SED. The SFR is mainly determined by $S_{\rm ff}$ which dominates the 108 GHz flux, because $S_{\rm ff}$ is only proportional to the SFR (Equation 2.5).

We calculated the dust optical depth at 691 GHz by $\tau_\nu = (\nu/\nu_c)^\beta$ in order to evaluate the contribution of dust extinction to the CO (6–5) emission. It is known that some U/LIRGs suffer from strong dust extinction in high-J CO emission (e.g., $\tau_{\rm 350GHz} > 1$ for Arp 220; Sakamoto et al. 2008; Rangwala et al. 2011). In contrast to these studies, we found that the $\tau_{\rm 691GHz}$ is optically thin (0.06 - 0.21) in the nuclear region of NGC 1614 (central 1.″8) suggesting that the dust extinction for the CO (6–5) emission is negligible (Figure 2.5c).

2.4.3 Dust Mass and Gas Surface Density Derivation

We calculate the dust mass from the 352 GHz (852 μm) continuum emission assuming that the 352 GHz flux is dominated by the cold dust component (Figure 2.4) and using the following equation (Wilson et al. 2008),

$$M_{\rm dust} = 74200\, S_{352}\, D_{\rm L}^2\, \frac{e^{17/T_d} - 1}{\kappa_{352}}\ M_\odot \tag{2.7}$$

where S_{352} is the 352 GHz flux in Jansky, $D_{\rm L}$ is the luminosity distance in Mpc, and κ_{352} is the dust absorption coefficient (0.43 ± 0.04 cm^2 g^{-1}; Li & Draine 2001). We assumed $T_{\rm d}$ of 35 ± 2 K (Xu et al. 2015). The derived dust masses range between 3.3 $\times$ 10^5 and 2.6 $\times$ 10^6 $M_\odot$ (Table 2.3). We note that we used the Li & Draine (2001) dust model, because the κ_{352} derived from the SED fitting has a large error and the

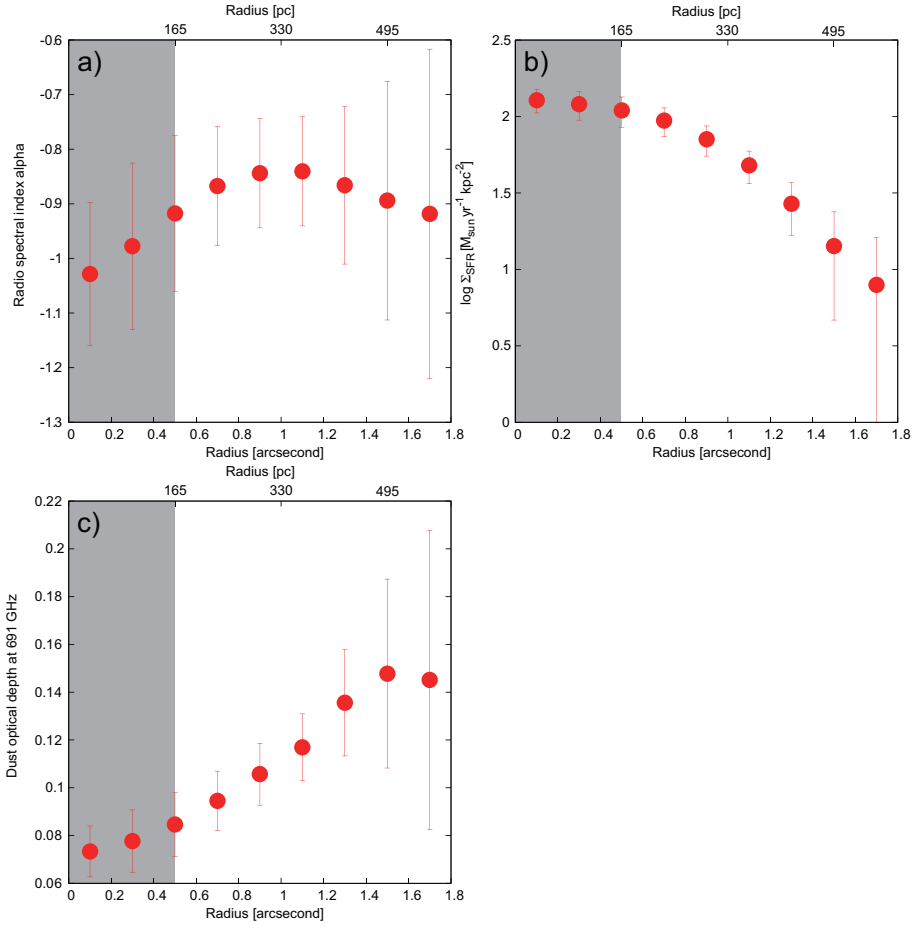

Figure 2.5. Results of the SED fitting, (a) spectral index α, (b) $\Sigma_{\rm SFR}$, and (c) dust optical depth at 691 GHz, as a function of radius. The shaded area indicates the convolved beam size.

assumption of the constant $T_{\rm d}$ of 35 $\pm$ 2 K may affect the derived β. High-resolution high-frequency observations are required to constrain the $T_{\rm d}$ gradient in the nuclear region of NGC 1614.

Assuming a gas-to-dust ratio of 264 $\pm$ 68 (Wilson et al. 2008), the surface densities of molecular gas ($\Sigma_{\rm H_2}$) are estimated to be in the range $10^{3.0}$ - $10^{3.8}$ $M_\odot$ pc^{-2}. We assumed the CO-to-H$_2$ conversion factor known to be appropriate for U/LIRGs ($\alpha_{\rm CO}$ = 0.8 $M_\odot$ (K km s^2)$^{-1}$; Bolatto et al. 2013b). This is consistent with the value derived by Sliwa et al. (2014) in NGC 1614 ($\alpha_{\rm CO}$ = 0.9 - 1.5 $M_\odot$ (K km s^2)$^{-1}$). The derived $\Sigma_{\rm H_2}$ are consistent with the values estimated from the high-resolution CO (6–

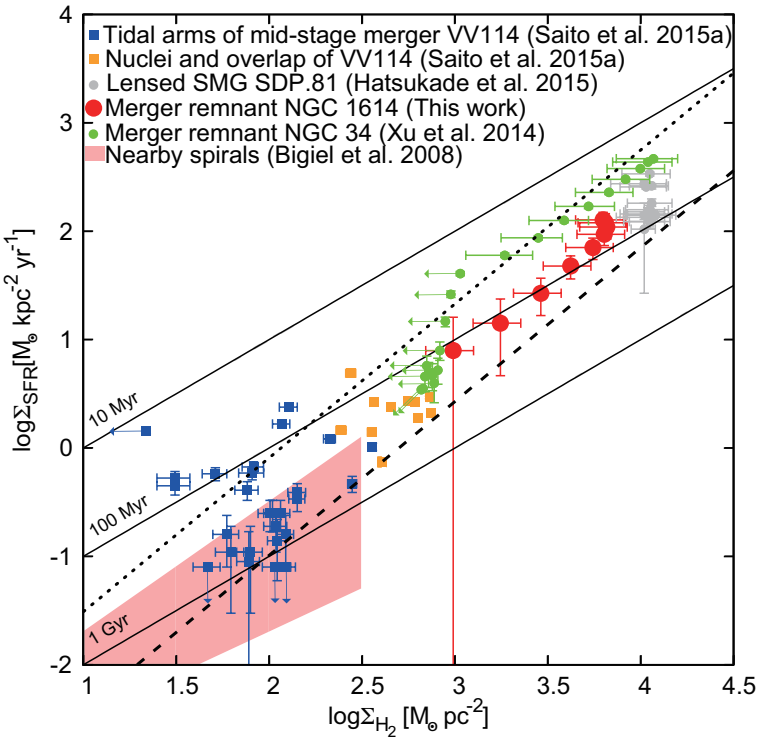

Figure 2.6. The spatially-resolved (sub-kpc) Kennicutt-Schmidt relation of merger-remnants NGC 1614 (red; this work), NGC 34 (green; Xu et al. 2014), a mid-stage merger VV 114 (blue and yellow; Saito et al. 2015), a lensed SMG SDP.81 (grey; Hatsukade et al. 2015), and nearby spirals (pink shaded area; Bigiel et al. 2008). The solid lines show a constant gas depletion time ($\tau_{\rm gas}$) of 10 Myr, 100 Myr, and 1 Gyr. The dotted and dashed line indicate the "starburst" sequence and the "normal disk" sequence (Daddi et al. 2010).

5) image (Xu et al. 2015). Here, we ignore the $S_{\rm nth}$ and the $S_{\rm ff}$ contributions to the 352 GHz flux (although Wilson et al. 2008 assumed these contribution by a factor of 0.6 to derive the gas-to-dust ratio of 440 $\pm$ 114), since our SED fittings yield that the 352 GHz flux is dominated by the cold dust emission (Figure 2.4).

2.5 Merger Evolution on the Star-forming Relation

We present the sub-kpc scale star-forming (Kennicutt-Schmidt; KS) relation for NGC 1614 (Figure 2.6), and compare with similar spatial resolution (0.3 - 0.8 kpc) data of U/LIRGs in the literature (VV 114, NGC 34, and SDP.81; Xu et al. 2014; Hatsukade et al. 2015; Saito et al. 2015). We also make a comparison with ~ 0.75 kpc resolution data of nearby spiral galaxies (Bigiel et al. 2008).

NGC 1614 (red points in Figure 2.6) has higher $\Sigma_{\rm H_2}$ ($= 10^{3.0-3.8}$ $M_\odot$ pc^{-2}) and $\Sigma_{\rm SFR}$ ($= 10^{0.9-2.1}$ $M_\odot$ yr^{-1} kpc^{-2}) than nearby spirals. In addition, we derive the molecular gas depletion time ($\tau_{\rm gas} = \Sigma_{\rm H_2}/\Sigma_{\rm SFR}$ yr) which is the time needed to consume the existing molecular gas by star formation. The nuclear region of NGC 1614 (< 300 pc) has shorter gas depletion time (averaged $\tau_{\rm gas} = 49$ - 77 Myr) than the outer region (averaged $\tau_{\rm gas} = 74$ - 226 Myr) (Table 2.3). The region with the shorter $\tau_{\rm gas}$ coincides with the starburst ring (Alonso-Herrero et al. 2001), which suggests that most of the intense SB in NGC 1614 occur within the ring rather than the outer region.

VV 114 is a gas-rich mid-stage merging galaxy with an infrared luminosity of $10^{11.71}$ $L_\odot$ (Armus et al. 2009). Although the system has a possible buried AGN as identified by dense molecular gas tracers (Iono, Saito et al. 2013) and the unresolved hard X-ray emission (Grimes et al. 2006), the extended infrared continuum, Paschen α (Tateuchi et al. 2015), and low-J CO emission (Iono et al. 2004b) mainly come from kpc-scale clumpy star-forming regions. We used the ALMA CO (1–0) and the miniTAO Paschen α emission to derive the $\Sigma_{\rm H_2}$ and $\Sigma_{\rm SFR}$ of VV 114, respectively (see Saito et al. 2015 for details). VV 114 has the lowest star formation among the four galaxies shown in Figure 2.6. The blue points indicate star-forming regions in tidal arms, and the yellow points indicate the nuclei and overlap region between the galaxy disks. Most of SF regions have the $\tau_{\rm gas}$ between 100 Myr and 1 Gyr. These values are shorter than normal spiral galaxies (Bigiel et al. 2008), and they are slightly higher than the "normal disk" sequence (index = 1.4) which is mainly dominated by nearby

spiral galaxies with moderate star formation (Daddi et al. 2010).

NGC 34 (green points in Figure 2.6) is one of the bright merger remnants ($L_{\rm IR}$ = $10^{11.49}$ $L_{\odot}$; Armus et al. 2009) with a rotating cold gas disk ($R \sim 3$ kpc; Ueda et al. 2014) and warm compact gas disk ($R \sim 320$ pc; Xu et al. 2014) similar to NGC 1614. We used the ALMA 435 μm dust and the VLA 8.44 GHz emission to derive the $\Sigma_{\rm H_2}$ and $\Sigma_{\rm SFR}$ of NGC 34, respectively (see Xu et al. 2014 in details). NGC 34 has a systematically higher $\Sigma_{\rm SFR}$ than NGC 1614 (i.e., $\tau_{\rm gas}$ of NGC 34 is shorter than that of NGC 1614). As suggested by Xu et al. (2015), one possibility to explain the difference is the characteristics of the progenitor galaxies. NGC 1614 is known as a minor merger, a colliding system between a massive and a dwarf galaxy with the mass ratio of > 4 (Väisänen et al. 2012), whereas NGC 34 is known as a major merger (Xu et al. 2014). Since major mergers efficiently induce gas inflows toward their nuclei due to the strong tidal interaction (e.g., Cox et al. 2008), the central starbursts in major mergers can be more intense than that of minor mergers.

SDP.81 (grey points in Figure 2.6) is one of the brightest lensed submillimeter galaxies (z = 3.042; Intrinsic $L_{\rm FIR}$ = $10^{12.70}$ $L_{\odot}$) discovered in the Herschel Astrophysical Terahertz Large Area Survey (Eales et al. 2010). Using a gravitational lens model, Hatsukade et al. (2015) found evidence of a rotating molecular gas disk with spatially-decoupled stellar components which suggests central dusty starbursts or merging signatures between two gas-rich galaxies (i.e., tidal tails or arms). Hatsukade et al. (2015) used the ALMA CO (5–4) and the ALMA rest-frame 125 μm emission to derive the $\Sigma_{\rm H_2}$ and $\Sigma_{\rm SFR}$ of SDP.81, respectively. The $\tau_{\rm gas}$ of SDP.81 ($\sim$ 50 Myr) is longer than that of NGC 34 and similar to that of the NGC 1614 nucleus. All of the clumps that are distributed over the kpc-scale disk of SDP.81 show active SF, which is similar to the nuclear region of NGC 1614 and NGC 34 (central 200 pc).

Overall, the sub-kpc KS relation for U/LIRGs has a larger index than unity (~ 1.4; Figure 2.6). The index is larger than the fitted value for spatially-resolved (sub-kpc) nearby spiral galaxies (1.0 ± 0.2; Bigiel et al. 2008), which suggests that molecular clumps in U/LIRGs (especially their nuclei) form stars with higher efficiency than in spirals. Furthermore, although the sample size is not enough statistically, our U/LIRG sample is distributed between the "normal disk" and the "starburst" sequence both

of which have a same index of 1.4 (Daddi et al. 2010). This is consistent with a numerical simulation provided by Bournaud et al. (2011) who suggest that galaxy mergers between two gas-rich disks can evolve toward the "starburst" mode (i.e., the $\tau_{\rm gas}$ becomes shorter as the merger-stage proceeds from VV 114 to NGC 1614 to NGC 34).

Finally we note that, since the $\Sigma_{\rm H_2}$ of all the U/LIRGs are derived by simply assuming a CO luminosity-to-H_2 mass conversion factor ($\alpha_{\rm CO}$) of 0.8 $M_\odot$ (K km s^{-1} pc^2)$^{-1}$, which is the standard value for U/LIRGs (e.g., Bolatto et al. 2013b), and/or adopting observed gas-to-dust ratio, data points in Figure 2.6 systematically shift when we adopt other $\alpha_{\rm CO}$. Therefore, the index of 1.4 does not change significantly.

2.6 Summary of This Seciton

Our new cycle 2 ALMA observations toward NGC 1614 of the 108 and 233 GHz continuum, combined with archival cycle 0 ALMA data of the 352 and 691 GHz continuum, and archival VLA data of the 4.81 and 8.36 GHz emission show a similar structure between each emission, although there are systematic differences between the lower frequency emission ($\leq$ 108 GHz) and the higher frequency emission ($\geq$ 233 GHz). The higher frequency emission has a more extended distribution toward the north-south direction, while both the lower and higher frequency emission show an offset peak relative to the nucleus, which was detected in the higher-resolution 5 GHz and Paschen α images, and a ring-like residual after subtracting the fitted 2D gaussian. This is the first result to resolve the radio-to-FIR continuum emission in LIRGs with 1.″0 resolution simultaneously.

Using the starburst SED template, we confirmed that the spatial differences of the SED may be due to the differences of dominant emitting mechanism; i.e., (1) 4.81 and 8.36 GHz fluxes are dominated by the non-thermal synchrotron, (2) 108 GHz flux is dominated by the thermal free-free emission, (3) 352 and 691 GHz fluxes are dominated by the thermal dust emission.

We also estimated the spatially-resolved (1.″0 $\times$ 1.″0) star formation rate surface densities and molecular gas surface densities. By combining with data in the liter-

ature, we suggest a trend that the molecular gas depletion time decreases as galaxy merger stage proceeds. This is consistent with the prediction from numerical simulations of star-forming activities as a function of the merger stage.

Chapter 3

Spatially-resolved CO SLED of the Nearby LIRG NGC 1614

3.1 Abstract

In this Chapter, we present high-resolution (1.″0) ALMA observations of CO (1–0) and CO (2–1) rotational transitions toward the nearby IR-luminous merger NGC 1614 supplemented with ALMA archival data of CO (3–2), and CO (6–5) transitions. The CO (6–5) emission arises from the starburst ring (central 590 pc in radius), while the lower-J CO lines are distributed over the outer disk ($\sim$ 3.3 kpc in radius). Radiative transfer and PDR modeling reveal that the starburst ring has a single warmer gas component with more intense far-ultraviolet radiation field ($n_{\rm H_2} \sim 10^{4.6}$ cm^{-3}, $T_{\rm kin}$ $\sim$ 42 K, and $G_0 \sim 10^{2.7}$) relative to the outer disk ($n_{\rm H_2} \sim 10^{5.1}$ cm^{-3}, $T_{\rm kin} \sim$ 22 K, and $G_0 \sim 10^{0.9}$). A two-phase molecular interstellar medium with a warm and cold ($>$ 70 K and $\sim$ 19 K) component is also an applicable model for the starburst ring. A possible source for heating the warm gas component is mechanical heating due to stellar feedback rather than PDR. Furthermore, we find evidence for non-circular motions along the north-south optical bar in the lower-J CO images, suggesting a cold gas inflow. We suggest that star formation in the starburst ring is sustained by the bar-driven cold gas inflow, and starburst activities radiatively and mechanically power the CO excitation. The absence of a bright active galactic nucleus can be

explained by a scenario that cold gas accumulating on the starburst ring is exhausted as the fuel for star formation, or is launched as an outflow before being able to feed to the nucleus.

3.2 Previous CO Observations toward NGC 1614

The global CO SLED of NGC 1614 is characterized by a steep decline towards higher-J transitions (Rosenberg et al. 2015). High-resolution ($\sim 0\farcs25 \sim 83$ pc) ALMA Band 9 observations revealed that the CO (6–5) distribution coincides with a starburst ring (r $<$ 350 pc) detected in Pa α (Figure 2.1c; Alonso-Herrero et al. 2001) and 8.4 GHz radio continuum emission (Xu et al. 2015), while the CO (2–1) and CO (3–2) emission are more extended (Wilson et al. 2008; König et al. 2013; Sliwa et al. 2014). Recent high-sensitivity CO (2–1) observations revealed the presence of a high-velocity wing, which might be associated with a nuclear molecular outflow (García-Burillo et al. 2015), whereas deep CO (1–0) imaging found that extended molecular gas components associated with the southern tidal tail and a dust lane (König et al. 2016).

3.3 ALMA Observations and Data Reduction

In this Section, we present observation setup of Cycle 0 and Cycle 2 ALMA and applied procedure for data reduction.

3.3.1 Band 3 and Band 6 Data: 12 m Array

The CO (1–0) and CO (2–1) observations toward NGC 1614 were carried out for our ALMA Cycle 2 program (ID: 2013.1.01172.S, PI: T. Saito) using thirty-five 12 m antennas (see Section 2.2.1 in details). The Band 3 and Band 6 receivers were tuned to the CO (1–0) and CO (2–1) emission lines in the upper sideband, respectively. The correlator was configured to have four spectral windows (SPW), two of which were set to each sideband, each of the SPWs with 1.129 MHz resolution (~ 3.0 km s^{-1} and

1.4 km s^{-1} for Band 3 and Band 6, respectively).

3.3.2 Ancillary Data

Band 7 and Band 9 Data: 12 m Array

NGC 1614 was observed during Cycle 0 using ALMA in Bands 7 and 9 (ID: 2011.0.00182.S and 2011.0.00768.S), and the data were originally published in Sliwa et al. (2014) and Xu et al. (2015) (see also Section 2.2.2 in details). We obtained the calibrated archival visibility data of the CO (3–2) and the CO (6–5) from the ALMA archive. Detailed information of the Cycle 0 and 2 data are shown in Table 3.1.

Band 3 Data: Atacama Compact Array and 12 m Array

The CO (1–0) observations toward NGC 1614 were also carried out during Cycle 2 (ID: 2013.1.00991.S; König et al. 2016) using both ten 7 m antennas of ACA (Iguchi et al. 2009) and thirty-one 12 m antennas of the 12 m array. These ancillary data are used to increase the sensitivity and recover extended emission that we ignore due to the *uv*-clipping (Section 3.3.1). Thus, we use those data to study the global gas kinematics of NGC 1614. we retrieved those data from the ALMA archive, and used one SPW which was tuned to the CO (1–0) line. Detailed description of this project is found in König et al. (2016), and we list some parameters in Table 3.1.

3.3.3 Reduction Procedure

12 m Array Data

We performed calibration and imaging using `CASA` (version 3.4, 4.1.0, and 4.2.2 for Band 7, 9, and 3/6, respectively; McMullin et al. 2007). Detailed procedure for data processing is summarized in Section 2. Before imaging, we flagged the *uv* range below 45 kλ, so that the maximum recoverable scale (MRS; Lundgren 2013) of each ALMA observation is consistent. The minimum *uv* distance is determined by the configuration of the CO (6–5) observation. Since the truncated *uv* range at 45 kλ corresponds to the MRS of $\sim$ 4.″6 ($\simeq$ 1.5 kpc), we ingore the missing flux

Table 3.1. Log of ALMA Observations

Band	UT date	Configuration				T_{sys}	Calibrator			T_{integ}
		Array	FoV	N_{ant}	$L_{baseline}$		Flux	Bandpass	Gain	
			($''$)		(m)	(K)				(min.)
(1)	(2)	(3)	(4)	(5)	(6)	(7)	(8)	(9)	(10)	(11)
B3	2014 Jun. 30	ACA 7 m	95.6	10	7.3 - 48	42 - 170	J0501-0159	J0423-013	J0427-0700	49.1
B3	2014 Dec. 04	ALMA 12 m	55.7	31	15 - 290	31 - 120	Uranus	J0423-0120	J0423-0120	13.1
B3	2014 Aug. 30	ALMA 12 m	55.7	35	28 - 1060	50 - 130	J0423-013	J0423-0120	J0423-0120	16.9
B6	2014 Aug. 14	ALMA 12 m	27.8	35	15 - 349	70 - 160	Uranus	J0423-0120	J0423-0120	7.3 × 3
B7	2012 Jul. 31/Aug. 14	ALMA 12 m	18.6	27	18 - 431	100 - 210	Callisto	J0522-364	J0423-013	88.8
B9	2012 Aug. 13/28	ALMA 12 m	9.3	23	20 - 394	500 - 1100	Ceres	J0423-013	J0423-013	49.4

Note. — Column 2: Observed date. Column 3: Dish size. Column 4: FWHM of the primary beam at the frequency of the target CO line. Column 5: Number of available antennas. Column 6: Projected length of assigned baseline for NGC 1614. Column 7: Single-sideband system temperature toward NGC 1614. Column 8–10: Observed flux calibrator, bandpass calibrator, and phase calibrator. Column 11: Total integration time on NGC 1614. The Band 6 observation has three pointing fields.

effect on structures smaller than 4.″6 throughout this Section. All of the images are convolved to the same resolution (1.″0 × 1.″0). The systematic errors on the absolute flux calibration using a solar system object are estimated to be 5%, 10%, 10%, and 15% for both sidebands in Band 3, Band 6, Band 7, and Band 9, respectively (Lundgren 2013). The Band 3 observation has a quasar as the flux calibrator, so we estimate the absolute systematic error on the flux calibration for our Band 3 data by using the ALMA Calibrator Source Catalogue[1]. The flux uncertainty of J0423-013 on 2014 August 30 is 1.9-3.7% at 103.5 GHz. Therefore, we adopt the flux uncertainty of 5% to be conservative. Since the recovered flux of each CO transition compared to single-dish observations (Sanders et al. 1991; Albrecht et al. 2007; Wilson et al. 2008; Xu et al. 2015) is very low (27 - 59 %), NGC 1614 has large amounts of ambient molecular gas structures larger than 1.5 kpc even in the CO (6–5). The detailed data properties and line information are listed in Table 3.2.

ACA Data and Combine with 12 m Array Data

We used `CASA` (version 4.2.1 and 4.2.2) to process the data. In order to combine the CO (1–0) data shown in Section 3.3.2 with the data described in Section 3.3.1, we used `statwt`[2] task to recalculate visibility weights for all the data. The resultant $L_{\rm baseline}$ is 7.3 - 1060 m. This corresponds to the MRS of 17.″6 ($\sim$ 5.8 kpc). We constructed a data cube with the velocity resolution of 20 km s^{-1}. The flux calibrator for the ACA observation is a quasar J0501-0159. Using the ALMA Calibrator Source Catalogue[13], the flux uncertainty of J0501-0159 on 2015 June 30 is estimated to be $\sim$ 12% at 97.4 GHz. Therefore, we adopt the flux uncertainty of 12% when we use the ACA-combined CO (1–0) data. The achieved rms noise level is 1.4 mJy beam^{-1} with the synthesized beam size of 1.″02 × 0.″57 (position angle = $-88°$). Comparing with the CO (1–0) flux obtained by NRAO 12m (Sanders et al. 1991), the recovered flux is 113 ± 26 % indicating that we recovered most (or probably all) of the CO (1–0) emission. The total H_2 mass is (4.1 ± 0.5) × 10^9 $M_\odot$ assuming 1/5 of the Milky Way CO-to-H_2 conversion factor ($\alpha_{\rm MW}$ = 4.3 $M_\odot$/(K km s^{-1} pc^2)$^{-1}$; Downes &

[1]https://almascience.nrao.edu/sc/
[2]https://casaguides.nrao.edu/index.php/DataWeightsAndCombination

Table 3.2. CO Line and Imaging Properties

CO Line	$\nu_{\rm rest}$ (GHz)	$E_{\rm u}/k$ (K)	Band	MRS ($''$)	uv-weight	Beam size ($''$)	rms (mJy b^{-1})	$S_{\rm CO}\Delta v$ (Jy km s^{-1})	Recovered flux (%)	Ref.
(1)	(2)	(3)	(4)	(5)	(6)	(7)	(8)	(9)	(10)	(11)
J = 1–0 (ACA+12 m)	115.271	5.53	B3	17.6	briggs	1.0 × 0.6	1.4	295.3 ± 1.8	113 ± 26	1, a
J = 1–0 (12 m)	115.271	5.53	B3	4.6	briggs	1.0 × 1.0	1.6	69.3 ± 1.1	27 ± 5	This work, a
J = 2–1 (12 m)	230.542	16.60	B6	4.6	uniform	1.0 × 1.0	3.5	325.4 ± 2.7	40 ± 9	This work, b
J = 3–2 (12 m)	345.796	33.19	B7	4.6	briggs	1.0 × 1.0	3.0	866.8 ± 2.2	59 ± 6	2, c
J = 6–5 (12 m)	691.473	116.16	B9	4.6	briggs	1.0 × 1.0	8.0	826.9 ± 3.2	58 ± 10	2, 3, d

Note. — Column 1: Observed CO transition. Column 2: Rest frequency of the transition. Column 3: Upper state energy of the transition. Column 5: Maximum recoverable scale (MRS) of the visibility data; See text. Column 6: Visibility (uv-plane) weighting for imaging. "briggs" means Briggs weighting with `robust` = 0.5. Column 7: Convolved beam size. All the images, except for the ACA-combined CO (1–0) image, in this Section and Section 2 are convolved into the same resolution of $1\farcs0$, which is larger than the synthesized beam size. Column 8: Noise rms for data with the velocity resolution of 30 km s^{-1}. Column 9: Integrated intensity inside the 3% contour of the peak value. We only consider the statistical error in this column. Column 10: The ALMA flux divided by the single dish flux. We consider the statistical and the systematic error of the flux calibration. Column 11: Reference of ALMA data (1. König et al. (2016), 2. Sliwa et al. (2014), 3. Xu et al. (2015)) and single dish data (a. NRAO 12m; Sanders et al. (1991), b. SEST 15m; Albrecht et al. (2007), c. JCMT 15m; Wilson et al. (2008), d. Herschel/SPIRE; Xu et al. (2015)).

Solomon 1998; Bolatto et al. 2013b). When comparing with ACA-only CO (1–0) flux measured by König et al. (2016) ($\sim$ 241 Jy km s^{-1}), the recovered flux is $\sim$ 123 %. This difference might be due to the differences of mask shape to measure the CO flux in R.A., Decl., and velocity axes (i.e., low surface brightness, high velocity wings). Detailed information of the ACA and the 12 m array data is shown in Table 3.1, and the line information are listed in Table 3.2.

3.4 Results

The *uv*-matched CO integrated intensity, velocity field, and velocity dispersion maps are shown in Figure 3.1, except for the ACA-combined CO (1–0) image (Figure 3.2a). The channel maps are shown in Appendix A.

3.4.1 *uv*-matched CO Intensity, Velocity field, and Velocity Dispersion

The *uv*-matched CO distributions of NGC 1614 can be divided into two regions: the starburst ring (central 590 pc in radius) and an outer disk ($\sim$ 3.3 kpc in radius). The starburst ring is detected in X-ray, polycyclic aromatic hydrocarbon (Herrero-Illana et al. 2014), Pa α (Alonso-Herrero et al. 2001), radio-to-FIR continuum (Olsson et al. 2010), HCN (4–3), and HCO$^+$ (4–3) emission (Imanishi & Nakanishi 2013a; Sliwa et al. 2014). Most of the CO emission in the starburst ring arise from the western side. The asymmetry in the starburst ring coincides with the radio-to-FIR continuum and the HCO$^+$ (4–3) emission. On the other hand, the outer disk is only detected in extended Pa α and soft X-ray emission (Herrero-Illana et al. 2014), indicating a site of moderate star formation relative to the ring (but we still have missing flux for extended, low surface brightness CO (6–5) emission). All CO (1–0) peaks outside the starburst ring coincide with the peaks detected in Pa α (Figure 2.1c).

The overall velocity structure of all the CO transitions seems to be dominated by rotation. This is consistent with the velocity modeling with tilted concentric rings provided by Ueda et al. (2014). The velocity field and dispersion of the starburst

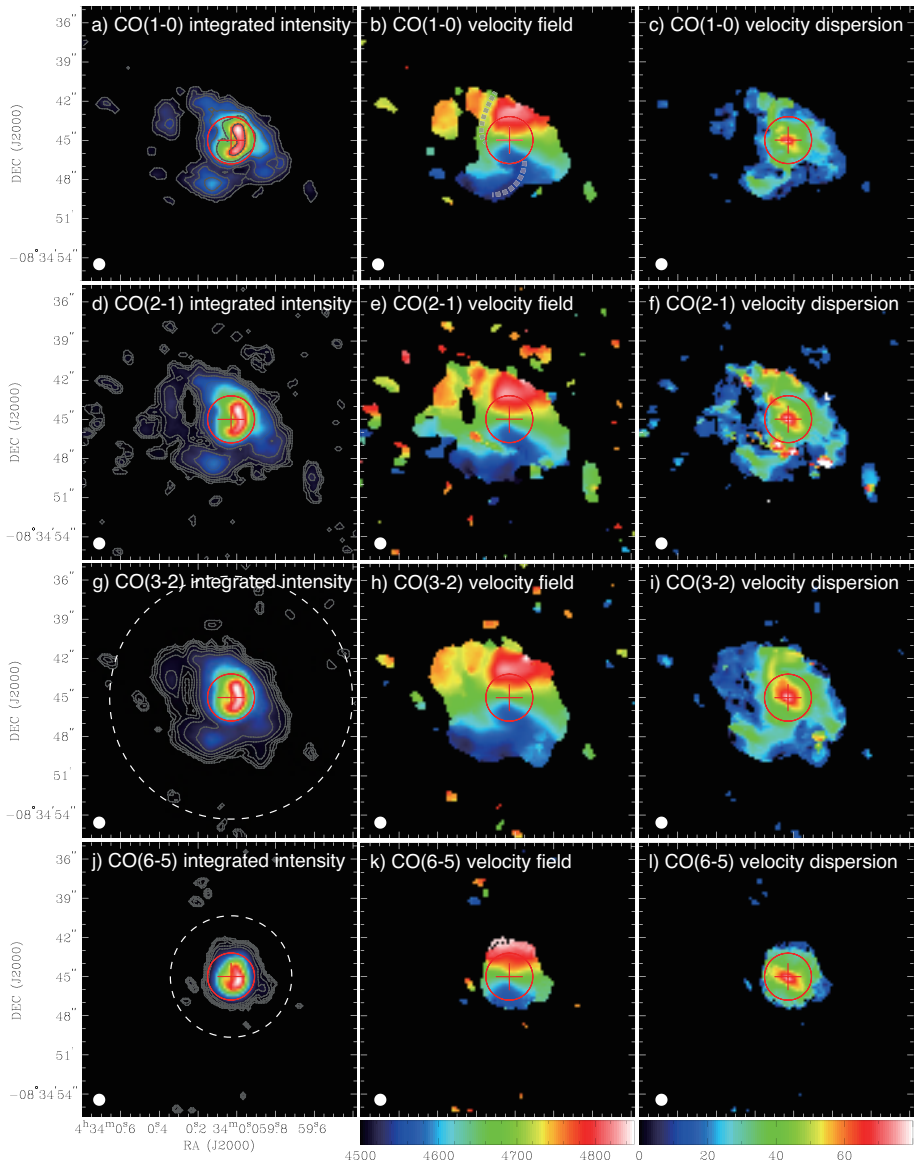

Figure 3.1. (a) *uv*-clipped CO (1–0) integrated intensity image of NGC 1614. The contours are 0.36, 0.72, 1.44, 2.88, 5.76, and 11.52 Jy beam^{-1} km s^{-1}. The red cross indicates the nucleus which is detected in Pa α and radio continuum emission (Olsson et al. 2010; Herrero-Illana et al. 2014). The red circle indicates the approximate outer edge of the starburst ring (König et al. 2013; Herrero-Illana et al. 2014; Xu et al. 2015; see also Section 2). (b) *uv*-clipped CO (1–0) velocity field image. The velocity field in color scale ranges from 4500 km s^{-1} to 4850 km s^{-1}. The dashed grey lines show the positions of non-circular motion. (c) *uv*-clipped CO (1–0) velocity dispersion image. The velocity dispersion in color scale ranges from 0 km s^{-1} to 80 km s^{-1}. (d) The same as (a) but for CO (2–1). The contours are 1.0, 2.0, 4.0, 8.0, 16.0, and 32.0 Jy beam^{-1} km s^{-1}. (e/f) The same as (b/c), respectively, but for CO (2–1). (g) The same as (a) but for CO (3–2). The contours are 0.72, 1.44, 2.88, 5.76, 11.52, and 23.04 Jy beam^{-1} km s^{-1}. (h/i) The same as (b/c), respectively, but for CO (3–2). (j) The same as (a) but for CO (6–5). The contours are 2.4, 4.8, 9.6, 19.2, 38.4, and 76.8 Jy beam^{-1} km s^{-1}. (k/l) The same as (b/c), respectively, but for CO (6–5). The fields of view of the CO (3–2) and CO (6–5) data are shown as white dashed circles.

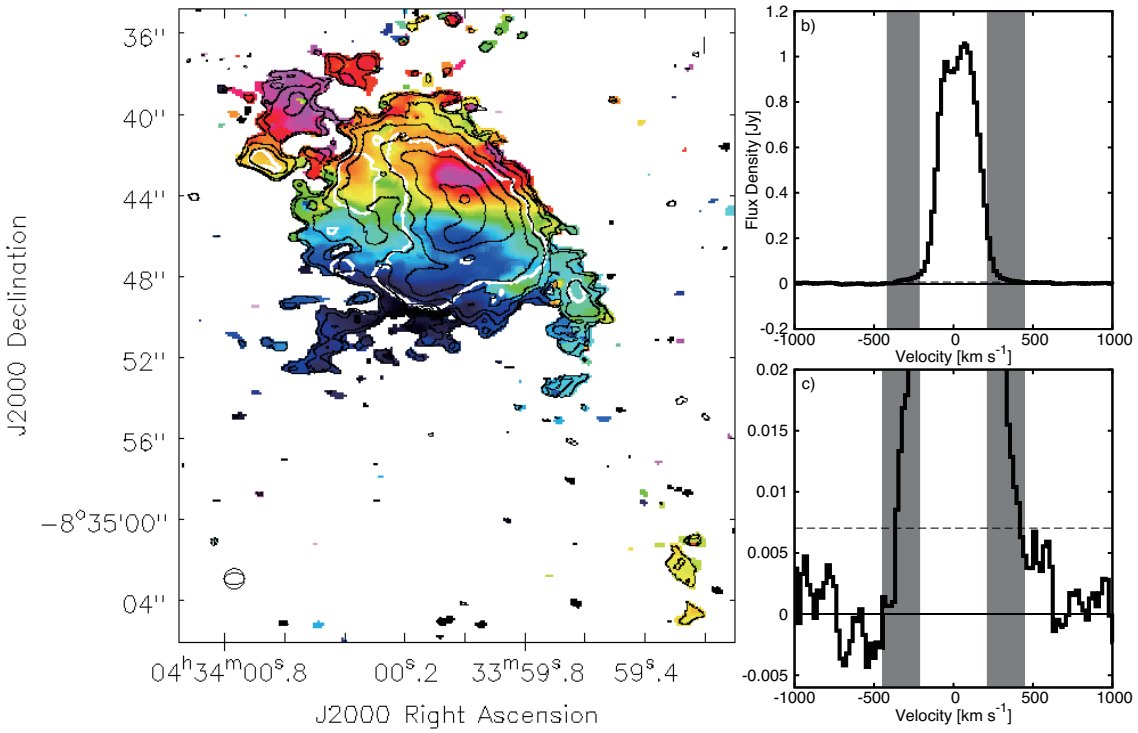

Figure 3.2. (a) ACA+12 m-combined CO (1–0) integrated intensity [black contour] and velocity field [color] images of NGC 1614. The contours are 8.8 × (0.02, 0.04, 0.08, 0.16, 0.32, 0.64, and 0.96) Jy beam^{-1} km s^{-1}. The velocity field in color scale ranges from 4500 km s^{-1} to 4850 km s^{-1}. The white contour shows the outline of the *uv*-clipped 12 m-only CO (1–0) image at the level of 0.36 Jy beam^{-1} km s^{-1} (Figure 3.1a). (b) CO (1–0) spectrum toward the central 4.″6 aperture. (c) Zoomed-in CO (1–0) spectrum of Figure 3.2b. The shaded area shows the CO line wings suggested by García-Burillo et al. (2015).

ring smoothly connect to those of the outer disk, which indicates that the kinematics (e.g., position angle, inclination) are similar. We identify non-circular motions in a region with a length of 9″(∼ 3 kpc) that is extended from north to south of the disk (dashed lines in Figure 3.1b) in all CO images, except for the CO (6–5). The apparent "S"-shape feature in the velocity field suggests the presence of non-circular motions (e.g., Kalnajs 1978) in the region where the dust lane connects with the starburst ring or a warped disk (e.g., Centaurus A; Espada et al. 2012). A discussion of the central gas geometry of NGC 1614 will be provided in Section 3.6.6. The apparent characteristics are similar to the nearby barred spiral galaxy NGC 1097 which is a

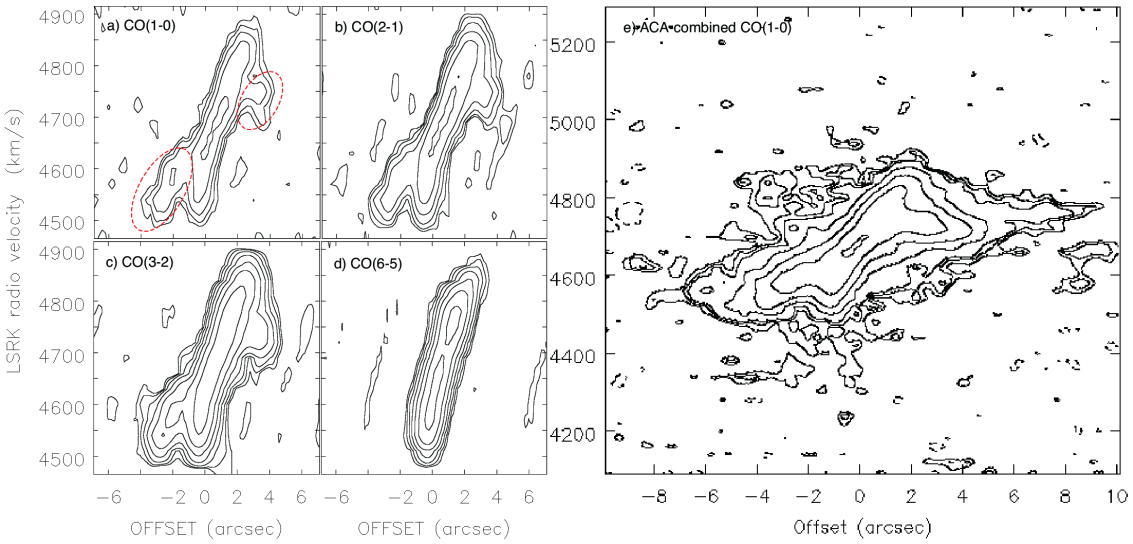

Figure 3.3. (a/b/c/d) Spatially-averaged position-velocity diagram of each CO transition along the north-south direction (width = 13.″4) through the radio nucleus. The nth contours are at $2^n\sigma$ (n = 1, 2, 3 ...). σ is the noise rms listed in Table 3.2. Red circles show the non-circular motion detected in lower-J transitions. (e) Spatially-averaged position-velocity diagram of the ACA-combined CO (1–0) along the north-south direction. The contours are 0.5 × (-2, 2, 3, 4, 8, 16, 32, and 64) mJy beam^{-1}.

minor merger system (Lin et al. 2013).

We investigate the position-velocity diagrams (PVDs) per the different CO transitions along the north-south direction with a width of 13.″4, length of 15.″0 through the nucleus (Figure 3.3a, 3.3b, 3.3c, and 3.3d). The width and length of these PVDs covers all of the CO emission (Figure 3.1). The PVDs show rigid rotation (i.e., starburst ring) in all CO transitions and non-circular motions (dashed ellipses in Figure 3.3a) except for the CO (6–5). The direction of the PVD cut is similar to the kinematical major axis determined from the CO (2–1) velocity field (352°± 1°; Ueda et al. 2014).

While the large scale kinematics can be explained by both circular and non-circular motion, the central region appears to show outflows. García-Burillo et al. (2015) found high velocity CO (1–0) wings (210 km s^{-1} < $|v - v_{\rm sys}|$ < 450 km s^{-1}, where $v_{\rm sys}$ = 4763 km s^{-1}) with the P.A. of 82° in the central region. They suggested these components are a putative bipolar outflow with an outflow rate of $\sim$ 40 $M_\odot$ yr^{-1}. The

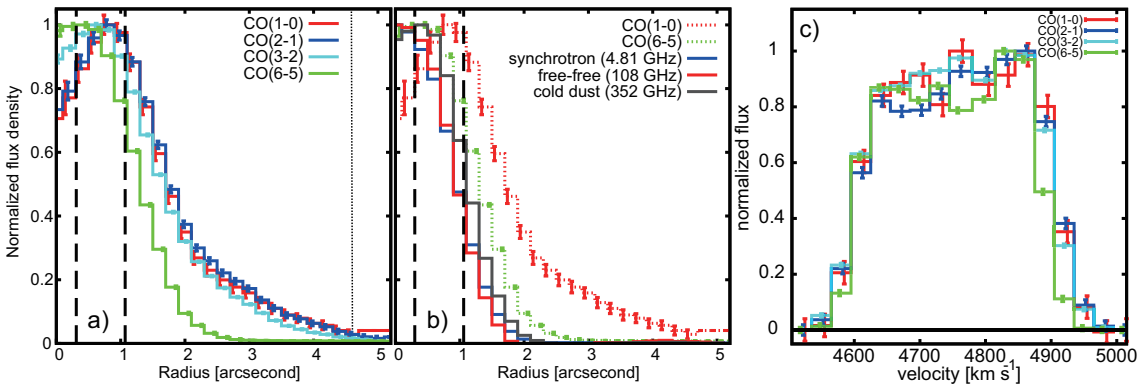

Figure 3.4. (a) Azimuthally-averaged normalized radial distribution of each CO transition of NGC 1614 centered at the radio nucleus (Olsson et al. 2010). We only consider the statistical error. The dashed lines show the approximate inner and outer radii of the nuclear starburst ring (Xu et al. 2015). The dotted line shows the approximate outer radius of the field of view of the CO (6–5) data. (b) Comparison between each CO transition (dotted line) and each continuum emission (solid line; see Section 2). All the data for the different CO transitions are convolved to the same resolution of 1.″0. (c) Normalized CO Spectra of NGC 1614 toward the central 4.″6 aperture.

direction and the outflow rate is similar to those of the ionized gas outflow (Bellocchi et al. 2012). We did not detect the line wings in all CO transitions, although they are detected in the ACA-combined CO (1–0) image (see Section 3.4.2).

In Figure 3.4a, we show the normalized radial distribution of the CO SLED of NGC 1614. The CO (6–5) emission is centrally concentrated, while the lower-J CO transitions show an extended component (i.e., the outer disk) as well as the ring. The peak radius of the starburst ring shifts toward outside as the CO transition shifts to lower-J. This indicates the presence of a radial excitation gradient in the starburst ring (see Section 3.5.1). In Figure 3.4b, as a comparison, we plot the normalized radial distribution of the radio-to-FIR SED of NGC 1614 with the same angular resolution and MRS (Section 2). All of the continuum emission (synchrotron, free-free, and cold dust) are more compact than the lower-J CO transitions, but the sizes are similar to the extent of the CO (6–5) emission. This suggests that the CO (6–5) is a better tracer of star formation than lower-J CO transitions (e.g., Xu et al. 2015). Although differences are seen in the spatial distribution between the transitions, there are no

significant differences in the velocity profile within the central 2.″3 radius as shown in Figure 3.4c.

3.4.2 ACA+12 m-combined CO (1–0) Data

We show the CO (1–0) image that is generated by combining the ACA data with the 12 array data in Figure 3.2a. The global velocity field does not change significantly, although additional extended structures toward the north-east (redshifted) and south-west (blueshifted) appear. These arm-like structures are located along the optical dust lanes, as already found by ACA-only CO (1–0) image (König et al. 2016), and Pa α (Figure 1.10c). The low S/N high-velocity wings (Figure 3.2b and 3.2c) are consistent with the presence of a putative outflow suggested by García-Burillo et al. (2015).

We investigate the PVD of the ACA-combined image along the north-south (along the kinematical major axis with a width of 13.″4; Figure 3.3e) and east-west direction (along the kinematical minor axis with a width of 4.″6; Figure 3.5a) through the radio nucleus (Olsson et al. 2010). Along the major axis, we found more extended components than the *uv*-clipped CO (1–0) image. The ACA data shows features that are consistent with bar-induced inflow motions predicted by Iono et al. (2004a). In contrast, as shown in the PVD along the minor axis which emphasizes low surface brightness components within the 4.″6 width, there are high-velocity components around the nuclear region. Since the high-velocity components show the same spatial and spectral distributions as the molecular gas outflow suggested by García-Burillo et al. (2015), we regard the high-velocity components as the molecular gas outflow. We constructed the integrated intensity image of the blueshifted (4340 - 4460 km s^{-1}) and redshifted (4940 - 5000 km s^{-1}) outflows in Figure 3.5b. The extracted velocity ranges contain high-velocity wings stronger than 3σ. The CO (1–0) outflow shows an extended blueshifted (redshifted) emission toward the south-east (north-west) direction. The molecular gas outflow seems to surround the ionized gas outflow (Bellocchi et al. 2012). This picture is consistent with the molecular gas outflow entrained by the ionized gas outflow in the nearby starburst galaxy NGC 253 and M51 (Bolatto

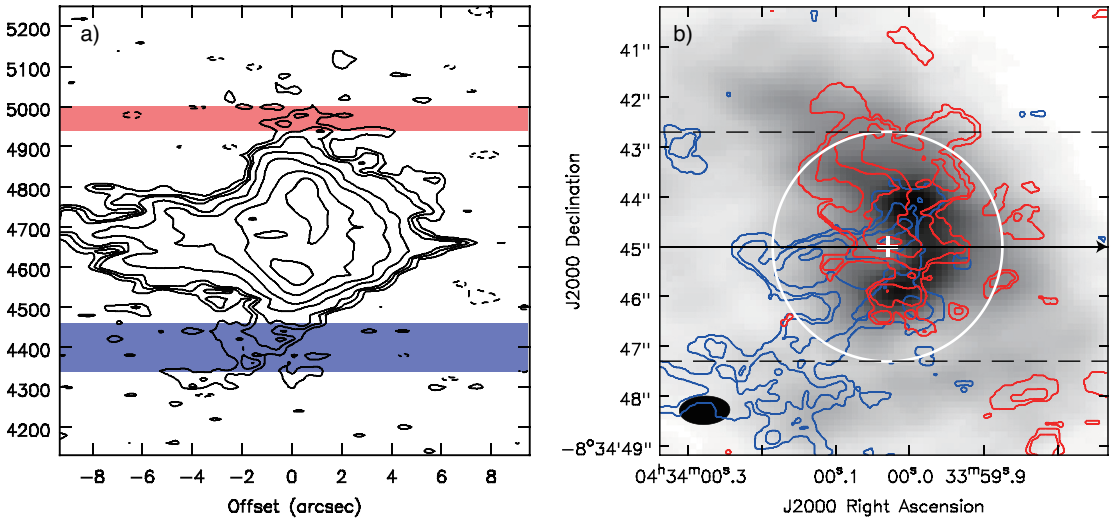

Figure 3.5. (a) Spatially-averaged position-velocity diagram of the ACA-combined CO (1–0) data along the east-west direction (width = 4.″6). The contour are 0.5 × (-2, 2, 3, 4, 8, 16, 32, and 64) mJy beam^{-1}. This PVD only contains velocity components between the dashed lines in Figure 3.5b. (b) Integrated intensity contour images of the high-velocity components (i.e., molecular outflow suggested by García-Burillo et al. 2015) overlaid on the ACA-combined CO (1–0) image (Figure 3.2a) with grey scale. The blue and red contours show blueshifted and redshifted components, respectively. The blue contours are 0.45 × (0.16, 0.32,0.64, and 0.96) Jy beam^{-1} km s^{-1}, whereas the red contours are 0.32 × (0.16, 0.32,0.64, and 0.96) Jy beam^{-1} km s^{-1}. The white circle indicates the approximate outer edge of the starburst ring (König et al. 2013; Herrero-Illana et al. 2014; Xu et al. 2015; see also Section 2).

et al. 2013a; Querejeta et al. 2016).

3.4.3 CO Line Ratios

We show CO (2–1)/CO (1–0), CO (3–2)/CO (1–0), and CO (6–5)/CO (1–0) line ratio images in Figure 3.6a, 3.6b, and 3.6c, respectively. We divide the integrated intensity maps (Figure 3.1d, 3.1g, and 3.1j) by the CO(1-0) integrated intensity map (Figure 3.1a) to make the line ratio maps. After that, we masked all the line ratio maps by using the CO (1–0) outline which is shown in Figure 3.6. The CO (2–1)/CO (1–0) and CO (3–2)/CO (1–0) line ratios show higher values than the optically-thick thermalized value, while the CO (6–5)/CO (1–0) line ratio is moderate. Those

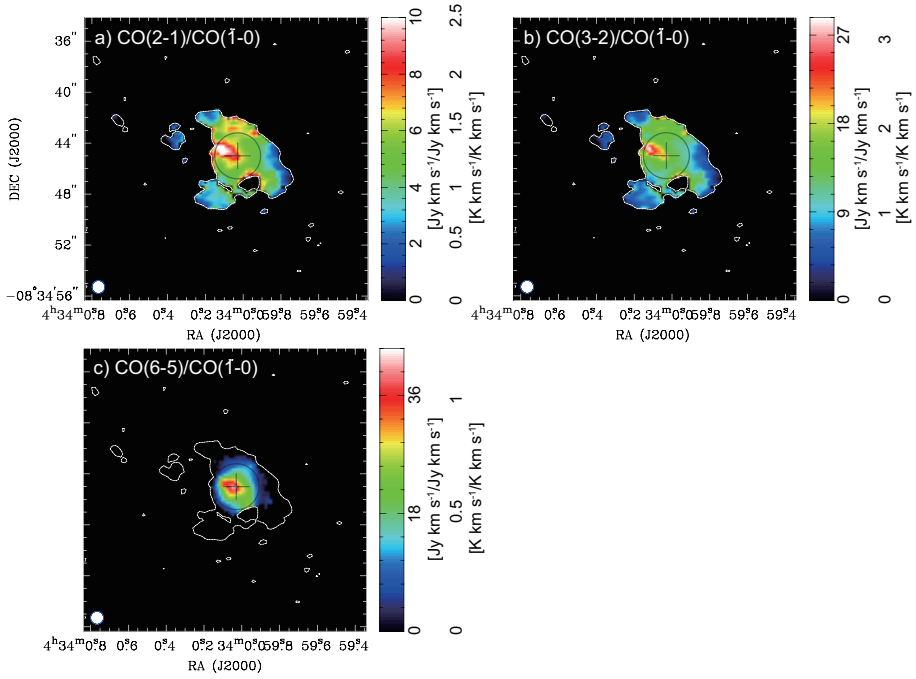

Figure 3.6. (a) Image of the *uv*-matched CO (2–1)/CO (1–0) intensity ratio for NGC 1614. The ratio in color scale ranges from 0 to 10 in Jy km s^{-1}/(Jy km s^{-1})$^{-1}$ (0 to 2.5 in K km s^{-1}/(K km s^{-1})$^{-1}$). The contour shows the CO (1–0) outline (0.54 Jy beam^{-1} km s^{-1}). The black cross indicates the nucleus which is detected in Pa α and the radio continuum emission (Herrero-Illana et al. 2014). The black circle indicates the approximate outer edge of the starburst ring (König et al. 2013; Herrero-Illana et al. 2014; Xu et al. 2015; Section 2). (b) Image of the *uv*-matched CO (3–2)/CO (1–0) intensity ratio. The ratio in color scale ranges from 0 to 28.8 in Jy km s^{-1}/(Jy km s^{-1})$^{-1}$. (c) Image of the *uv*-matched CO (6–5)/CO (1–0) intensity ratio. The ratio in color scale ranges from 0 to 43.2 in Jy km s^{-1}/(Jy km s^{-1})$^{-1}$.

high CO (2–1)/CO (1–0) and CO (3–2)/CO (1–0) line ratios indicate low optical depths for the CO (1–0) line (e.g., Downes & Solomon 1998) and/or the presence of multiple phase ISM (e.g., CO (3–2)/CO (1–0) ratio in Arp 220; Rangwala et al. 2011). The peak position of each line ratio is located at 1″east of the nucleus. Since it coincides with the eastern part of a possible ionized and molecular gas outflow (Bellocchi et al. 2012; García-Burillo et al. 2015), the high line ratio component might be due to the interaction between the outflow and the starburst ring. Strong outflow can heat surrounding ISM kinematically. This results in highly excited (i.e., low-

J depopulation) or highly turbulent (i.e., low optical depth) molecular gas around the shock interface, and thus high line ratios. High CO (3–2)/CO (1–0) ratio is also observed in the circumnuclear disk (CND) of Seyfert 2 galaxy NGC 1068 (See Section 7.2 of García-Burillo et al. 2014). The high ratio in the CND are located parallel to the bipolar jet, which may indicate that the CND is affected by the nuclear jet. A similar situation is found in the nuclear region of NGC 1614 (Figure 3.6), which may indicate outflow-ring interaction. However, further molecular gas and ionized gas observations are necessary to confirm this scenario quantitatively.

3.5 CO SLED Modeling

3.5.1 Single-phase RADEX Model

We used the non-LTE radiative transfer code RADEX (van der Tak et al. 2007) and varied the parameters until the residuals between the observed line fluxes and the modeled line fluxes are minimized in a χ^2 sense. Assuming a single-phase ISM (i.e., the gas physics can be represented by a single set of the excitation parameters), an expanding sphere geometry (dv = 200 km s^{-1}), the cosmic microwave background temperature ($T_{\rm bg}$ = 2.73 K), and a [CO]/[H_2] abundance (3×10^{-4}) which is similar to the standard value observed in Galactic molecular clouds (Blake et al. 1987), we derived the physical conditions of molecular gas. The upper state energies and the Einstein coefficients were taken from the *Leiden Atomic and Molecular Database* (LAMDA; Schöier et al. 2005). We varied the gas kinetic temperature within a range of $T_{\rm kin}$ = 10 - 300 K (d$T_{\rm kin}$ = 1 K), the gas density of $n_{\rm H_2} = 10^2$ - 10^7 cm^{-3} (d$n_{\rm H_2}$ = $10^{0.1}$ cm^{-3}), and the gas column density of $N(\rm H_2) = 10^{20.5}$ - $10^{23.5}$ cm^{-2} (d$N(\rm H_2)$ = $10^{0.1}$ cm^{-2}).

We show results of the RADEX modeling at the outer region contained within a radius of 2.″8 - 3.″0 in Figure 3.7. Line ratios related to CO (6–5) show different distributions to lower-J CO line ratios in the parameter planes, demonstrating the importance of the CO (6–5) data. The results as a function of radius are shown in Figure 3.8a, 3.8b, and 3.8c. The minimum reduced-χ^2 of the central 1.″8 is relatively

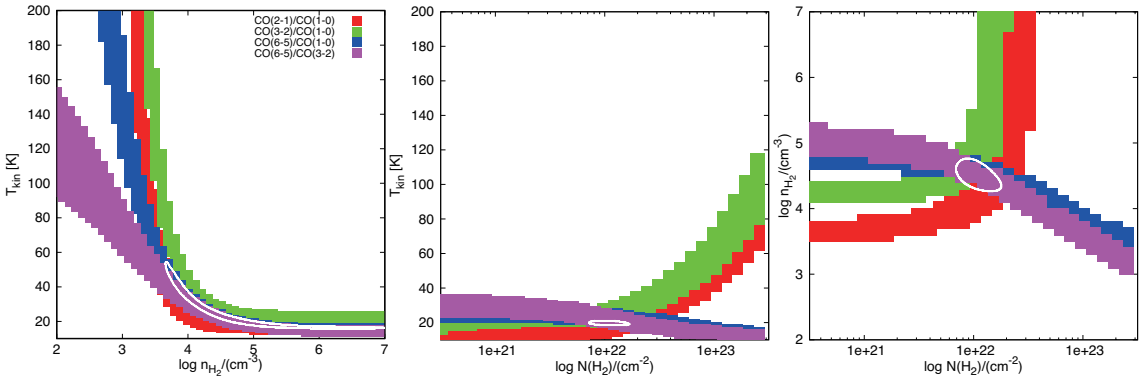

Figure 3.7. Results of the single-phase RADEX modeling at the outer region contained within a radius of 2.″8 - 3.″0 (924 pc - 990 pc): (a) log $n_{\rm H_2}$ - $T_{\rm kin}$ plane, (b) log $N(\rm H_2)$ - $T_{\rm kin}$ plane, and (c) log $N(\rm H_2)$ - log $n_{\rm H_2}$ plane. All planes are cut through the best-fit point. Each colorized area corresponds to the 1σ range of each observed line ratio. The white outline shows the 90% confidence contour of the fit.

poor (> 3.6), whereas that of the outer region (r $> 1.''8$) is < 3.6. Gas density is high ($\sim 10^5$ cm^{-3}) independently of the distance from the nucleus. On the other hand, both the $T_{\rm kin}$ (= 20 - 70 K) and $N(\rm H_2)$ (= $10^{22.0-22.9}$ cm^{-3}) decrease as the radius increases. Their peaks coincide with the radius of the starburst ring (100 - 350 pc; König et al. 2013; Xu et al. 2015). The derived $T_{\rm kin}$ are slightly higher than the results of a similar modeling for NGC 1614 by Sliwa et al. (2014). This can be explained by the different spatial sampling between our analysis and theirs. In order to match the MRS between datasets, Sliwa et al. (2014) used single-dish data to compensate for the missing short baselines of their interferometric CO (2–1) and CO (3–2) data, while we clipped the inner uv data at 45 kλ (see Section 3.3).

We calculated the optical depth for each transition (Figure 3.9), yielding that $\tau_{\rm CO(1-0)}$ shows moderate optical depth (< 1), $\tau_{\rm CO(2-1)}$ and $\tau_{\rm CO(3-2)}$ are optically thick (1 - 10), and $\tau_{\rm CO(6-5)}$ becomes thin as the radius increases (8 to 0.1). The derived $\tau_{\rm CO(1-0)}$ for NGC 1614 is consistent with that estimatd for a mid-stage merger VV 114 (~ 1; Saito et al. 2015), the central region of a close galaxy pair NGC 6240 (0.2 - 2; Iono et al. 2007), and that for the overlap region of the mid-stage merger Arp 299 (0.5 - 1.5; Sliwa et al. 2012). This suggests that luminous mergers have CO (1–0) line

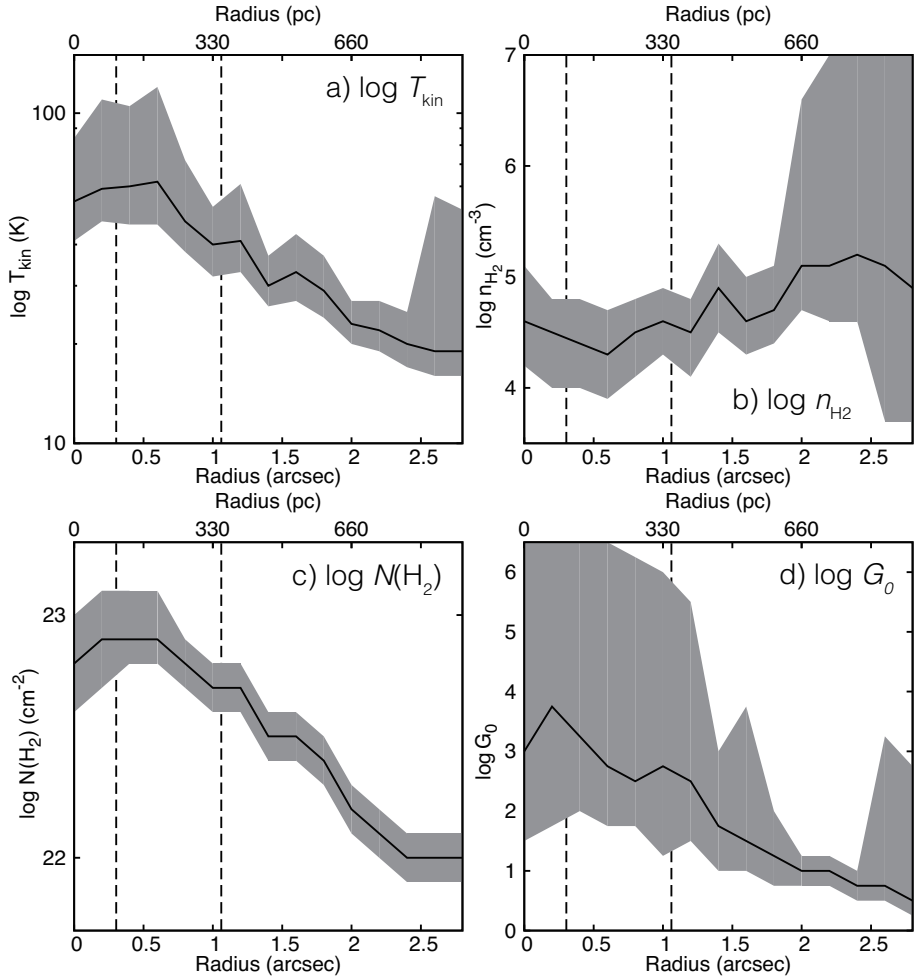

Figure 3.8. Results of the RADEX and PDR Toolbox modeling as a function of the radius; (a) kinetic temperature, (b) molecular gas density, (c) column density of molecular hydrogen, and (d) far-UV radiation field. The dashed lines show the approximate inner and outer radii of the nuclear starburst ring (Xu et al. 2015). The shaded areas show the 90% confidence.

of moderate optical depths and thick high-J CO condition (e.g., Downes & Solomon 1998).

We reconstructed the best-fit CO SLED from models in order to compare with the observational data (Figure 3.10a and 3.10b). The CO SLEDs in the outer disk ($>$ 1.″8) show good agreement with the observations, while those in the starburst ring ($<$ 1.″8) systematically underestimated the CO (3–2)/CO (1–0) and CO (6–5)/CO (1–0) ratios. One possibility to explain the systematic difference is that the starburst ring

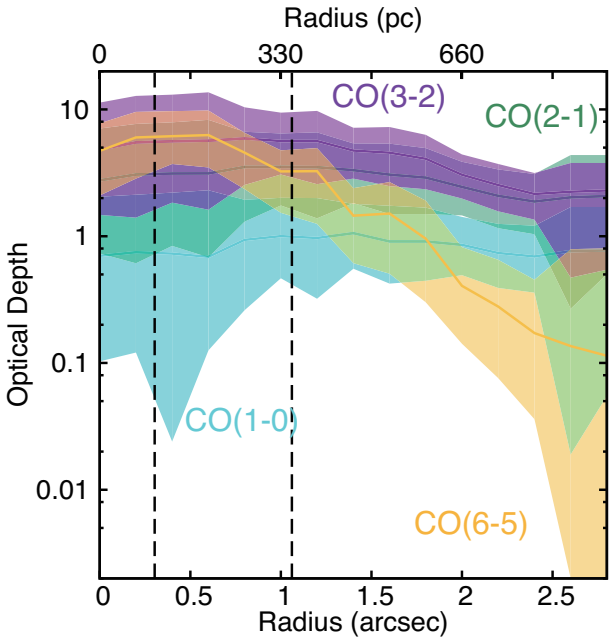

Figure 3.9. Optical depth of each CO transition as a function of the radius. The dashed lines show the approximate inner and outer radii of the nuclear starburst ring (Xu et al. 2015). The shaded areas show the 90% confidence.

of NGC 1614 has an additional warmer ISM, as suggested by Sliwa et al. (2014). The additional warm gas can move the modeled CO (3–2)/CO (1–0) and CO (6–5)/CO (1–0) ratios toward a higher value by fixing the lower-J CO fluxes.

We note that the flux differences between the observations and the model are unlikely to be caused by dust extinction. Although some U/LIRGs show high dust opacities even in the submillimeter wavelengths (e.g., Rangwala et al. 2011; Wilson et al. 2014), the cold dust in the starburst ring of NGC 1614 is still optically thin at 691 GHz (0.06 - 0.21; Section 2).

3.5.2 Comparing with the Narayanan & Krumholz Model

We compare the observed CO SLED (Figure 3.10a) with the model of Narayanan & Krumholz (2014), which can parameterize the CO SLED of galaxies by a power-law function of $\Sigma_{\rm SFR}$. Using the $\Sigma_{\rm SFR}$ derived in Section 2, we reconstructed the CO SLED

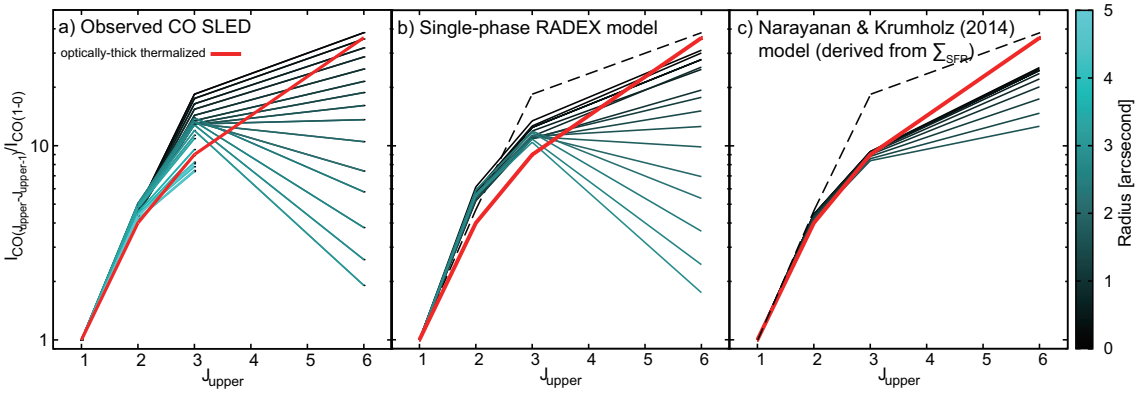

Figure 3.10. (a) Observed CO spectral line energy distributions (SLEDs) of NGC 1614 for concentric rings with the radius from 0.″2 to 5.″0. The color scale ranged from 0.″0 to 5.″0 (0.″2 step from top to bottom lines) shows the radius of the concentric rings which are used for the photometry. The red line indicates a thermalized and optically-thick CO SLED as a reference. (b) Modeled CO SLED reconstructed by the single-phase RADEX. The dashed line shows the observed CO SLED within the central 0.″2 radius. (c) Modeled CO SLED reconstructed from the Narayanan & Krumholz (2014) model. The $\Sigma_{\rm SFR}$ derived from the radio-to-FIR SED (Section 2) is used as the input parameter.

(Figure 3.10c). This model is consistent with the observed CO SLED. On the other hand, the CO (3–2)/CO (1–0) and CO (6–5)/CO (1–0) ratios are underestimated with the single-phase RADEX as already suggested in Section 3.5.1. A multi-phase ISM model is one of the possible explanations. Because our analysis includes only four CO transitions and can only constrain a small number of free parameters, we will focus on a two-phase ISM model rather than a multiple-phase ISM (Section 3.6.4). The $\Sigma_{\rm SFR}$ used here is extinction-free because we used the low frequency continuum from 4.81 to 691 GHz in Section 2. Thus, we can ignore the extinction effect in this comparison.

3.5.3 PDR Model

We used the PDR Toolbox (Kaufman et al. 2006), which can model the beam-averaged incident far-ultraviolet (FUV; 6 eV $< E <$ 13.6 eV) radiation field intensity (G_0 in the unit of 1.6 $\times$ 10^{-3} erg cm^{-2} s^{-1}) and PDR hydrogen nucleus density (n cm^{-3} = $n_{\rm H}$ + $2n_{\rm H_2}$) from the flux density of each CO transition, in order to

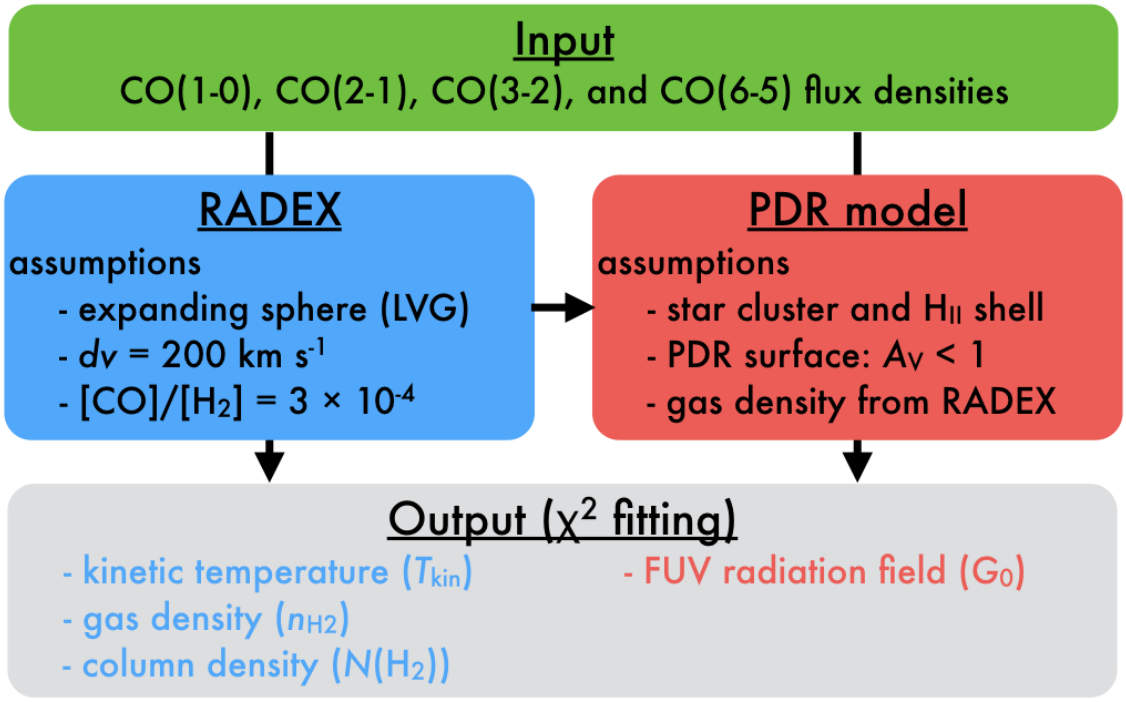

Figure 3.11. Schematic illustration of the modeling procedure using RADEX and PDR Toolbox.

better understand the starburst activities of NGC 1614. We varied n within the 90% confidence range of $2n_{\rm H_2}$ derived by the single-phase RADEX (dn = $10^{0.25}$ cm^{-3}) and G_0 within a range of $10^{-0.50}$ - $10^{6.50}$ (dG_0 = $10^{0.25}$). A schematic illustration of the modeling procedure using RADEX and PDR Toolbox is shown in Figure 3.11. Here we assumed that the $n_{\rm H}$ is negligible compared to the $2n_{\rm H_2}$ term because the central kpc of mergers are often dominated by the molecular phase (e.g., Iono et al. 2005; Kaneko et al. 2014). This assumption is consistent with the compact CO distributions (Figure 3.1) and the extended arc-like HI distribution (Figure 2.1a) around the kpc region of NGC 1614. The results are shown in Figure 3.8d. The minimum reduced-χ^2 is $\sim$ 1 for both grids. The starburst ring has higher G_0 ($> 10^{1.5}$, average = $10^{2.7}$) than the outer disk ($< 10^{1.5}$, average = $10^{0.9}$). The average value of the whole galaxy is $\sim 10^{2.3}$.

In order to check the reliability of the derived G_0, we roughly estimate the averaged FUV radiation field on dust-obscured star-forming region using the prescription

provided by Papadopoulos et al. (2014),

$$G_0(L_{\rm IR}) \sim 3 \times 10^2 \lambda_*({\rm pc}) \left(\frac{L_{\rm IR}}{10^{10}\ L_\odot}\right) \left(\frac{R_{\rm SB}}{100\ {\rm pc}}\right)^{-3} [1 - e^{-(R_{\rm SB}/\lambda_*)}], \quad (3.1)$$

where λ_* is the mean distance of FUV photons propagation before being absorbed, $R_{\rm SB}$ is the size of the starburst ring ($\sim$ 350 pc; Xu et al. 2015). For the clumpy PDR model, λ_* is < 1 pc (Meixner & Tielens 1993). The derived $G_0(L_{\rm IR})$ is $< 10^{2.5}$, which is consistent with the average G_0 derived from the CO SLED.

3.6 Discussion

3.6.1 The "S"-shape velocity field

The "S"-shape morphology in the velocity field suggests the presence of a north-south bar or a warped disk morphology. It coincides with the leading edge of the main near-IR bar suggested by Olsson et al. (2010), so we suggest that the north-south bar results in the "S"-shape non-circular motions (i.e., inflow) detected in the lower-J CO transitions. The presnce of the cold gas inflow along the bar is also suggested by Olsson et al. (2010). In addition, analysis of N-body/SPH simulation performed by Iono et al. (2004a) revealed that tidal interaction between gas-rich disks can produce gas flows directly toward the central regions due to the production of both transient arms and long-lived $m = 2$ bars (i.e., bar instability). They also found that the inflowing gas is characterized by distinct diffuse gas clumps in the PVDs, while dense gas only present in the central rigid rotating component. This simulation result is consistent with our observations including non-detection of the non-circular motion in the CO (6–5) image.

3.6.2 Power Source of the Single-phase ISM

We compare $T_{\rm kin}$ and G_0 with $\Sigma_{\rm SFR}$, which is derived by modeling the radio-to-FIR SED (Section 2), in Figure 3.12. There is a positive correlation with a correlation coefficient of $r = 0.91$ between $\log \Sigma_{\rm SFR}$ and $\log G_0$. This is a sensible result because

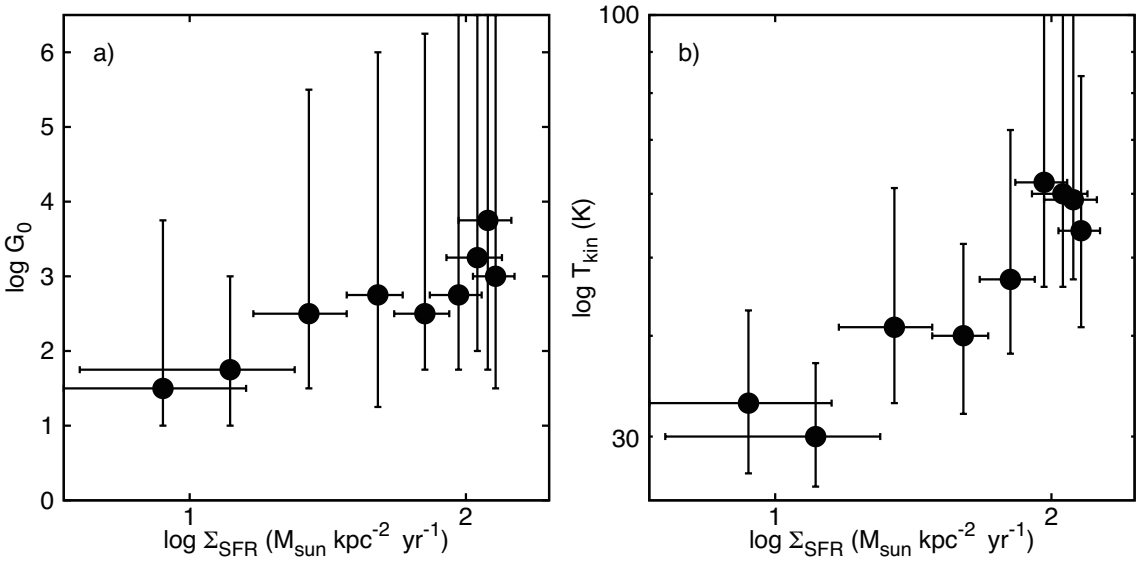

Figure 3.12. (a) Plot of the star formation rate surface density vs. the FUV radiation field at each concentric ring. The errors correspond to the 90% confidence. (b) Plot of the star formation rate surface density vs. the kinetic temperature at each concentric ring.

both parameters are related to star formation. The relation between $\log \Sigma_{\rm SFR}$ and $\log T_{\rm kin}$ also shows a positive correlation ($r = 0.93$). Using a PDR model described in equation 3 of Papadopoulos et al. (2014) and assuming $T_{\rm kin} > T_{\rm dust}$ which is found by PDR models (e.g., Hollenbach & Tielens 1999), the derived $T_{\rm kin}$ of 20 - 70 K corresponds to $\log G_0$ of $< 10^{1.4-4.6}$. This is consistent with the result of the CO SLED model described in Section 3.5.3. These models and a simple comparison indicates that the dusty starburst in NGC 1614 is enough to power the CO excitation up to $J_{\rm upp} = 6$ even if we just assume a single-phase molecular gas ISM for the starburst ring.

3.6.3 Spatially resolved CO-to-H_2 Conversion Factor

Molecular hydrogen mass is one of the most fundamental parameters to characterize galaxies in relation to their starbursts and AGNs. Although the galactic-scale CO (1–0) luminosity to H_2 mass conversion factor ($M_{\rm H_2}/L'_{\rm CO(1-0)} \equiv \alpha_{\rm CO(1-0)}$) in nearby U/LIRGs has been well studied (Bolatto et al. 2013b, for a review), the spa-

tial properties are not fully understood.

We measure the $\alpha_{\mathrm{CO(1-0)}}$ as a function of radius using,

$$\alpha_{\mathrm{CO(1-0)}} = 1.36 \frac{m_{\mathrm{H_2}}\, N(\mathrm{H_2})\, S_{\mathrm{ring}}}{L'_{\mathrm{CO(1-0)}}}\, M_{\odot}\, (\mathrm{K\,km\,s^{-1}\,pc^2})^{-1}, \tag{3.2}$$

where $m_{\mathrm{H_2}}$ is the mass of the hydrogen molecule, $N(\mathrm{H_2})$ is the column density derived by RADEX (Section 3.5.1), S_{ring} is the area of the concentric rings, and $L'_{\mathrm{CO(1-0)}}$ is the CO (1–0) luminosity. We multiply 1.36 to account for the helium abundance relative to hydrogen. The derived $\alpha_{\mathrm{CO(1-0)}}$ at the starburst ring is 0.2 - 0.5 ($\frac{3\times10^{-4}}{\mathrm{[CO]/[H_2]}}$) except for the central hole (central 0.″2 radius) which yields $\sim$ 0.05 ($\frac{3\times10^{-4}}{\mathrm{[CO]/[H_2]}}$) (Figure 3.13). This is lower than 0.9 - 1.5 ($\frac{3\times10^{-4}}{\mathrm{[CO]/[H_2]}}$) at the starburst ring and 0.1 ($\frac{3\times10^{-4}}{\mathrm{[CO]/[H_2]}}$) at the central hole derived by Sliwa et al. (2014). The difference between both models can be explained by the presence of virialized giant molecular clouds (GMCs) and the different treatment of the missing flux. Assuming that GMCs in the central region of NGC 1614 are virialized, $\alpha_{\mathrm{CO(1-0)}}$ depends on gas density and kinetic temperature ($\alpha_{\mathrm{CO(1-0)}} \propto \rho^{0.5} T_{\mathrm{kin}}^{-1}$ where ρ is the gas density; Solomon & Vanden Bout 2005; Bolatto et al. 2013b). As a consequence of the different missing flux treatment, the results of our RADEX modelings for the starburst ring are warmer (27 - 120 K and $10^{3.9-5.3}$ cm^{-3}) than the results in Sliwa et al. (2014) (19 - 64 K and $10^{3.0-6.5}$ cm^{-3}) (see also Section 3.5.1). Assuming the same gas density (ρ) and beam filling factor for both models, $\alpha_{\mathrm{CO(1-0)}}$ derived from our model shall indeed be $\sim$ 2 times lower than the Sliwa et al. (2014) value, indicating that both models are consistent.

We note that the treatment of the missing flux (i.e., how to achieve the same MRS for all transitions) should be different depending on the situation. When we have short-spacing data for "all" transitions, we should combine the data with data obtained with the compact configurations, which allows us to recover extended structures. In the case of this Section, single-dish or ACA data for several transitions are lacking, and thus we chose to clip the inner uv, making $\alpha_{\mathrm{CO(1-0)}}$ different from Sliwa et al. (2014).

Comparing with local LIRGs, it is known that nearby spirals show larger $\alpha_{\mathrm{CO(1-0)}}$ (e.g., Bolatto et al. 2013b). Sandstrom et al. (2013) constructed $\alpha_{\mathrm{CO(1-0)}}$ as a function

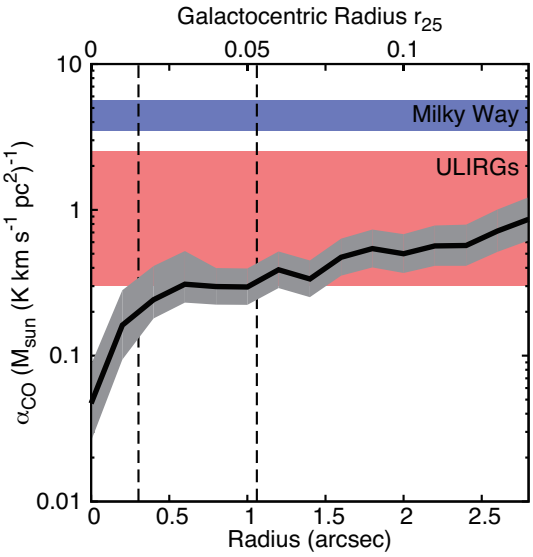

Figure 3.13. The CO-to-H_2 conversion factor ($= \alpha_{CO(1-0)} = M_{H_2}/L'_{CO(1-0)}$) as a function of the radius derived by the signle-phase RADEX model (i.e., $N(H_2)$). The dashed lines show the approximate inner and outer radii of the nuclear starburst ring (Xu et al. 2015). The shaded areas show the 90% confidence. The blue and red regions show approximate $\alpha_{CO(1-0)}$ for the Milky Way and ULIRGs (Bolatto et al. 2013b).

of galactocentric radius ($r_{25} = r/R_{25}$, where R_{25} is the B-band isophotal radii at 25 mag arcsec^{-2}) for 26 spiral galaxies, and found lower $\alpha_{CO(1-0)}$ at the galaxy centers ($r_{25} < 0.2$) by a factor of $1 \sim 5$ relative to their disks ($r_{25} = 0.4$ - 1.0). Using R_{25} of 6.5 kpc ($\sim 20''$) derived by $R_{25} = 1.9 \times R_{\rm eff}$ (Bellocchi et al. 2013) and $R_{\rm eff} = 3.44$ kpc (Ueda et al. 2014) for NGC 1614, the outer radius of the central hole, the starburst ring, and the CO disk of NGC 1614 are $r_{25} \sim 0.01$, 0.05, and 0.14, respectively (Figure 3.13). This indicates that NGC 1614 shows a similar radial $\alpha_{CO(1-0)}$ trend to nearby spirals, but it has a more compact distribution and lower $\alpha_{CO(1-0)}$ value than that of nearby spirals for a given galactocentric radius.

We calculate the conversion factor for CO (3–2) ($M_{H_2}/L'_{CO(3-2)} \equiv \alpha_{CO(3-2)}$) and CO (6–5) ($M_{H_2}/L'_{CO(6-5)} \equiv \alpha_{CO(6-5)}$) in Figure 3.14 assuming the single-phase ISM. The radial distribution of $\alpha_{CO(3-2)}$ is almost the same as that of $\alpha_{CO(1-0)}$, while the $\alpha_{CO(6-5)}$ shows a steeper shape, except for the nuclear region ($< 1''.0$), which shows a similar value of $\alpha_{CO(1-0)}$ because of the sub-thermalized conditions in the outer

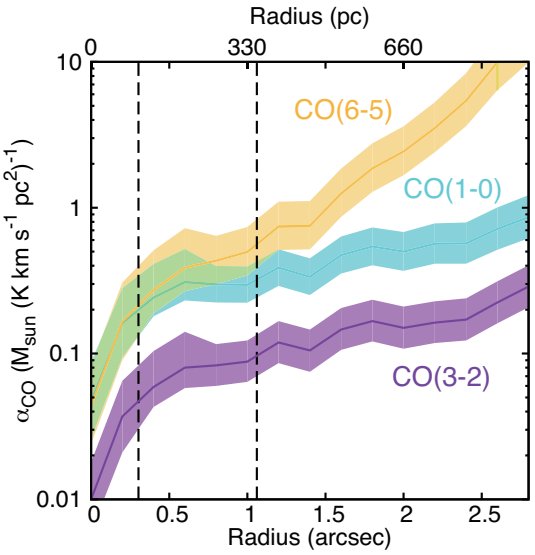

Figure 3.14. The CO-to-H_2 conversion factor for CO (1-0), CO (3–2), and CO (6–5) lines as a function of the radius. The dashed lines show the approximate inner and outer radii of the nuclear starburst ring (Xu et al. 2015). The shaded areas show the 90% confidence.

region.

3.6.4 Two-phase Modeling for the Starburst Ring

Two-phase ISM model

Herschel and other single-dish observations revealed that the CO SLED of nearby U/LIRGs can be represented by multi-phase molecular gas ISM model (e.g., van der Werf et al. 2010; Rangwala et al. 2011). Although the spatial properties of the CO SLED for U/LIRGs are unclear because of the limited number of high-resolution CO data, our high-resolution CO (1–0) and CO (2–1) observations, as well as the archival CO (3–2) and CO (6–5) data, allow us to study this for a LIRG for the first time.

Before discussing the two-phase molecular gas ISM in NGC 1614, we note that the dust ISM in the starburst ring can be described by warm and cold components. Pereira-Santaella et al. (2015) reported the presence of a warm dust component in the starburst ring ($\sim$ 110 K) revealed by modeling of the mid-IR emission, although there is also a cold dust component ($\sim$ 35 K; Xu et al. 2015). In an ISM where the

gas and dust are intermingled, the molecular gas component separates into a warm component of $T_{\rm warm} \sim 110$ K and a cold component of $T_{\rm cold} \sim 35$ K. This can be addressed by RADEX with simple assumptions.

In order to model the warm and cold gas components, we minimize the number of free parameters by fixing the cold gas component using the observed line ratios at the outer region contained within a radius of 2.″8 - 3.″0. This region shows a good agreement with a single-phase model with a temperature of $T_{\rm cold} \sim 19$ K (Figure 3.8a). Here we assume that cold molecular clouds, which dominate the outer region, dominate the cold gas component in the starburst ring. We calculate the contribution of the warm gas component to the total CO luminosity by using,

$$r = \frac{L'_{\rm CO(2-1),warm}}{L'_{\rm CO(2-1),obs}}, \tag{3.3}$$

where $L'_{\rm CO(2-1),warm}$ is the CO (2–1) luminosity of the warm gas component and $L'_{\rm CO(2-1),obs}$ is the observed CO (2–1) luminosity within the central 1.″8 radius.

In the fitting routine, we varied r within a range of 0 - 0.009 (dr = 0.001), 0.01 - 0.09 (dr = 0.01), and 0.1 - 0.9 (dr = 0.1) to estimate the CO luminosities of the warm gas and cold gas components. Then, we varied the warm gas kinetic temperature within a range of $T_{\rm warm}$ = 10 - 800 K (d$T_{\rm warm}$ = 10 K) and the warm gas column density of $N({\rm H_2})_{\rm warm}$ = 10^{19} - 10^{24} cm^{-2} (d$N({\rm H_2})_{\rm warm}$ = $10^{0.1}$ cm^{-2}). We fixed [CO]/[H$_2$] (= 3×10^{-4}) and the gas density of the warm gas component as $n_{\rm warm}$ = $10^{2.0}$ (grid A), $10^{3.0}$ (grid B), and $10^{4.0}$ cm^{-3} (grid C). The results are shown in Figure 3.15. The minimum χ^2 are 1.30 (grid A), 1.05 (grid B), and 0.85 (grid C), which are smaller than the χ^2 values of the single-phase modeling for the starburst ring (r < 1.″8). The 90% confidence ranges of $T_{\rm warm}$ are 300 - 370, > 250, and 70 - 450 K, whereas those of $N({\rm H_2})_{\rm warm}$ are > $10^{23.7}$, > $10^{22.9}$, and $10^{23.0-23.6}$ for the grid A, B, and C, respectively. The 90% confidence ranges of r are < 0.1 (best-fit = 0), < 0.8 (best-fit = 0), and < 0.6 (best-fit = 0.003) for the grids A, B, and C, respectively, indicating less contribution of the warm gas component to the lower-J CO fluxes. This two-phase ISM model in NGC 1614 is similar to that found in the nearby ULIRG Arp 220, showing that a warm gas component has almost no contribution to CO lines lower than J = 3–2 (Rangwala et al. 2011).

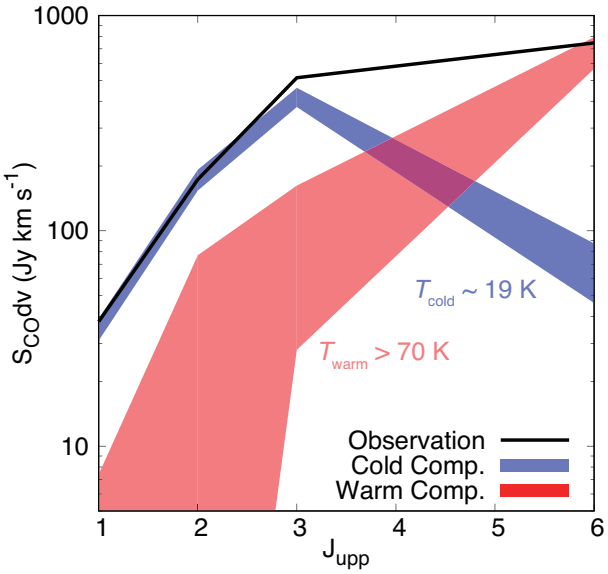

Figure 3.15. Two-phase CO SLED model. Dark line shows the observed CO SLED toward a central 1.″8 (594 pc) radius. The red and blue areas show the 90% confidence range of the warm and cold component, respectively. The areas cover the results from the grid A, B, and C.

Using the PDR model (Section 3.5.3) assuming $n = 10^{2.0-5.0}$ cm^{-3}, we find that the FUV field (G_0) of the inferred warm gas component is higher than $10^{6.5}$. Considering the relatively low Σ_{SFR} (Section 2) and the absence of a heavily obscured AGN, such extreme radiation field is unreasonable for NGC 1614.

In summary, the starburst ring of NGC 1614 can be described by a two-phase molecular gas ISM with a cold component of $\sim$ 19 K (dominated by normal GMCs) and a warm component of $>$ 70 K (warm ISM directly related to powerful activities). The observed star-forming activities (i.e., clumpy PDRs) are not possible heating sources of the warm gas. We note that these models are consistent with a two-phase dust ISM ($\sim$ 35 K and $\sim$ 110 K) of the starburst ring (Pereira-Santaella et al. 2015; Xu et al. 2015) and multi-phase models for other U/LIRGs (e.g., van der Werf et al. 2010; Rangwala et al. 2011).

Power source of the warm gas

The observed high-J CO fluxes are systematically higher than those in the Narayanan & Krumholz model (Section 3.5.2). Also, FUV radiation heating due to the observed star-forming activities cannot reproduce the possible warm gas component (Section 3.6.4) assuming the two-phase model. Here we employ the mechanical heating (i.e., shock excitation) as an alternative mechanism to power the warm gas. We found the characteristic peaks of the CO line ratios along with the putative outflow (Section 3.4.3), which are similar to what has been observed in the nearby Seyfert galaxy NGC 1068. NGC 1068 has a CND which is thought to be heated by the nuclear jet (García-Burillo et al. 2014). The similarity between these galaxies may suggest that in the central 1.″8 of NGC 1614 the CO emission is significantly affected by the kinematical interaction between the starburst ring and the putative outflow. The outflow can heat the starburst ring kinematically, producing highly excited molecular gas components around the shocked region. This scenario is consistent with the detection of H_2 1–0 S(1) line within the central 1.″8 radius (Alonso-Herrero et al. 2001; Kotilainen et al. 2001), suggesting that nearly 1/3 of the total near-IR H_2 is produced by shocks. Stellar feedback such as supernova explosions and stellar winds are also possible sources of mechanical heating. Therefore, we compare the kinetic luminosity of the outflow and the degree of stellar feedback with the total CO luminosity of the warm gas.

We derive the kinetic luminosity from the supernovae ($L_{\rm SN}$) using (Maloney 1999),

$$L_{\rm SN} \sim 3 \times 10^{43} \left(\frac{\nu_{\rm SN}}{1\ {\rm yr}^{-1}} \right) \left(\frac{E_{\rm SN}}{10^{51}\ {\rm erg}} \right)\ {\rm erg\ s}^{-1}, \tag{3.4}$$

where $\nu_{\rm SN}$ is the supernova rate and $E_{\rm SN}$ is the energy of a supernova ($\sim 10^{51}$ erg; Rangwala et al. 2011). Using the $\nu_{\rm SN}$ of ~ 0.9 (Rosenberg et al. 2012), we obtain $L_{\rm SN}$ of $\sim 2.7 \times 10^{43}$ erg s^{-1}. Assuming the energy from stellar winds is similar to supernovae (McCray & Kafatos 1987), the total kinetic luminosity from the stellar feedback is $\sim 5.4 \times 10^{43}$ erg s^{-1}. On the other hand, the kinetic luminosity from the putative outflow is $\sim 2.5 \times 10^{42}$ erg s^{-1} (García-Burillo et al. 2014). Comparing with the inferred CO luminosity of the warm gas component ($\sim 1.2 \times 10^{41}$ erg s^{-1}; sum up

to $J_{\rm upp} = 23$), both the outflow and the stellar feedback are possible heating sources of the warm gas component even when we adopt a low energy injection efficiency of $< 5\%$. Although the molecular outflow is a possible source in terms of the energy, the high resolution CO (6-5) image (Xu et al. 2015) shows that the distribution is closely related to the starburst ring, not the outflow (Figure 3.5a). This indicates that stellar feedback is more likely to be the heating source for higher-J CO rather than the putative molecular outflow when we consider both energy and spatial CO (6–5) distribution. We note that the mechanical energy is also a possible heating source in Arp 220 (Rangwala et al. 2011), NGC 6240 (Meijerink et al. 2013), and other U/LIRGs (Greve et al. 2014).

3.6.5 Balance of Molecular Gas in NGC 1614

In order to evaluate the effect of the molecular gas inflow, we estimate molecular gas inflow rate (IFR) using,

$$\mathrm{IFR} = \frac{M_{\rm in} v_{\rm in}}{r_{\rm in}}\ M_\odot\ \mathrm{yr}^{-1} \tag{3.5}$$

where $M_{\rm in}$ is the inflowing H_2 mass, $v_{\rm in}$ is the inflowing velocity, and $r_{\rm in}$ is the distance from the starburst ring (e.g., Combes et al. 2013). Assuming the inflowing component is along the gas disk, equation 3.5 can be calculated as follows.

$$\begin{aligned} \mathrm{IFR} &= M_{\rm in}\left(\frac{v_{\rm los}}{\cos\theta}\right)\left(\frac{\sin\theta}{r_{\rm proj}}\right) \\ &\sim 54\left(\frac{\tan\theta}{\tan 33^\circ}\right)\left(\frac{\alpha_{\rm CO}}{0.2\ \alpha_{\rm MW}}\right)\ M_\odot\ \mathrm{yr}^{-1} \end{aligned} \tag{3.6}$$

where $v_{\rm los}$ is the line-of-sight velocity relative to the rotation velocity at the projected distance ($r_{\rm proj}$), θ is the inclination of the disk, and the $\alpha_{\rm MW}$ is the CO-to-H_2 conversion factor for the Galaxy (= 4.3; Bolatto et al. 2013b). Here we adopt θ of 33°and $\alpha_{\rm CO}$ of $0.2\alpha_{\rm MW}$ which are the same values to derive the molecular gas outflow rate (OFR; García-Burillo et al. 2015). We estimate the flux density of the inflowing gas components using Figure 3.3e. The northern (southern) inflowing component has 25.8

(19.3) Jy km s^{-1}, which corresponds to $M_{\rm in}$ of $10^{8.40}\left(\frac{\alpha_{\rm CO}}{0.2\,\alpha_{\rm MW}}\right)$ ($10^{8.27}\left(\frac{\alpha_{\rm CO}}{0.2\,\alpha_{\rm MW}}\right)$) $M_\odot$. The $v_{\rm los}$ and $r_{\rm proj}$ of the northern (southern) component are 80 (40) km s^{-1} and 500 (500) pc, respectively. The derived IFR is 54 $M_\odot$ yr^{-1} with the uncertainty by a factor of three, which mainly due to the uncertainties of $v_{\rm los}$ and $r_{\rm proj}$.

Comparing the SFR in the starburst ring (32.8 $M_\odot$ yr^{-1}; Xu et al. 2015) and OFR (40 $\pm$ 12 $M_\odot$ yr^{-1}; García-Burillo et al. 2015), and assuming that the IFR, OFR, and SFR continue constantly, we can investigate the balance between molecular gas input and output in the starburst ring of NGC 1614.

$$\frac{\rm IFR}{\rm SFR + OFR} \sim \begin{cases} 0.7 & (\theta = 33^\circ, \alpha_{\rm CO} = 0.2\,\alpha_{\rm MW}) \\ 1.2 & (\theta = 33^\circ, \alpha_{\rm CO} = \alpha_{\rm MW}) \end{cases} \tag{3.7}$$

Independent of the adopted $\alpha_{\rm CO}$, the molecular gas input and output are roughly balanced, indicating that NGC 1614 can sustain both star-forming activities and an outflow in the starburst ring until exhausting the molecular gas reservoir in the starburst ring and the outer region via bar-driven inflow. The total molecular gas depletion time due to star formation and outflow (= $M_{\rm H_2}$/(SFR + OFR)) ranges from 17.7 $\pm$ 4.6 Myr ($\alpha_{\rm CO} = \alpha_{\rm MW}$) to 56.6 $\pm$ 9.3 Myr ($\alpha_{\rm CO} = 0.2\alpha_{\rm MW}$). This is consistent with the typical duration timescale of U/LIRG phase predicted by numerical merger simulations (dozens of Myr; Saitoh et al. 2009; Teyssier et al. 2010). The luminous merger remnant NGC 1614 may quench itself until the next dozens of Myr due to depletion of the cold molecular gas reservoir (if the molecular outflow and star formation continue constantly).

3.6.6 Central Gas Geometry of NGC 1614

We summarize all results provided by this Section and Section 2 and previous studies into a simple schematic picture (Figure 3.16). We used a position angle of $\sim$ -352°and an inclination of $\sim$36°as estimated by Ueda et al. (2014), for the cold gas disk and the starburst ring. This is consistent with the results provided by García-Burillo et al. (2015). We found "S"-shape non-circular motions along the leading edge of the north-south near-IR bar in the lower-J CO velocity fields and PVDs. The near-IR

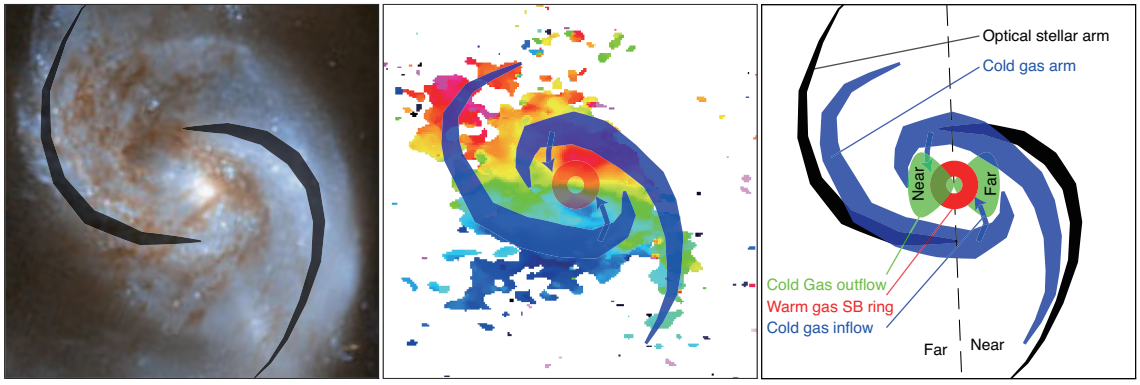

Figure 3.16. (left) Possible optical arms overlaid on the HST/ACS image of NGC 1614 [Credit: NASA, ESA, the Hubble Heritage Team (STScI/AURA)-ESA/Hubble Collaboration and A. Evans (University of Virginia, Charlottesville/NRAO/Stony Brook University)]. (b) Possible main molecular gas arms [blue], cold gas inflow [blue arrows], and the starburst ring detected in CO (6–5) [red] (Xu et al. 2015). (c) Schematic illustration of the possible geometry of NGC 1614.

bar connects to the near-IR spiral arms (Olsson et al. 2010). Moreover, the northern part of the molecular bar was detected in SMA CO (2–1) observations (dashed line in Figure 3 of König et al. 2013). König et al. (2016) also suggested that the northern molecular gas components are diffuse gas clouds which are now funneled into the nuclear region, although the flowing direction is different from the picture shown in Figure 3.16. The central starburst ring (SFR $\sim$ 32.8 $M_{\odot}$ yr^{-1}; Xu et al. 2015) was detected in star formation tracers (Alonso-Herrero et al. 2001; Herrero-Illana et al. 2014; Pereira-Santaella et al. 2015, see also Section 2) and dense/warm gas tracers (Sliwa et al. 2014; Xu et al. 2015). The nucleus has no strong AGN (Imanishi & Nakanishi 2013a; Herrero-Illana et al. 2014; Pereira-Santaella et al. 2015) or heavily obscured AGN (Xu et al. 2015). The upper limit of the AGN luminosity suggests that it might be possible for driving the putative molecular gas outflow with the outflow rate of 40 $M_{\odot}$ yr^{-1} as well as the starburst activities (García-Burillo et al. 2015). The detection of the molecular outflow coincides with the geometry of the ionized gas outflow with no redshifted component due to the extinction by the large column of dust in the inclined disk (Bellocchi et al. 2012).

Radiative transfer modeling with RADEX suggest that the starburst ring will

have a single-phase ($\sim$ 42 K) or two-phase ($\sim$ 19 K and $>$ 70 K) molecular gas ISM, while the outer disk has a single cold gas ISM ($\sim$ 22 K). The single-phase model is consistent with the FUV radiation field estimated by PDR models. However, star-forming activities are not enough to power the warm gas component in the starburst ring if the two-phase ISM is valid. Alternatively, we suggest the mechanical heating from the supernovae and stellar winds as a heating source of the warm gas component.

3.7 Summary of This Section

Here we present a detailed study of the molecular gas ISM in the luminous merger remnant NGC 1614 through high-resolution, high-sensitivity, and *uv*-matched ALMA observations of the CO (1–0), CO (2–1), CO (3–2), and CO (6–5) lines. The results are summarized as follows:

1. The CO (6–5) line shows a compact distribution which coincides with the starburst ring detected in Pa α and radio-to-FIR continuum emission, while the other lower-J CO lines are extended. This indicates that the CO (6–5) can be used as a better tracer of star formation as already suggested by Xu et al. (2015).

2. We find a "S"-shape non-circular motion along the near-IR north-south bar in the CO (1–0), CO (2–1), and CO (3–2) velocity fields. Comparing with numerical simulations, this may be a bar-driven cold gas inflow connecting to the starburst ring.

3. Radiative transfer modeling with RADEX reveal that the molecular gas ISM in NGC 1614 can be described in a single-phase or two-phase model. The single-phase model shows a radial gradient of the gas kinetic temperature from 70 to 20 K and the H_2 column density from $10^{22.9}$ to $10^{22.0}$ cm^{-2} with peaks at the starburst ring. This single-phase model agrees with the observational results, while there is a systematic underestimation of the CO (3–2) and CO (6–5) flux. The Narayanan & Krumholz CO SLED model using the observed $\Sigma_{\rm SFR}$ also

shows the same trend. To account for the underestimation in both models, we verify the two-phase model to the line ratios in the central 1.″8 radius.

4. The two-phase RADEX model for the starburst ring shows a good agreement with a cold gas component of $\sim$ 19 K and a warm gas component of $>$ 70 K, while there are number of assumptions at this stage. This is consistent with the two-phase dust ISM ($\sim$ 35 K and $\sim$ 110 K) revealed by high-resolution ($<$ 0.″5) mid-IR and far-IR observations and two-phase modelings for other nearby U/LIRGs. Higher-J CO observation ($J_{\rm upp} \geq 7$) is critical to characterize the molecular gas ISM in the starburst ring of NGC 1614.

5. Considering that the observed star-forming activities are not enough to power the warm gas component inferred from the two-phase RADEX, we suggest mechanical heating from supernovae and stellar winds as an alternative power source.

6. The summation between the cold molecular gas outflow rate (OFR) and the star formation rate (SFR) in the starburst ring is comparable to the cold gas inflow rate (IFR), showing evidence of the balance between the molecular gas input and output at the starburst ring. Assuming IFR, OFR, and SFR continue constantly, it takes dozens of Myr to exhaust all H_2 mass in NGC 1614. This is consistent with the typical U/LIRG duration timescale suggested by numerical merger simulations.

Chapter 4

Merger-induced Shocks in the Nearby LIRG VV 114 through Methanol Lines

4.1 Abstract

In this Chapter, we report the detection of two CH_3OH lines ($J_K = 2_K$–1_K and 3_K–2_K) between the progenitor's disks ("Overlap") of the mid-stage merging galaxy VV 114 obtained using the ALMA Band 3 and Band 4. The detected CH_3OH emission show an extended filamentary structure ($\sim$ 3 kpc) across the progenitor's disks with relatively large velocity width (FWZI $\sim$ 150 km s^{-1}). The emission is only significant in the "overlap" and not detected in the two merging nuclei. Assuming optically-thin emission and LTE, we found X_{CH_3OH} peaks at the "Overlap" ($\sim 8 \times 10^{-9}$), which is almost an order of magnitude larger than that at the eastern nucleus. We suggest that kpc-scale shocks driven by galaxy-galaxy collision may play an important role to enhance the CH_3OH abundance at the "Overlap". This scenario is consistent with that shock-induced large velocity dispersion components of ionized gas have been detected in optical wavelength at the same region. Conversely, low X_{CH_3OH} at the nuclear regions might be attributed to the strong photodissociation by nuclear starbursts and/or putative AGN, or inefficient production of CH_3OH on dust grains due to initial high temperature conditions (i.e., desorption of the precursor molecule, CO, into gas-phase before forming CH_3OH on dust grains). These

ALMA observations demonstrate that CH_3OH is a unique tool to address kpc-scale shock-induced gas dynamics and star formation in merging galaxies.

4.2 Observations and Data Overview

We observed VV 114 using Band 3 and Band 4 of ALMA with the spectral scan mode (Mathys et al. 2013) as a cycle 2 program (ID: 2013.1.01057.S). The correlator was configured to cover 84 - 111 GHz and 127 - 154 GHz using eight tunings. In this Thesis, we present the tunings containing the multiple CH_3OH (2_K–1_K) ($\nu_{\rm obs} \sim$ 94.84 GHz) and CH_3OH (3_K–2_K) ($\nu_{\rm obs} \sim$ 142.24 GHz) lines. Observation setups of other tunings are summarized in Appendix B. We observed blended sets of thermal rotational transitions of CH_3OH. Detected transitions are listed in Table 4.1. Other transitions (e.g., $J_K = 0_0$–1_{-1}) are not robuestly detected. Since such non-detections do not put meaningful upper limits in the analysis shown later, we ignore them in this Thesis. The CH_3OH (2_K–1_K) data (Band 3) were obtained on 2014 July 3, 2014 July 4, and 2015 June 11 with the single-sideband system temperature ($T_{\rm sys}$) of 39 - 103 K, whereas the CH_3OH (3_K–2_K) data (Band 4) was obtained on 2015 May 25 with $T_{\rm sys}$ of 47 - 124 K. Thirty-one to thirty-eight (thirty-six) 12 m antennas with the projected baseline length of 19 - 778 m (21 - 539 m) were assigned for the Band 3 (Band 4) observations. Each tuning has four spectral windows to cover each sideband. The spectral window has a bandwidth of 1.875 GHz with 1.938 MHz resolution, while they were binned together to create better signal-to-noise ratio data cubes. The total on-source time of the Band 3 and Band 4 observations are 47.4 minutes and 20.0 minutes, respectively. Neptune and Uranus were used for the flux calibration of the both the bands. J0137-2430 and J2258-2758 were used for the bandpass calibration of the both the bands. Either of J0116-2052 and J0110-0741 was used for the phase calibration of Band 3, whereas J0110-0741 was used for the phase calibration of Band 4.

The data reduction, calibration, and imaging were carried out using `CASA` (McMullin et al. 2007). All maps were reconstructed with the natural weighting to minimize noise levels. We made the data cubes with a velocity resolution of 50 km s^{-1} ($\sim$ 14.4 MHz) for CH_3OH (2_K–1_K) and 20 km s^{-1} ($\sim$ 9.8 MHz) for CH_3OH (3_K–2_K).

Table 4.1. Information of the detected CH_3OH lines and their imaging properties

Transition	Blended J_K	$\nu_{\rm rest}$ (GHz)	$\nu_{\rm obs}$ (GHz)	$E_{\rm u}$ (K)	Sμ^2	Beam Size ($''$)	Beam P.A. ($^\circ$)	δv (km s^{-1})	Noise rms[a] (mJy beam^{-1})
2_K–1_K	2_{-1}–1_{-1}, E	96.73936	94.88251	12.5	1.21	1.47 × 1.12	−88.8	50	0.37
	2_0–1_0, A^{++}	96.74138	94.88449	7.0	1.62				
	2_0–1_0, E	96.74455	94.88760	20.1	1.62				
	2_1–1_1, E	96.75551	94.89835	28.0	1.24				
3_K–2_K	3_0–2_0, E	145.09371	142.30873	27.1	2.42	1.60 × 1.04	+67.8	20	0.69
	3_{-1}–2_{-1}, E	145.09737	142.31232	19.5	2.16				
	3_0–2_0, A^{++}	145.10315	142.31799	13.9	2.43				
	3_2–2_2, A^{--}	145.12441	142.33884	51.6	1.36				
	3_2–2_2, E	145.12619	142.34058	36.2	1.33				
	3_{-2}–2_{-2}, E	145.12639	142.34078	39.8	1.35				
	3_1–2_1, E	145.13186	142.34614	35.0	2.21				
	3_2–2_2, A^{++}	145.13346	142.34772	51.6	1.36				

[a]Noise rms in the data which have velocity resolution of δv.

Before imaging, we combined the cycle 0 CH_3OH (2_K–1_K) data (ID: 2011.0.00467.S) in order to increase the sensitivity, and continuum emission was subtracted in the *uv*-plane. We note that we recalibrated the cycle 0 data using the Butler-JPL-Horizons 2012 model. Other imaging properties are listed in Table 4.1, and are introduced in Appendix B. The systematic error of absolute flux scaling factor using a solar system object is 5% for Band 3 and Band 4 (Lundgren 2013). The flux densities of the bandpass and phase calibrators were in good agreement with measurements provided by the ALMA Calibrator Source Catalogue[1]. We ignore the difference of the missing flux effect between Band 3 and Band 4, since the maximum recoverable scale of the assigned configuration for the Band 3 and Band 4 observations (18″and 13″, respectively) is comparable or larger than the filament of VV 114 detected in ^{13}CO (1–0) and dust continuum (Saito et al. 2015).

4.3 Results

Images of the integrated intensity, velocity field, and velocity dispersion are shown in Figure 4.1. The total CH_3OH (2_K–1_K) and CH_3OH (3_K–2_K) integrated intensities are 0.91 ± 0.11 and 2.31 ± 0.18 Jy km s^{-1}, respectively. We checked possible blending with other species using the molecular line database Splatalogue[2] and also line detections reported by Watanabe et al. (2014), Aladro et al. (2015) and Costagliola et al. (2015), because some extragalactic line surveys reached line confusion limits. We found no potential bright lines around CH_3OH (2_K–1_K). Although there is *c*-C_3H_2 (3_{12}-2_{21}) ($\nu_{\rm rest}$ = 145.08961 GHz) around CH_3OH (3_K–2_K) ($\nu_{\rm rest}$ = 145.09–145.14 GHz), its contribution to the CH_3OH (3_K–2_K) intensities may be negligible, because any other *c*-C_3H_2 transitions are not robustly detected toward the Overlap region in our Band 3/4 data. This is consistent with that the starburst galaxy NGC 253 that is thought to be dominated by shocks and shows weaker *c*-C_3H_2 line emissions than the CH_3OH (2_K–1_K) line (Aladro et al. 2015). Toward SB (Figure 4.2), we detected some *c*-C_3H_2 transitions (e.g., $J_{KaKc} = 4_{04}$–3_{13}), which were not stronger than

[1]https://almascience.nrao.edu/sc/
[2]http://www.splatalogue.net/

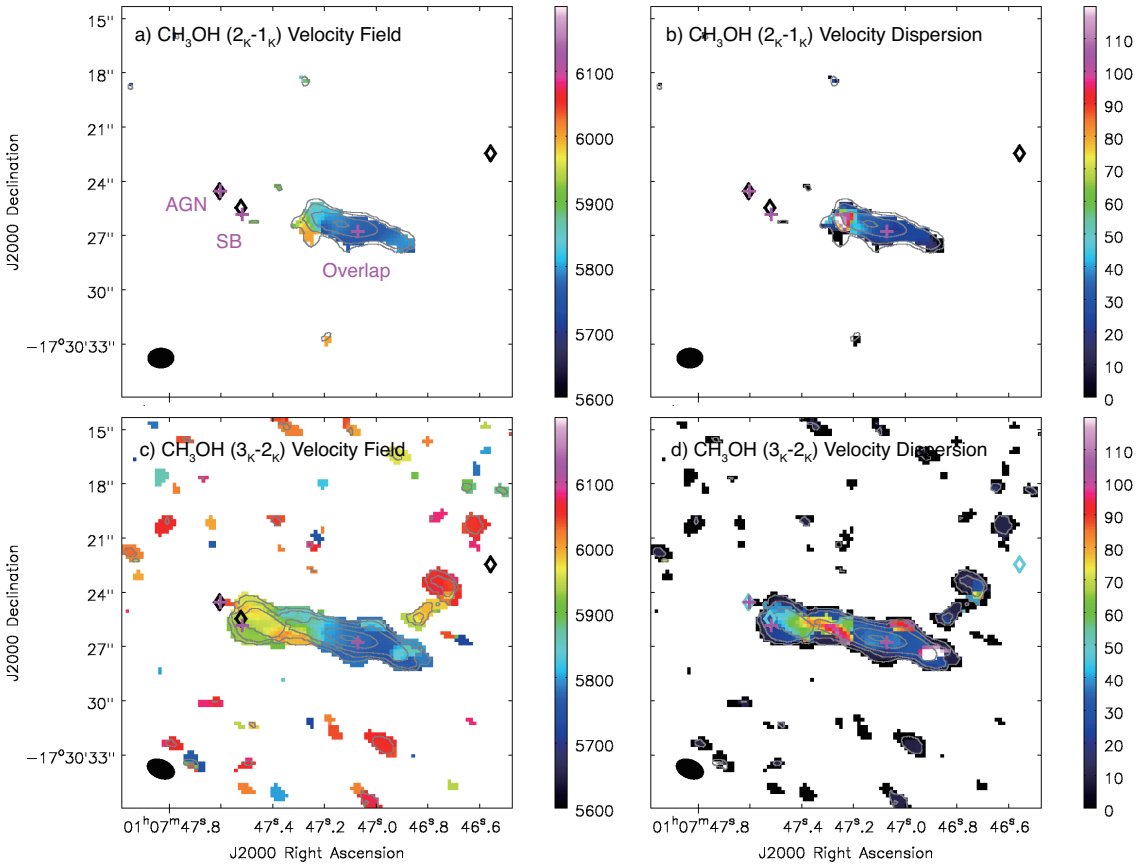

Figure 4.1. (a) Integrated intensity contour of CH_3OH (2_K–1_K) overlaid on the velocity field. The contours are 0.32 × (0.16, 0.32, 0.64, and 0.96) Jy beam^{-1} km s^{-1}. The crosses show the peak positions of the HCO^+ (4–3) emission. AGN, SB, and Overlap correspond to E0, E1, and W0 defined by Iono, Saito et al. (2013), respectively. (b) Integrated intensity contour of CH_3OH (2_K–1_K) overlaid on the velocity dispersion. (c) The same as (a) but for CH_3OH (3_K–2_K). The contours are 0.67 × (0.08, 0.16, 0.32, 0.64, and 0.96) Jy beam^{-1} km s^{-1}. The synthesized beams are shown in the bottom-left corner. The diamonds show the K_s-band stellar nuclei. (d) The same as (b) but for CH_3OH (3_K–2_K).

CH_3OH (3_K–2_K), and so CH_3OH (3_K–2_K) intensity might be slightly overestimated. However, this does not change our discussion and conclusion (see Section 5.5.5).

Figure 4.1 shows an extended filamentary structure, which coincides with previous molecular gas and dust images (Iono, Saito et al. 2013; Saito et al. 2015). The strongest peak is located at Overlap, whereas the emission is only marginally detected

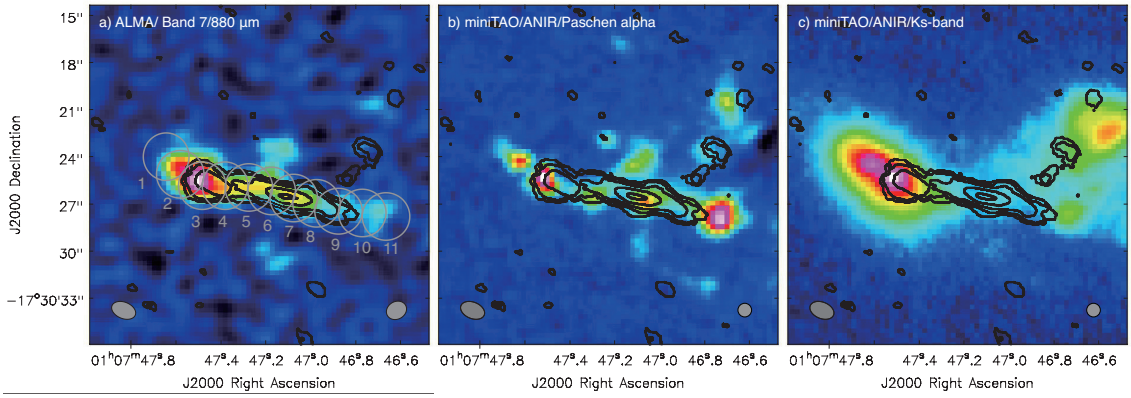

Figure 4.2. Integrated intensity contour of CH_3OH (3_K–2_K) overlaid on (a) 880 μm dust emission, (b) Paschen α emission, and (c) Ks-band (Saito et al. 2015; Tateuchi et al. 2015). The synthesized beam of the CH_3OH (3_K–2_K) image is shown in the bottom-left corner. The beam size of each color image is shown in the bottom-right corner. The eleven gray circles shown in Figure 4.2a are used for the photometry along the filament.

in the stellar nuclei seen in the Ks-band (Figure 4.2c). The global distribution is consistent with ^{13}CO and HCO^+ lines (molecular gas; Iono, Saito et al. 2013; Saito et al. 2015) and 880 μm continuum (dust; Figure 4.2a), although all of them except for CH_3OH show strong peaks at AGN and SB. In contrast, CH_3OH does not coincide with Paschen α emission (H_{II} regions and/or ionized gas shocks; Figure 4.2b). The Ks-band continuum, mainly tracing an old stellar component (Figure 4.2c), has no peaks at Overlap. This indicates that the CH_3OH filament of VV 114 is a relatively young structure compared with the age of the progenitor galaxies, which is likely due to a galaxy-galaxy collision as predicted by numerical simulations of a gas-rich major merger (Saitoh et al. 2009; Teyssier et al. 2010). These morphological comparisons suggest that CH_3OH lines trace a kpc-scale gas structure at the collision interface of the galaxy-galaxy interaction. To determine the physical properties of Overlap, we employ the rotation diagram method (Goldsmith & Langer 1999) in the next Section.

4.4 LTE Calculation of Rotation Temperature and Column Density

Assuming LTE and optically thin conditions for the CH_3OH lines, we can estimate the column density (N_{CH_3OH}) and rotation temperature (T_{rot}) using the rotation diagram. However, we need a special treatment in the case of VV 114, because the detected CH_3OH emission was blended by multiple A-type and E-type rotational transitions (e.g., Rabli & Flower 2010) due to the coarse velocity resolution and observed large velocity widths (FWZI $\sim$ 150 km s^{-1}) as seen in a spectrum toward Region 6 (Figure 4.3a) and a position-velocity diagram along the CH_3OH filament (Figure 4.3b). By assuming that both types of CH_3OH have the same beam-averaged column density (N_{CH_3OH}), the CH_3OH flux can be expressed by using the least squares method with the following equation (e.g., Martín et al. 2006a; Watanabe et al. 2014),

$$W_\nu = \sum_i \frac{8\pi^3 S_i \mu_0^2 \nu_i N_{CH_3OH}}{3kQ_{rot}} \left\{ 1 - \frac{\exp(h\nu_i/kT_{rot}) - 1}{\exp(h\nu_i/kT_{bg}) - 1} \right\} \exp\left(-\frac{E_{u,i}}{kT_{rot}} \right), \quad (4.1)$$

where W_ν is the flux density, S_i is the line strength, μ_0 is the dipole moment, ν_i is the frequency of the transition, Q_{rot} is the rotational partition function, k is the Boltzmann constant, h is the Planck constant, T_{bg} is the cosmic microwave background temperature (= 2.73 K), and E_u is the upper state energy. We take the transition parameters necessary for calculating the equation (Table 4.1) from Splatalogue[2] and the Cologne Database for Molecular Spectroscopy[3] (Müller et al. 2001, 2005).

We performed the calculation for eleven apertures of 3″diameter along the filament shown in Figure 4.2, and an example for Region 6 is shown in Figure 5.2a. Parameters used for the calculation and the results are listed in Table 4.2. Each point in Figure 5.2a corresponds to the upper-state column density of each unresolved transition, which decomposed by using the best-fit T_{rot}. The average T_{rot} is 7.4 $\pm$ 0.5 K for regions detected in both blended CH_3OH sets (i.e., Region 5–8). For regions without CH_3OH (2_K–1_K) detection (Region 1–4 and 9–11), we used T_{rot} = 7.4 K to derive N_{CH_3OH}. The average N_{CH_3OH} is (2.3 $\pm$ 1.0) $\times$ 10^{14} cm^{-2}, although this is an average

[3]http://www.astro.uni-koeln.de/cdms/catalog#partition

Table 4.2. Information of the rotation diagram and gas and star formation properties

ID	R.A. (°)	Decl. (°)	$S_{2_K-1_K}dv$ (Jy km s^{-1})	$S_{3_K-2_K}dv$ (Jy km s^{-1})	$T_{\rm rot}$[a] (K)	$N_{\rm CH_3OH}$ (10^{14} cm^{-2})	$\Sigma_{\rm SFR}$[b] ($M_\odot$ kpc^{-2} yr^{-1})	$N_{\rm H_2}$[c] (10^{22} cm^{-2})	$X_{\rm CH_3OH}$ (10^{-9})
1	16.9485	-17.5067	< 0.26	< 0.32	···	< 0.9	11.9 ± 0.5	4.7 ± 0.4	< 1.9
2	16.9482	-17.5070	< 0.27	0.29 ± 0.08	···	0.8 ± 1.2	28.2 ± 0.9	9.8 ± 1.0	0.8 ± 1.2
3	16.9478	-17.5072	< 0.26	0.68 ± 0.10	···	1.9 ± 1.5	27.0 ± 0.9	9.8 ± 1.0	1.9 ± 1.5
4	16.9474	-17.5072	< 0.27	0.85 ± 0.11	···	2.4 ± 1.6	14.1 ± 0.5	7.4 ± 0.6	3.2 ± 2.2
5	16.9470	-17.5072	0.44 ± 0.09	0.81 ± 0.11	6.1 ± 0.7	2.9 ± 1.7	9.5 ± 0.4	5.6 ± 0.5	5.1 ± 3.1
6	16.9465	-17.5073	0.51 ± 0.09	1.20 ± 0.12	7.8 ± 0.9	3.2 ± 1.6	7.5 ± 0.4	4.5 ± 0.5	7.2 ± 3.6
7	16.9461	-17.5074	0.57 ± 0.09	1.20 ± 0.11	7.0 ± 0.7	3.6 ± 1.6	6.2 ± 0.3	4.7 ± 0.4	7.6 ± 3.5
8	16.9457	-17.5075	0.33 ± 0.07	0.86 ± 0.11	8.9 ± 1.5	2.1 ± 1.2	4.9 ± 0.3	2.8 ± 0.3	7.6 ± 4.6
9	16.9453	-17.5076	< 0.26	0.56 ± 0.09	···	1.6 ± 1.3	5.5 ± 0.3	1.6 ± 0.3	9.5 ± 8.3
10	16.9449	-17.5076	< 0.26	< 0.32	···	< 0.9	6.5 ± 0.3	1.7 ± 0.3	< 5.4
11	16.9444	-17.5077	< 0.26	< 0.32	···	< 0.9	5.7 ± 0.3	1.4 ± 0.3	< 6.5

[a]For regions without CH_3OH (2_K–1_K) detection, we adopt 7.4 K to derive $N_{\rm CH_3OH}$.

[b]Star formation rate surface density derived from the 110 GHz continuum emission (Saito et al. 2015).

[c]Molecular hydrogen column density derived from the 880 μm dust continuum emission (Saito et al. 2015).

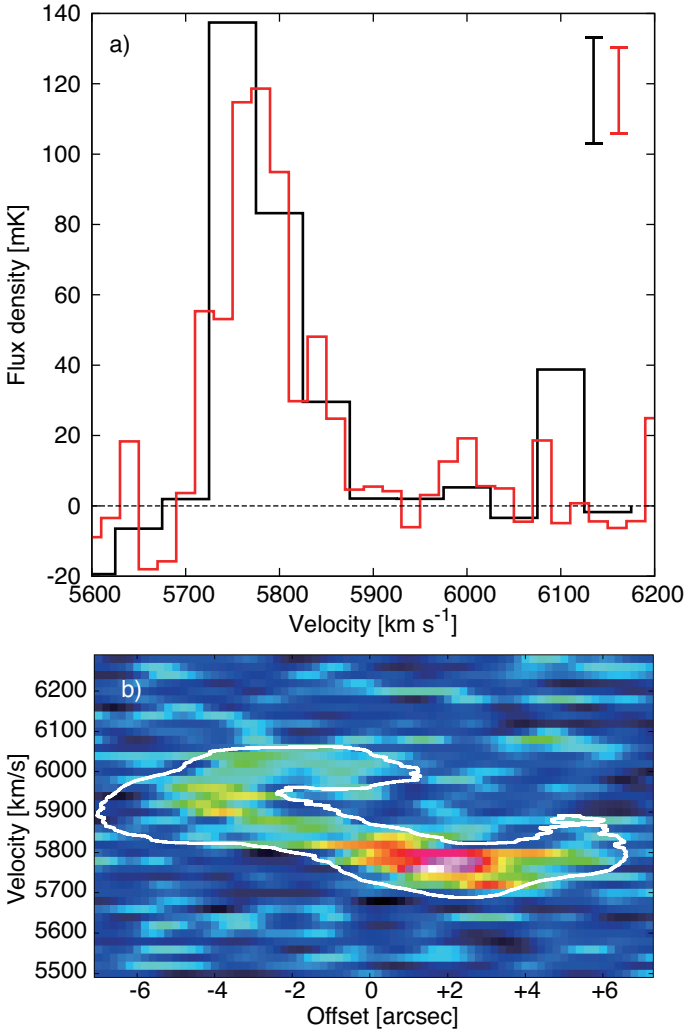

Figure 4.3. (a) Observed spectrum of CH_3OH (2_K–1_K) (black) and CH_3OH (3_K–2_K) (red) toward Region 6 (see Figure 4.2a). The bars shown in the top right represent a typical statistical error bars associated with the data. (b) Position-velocity diagram of CH_3OH along the filament of VV 114 (position angle = 79.4°, length = 14.2″, and width = 1.″8). The white outline shows the 20σ contour of CO (1–0) (Saito et al. 2015).

of the beam-averaged column densities due to the uncorrected beam filling factor ($\eta_{\rm bf}$). To ignore the unknown $\eta_{\rm bf}$ effect, we divided the $N_{\rm CH_3OH}$ by the H_2 column density ($N_{\rm CH_3OH}/N_{\rm H_2} = X_{\rm CH_3OH}$) assuming that the $N_{\rm H_2}$ tracer has the same $\eta_{\rm bf}$. In this Thesis, we employed the 880 μm dust continuum map (Figure 4.2a) to derive molecular gas mass (i.e., $N_{\rm H_2}$) using the formulation described in Scoville et al. (2016).

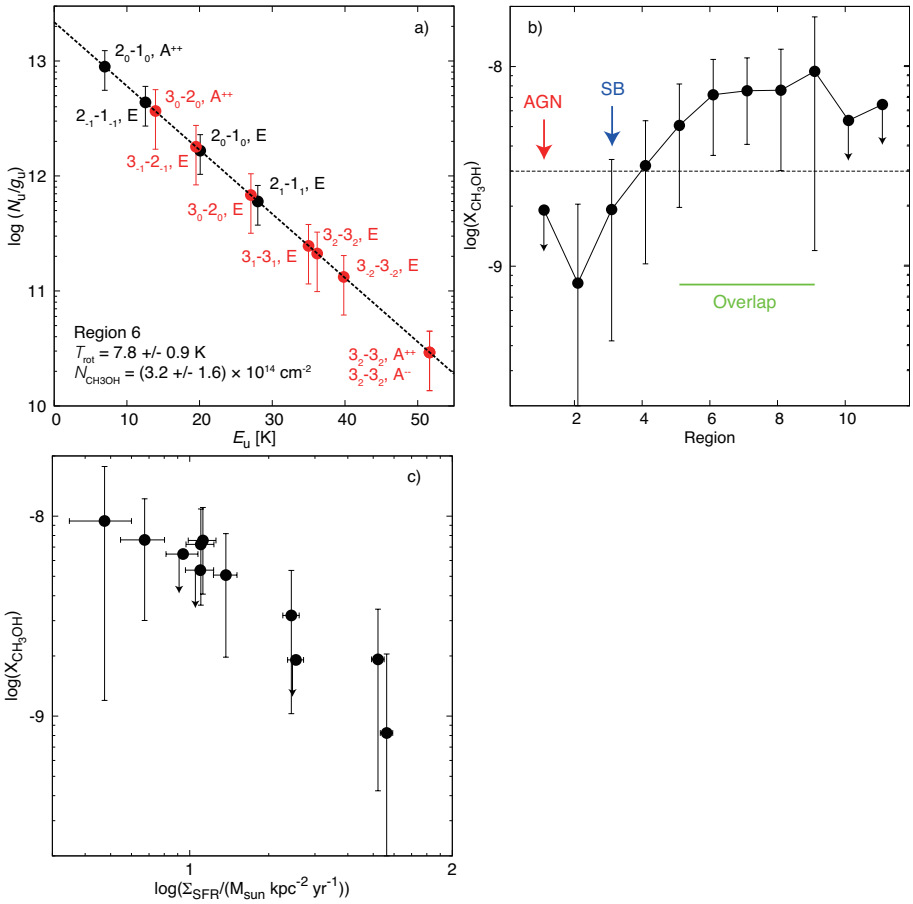

Figure 4.4. (a) Rotation diagram of CH_3OH for Region 6. Black and red points show $J = 2$–1 and 3–2 transitions, respectively. The dotted line shows the best-fit. (b) X_{CH_3OH} distribution along the dust filament of VV 114. The arrows show the 3σ upper limits. The dashed line shows $X_{CH_3OH} \sim 3 \times 10^{-9}$, which is the value for the spiral arm of M51 using $\sim$ 1 kpc aperture (Watanabe et al. 2014). (c) X_{CH_3OH} as a function of Σ_{SFR}.

Assuming a constant dust temperature (T_{dust}) of 25 K, we derived X_{CH_3OH} along the filament. As shown in Figure 5.2b, the X_{CH_3OH} distribution is clearly peaked around Overlap (Region 6–8), whereas the AGN (Region 1) and SB (Region 3) positions show almost an order of magnitude lower values. The errors shown in Figure 5.2b do not include the systematic uncertainty due to the 880 μm to N_{H_2} conversion.

The adopted T_{rot} of 7.4 K for Region 1–2 and 9–11 is consistent with the non-detections of the observed CH_3OH (2_K–1_K) flux, although Region 3 and 4 should

be detected when assuming 7.4 K. This might be attributed to (a) higher $T_{\rm rot}$ than 7.4 K and/or (b) CH_3OH (3_K–2_K) overestimation due to a contamination from c-C_3H_2 (3_{12}-2_{21}) emission. In case (a), since we need to increase $T_{\rm rot}$ to $\sim$ 10 K at least, the derived $N_{\rm CH_3OH}$ will decrease ($\sim$ 20%), and thus $X_{\rm CH_3OH}$ will decrease. In case (b), the intrinsic CH_3OH (3_K–2_K) fluxes will decrease 15% and 30% at Region 3 and 4, respectively, so that $X_{\rm CH_3OH}$ will decrease. For both cases, $X_{\rm CH_3OH}$ will decrease by a few tens of % around the eastern nucleus, so that our discussion and conclusion will not change. We note that the global $X_{\rm CH_3OH}$ trend is robust even if AGN and SB have higher $T_{\rm rot}$ and $T_{\rm dust}$ conditions, since $X_{\rm CH_3OH}$ only increases twice at most when adopting $T_{\rm rot}$ = 7.4–14.8 K and $T_{\rm dust}$ = 25–50 K.

Comparing with CH_3OH observations toward giant molecular complexes in the spiral arm of M51 with 1 kpc resolution ($X_{\rm CH_3OH} \sim 3 \times 10^{-9}$; Watanabe et al. 2014) as a reference of the extragalactic (i.e., kpc scale) quiescent regions, Region 1–3 of VV 114 show a few times lower $X_{\rm CH_3OH}$, although Region 5–9 show a few times higher $X_{\rm CH_3OH}$.

4.5 Discussion and Summary of This Section

To understand the characteristic CH_3OH distribution along the filament of VV 114, we compare $X_{\rm CH_3OH}$ with star formation rate surface density ($\Sigma_{\rm SFR}$) as shown in Figure 5.2c. We employed 110 GHz continuum (Saito et al. 2015) assuming that free-free (bremsstrahlung) emission dominates, and applied the free-free flux to SFR conversion (e.g., Yun & Carilli 2002). Such assumption is appropriate for starburst galaxies (e.g., M82; Condon 1992) and starburst-dominated LIRGs (e.g., NGC 1614; Saito et al. 2016a). The 110 GHz image has a similar MRS ($\sim$ 21″) and synthesized beam ($\sim$ 2″) to CH_3OH images. We note that $\Sigma_{\rm SFR}$ for Region 1 and Region 2 are upper limits, because of the presence of the putative AGN (i.e., contribution from nonthermal synchrotron emission). The derived log $\Sigma_{\rm SFR}$ shows a decreasing trend as a function of $X_{\rm CH_3OH}$ with the correlation coefficient of -0.94. When we exclude a putative AGN contribution (i.e., Region 2), the correlation coefficient becomes -0.97. This can be explained by efficient photodissociation of CH_3OH due to massive star formation and

putative AGN in the nuclear region (e.g., Martín et al. 2009) or desorption of CO (i.e., the precursor molecule of CH_3OH) from dust grain surfaces into gas-phase before forming CH_3OH molecules due to initial high temperature conditions. This is consistent with two orders of magnitude lower Σ_{SFR} at the spiral arm of M51 (Watanabe et al. 2014).

However, the photodissociation scenario is insufficient to fully explain the CH_3OH distribution in VV 114, because Overlap shows higher X_{CH_3OH} and also higher Σ_{SFR} than M51. Thus, we need another efficient mechanism, such as hot-core or shock, in order to explain high X_{CH_3OH} at Overlap. Here, we estimate a possible CH_3OH (2_K–1_K) flux assuming that hot-core-like environments dominate Overlap. We used a single-dish measurement toward one of the local hot-cores NGC 2264 CMM3 (deconvolved major FWHM $\sim$ 0.076 pc, $M = 40\ M_\odot$, $I_{CH_3OH(2_K-1_K)} = 39.7$ K km s^{-1}, $D =$ 738 pc), which is believed to form a massive star of 8 $M_\odot$ (Watanabe et al. 2015, and references therein). To account for all the molecular gas mass of Region 6 ($\sim 8.1 \times 10^8\ M_\odot$) of VV 114, we need $\sim 2.0 \times 10^7$ CMM3. Since the CH_3OH (2_K–1_K) flux of CMM3 at 87 Mpc is $\sim 2.9 \times 10^{-9}$ K km s^{-1}, the total flux of CMM3-like hot-cores at Region 6 is ~ 0.058 K km s^{-1}. This is 0.5% of the observed CH_3OH (2_K–1_K) flux at Region 6 (11.9 ± 1.4 K km s^{-1}). On average, between Region 5 and Region 9, the possible contribution from hot-core-like environments is only 0.6%. When we use other representative hot-core environments OMC-1, Sgr B2(N), and Sgr B2(M) (Lis et al. 1993; Jones et al. 2008; Bally et al. 2011; Watanabe et al. 2015) instead of NGC 2264 CMM3, the contribution from hot-cores at Region 6 is still small (0.7-0.9%, 6.2%, and 23.5%, respectively). We list parameters used for these comparisons in Table 4.3. We note that the derived percentages are upper limits, because we assumed an extreme case that all gas masses contained in Region 6 are associated to hot-cores. Similar estimation of a possible CH_3OH flux from large collections of a molecular outflow from a massive star shows a similar conclusion (Meier et al. 2014). Additionally, in our Galaxy, supernovae are also sources producing strong shocks. For example, a supernova remnant W44 shows strong thermal CH_3OH lines. However, non-thermal CH_3OH emission (i.e., maser) is stronger than thermal lines. If W44-like supernovae are dominant at the Overlap region, we should detect strong CH_3OH

maser there. Such extragalactic CH_3OH maser detection is only reported at the center of NGC 1068 (Wang et al. 2014), so supernova is not the CH_3OH source at the Overlap region of VV 114. The simple comparisons clearly suggest that local CH_3OH sources (i.e., hot-core, outflow, and supernova) cannot reproduce observed CH_3OH properties at the Overlap region. We also note that the broad spatial distribution of the CH_3OH filament ($\sim$ 3-4 kpc) is different from that of star formation tracers such as Paschen α and HCO^+ (4–3). This indicates that the CH_3OH emission in VV 114 does not come from activities related to star formation.

Therefore, we suggest that kpc-scale shocks are only applicable mechanisms to explain the high X_{CH_3OH} at Overlap. The possible origin of the large-scale shocks is a gas-rich galaxy-galaxy collision, because Overlap is located between the progenitor's galaxies without apparent progenitor's spiral arms, bars, or nuclei. This shocked CH_3OH scenario at Overlap is consistent with the explanation of large velocity dispersion components of ionized gas detected at the same region (Rich et al. 2011). The shocked ionized gas shows the same systemic velocity as the CH_3OH. This shows the evidence that ionized gas shocks colocate with molecular gas shocks at Overlap, indicating that merger-induced shocks can affect both molecular and ionized gas ISM.

In summary, merger-induced shocks are the most likely scenario to explain the kpc-scale CH_3OH filament (and large dispersion components of ionized gas) across the progenitors of VV 114. The X_{CH_3OH} distribution peaks at Overlap, although the eastern nucleus, which harbors dense clumps associated with a compact starburst and a putative AGN, shows almost an order of magnitude lower abundances. X_{CH_3OH} clearly anticorrelates with Σ_{SFR}, indicating that strong photodissociation (i.e., efficient destruction) or desorption of CO (i.e., inefficient production) on dust grains due to star-forming activities or AGN plays an important role to suppress CH_3OH emission at the nuclear regions. This is the first result of merger-induced shocks in molecular gas ISM through CH_3OH lines. As a future development, higher-J CH_3OH observations are required to address more realistic, finite optical depth and non-LTE excitation conditions (e.g., Goldsmith & Langer 1999; Mangum & Shirley 2015). Avoiding the multiple K-ladder blending, isolated transitions (e.g., $J_K = 0_0$–1_{-1} at 108.89396 GHz) are also important. Followup observations of shock tracers in

Table 4.3. Contribution of some representative hot-cores to Region 6

	Unit	NGC 2264 CMM3	OMC-1	Sgr B2(N)	Sgr B2(M)
Distance	pc	738	437	8.34×10^3	8.34×10^3
Mass	$M_\odot$	40	60-80	9100	2900
$I_{CH_3OH(2_K-1_K)}$	K km s^{-1}	39.7	309	907	1114
# of hot-core at Region 6		2.0×10^7	$(1.0\text{-}1.4) \times 10^7$	8.9×10^4	2.8×10^5
$I_{CH_3OH(2_K-1_K)}$ at 87 Mpc	K km s^{-1}	2.9×10^{-9}	7.8×10^{-9}	8.3×10^{-6}	1.0×10^{-5}
$I_{CH_3OH(2_K-1_K)}$ from hot-cores at Region 6	%	0.5	0.7-0.9	6.2	23.5

submillimeter wavelength (e.g., SiO, H_2O) and other wavelengths (e.g., near-IR warm H_2; Sugai et al. 1999; Herrera et al. 2012) can be used to confirm the shock scenario at Overlap. Direct observations of CH_3OH, water, and CO ice are also important to quantitatively confirm the sublimation mechanism at the Overlap region.

Chapter 5

Imaging $J = 1$–0, 3–2, and 4–3 Lines of HCN and HCO^+ toward VV 114

5.1 Observations and Data Reduction

In this Chapter, we present high-resolution imaging of multiple HCN and HCO^+ ($J = 1$–0, 3–2, and 4–3 with $\sim 1\farcs5$, $0\farcs5$, and $0\farcs2$ resolution, respectively), HNC ($J = 1$–0), and CS ($J = 7$–6) lines toward the nearby luminous infrared galaxy VV 114 ($1'' = 400$ pc) with ALMA Band 3, 6, and 7. We found that all flux densities, excitation ratios, and HCN/HCO^+ ratios strongly correlate with surface densities of star formation rate, except for the position of the putative AGN, showing that star formation is closely related to dense gas properties at the central filament of VV 114. There is no correlation between star formation efficiency and dense gas fraction (i.e., higher SFE_{H_2} and lower f_{dense} at the eastern nucleus than the Overlap region), that is robust even when considering uncertainties of the CO-to-H_2 and HCN-to-dense-gas-mass conversion factors. This can be explained by the presence of more turbulent, diffuse molecular gas at the Overlap region, whose turbulence has started to be dissipated to form new stars. The intracloud turbulence at the Overlap region might be excited by galaxy-merger-induced shocks. This is consistent with the shock enhancement of CH_3OH abundance. We also derived excitation parameters by assuming optically-thin and local thermodynamic equilibrium conditions, and found that

warmer, HCN-richer molecular gas medium is dominated around the eastern nucleus harboring both AGN and starburst activities. The HCN abundance is remarkably flat ($\sim 3.5 \times 10^{-9}$) independently of the environments (i.e., AGN, star formation, and shock).

5.2 Observations and Data Reduction

5.2.1 Cycle 2 ALMA: $J = 1$–0

The Band 3 line survey toward VV 114 was carried out during the ALMA cycle 2 period (ID: 2013.1.01057.S, PI: T. Saito). Although the aim of this project is an unbiased line survey (84–111 GHz and 127–154 GHz) to study the chemistry in the filament of VV 114, here we only present two tunings which include bright dense gas tracers, HCN (1–0) ($\nu_{\rm obs}$ = 86.88826 GHz), HCO^+ (1–0) ($\nu_{\rm obs}$ = 87.43399 GHz), and the ground transition of an isomer of hydrogen cyanide, HNC (1–0), ($\nu_{\rm obs}$ = 88.88001 GHz) lines. The full description of this project will be provided in Appendix B.

A tuning (B3-1) covers the HCN (1–0) and HCO^+ (1–0) lines in the lower sideband, and another tuning (B3-2) covers HNC (1–0) lines in the lower sideband. B3-1 (B3-2) was obtained on 2014 June 17, July 2, 2015 June 4, and 5 (2014 July 3) with the single-sideband system temperature ($T_{\rm sys}$) of 38 – 90 K (33 – 78 K). The assigned antenna configuration for B3-1 (B3-2) had thirty – thirty-eight (thirty-one) 12 m antennas with the projected baseline length ($L_{\rm baseline}$) of 18 – 780 m (19 – 650 m), which corresponds to the maximum recoverable scale (MRS; Lundgren 2013) of $\sim 22''(\sim 22'')$ in the lower sideband. Each tuning has four spectral windows (spws) to cover each sideband. Each spw has a bandwidth of 1.875 GHz with 1.938 MHz resolution. The total on-source time of B3-1 (B3-2) is 47.4 minutes (23.7 minutes). Neptune or Uranus was used for the flux calibrator, while J0137–2430 or J2258–2758 was used as the bandpass calibrator for both tunings. Either of J0110-0741 or J0116-2052 was observed as the phase calibrator.

5.2.2 Cycle 3 ALMA: $J = 3$–2

Band 6 observation toward VV 114 was carried out during the ALMA cycle 3 period (ID: 2015.1.00973.S, PI: T. Saito). The upper sideband was tuned to cover HCN (3–2) and HCO^+ (3–2) lines. The data was obtained on 2016 May 23 with T_{sys} of 62 - 180 K. The assigned configuration had thirty-seven 12 m antennas with $L_{baseline}$ of 16.7 - 641.5 m (MRS $\sim 9''$). Each tuning has four spws to cover each sideband. Two of the spws including the target lines have a bandwidth of 1.875 GHz with 7.812 MHz resolution, whereas the other two have a bandwidth of 2.000 GHz with 15.625 MHz resolution. The total on-source time is $\sim$ 30.4 minutes. Pallas, J0006-0623, J0118-2141 were used as the flux, bandpass, and phase calibrators. However, in this Section, we estimate the absolute flux scaling factor using the bandpass calibrator, because the visibility model of asteroids in `CASA` is not reliable currently (see Section 5.2.4).

5.2.3 Cycle 2 ALMA: $J = 4$–3

VV 114 was observed with the long baseline mode of cycle 2 ALMA at Band 7 (ID: 2013.1.00740.S, PI: T. Saito). The field and frequency setups of the long baseline observations are same as our previous HCN (4–3) and HCO^+ (4–3) observations (Iono, Saito et al. 2013; Saito et al. 2015) except for the channel width (976.562 kHz for Cycle 2 data). The data were obtained on 2015 June 28 (B7-1) and July 18 (B7-2) with the T_{sys} of 75 - 205 and 90 - 310 K, respectively. The assigned array configuration of B7-1 and B7-2 had forty-one 12 m antennas with $L_{baseline}$ of 43.3 m - 1.6 km and thirty-eight 12 m antennas with $L_{baseline}$ of 15.1 m - 1.6 km, respectively. The combined data has MRS of $7''$. Each tuning has four spws to cover each sideband. All spws have a bandwidth of 1.875 GHz with 976.562 kHz resolution. The total on-source time of each data is $\sim$ 41.2 minutes. J2258-279, J2348-1631, and J0132-1654 were used as the flux, bandpass, and phase calibrators for both data, respectively.

5.2.4 Data Reduction

Processing the new Band 3, Band 6, and Band 7 data, including calibration and imaging, was done by `CASA` version 4.2.2, 4.5.3, and 4.2.2, respectively (McMullin et al. 2007). Images are reconstructed with the natural (robust = 2.0) or briggs (robust = 0.5) weighting. We made the data cubes with a velocity resolution of 20, 30, or 50 km s^{-1} depending on achieved noise rms and signal-to-noise ratio of the target lines. Continuum emission was subtracted in the *uv*-plane by fitting the line free channels in both USB and LSB with a first order polynomial function. The line-free channels were used to make a continuum image using the multi-frequency synthesis method. Imaging properties are listed in Table 5.1. All images shown in this Section, except for line ratios, are not corrected for the primary beam correction.

We use HCN (4–3) and HCO^+ (4–3) data taken by cycle 0 ALMA (Iono, Saito et al. 2013; Saito et al. 2015) to combine with the cycle 2 data (ID: 2011.0.00467.S, PI: D. Iono). In those previous papers, we carried out the absolute flux calibrations with the Butler-Horizons-2010 (BH2010) models. However, the flux models were updated, called Butler-JPL-Horizons 2012 (BJH2012), so that we corrected the previous HCN (4–3) and HCO^+ (4–3) fluxes using the new models following the description in the CASA guides[1]. The flux calibrator used for the cycle 0 data was Uranus, and the difference of the "zero-spacing" flux density of Uranus between the models (i.e., BJH2012/BH2010 - 1) at 349 GHz is +0.03. Therefore, we multiply the flux densities of the cycle 0 data by 1.03 before combine. Furthermore, we used a `CASA` task, `statwt`[2], to recalculate visibility weights for the cycle 0 data.

The systematic error on absolute flux scaling factor using a solar system object is 5% for Band 3 data (Lundgren 2013). As described in Section 5.2.2, we used the bandpass calibrator as the flux calibrator for the Band 6 data in order to avoid using the unreliable flux model of Pallas. Using the ALMA Calibrator Source Catalogue[3], the flux uncertainty of J0006-0623 at 260 GHz on 2016 May 23 was estimated to be 7.9%. This was estimated by fitting the measurement at 91.5, 103.5 and 343.5 GHz

[1] https://casaguides.nrao.edu/index.php/Solar_System_Models_in_CASA_4.0
[2] https://casaguides.nrao.edu/index.php/DataWeightsAndCombination
[3] https://almascience.nrao.edu/sc/

on 2016 May 25 using $S_\nu \propto \nu^\alpha$, where S_ν is the flux density, ν is the observed frequency, and α is the spectral index. The derived α of J0006-0623 is -0.48 $\pm$ 0.01, which is similar to the typical index for quasars (Table B.3). Therefore, we adopt the flux uncertainty of the Band 6 data as 8% throughout this Section. Since the flux uncertainties of J2258-279 at 343.5 GHz (i.e., new Band 7 data) on 2015 June 29 and July 20 are $\sim$ 7.7% and 15.4%, respectively, we adopt the flux uncertainty of 15% for the Band 7 data. If flux measurements for our bandpass and phase calibrators in a time separation (between our observing date and the measurement) less than a week are available in the catalogue, we check the validity of the absolute flux calibrations using their fluxes at each spw. For the B3-1 data, fluxes of our data and the monitored values of J0116-2052 and J2258-2758 are consistent ($<$ 9%). For the B3-2 data, the flux differences of J0116-2052 are less than 6%. The flux differences of J0118-2141, which was used for the Band 6 observation, are less than 30%. This is a relatively large value maybe due to no measurement with Band 6 (i.e., uncertain interpolation between Band 3 and Band 7). Calibrators and a check source for the new Band 7 data were not monitored within 154 days from our observing dates.

MRS of each data is different due to the differences of the observed frequency and the minimum $L_{\rm baseline}$. When we discuss line ratios between data which have different MRS, we clipped all visibility data inside 18 kλ in order to achieve the same MRS, which allows us to ignore different missing flux effects between any sets of line ratio map.

5.3 Results

The 254 GHz (Band 6) and 350 GHz (Band 7) continuum images are shown in Figure 5.1a and 5.1b, respectively. The total flux density of VV 114 at 260 GHz and 350 GHz are 17.4 $\pm$ 1.4 mJy and 44.7 $\pm$ 6.7 mJy, respectively. Their overall spatial distributions along the filament across VV 114 coincide with each other and the previous 340 GHz (i.e., dust) continuum images (Wilson et al. 2008; Saito et al. 2015). They also coincide with low-resolution 110 GHz (i.e., free-free) (Saito et al. 2015) and the 1.4 GHz (i.e., synchrotron) radio continuum image (Yun et al. 1994).

Table 5.1. Line and Imaging Properties

Line	J	Band	$\nu_{\rm rest}$ (GHz)	$E_{\rm u}/k$ (K)	MRS ($''$)	uv-weight[a]	Beam size ($''$)	ΔV (km s^{-1})	rms[b] (mJy b^{-1})	$S_{\rm line}\Delta v$ (Jy km s^{-1})	Recovered flux (%)	Ref.[c]
HCN	1–0	3	88.63160	4.25	22	briggs	1.45 × 1.06	20	0.4	3.53 ± 0.24	40 ± 5	1
	3–2	6	265.88643	25.52	9	natural	0.60 × 0.47	30	0.4	8.36 ± 0.73	···	···
	4–3	7	354.50548	42.53	7	natural	0.19 × 0.15	30	0.3	5.99 ± 0.93	> 18	2
HCO^+	1–0	3	89.18852	4.28	22	briggs	1.45 × 1.04	20	0.5	12.18 ± 0.69	52 ± 4	1
	3–2	6	267.55763	25.68	9	natural	0.60 × 0.47	30	0.4	29.83 ± 2.44	···	···
	4–3	7	356.73422	42.80	7	natural	0.19 × 0.15	30	0.4	18.52 ± 2.85	46 ± 14	2
HNC	1–0	3	90.66357	4.35	22	natural	1.43 × 1.29	50	0.6	1.03 ± 0.20	27 ± 7	1
CS	7–6	7	342.88285	65.83	7	natural	0.18 × 0.15	50	0.3	0.41 ± 0.10	> 1	2

[a]Visibility (uv-plane) weighting for imaging. "briggs" means Briggs weighting with robust = 0.5.

[b]Noise rms in the data which have velocity resolution of ΔV.

[c]Reference of the single-dish flux. (1) Privon et al. (2015); (2) Zhang et al. (2014)

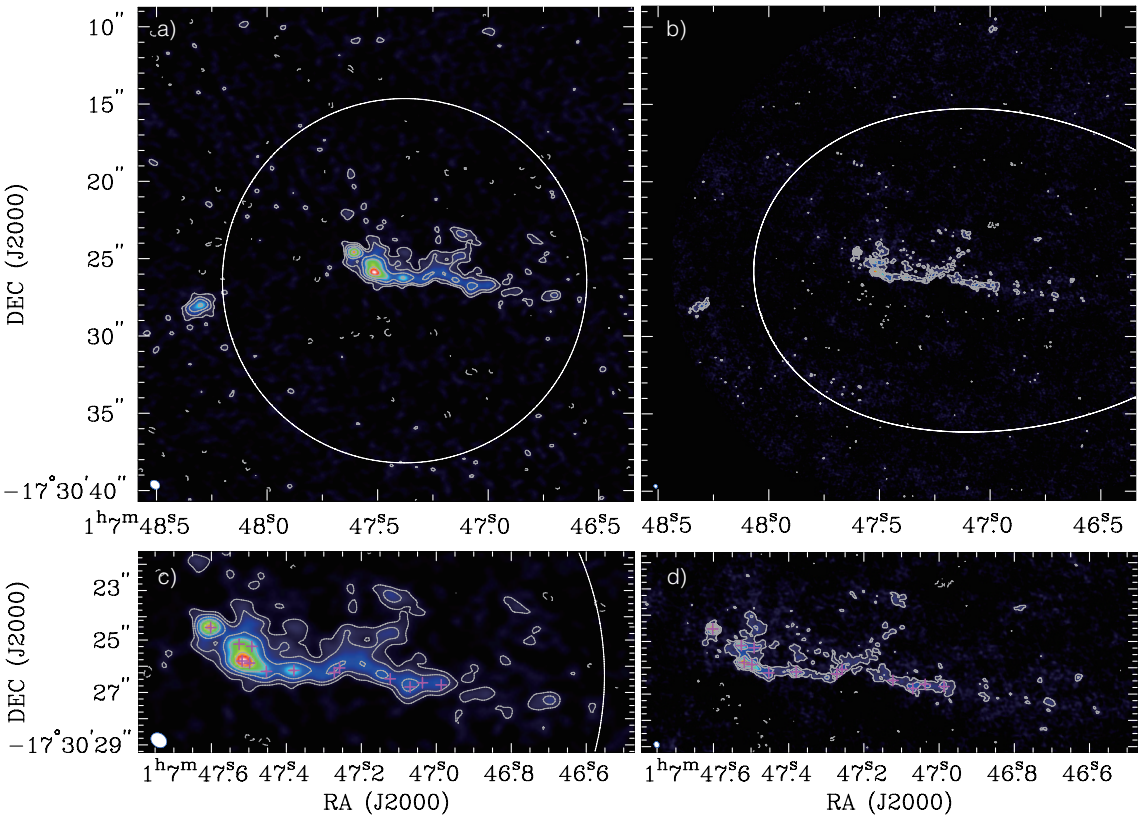

Figure 5.1. (a) The 254 GHz continuum image for VV 114. The contours are 29 × (-3, 3, 6, 12, 24, 36, and 48) μJy beam^{-1}. The white line shows the 50% contour of the primary beam (i.e., field of view). (b) The 350 GHz continuum image for VV 114. The contours are 26 × (-3, 3, 6, 12, 24, 36, and 48) μJy beam^{-1}. Zoomed-in views of (a) and (b) are shown in Figure 5.1(c) and Figure 5.1(d), respectively. All 350 GHz peaks stronger than 8σ are marked as crosses.

The filamentary structure consists of dozens of clumps. The easternmost point-like source coincides with the putative AGN (Iono, Saito et al. 2013).

The integrated intensity, velocity field, and velocity dispersion images of all transitions are shown in Figure 5.2, 5.3, and 5.4. All lines are mainly detected at the central filamentary structure which was detected in many molecular lines as well as ionized gas tracers (Tateuchi et al. 2015), indicating a site of intense star formation as already seen in the radio-to-FIR continuum. The filament consists of three main blobs located at the eastern nucleus, which may harbor a putative AGN ("AGN") and starbursting clumps ("SB"), and between the progenitor's disks ("Overlap" re-

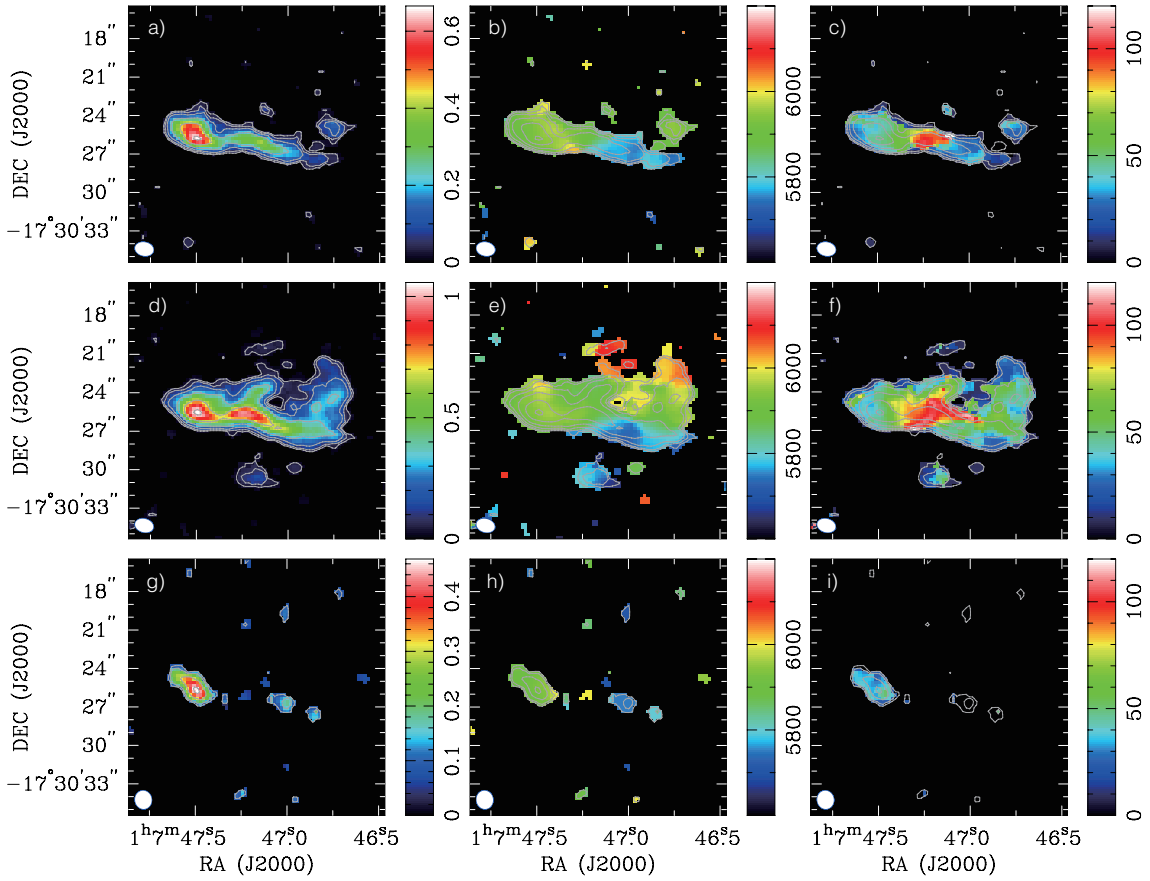

Figure 5.2. (a) Integrated intensity image of HCN (1–0) for VV 114 in the unit of Jy beam^{-1} km s^{-1}. The synthesized beam is shown in the bottom left corner. The contours are 0.67 × (0.04, 0.08, 0.16, 0.32, 0.64, and 0.96) Jy beam^{-1} km s^{-1}. (b) Velocity field image of HCN (1–0) for VV 114 in the unit of km s^{-1}. The integrated intensity image is overlaid as contours. (c) Velocity dispersion image of HCN (1–0) for VV 114 in the unit of km s^{-1}. The integrated intensity image is shown as contours. (d/e/f) Same as (a/b/c) but for HCO$^+$ (1–0). The contours are 1.06 × (0.04, 0.08, 0.16, 0.32, 0.64, and 0.96) Jy beam^{-1} km s^{-1}. (g/h/i) Same as (a/b/c) but for HNC (1–0). The contours are 0.47 × (0.16, 0.32, 0.64, and 0.96) Jy beam^{-1} km s^{-1}.

gion). For given J, the HCO$^+$ emission is more extended and brighter than the HCN emission, and this is likely due to the different critical densities. HNC (1–0) has two peaks at AGN and SB (see also Figure 5.5). Although clumps in the eastern galaxy reported by Iono, Saito et al. (2013) and Saito et al. (2015) are clearly resolved in the Band 6 and Band 7 data, they are only marginally resolved in the Band 3 data

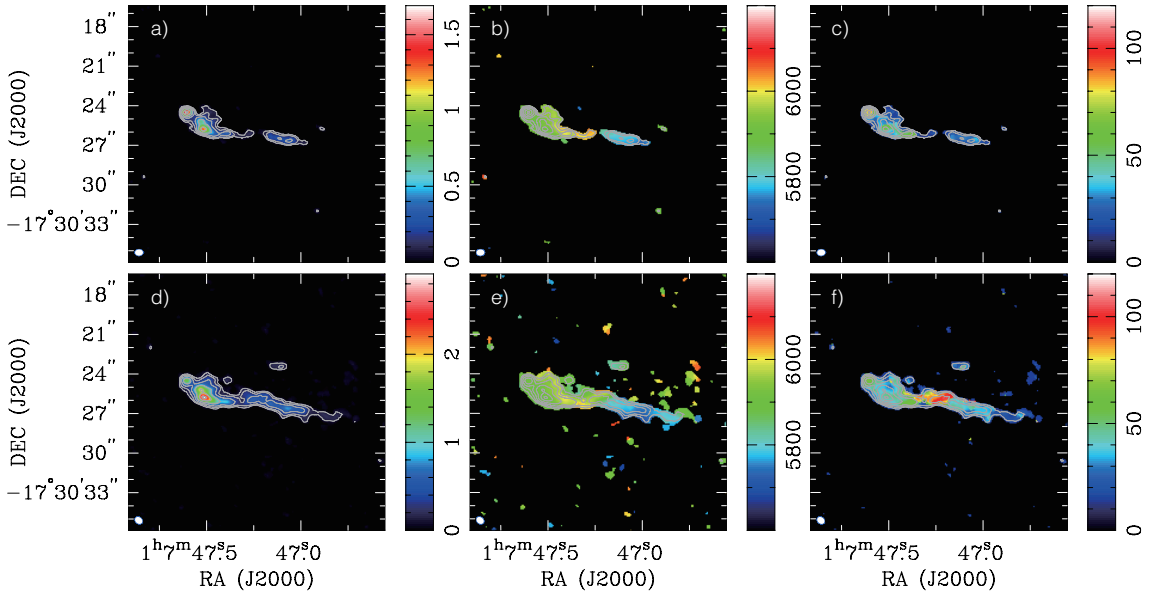

Figure 5.3. (a/b/c) Same as Figure 5.2a, ,b and c, but for HCN (3–2). The contours are 1.69 × (0.04, 0.08, 0.16, 0.32, 0.64, and 0.96) Jy beam^{-1} km s^{-1}. (d/e/f) Same as Figure 5.2a, ,b and c, but for HCO^+ (3–2). The contours are 2.91 × (0.04, 0.08, 0.16, 0.32, 0.64, and 0.96) Jy beam^{-1} km s^{-1}.

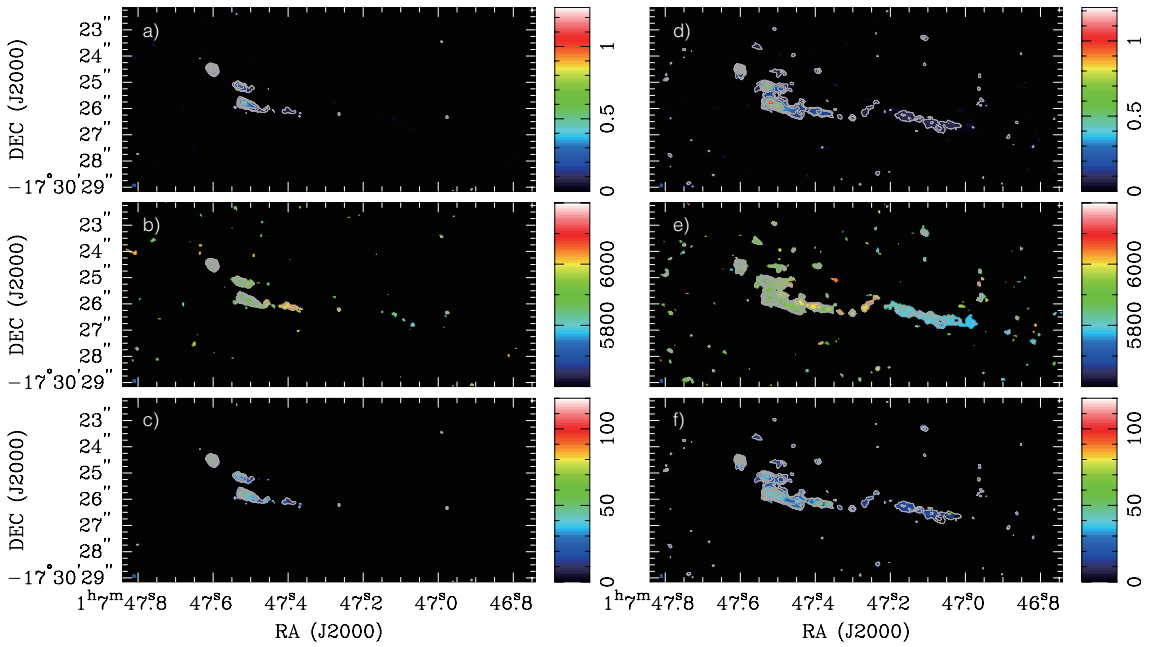

Figure 5.4. (a/b/c) Same as Figure 5.2a, ,b and c, but for HCN (4–3). The contours are 1.27 × (0.04, 0.08, 0.16, 0.32, 0.64, and 0.96) Jy beam^{-1} km s^{-1}. (d/e/f) Same as Figure 5.2a, ,b and c, but for HCO^+ (4–3). The contours are 1.22 × (0.04, 0.08, 0.16, 0.32, 0.64, and 0.96) Jy beam^{-1} km s^{-1}.

Table 5.2. Flux densities inside 3.″0 apertures along the filament of VV 114

ID[a]	$S_{\rm HCN(1-0)}dv$ (Jy km s^{-1})	$S_{\rm HCN(3-2)}dv$ (Jy km s^{-1})	$S_{\rm HCN(4-3)}dv$ (Jy km s^{-1})	$S_{\rm HCO^+(1-0)}dv$ (Jy km s^{-1})	$S_{\rm HCO^+(3-2)}dv$ (Jy km s^{-1})	$S_{\rm HCO^+(4-3)}dv$ (Jy km s^{-1})
1	0.38 ± 0.06	2.28 ± 0.19	2.56 ± 0.41	0.36 ± 0.06	3.33 ± 0.27	5.26 ± 0.80
2	1.08 ± 0.08	4.53 ± 0.37	5.62 ± 0.85	1.46 ± 0.10	10.12 ± 0.81	16.08 ± 2.42
3	1.11 ± 0.08	3.87 ± 0.31	4.57 ± 0.70	1.99 ± 0.12	10.85 ± 0.87	16.22 ± 2.44
4	0.80 ± 0.07	1.88 ± 0.16	1.78 ± 0.28	1.85 ± 0.12	6.23 ± 0.50	7.62 ± 1.15
5	0.58 ± 0.07	0.83 ± 0.09	< 0.28	1.68 ± 0.12	4.25 ± 0.35	1.96 ± 0.32
6	0.58 ± 0.07	0.79 ± 0.08	0.31 ± 0.08	1.52 ± 0.11	4.32 ± 0.35	3.24 ± 0.50
7	0.55 ± 0.06	0.72 ± 0.07	0.49 ± 0.10	1.19 ± 0.09	3.79 ± 0.31	4.31 ± 0.66
8	0.43 ± 0.05	0.54 ± 0.07	0.27 ± 0.08	1.07 ± 0.08	2.80 ± 0.23	3.01 ± 0.47
9	0.24 ± 0.04	0.34 ± 0.05	< 0.27	0.93 ± 0.08	2.14 ± 0.18	2.00 ± 0.32
10	< 0.17	0.32 ± 0.05	< 0.28	0.71 ± 0.07	2.09 ± 0.18	1.53 ± 0.26
11	< 0.17	< 0.26	< 0.28	0.18 ± 0.06	< 0.29	< 0.38

[a]Aperture ID defined in Section 4.

due to the coarse beam size. The velocity field and dispersion maps are similar to those of the filament detected in CO (1–0) and ^{13}CO (1–0) lines. The widest velocity dispersion is found around the Overlap region in the HCN (1–0), HCO$^+$ (1–0), and HCO + (3–2) images (Figure 5.2c, 5.2f, and 5.3e, respectively). As clearly seen in the velocity field of HCO$^+$ (3–2) lines (Figure 5.3e), the wide dispersion ($>$ 100 km s^{-1}) is explained by the superposition of the eastern redshifted component and the central blueshifted component (i.e., a double-peaked profile), not due to the intrinsic velocity dispersion of molecular gas clumps there. We use eleven 3.″0 ($\sim$ 1.2 kpc in diameter) apertures along the filament of VV 114 provided in Section 4 in order to measure the flux densities of line and continuum emissions, which are used for the estimates of star formation rate surface density ($\Sigma_{\rm SFR}$) and molecular gas surface density ($\Sigma_{\rm H_2}$) (see Section 4). The measured fluxes are listed in Table 5.2.

5.3.1 Clumpy Dense Gas Filament across VV 114

The 80 pc resolution images of HCN (4–3) and HCO$^+$ (4–3) emission (Figure 5.4) clearly show clumpy dense gas structures along the filament. The HCO$^+$ filament

has the total length of $\sim$ 6 kpc and the width of $\leq$ 200 pc, and consists of dozens of giant molecular clouds (GMCs), most of which coincide with the 350 GHz continuum peaks (Figure 5.1b and 5.1d). Such morphological characteristics of VV 114, including an enhanced abundance of a molecular gas shock tracer, CH_3OH, found at Overlap (Section 4), share strong similarities with the theoretical prediction that a colliding gas-rich galaxy pair forms a filamentary structure at the collision interface (i.e., shock front) between the progenitor's disks (e.g., Saitoh et al. 2009; Teyssier et al. 2010).

5.3.2 The Eastern Nucleus

We show zoom-up images of line and continuum emissions around the eastern nucleus in Figure 5.5. Except for the coarse resolution Band 3 data, the nucleus is resolved into multiple clumps. However, each clump is not spatially resolved (or some are slightly spatially extended) even by the 80 pc beam of the Band 7 data. All line peaks roughly coincide with the 350 GHz continuum peaks, indicating that cold dust grains around the nuclear region are concomitant with dense molecular ISM with 80 pc scale. In VV 114, the spatial coincidence between dense gas and dust emission is seen from kpc-scale to 80 pc-scale.

Although the Band 7 data provide the highest angular resolution image of VV 114 up to date, the HCN (4–3), HCO^+ (4–3), and 350 GHz continuum images cannot resolve the putative AGN (Iono, Saito et al. 2013), which gives a size upper limit of $\sim$ 80 pc in diameter. The AGN core also shows a bright CS (7–6) emission (Figure 5.6), which was tentatively detected previously (Saito et al. 2015). Assuming that the AGN position of all images has a negligible flux contribution from surrounding extended emission, we measure line and continuum fluxes for the easternmost 350 GHz peak at $(\alpha, \delta)_{\rm J2000} = (01^{\rm h}07^{\rm m}47.60, -17°30'24''.52)$, and regard it as molecular ISM dominantly affected by the putative AGN of VV 114. We measure peak fluxes at E0 (AGN), as well as E1 (a dense clump at $\sim 1''.5$ southwest from E0), defined by Iono, Saito et al. (2013), and listed in Table 5.3. Fluxes at E1 might be strongly contaminated by other clumps in the Band 6 and Band 7 images, so we only measured line and continuum fluxes in Band 7 here. Spectra of all Bands toward the AGN position are shown

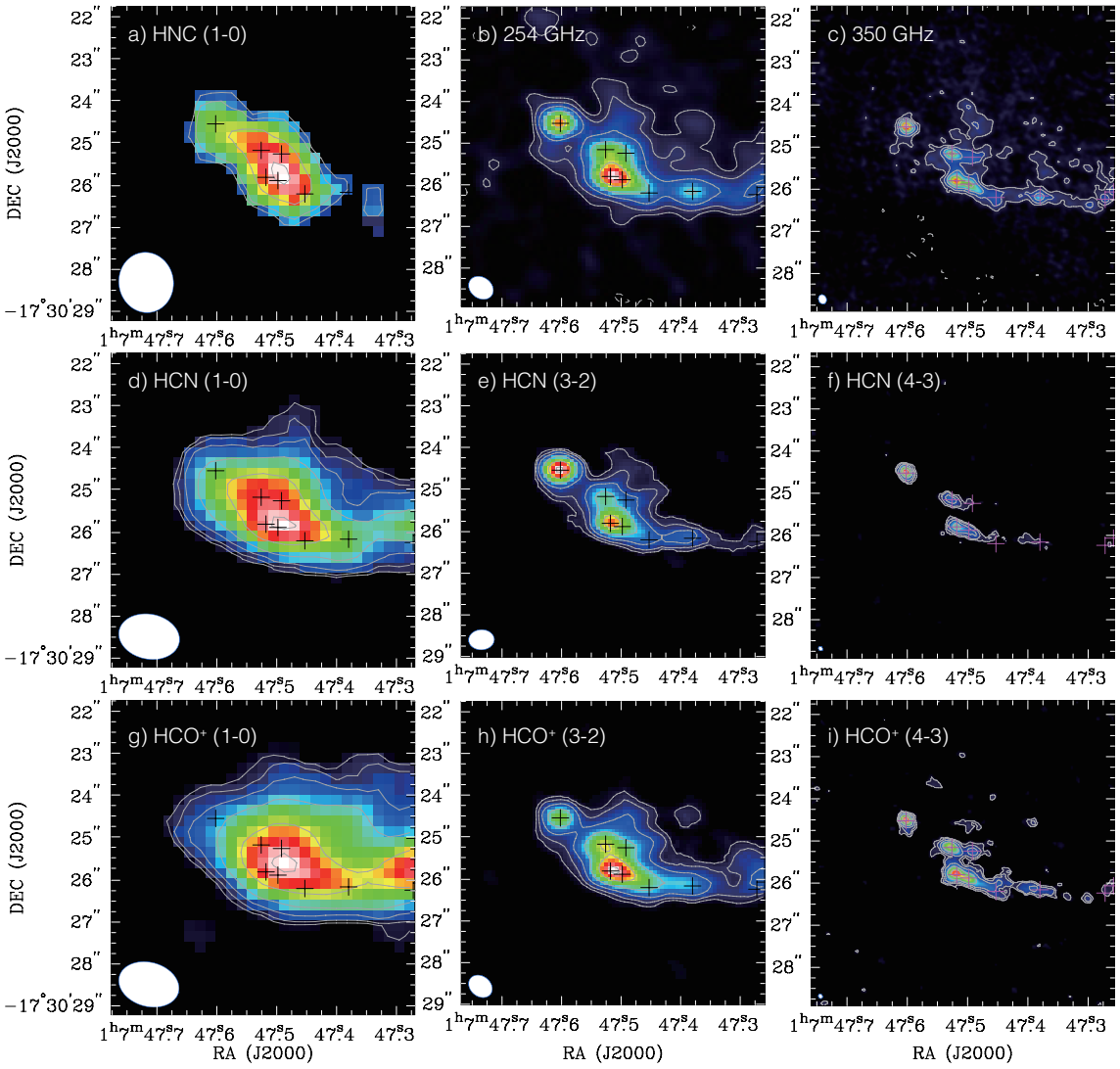

Figure 5.5. Zoomed-in integrated intensity images of (a) HCN (1–0), (b) 254 GHz continuum, (c) 350 GHz continuum, (d) HCN (1–0), (e) HCN (3–2), (f) HCN (4–3), (g) HCO^+ (1–0), (h) HCO^+ (3–2), and (i) HCO^+ (4–3). The contours are same as previous figures. All 350 GHz peaks stronger than 8σ are marked as crosses.

in Figure 5.7. All lines show broad Gaussian-like profile (FWHM $\sim$ 200 km s^{-1}), indicating a large dynamical mass of $M_{\rm dyn}$ of 9.3×10^7 $M_\odot$ assuming the inclination of 90° for simplicity.

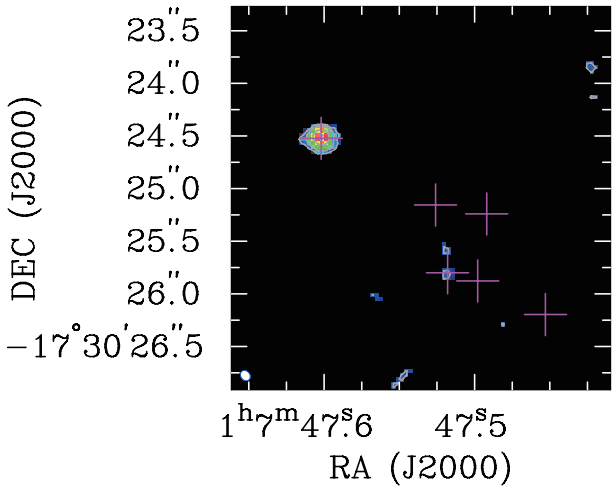

Figure 5.6. Zoomed-in integrated intensity image of CS (7–6). The contours are 0.26 × (0.16, 0.32, 0.64, and 0.96) Jy beam^{-1} km s^{-1}. All 350 GHz peaks stronger than 8σ are marked as crosses.

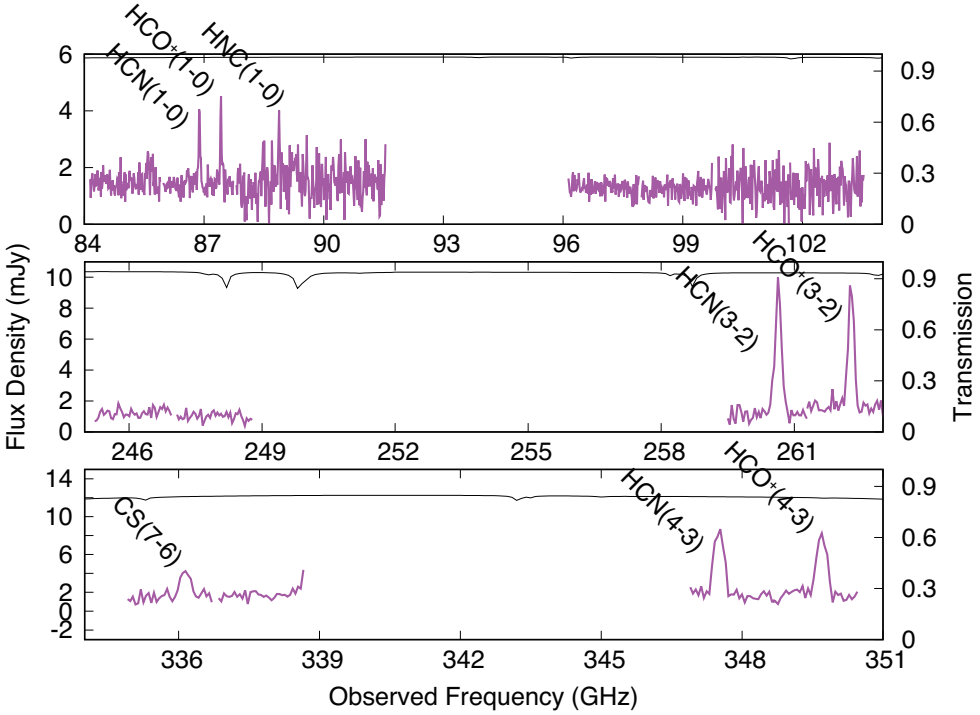

Figure 5.7. Spectra toward the putative AGN position (i.e., the unresolved core in the 350 GHz image) at all Bands. The velocity resolution is 50 km s^{-1}. Atmospheric transmission for precipitable water vapor (PWV) of 1 mm is shown in black lines.

Table 5.3. Flux densities at AGN (E0) and SB (E1) defined by Iono, Saito et al. (2013)

	Unit	AGN (E0)	SB (E1)
S_{254}	(mJy)	1.50 ± 0.12	···
S_{350}	(mJy)	1.98 ± 0.30	1.49 ± 0.23
$S_{\mathrm{HCN}(1-0)}dv$	(Jy km s^{-1})	0.34 ± 0.04	···
$S_{\mathrm{HCN}(3-2)}dv$	(Jy km s^{-1})	1.79 ± 0.15	···
$S_{\mathrm{HCN}(4-3)}dv$	(Jy km s^{-1})	1.60 ± 0.24	0.62 ± 0.10
$S_{\mathrm{HCO^+}(1-0)}dv$	(Jy km s^{-1})	0.31 ± 0.04	···
$S_{\mathrm{HCO^+}(3-2)}dv$	(Jy km s^{-1})	1.53 ± 0.13	···
$S_{\mathrm{HCO^+}(4-3)}dv$	(Jy km s^{-1})	1.54 ± 0.24	1.20 ± 0.18
$S_{\mathrm{HNC}(1-0)}dv$	(Jy km s^{-1})	0.29 ± 0.07	···
$S_{\mathrm{CS}(7-6)}dv$	(Jy km s^{-1})	0.33 ± 0.07	< 0.12

5.3.3 A Submillimeter Galaxy behind VV 114

The 254 GHz and 350 GHz continuum images (Figure 5.1) clearly show a strong, marginally resolved source at the eastern side of the field of views (FoVs = 50% contour of the primary beam). This source was originally identified by a strong 340 GHz point source and a strong line detection at 99.75 GHz (Tamura, Saito et al. 2014), suggesting the presence of a submillimeter galaxy (SMG) at z = 2.467 (but 3.622 is acceptable). If z = 3.622, our data used in this Section cover CO (14–13) line at 348.72 GHz, but it is not detected. Considering CO excitation observed toward local U/LIRGs (e.g., Kamenetzky et al. 2016), such high-J CO are not strong, so the absence of CO (14–13) is not enough to exclude z = 3.622.

5.4 Line Ratios

5.4.1 Excitation Ratios

Excitation of dense molecular gas in galaxies has been investigated for local galaxies and their bright nuclei (Krips et al. 2008; Izumi et al. 2013; Papadopoulos et al. 2014; Spilker et al. 2014), although its spatial variation in LIRGs was not studied yet

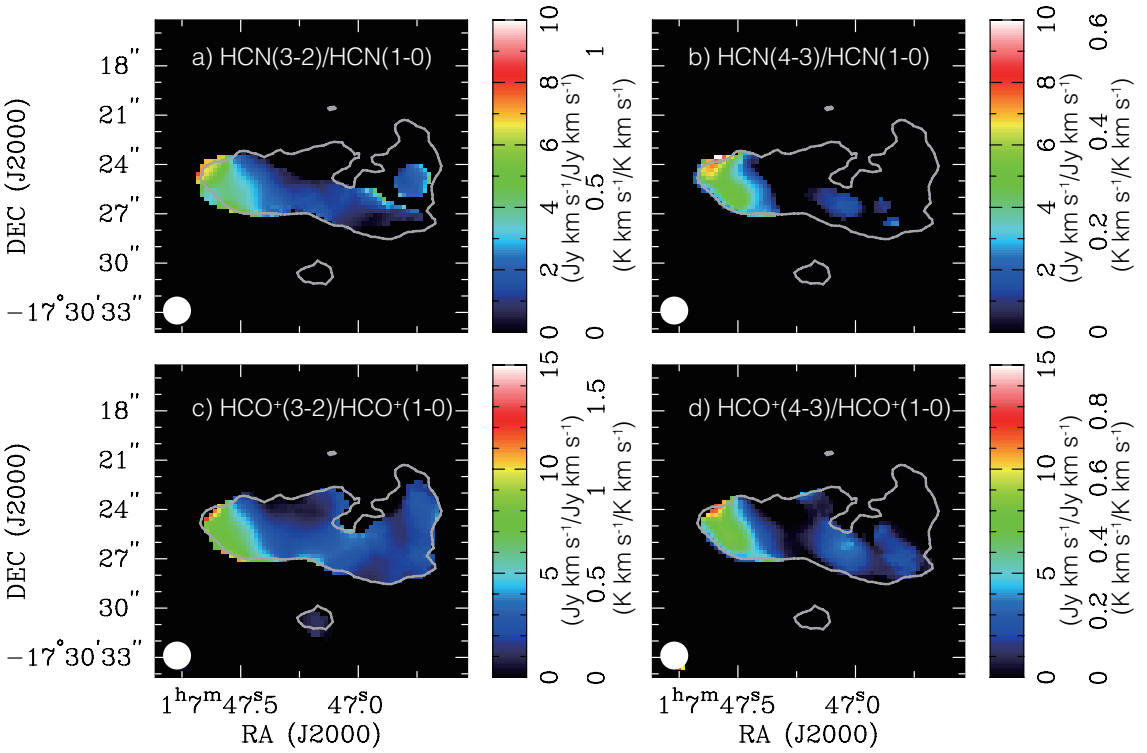

Figure 5.8. (a) Image of HCN (3–2)/HCN (1–0) integrated intensity ratio. The HCO^+ (1–0) outline (= 0.0766 Jy beam^{-1} km s^{-1}) is shown in a grey contour. (b) Image of HCN (4–3)/HCN (1–0) integrated intensity ratio. (c) Image of HCO^+ (3–2)/HCO^+ (1–0) integrated intensity ratio. (d) Image of HCO^+ (4–3)/HCO^+ (1–0) integrated intensity ratio.

due to the faintness of dense gas tracers. Here we show spatially-resolved HCN ($J_{\rm upp}$–$J_{\rm upp-1}$)/HCN (1–0) line ratios and HCO^+ ($J_{\rm upp}$–$J_{\rm upp-1}$)/HCO^+ (1–0) line ratios (hereafter HCN or HCO^+ excitation ratios) for a LIRG for the first time (Figure 5.8). All excitation ratios are made before clipping inner *uv*-coverage (see Section 5.2.4) and convolving to 1.″5 resolution ($\sim$ 600 pc). HCN (HCO^+) excitation ratios are masked by an outline of the smoothed HCN (1–0) (HCO^+ (1–0)) integrated intensity image at 0.095 (0.153) Jy beam^{-1} km s^{-1}.

Overall spatial distribution of the excitation ratios in VV 114 is coincident with each other, and peaks at the eastern edge of the filament. All excitation ratios did not exceed the optically-thick thermalized value (unity when using K km s^{-1} as the intensity unit) anywhere. Highly-excited region at the eastern nucleus extends

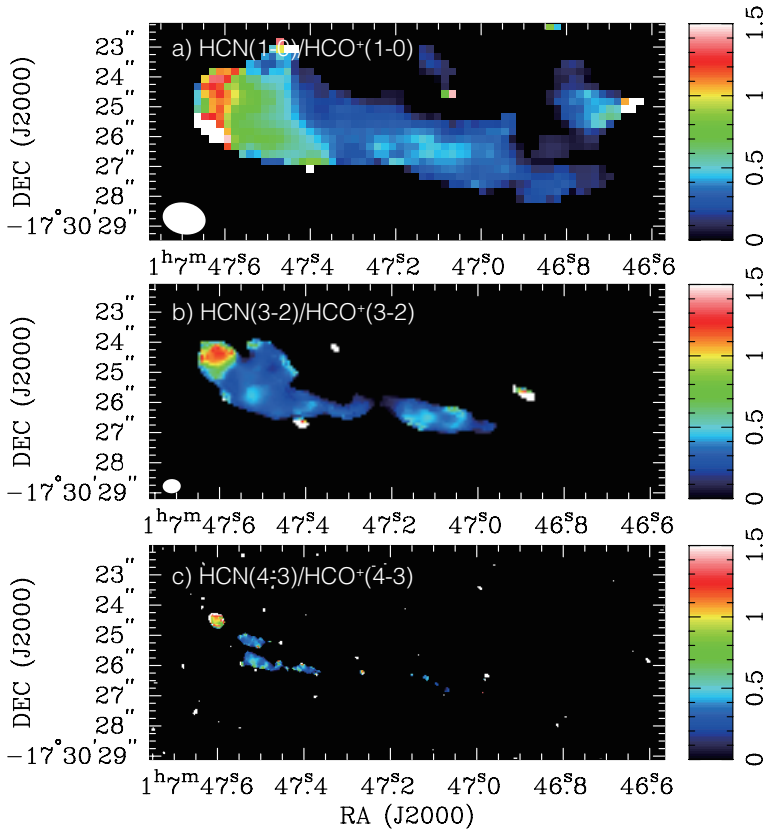

Figure 5.9. (a) Image of HCN (1–0)/HCO^+ (1–0) integrated intensity ratio. (b) Image of HCN (3–2)/HCO^+ (3–2) integrated intensity ratio. (c) Image of HCN (4–3)/HCO^+ (4–3) integrated intensity ratio.

from northeast to southwest, which coincides with the HNC (1–0) distribution (Figure 5.5a). The Overlap region is also relatively excited, but a few times lower than the ratios around the eastern nucleus. Excitation of diffuse molecular gas phase traced by lower-J CO or ^{13}CO excitation ratios (Sliwa et al. 2013; Saito et al. 2015) shows a similar distribution along the filament with the peak at the eastern edge, indicating that the mechanism of diffuse gas excitation is similar to that of dense gas excitation.

5.4.2 HCN/HCO^+ Ratios

Contrary to the excitation ratios, intensity ratios between HCN and HCO^+ at given J have been studied to characterize obscured power sources in galaxies (i.e.,

AGN or starburst), although HCN/HCO$^+$ ratios at several J are not broadly studied (Krips et al. 2008; Izumi et al. 2013) because of the line weakness and the instrumental limitations. Using the high quality data of multiple J HCN and HCO$^+$ transitions taken for VV 114, we made HCN/HCO$^+$ ratio images at J = 1–0, 3–2, and 4–3 as shown in Figure 5.9a, 5.9b, and 5.9c, respectively. Here we used integrated intensity images before correcting the primary beam attenuation and smoothing the synthesized beam, because image properties are almost same between HCN and HCO$^+$ at given J (Table 5.1).

All HCN/HCO$^+$ ratio images show the highest peak ($\sim$ 1.5) at the putative AGN position (E0) despite of different resolutions. The second peak is located at $\sim$ 1$''$.5 southwest of the AGN position (i.e., E1), which coincides with a strong peak found in all images shown in Figure 5.5 (i.e., star-forming dense clumps). The peak value varies from 0.7 to 0.45 as J increases, indicating the effect of gas excitation at the position. However, the Overlap region shows relatively high values of $\sim$ 0.4 independently of J. In terms of multiple J HCN and HCO$^+$ line ratios, VV 114, therefore, has three distinctive regions, i.e., AGN, star-forming clump(s), and Overlap region, which in turn show the kpc-scale variation of dense gas excitation and chemistry along the filament. The higher HCN/HCO$^+$ ratios obtained only at the putative AGN position is consistent with previous studies (Imanishi et al. 2016c, and references therein).

5.4.3 HNC/HCN and HCN/CS Ratio

We detected strong HNC (1–0) and CS (7–6) lines toward the AGN position. The HNC (1–0)/HCN (1–0) line ratio at E0 is 0.85 $\pm$ 0.23, indicating a comparable strength of HNC emission to HCN emission at the AGN position. When using the 3$''$.0 apertures, Region 3 shows the HNC (1–0)/HCN (1–0) ratio of $\sim$ 0.25 ($<$ 0.4 for other apertures). The AGN position shows significantly brighter HNC luminosity relative to other star-forming regions in VV 114. Such luminous or overluminous (i.e., HNC/HCN $\geq$ 1) HNC (1–0) emission is also seen in other active nuclei (e.g., Huettemeister et al. 1995; Aalto et al. 2002; Pérez-Beaupuits et al. 2007; Costagliola et al. 2011; Aladro et al. 2015, see also Aalto et al. 2007 for J = 3–2 transition).

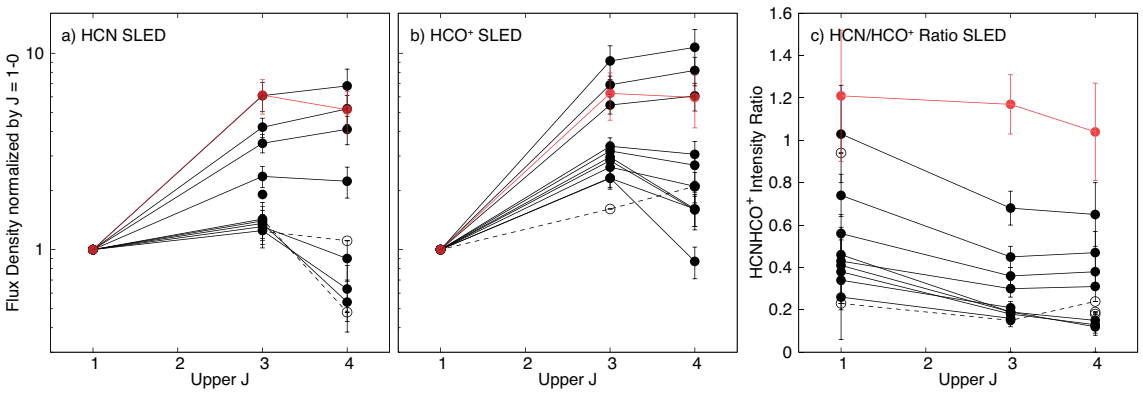

Figure 5.10. The spatially-resolved SLEDs of (a) HCN, (b) HCO^+, and (c) HCN/HCO^+ ratio. Black and red lines correspond to aperture photometry data (Region 1-11) and a single pixel value at the AGN position, respectively. The open circles and dashed lines show 3σ upper limits.

HCN (4–3)/CS (7–6) line ratio is suggested to be used as a diagnostic tracer of AGN activity when combining with the HCN (4–3)/HCO^+ (4–3) line ratio (e.g. Izumi et al. 2016). At the AGN position of VV 114 (E0), the HCN (4–3)/CS (7–6) ratio is relatively low (4.9 ± 1.3) compared with other clumps (> 5.2). On the submillimeter-HCN diagram using HCN (4–3)/HCO^+ (4–3) and HCN (4–3)/CS (7–6) ratios (Izumi et al. 2015), E0 is similar to NGC 4418 and IRAS12127–1412, both of which may harbor a dust-obscured AGN.

5.4.4 SLEDs

Recent observations have revealed a variety of excitation conditions in dense gas ISM from galaxy to galaxy by comparing dense gas spectral line energy distribution (SLED) (e.g., Rangwala et al. 2011; Papadopoulos et al. 2014). In Figure 5.10a and 5.10b, for the first time, we show spatially-resolved HCN and HCO^+ SLEDs, using the eleven apertures (Region 1-11) and data at the AGN position (E0), respectively. The HCO^+ SLEDs of VV 114, in general, tend to show larger values relative to the HCN SLEDs at given J, which, again, may be due to the effect of different critical densities at given J. Both SLEDs for Region 1-3 and E0 (i.e., eastern nucleus) peak at $J \geq 4$, whereas those for Region 4-11 (i.e., Overlap) peak at $J \leq 3$. On the other hand,

Region 1 and E0 (i.e., AGN position) only show high values (≥ 1) in spatially-resolved HCN/HCO$^+$ ratio SLEDs (Figure 5.10c). The shape of the HCN/HCO$^+$ ratio SLED at E0 is remarkably flat and high, indicating a specific dense gas condition relative to other regions. Since those spatially-resolved SLEDs depend on the variety of thermal and chemical processes in ISM along the filament, we model those in Section 5.5.5 to discuss driving mechanisms.

5.5 Discussions

5.5.1 $L_{\rm FIR} - L'_{\rm dense}$ Relation and Slope – J Dependence

Our HCN and HCO$^+$ data have the same beam size, source distance, sensitivity, and maximum recoverable scale, so we can probe the star-forming scaling relation without systematic errors to derive $L'_{\rm dense}$. In this Section, we used $\Sigma_{\rm SFR}$, based on 110 GHz continuum emission (Section 4), and HCN and HCO$^+$ flux densities as a proxy of $L_{\rm FIR}$ and $L'_{\rm dense}$, respectively. We further discuss the slope of $\Sigma_{\rm SFR}$ and flux density relations here. The intercept (i.e., $\rm SFE_{dense} = SFR/\mathit{M}_{dense}$) will be discussed in Section 5.5.2.

In Figure 5.11, $\Sigma_{\rm SFR}$ is plotted against all HCN and HCO$^+$ flux densities ($S_{\rm line}dv$). In general, all logarithmic flux densities roughly correlate with log $\Sigma_{\rm SFR}$ as already studied and pointed out in many past studies (e.g., Gao & Solomon 2004a,b; Privon et al. 2015; Usero et al. 2015). We estimate the slope of the log-log plots by fitting the data points except for Region 1, where considerable contamination by the putative AGN is possible. The derived slope for the HCN (1–0), HCN (3–2), HCN (4–3), HCO$^+$ (1–0), HCO$^+$ (3–2), and HCO$^+$ (4–3) plots are 2.03 $\pm$ 0.18, 0.83 $\pm$ 0.07, 0.65 $\pm$ 0.04, 1.69 $\pm$ 0.67, 1.30 $\pm$ 0.16, and 0.84 $\pm$ 0.14, respectively. Although both the number of data points and the covered x- and y-ranges are small, the slopes of the log-log plot seem to vary according to different dense gas tracers. To clarify the excitation dependence, we plot the slope as a function of upper-J in Figure 5.12, showing a decreasing trend as increasing upper-J of both HCN and HCO$^+$ (from $\sim$ 2 to $\sim$ 0.5). This can be explained by two simple mechanisms: (1) decreasing flux

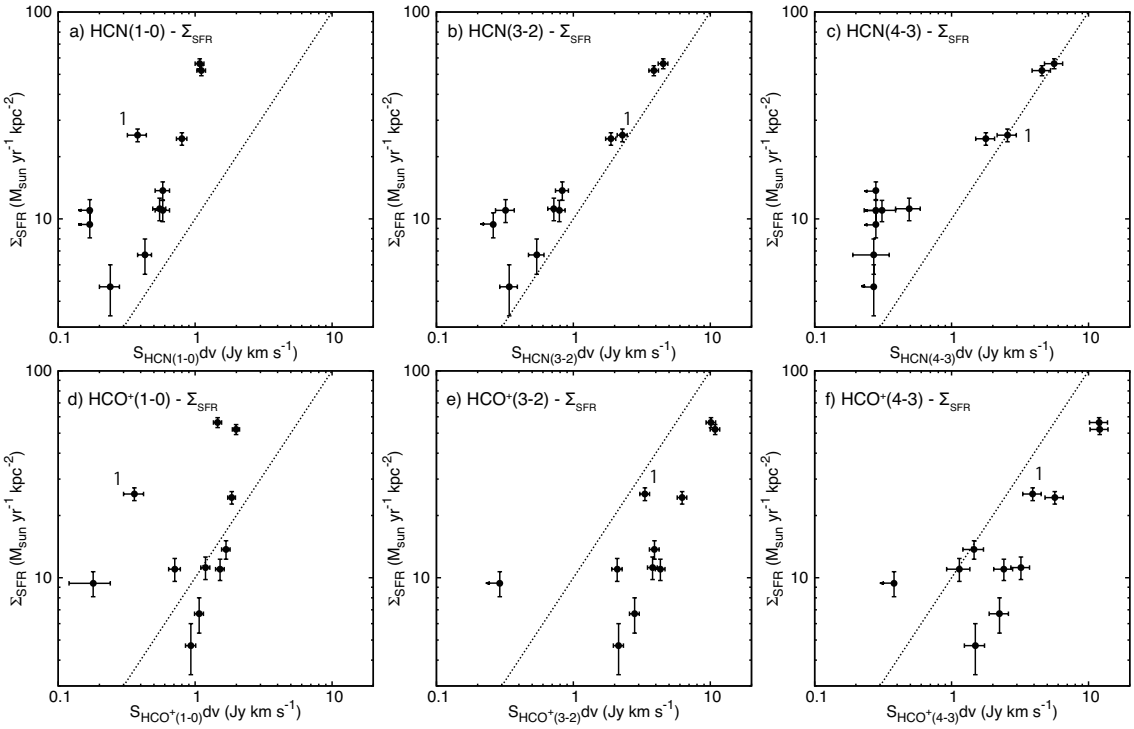

Figure 5.11. Plots of log $\Sigma_{\rm SFR}$ against flux densities of all HCN and HCO^+ transitions in log scale. These are same as log $L'_{\rm dense}$-log $L_{\rm IR}$ plots. The dotted line corresponds to a line with a slope of unity. Data point at the AGN position is denoted as "1".

density of high-J lines at lower $\Sigma_{\rm SFR}$ regime and/or (2) increasing flux density of high-J lines at higher $\Sigma_{\rm SFR}$ regime, as discussed in the followings.

1. At the lower $\Sigma_{\rm SFR}$ regime, FUV heating by star-forming activity is inefficient and not enough to thermalize high critical density tracers toward higher-J. Consequently, flux densities of J = 3–2 and 4–3 lines of HCN and HCO^+ decrease, and thus the slope becomes sublinear. Hydrodynamic simulations with non-LTE radiative transfer calculations (Narayanan et al. 2008) reproduced this trend for HCN transitions from J = 1–0 to 5–4, and the authors concluded that the trend results from subthermalized excitation for high critical density tracers. An analytic model provided by Krumholz & Thompson (2007) also reproduced a similar trend as a function of the critical density. In the case of VV 114, dense gas at the Overlap region corresponds to this.

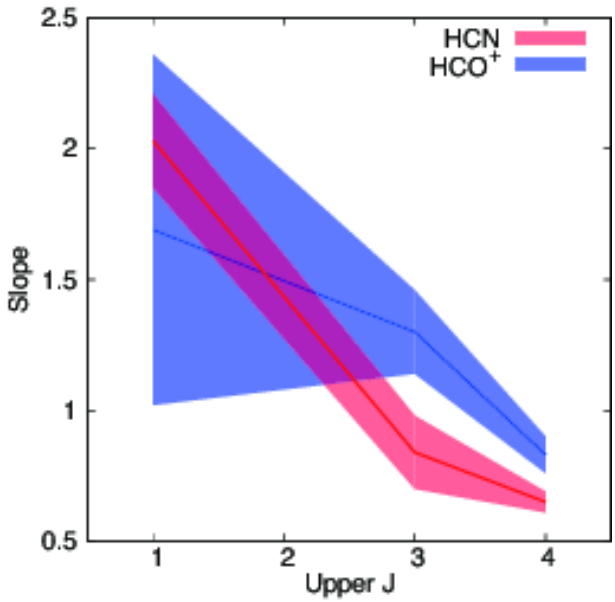

Figure 5.12. The slopes as a function of J shown in Figure 5.11. Red and blue tracks correspond to HCN and HCO^+ slopes, respectively. 1σ error ranges of the fitting are shown as colorized areas.

2. At the higher Σ_{SFR} regime, high critical density tracers can be highly excited by intense FUV radiation from massive star-forming regions (i.e., high temperature) or cold dense cores where will form new stars (i.e., high density). Furthermore, the presence of energetic activities (e.g., shock, AGN) tends to excite molecular gas ISM. Recent multiple J CO observations have revealed that higher-J CO lines are more dominantly heated by such energetic activities (Greve et al. 2014), and brighter galaxies at IR show more excited CO conditions (Kamenetzky et al. 2016). Expanding those evidences for CO lines to dense gas tracers, excitation of dense gas ISM at higher Σ_{SFR} regime (i.e., higher IR) should be enhanced by energetic activities. Thus, the presence of intense starbursts and energetic activities can boost fluxes of higher-J HCN and HCO^+ lines, leading to the sublinear slope. This is consistent with the explanation of a decreasing slope with increasing J of CO due to an increasing contribution of shock heating from supernovae (Greve et al. 2014). This interpretation is the case with the eastern nucleus of VV 114. We will quantitatively discuss the

excitation mechanisms of dense gas tracers in Section 5.5.5.

Considering the observational fact that AGN contribution to the total IR luminosity increases as the IR luminosity increases (e.g., Ichikawa et al. 2014), the presence of AGN can boost higher J HCN and HCO^+ fluxes. However, we exclude data point which might be dominated by AGN (i.e., Region 1) when deriving the slopes, so this is not an applicable explanation for the case with the filament of VV 114.

We, again, note that the Σ_{SFR} - flux density plots are equivalent to the FIR luminosity - line luminosity relations because all data points shown here can be assumed to have the same distance, aperture size, and filling factor, so the slopes do not change when we employ luminosity - luminosity plots for the discussion.

5.5.2 SFE_{H_2}, SFE_{dense}, and f_{dense}

Here we discuss the star formation activity which takes place in the filament of VV 114 using surface densities of SFR (Σ_{SFR}), molecular gas mass (Σ_{H_2}), and dense gas mass (Σ_{dense}). In addition, physically relevant quantities such as SFR_{H_2} ($= \Sigma_{SFR}/\Sigma_{H_2}$), SFE_{dense} ($= \Sigma_{SFR}/\Sigma_{dense}$), and dense gas fraction, f_{dense}, ($= \Sigma_{dense}/\Sigma_{H_2}$) are also used. We derived Σ_{H_2} from the N_{H_2} derived by Saito et al. (2016b). Σ_{dense} is calculated by dividing the dense gas mass (M_{dense}) by the aperture area (420 pc in diameter). M_{dense} is calculated by using the following equation (Gao & Solomon 2004b),

$$M_{dense} = \alpha_{HCN(1-0)} L'_{HCN(1-0)}\, M_\odot \tag{5.1}$$

where $\alpha_{HCN(1-0)}$ is the HCN (1–0) luminosity to dense gas mass conversion factor in $M_\odot$ (K km s^{-1} pc^2)$^{-1}$ and $L'_{HCN(1-0)}$ is the HCN (1–0) luminosity in K km s^{-1} pc^2. We adopted 10 $M_\odot$ (K km s^{-1} pc^2)$^{-1}$ for $\alpha_{HCN(1-0)}$ for simplicity (Gao & Solomon 2004b). Thus, all surface densities are directly proportional to the observed flux densities or luminosities. The derived surface densities are listed in Table 5.4.

We show normalized (i.e., peak = 1) surface densities along the filament of VV 114 in Figure 5.13a. All profiles peak at the eastern nucleus (Region 2 or 3), and show a decreasing trend toward the western side (Region 11). This indicates that the eastern

Table 5.4. $\Sigma_{\rm dense}$, $f_{\rm dense}$, $\rm SFE_{H_2}$, and $\rm SFE_{dense}$

ID	$\Sigma_{\rm dense}$ ($M_\odot$ pc^{-2})	$f_{\rm dense}$	$\rm SFE_{H_2}$ (Myr^{-1})	$\rm SFE_{dense}$ (Myr^{-1})
1	90 ± 13	0.13 ± 0.02	0.038 ± 0.004	0.28 ± 0.05
2	260 ± 20	0.18 ± 0.02	0.040 ± 0.004	0.22 ± 0.02
3	268 ± 18	0.19 ± 0.02	0.037 ± 0.004	0.19 ± 0.02
4	192 ± 17	0.18 ± 0.02	0.023 ± 0.003	0.13 ± 0.01
5	139 ± 17	0.17 ± 0.03	0.017 ± 0.002	0.10 ± 0.02
6	140 ± 18	0.22 ± 0.04	0.017 ± 0.003	0.08 ± 0.01
7	132 ± 14	0.19 ± 0.03	0.016 ± 0.003	0.08 ± 0.01
8	104 ± 13	0.26 ± 0.04	0.017 ± 0.004	0.06 ± 0.01
9	59 ± 11	0.26 ± 0.06	0.020 ± 0.006	0.08 ± 0.03
10	< 40	< 0.166	0.046 ± 0.009	< 0.28
11	< 41	< 0.203	0.047 ± 0.011	< 0.23

[a]Aperture ID defined by Saito et al. (2016b).

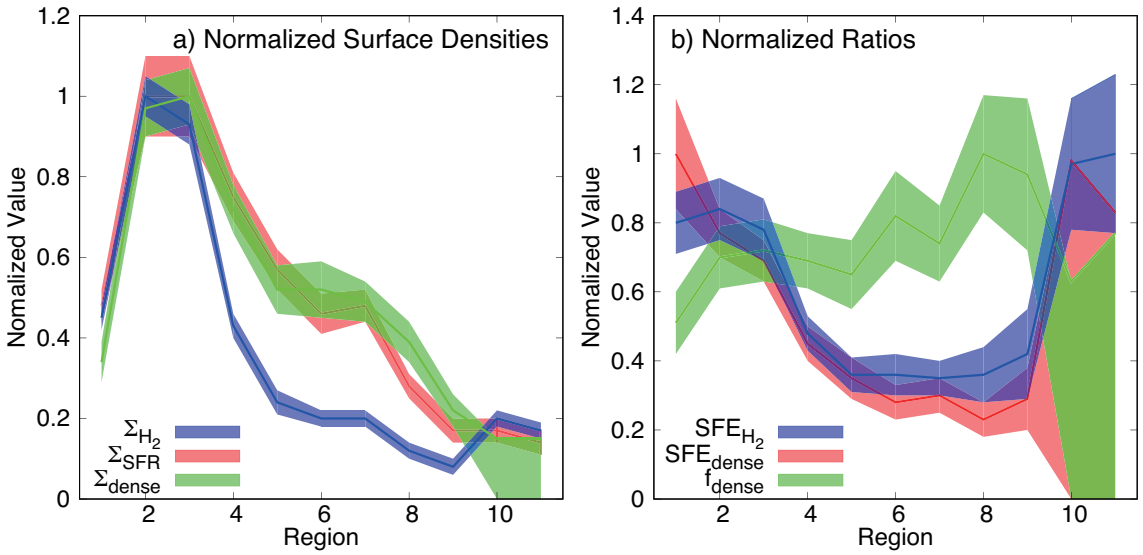

Figure 5.13. (a) Normalized distributions of $\Sigma_{\rm SFR}$ (blue), $\Sigma_{\rm H_2}$ (red), and $\Sigma_{\rm dense}$ (green) along the filament of VV 114. (b) Normalized distributions of $\rm SFE_{H_2}$ (blue), $\rm SFE_{dense}$ (red), and $f_{\rm dense}$ (green) along the filament of VV 114.

nucleus of VV 114 is the site of ongoing massive, intense star formation. On the other hand, the Overlap region (Region 5-8) show moderate star formation ($\sim 1/5$ of the nuclear star formation) with relatively large amount of diffuse and dense gas ($\sim 1/2$ of gas around the eastern nucleus). The situation is clearer when we use the surface density ratios (i.e., $\mathrm{SFE}_{\mathrm{H_2}}$, $\mathrm{SFE}_{\mathrm{dense}}$, and f_{dense}). Figure 5.13b shows the normalized surface density ratios along the filament of VV 114. We note that both the SFEs correspond to the intercept of the log L_{IR} - log L'_{line} relations. As expected, SFEs are high around the eastern nucleus (2-3 times higher than those at the Overlap region). The western side of the filament (Region 11) also shows a high $\mathrm{SFE}_{\mathrm{H_2}}$, which is comparable to that at Region 2 and 3. Region 11 coincides with a strong Hα (Zaragoza-Cardiel et al. 2016) and Paschen α (Tateuchi et al. 2015) peaks, so this may be a relatively unobscured (i.e., not dusty) star-forming region associated with the UV-bright western galaxy (Grimes et al. 2006). In contrast to the SFEs, f_{dense} shows a different trend, that is peaked around Region 8. The Overlap region has 1.5-2 times larger f_{dense} than Region 1-3 and 11. In summary, the eastern nucleus is the site of current massive starburst, whereas the Overlap region dominated by dense gas. In addition, the Overlap region is a site of moderate star formation, and has $M_{\mathrm{dense}} = (1.8 \pm 0.2) \times 10^8\ M_\odot$ (Region 6) of fuel for future star formation.

5.5.3 Turbulence-regulated Star Formation

In order to investigate what physical mechanism governs the observed quantities of star formation at the filament of VV 114, we employ a turbulence-regulated star formation model (Krumholz & McKee 2005). A simple formulation of the turbulence-regulated star formation model described by Usero et al. (2015) is useful to parameterize observed quantities (i.e., $\mathrm{SFE}_{\mathrm{H_2}}$ and f_{dense}) with molecular cloud properties. The equations are,

$$\mathrm{SFE}_{\mathrm{H_2}} = \epsilon_{\mathrm{SF}} \frac{(\mathcal{M}/100)^{-0.32}}{\tau_{\mathrm{ff}}(\bar{n})}, \tag{5.2}$$

$$f_{\mathrm{dense}} = \frac{1}{2}\left[1 + \mathrm{erf}\left(\frac{\sigma^2_{\mathrm{PDF}} - 2\log\left(n_{\mathrm{dense}}/\bar{n}\right)}{2^{3/2}\sigma_{\mathrm{PDF}}}\right)\right], \tag{5.3}$$

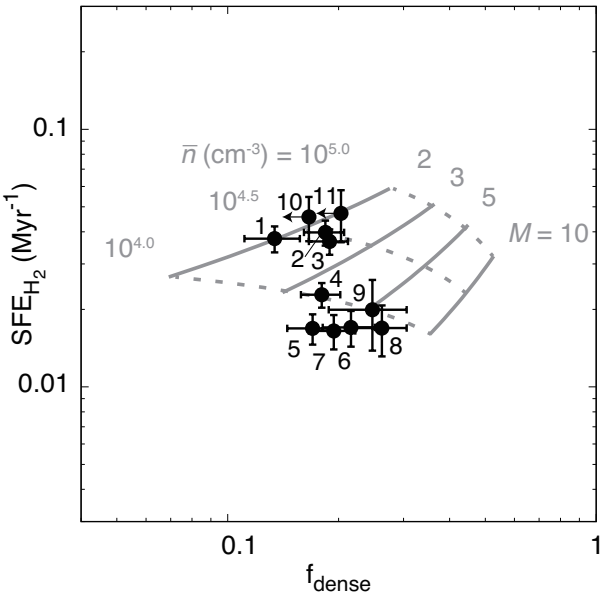

Figure 5.14. SFE_{H_2} plots against f_{dense}. Aperture IDs are shown for each data point. Grids of the turbulence-regulated star formation model are shown in grey curves (Krumholz & McKee 2005; Usero et al. 2015). Model curves with constant Mach number ($\mathcal{M}$) or constant average density ($\bar{n}$) are shown in solid or dashed curves, respectively.

$$\sigma^2_{\rm PDF} \approx \log\left(1+\frac{3\mathcal{M}^2}{4}\right), \tag{5.4}$$

where $\epsilon_{\rm SF}$ is the efficiency depending on the virial state of the clouds, $\mathcal{M}$ is the Mach number, $\tau_{\rm ff}(\bar{n})$ is the free-fall timescale ($= \sqrt{3\pi/(32\bar{n}G)}$) at given average volume density ($\bar{n}$), and $\sigma_{\rm PDF}$ is the width of the lognormal probability distribution function (PDF) of gas density within a cloud. This model explains the star formation in a virialized molecular cloud using two parameters, $\mathcal{M}$ and $\bar{n}$: (1) When turbulence in a cloud is higher (i.e., higher $\mathcal{M}$), it inhibits star formation leading to lower SFE_{H_2}, although it broadens the density PDF (i.e., increasing the fraction of HCN-emitting dense gas = higher f_{dense}). (2) When the average gas density ($\bar{n}$) increases, it shortens $\tau_{\rm ff}(\bar{n})$ (i.e., SFE_{H_2} increases), and naturally results in higher f_{dense}. Through this Section, we assume $n_{dense} = 2.8 \times 10^5$ cm^{-3} and $\epsilon_{\rm SF} = 0.28\%$, which are the same values as those used in Usero et al. (2015).

The observed log SFE_{H_2} against log f_{dense} are plotted in Figure 5.14. As already

seen in Figure 5.13, data points at the Overlap region shows systematically high $f_{\rm dense}$ and low $\rm SFE_{H_2}$. We overlaid the turbulence-regulated star formation model ($\mathcal{M}$-$\bar{n}$ grid) on this Figure. The grid clearly characterizes the Overlap region as turbulent lower-density ISM ($\mathcal{M} \sim 5$ and $\bar{n} \sim 10^{4.0}$ cm^{-3}) relative to the eastern nucleus ($\mathcal{M} \sim 2$ and $\bar{n} \sim 10^{4.5}$ cm^{-3}). The absolute values are uncertain because of the assumed conversion factors to derive the surface densities and the assigned SFR tracer. For example, when we use 8.4 GHz continuum emission as the SFR tracer (instead of the 110 GHz continuum), $\rm SFE_{H_2}$ decreases by a factor of ~ 2, hence $\mathcal{M}$ ($\bar{n}$) tends to increase (decrease). The effect of uncertainties in conversion factors on SFEs will be discussed later. However, since the general trend does not change independently of the used SFR tracer or adopted conversion factors, the relative differences between the eastern nucleus and the Overlap region also do not change.

Recalling the enhancement of methanol abundance at the Overlap region due to large-scale shocks driven by an interaction between the progenitor's galaxies (Section 4), we suggest a "shock-induced starburst" scenario to characterize the star formation at the same region. Molecular clouds at the Overlap region of VV 114 are collected and compressed by violent merger-induced shocks, and then shock-induced intracloud turbulence have started to be dissipated, so a part of them forms new stars. This view is consistent with the turbulence-regulated star formation model. This scenario is also consistent with the scenario of widespread star formation at the early-to-mid stages of major mergers predicted by numerical simulations (e.g., Saitoh et al. 2009). The eastern nucleus already shows intense star formation activity, which might be due to efficient gas inflow at the early-stage of a merger (Iono et al. 2004b).

There is another established star formation model, so-called density threshold model, which we did not apply here. This model suggests that the rate at which molecular gas turns into stars depends on the dense gas mass within a molecular cloud (i.e., $\Sigma_{\rm SFR} \propto \Sigma_{\rm dense} = f_{\rm dense}\Sigma_{\rm H_2}$; e.g., Lada et al. 2012), and thus it can simply explain the observed linear correlation between $L_{\rm IR}$ and $L'_{\rm HCN(1-0)}$ (e.g., Gao & Solomon 2004a,b). It, in turn, predicts a linear correlation between $\rm SFE_{H_2}$ ($= \Sigma_{\rm SFR}/\Sigma_{\rm H_2}$) and $f_{\rm dense}$. However, as we could see in Figure 5.14, VV 114 data do not show such a positive linear correlation clearly (the correlation coefficient = -0.55), showing that

the density threshold model is not appropriate for the VV 114 data.

We note that the situation seen in VV 114 does not change by adopting plausible (i.e., inconstant) conversion factors to derive $\Sigma_{\rm dense}$ and $\Sigma_{\rm H_2}$. The density threshold model also predicts constant $\rm SFE_{dense}$ from Galactic star-forming region to extragalactic star-forming region (i.e., $\Sigma_{\rm SFR} \propto \Sigma_{\rm dense}$), although the filament of VV 114 shows a decreasing trend toward west (Figure 5.13). We used a constant $\alpha_{\rm HCN}$ of 10 $M_\odot$ (K km s^{-1} pc^2)$^{-1}$ here. Considering that $\alpha_{\rm HCN}$ is a similar quantity to $\alpha_{\rm CO}$, and $\alpha_{\rm CO}$ is a few times lower at nuclear regions than other quiescent regions in galaxies (Sandstrom et al. 2013), $\alpha_{\rm HCN}$ at the eastern nucleus of VV 114 should not be larger than that at the Overlap region. In order to get a constant $\rm SFE_{dense}$ along the filament of VV 114, we need more (less) $\Sigma_{\rm dense}$ at the eastern nucleus (Overlap region), resulting in 2-3 times larger $\alpha_{\rm HCN}$ at the eastern nucleus, which is not an applicable value.

Similar to $\rm SFE_{dense}$, the difference of $\rm SFE_{H_2}$ between the nucleus and the Overlap region tends to increase when adopting plausible conversion factors. We used the formulation described by Scoville et al. (2016) to derive $\Sigma_{\rm H_2}$ from 880 μm continuum flux (see Section 4), assuming a constant $T_{\rm dust}$ of 25 K. However, intense nuclear starbursts at the eastern nucleus result in warmer gas temperature than that for the Overlap region (see Section 5.5.5). Since the derived $\Sigma_{\rm H_2}$ decreases with increasing $T_{\rm dust}$, $\rm SFE_{H_2}$ tends to increase (decrease) at the eastern nucleus (Overlap region), which enlarges the observed $\rm SFE_{H_2}$ gradient along the filament. In summary, the systematic uncertainties of the conversion factors do not change the trend seen in Figure 5.14.

5.5.4 Line Ratios vs. $\Sigma_{\rm SFR}$

Here we examine dependence of dense gas excitation ratios against $\Sigma_{\rm SFR}$ using measured data along the filament of VV 114 (Table 5.2) as done for CO excitation (Tsai et al. 2012; Rosenberg et al. 2015; Kamenetzky et al. 2016). As shown in Figure 5.15, all excitation ratios measured in VV 114 well correlate with $\Sigma_{\rm SFR}$, although Region 1 (i.e., AGN position) clearly deviates from the correlation. The correlation coefficients are 0.66, 0.70, 0.67, and 0.70, for HCN (3–2)/HCN (1–0) (Figure 5.15a),

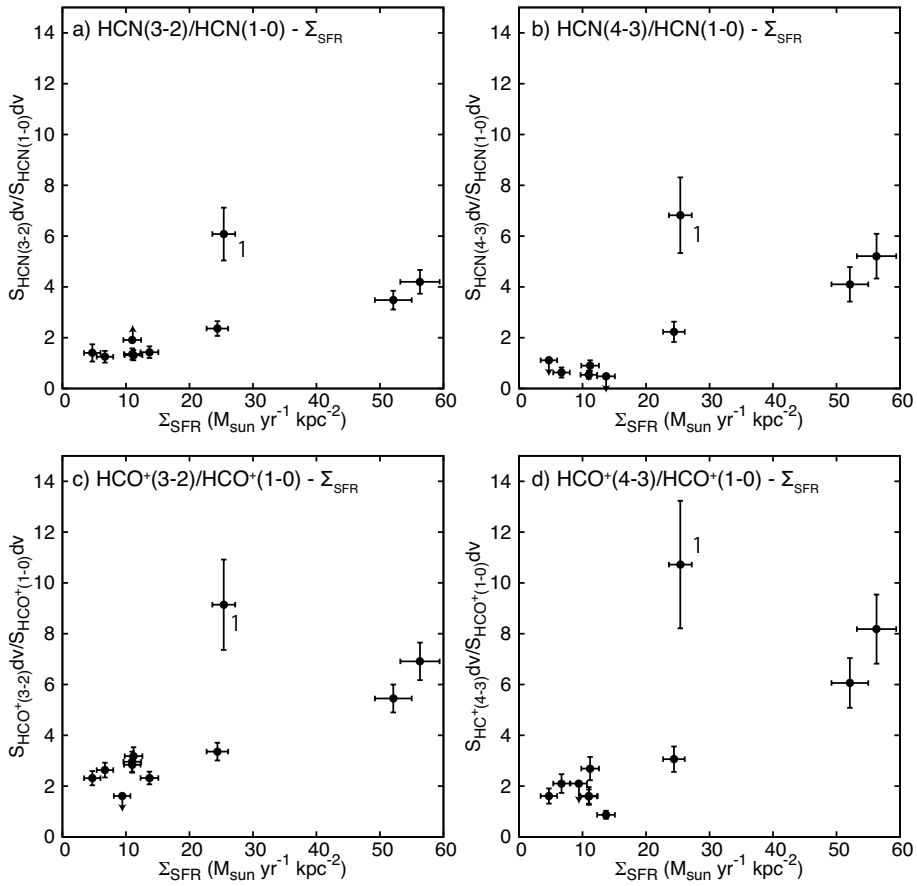

Figure 5.15. Excitation ratio plots against $\Sigma_{\rm SFR}$: (a) HCN (3–2)/HCN (1–0) ratio, (b) HCN (4–3)/HCN (1–0) ratio, (c) HCO^+ (3–2)/HCO^+ (1–0) ratio, and (d) HCO^+ (4–3)/HCO^+ (1–0) ratio. Data point at the AGN position is denoted as 1.

HCN (4–3)/HCN (1–0) (Figure 5.15b), HCO^+ (3–2)/HCO^+ (1–0) (Figure 5.15c), and HCO^+ (4–3)/HCO^+ (1–0) (Figure 5.15d), respectively, although the coefficients become 0.97, 0.99, 0.96, and 0.95, respectively when excluding Region 1. This indicates that the excitation condition at Region 1 is clearly different from that at other regions in the filament, and star formation activity may govern dense gas excitation except for Region 1. A conceivable explanation of the unusual excitation found in Region 1 is the influence of an AGN. Region 1 shows the highest excitation ratios in VV 114 but modest $\Sigma_{\rm SFR}$. The $\Sigma_{\rm SFR}$ at Region 1, derived by using 110 GHz continuum emission, may be an upper limit because of the non-thermal contribution from the

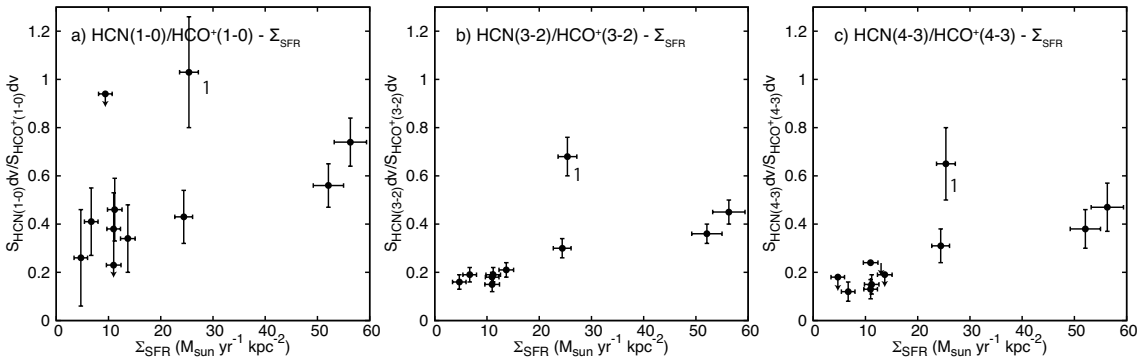

Figure 5.16. HCN/HCO$^+$ ratio plots against $\Sigma_{\rm SFR}$: (a) HCN (1–0)/HCO$^+$ (1–0) ratio, (b) HCN (3–2)/HCO$^+$ (3–2) ratio, and (c) HCN (4–3)/HCO$^+$ (4–3) ratio. Data point at the AGN position is denoted as 1.

putative AGN (Section 4), so Region 1 deviates more and more when excluding the possible AGN contribution. This is consistent with the results from high-resolution observations of multiple molecular lines toward the nearest type 2 AGN host LIRG NGC 1068 (García-Burillo et al. 2014; Viti et al. 2014). The circumnuclear disk of NGC 1068, whose ISM is thought to be dominantly affected by the central AGN, has at least a few times higher excitation ratios of CO, HCN, and HCO$^+$ relative to the starburst ring with hundred pc scale.

The HCN/HCO$^+$ line ratios show a similar trend against $\Sigma_{\rm SFR}$. The correlation coefficients are 0.46, 0.57, and 0.62, for HCN (1–0)/HCO$^+$ (1–0) (Figure 5.16a), HCN (3–2)/HCO$^+$ (3–2) (Figure 5.16b), and HCN (4–3)/HCO$^+$ (4–3) (Figure 5.16c), respectively, although the coefficients become 0.85, 0.87, and 0.93, respectively when excluding Region 1. Since, for given J, HCN has a few times higher critical density than HCO$^+$, the strong correlation between HCN/HCO$^+$ ratios and $\Sigma_{\rm SFR}$ is naturally explained by FUV heating from star-forming regions as with the correlation between excitation ratios and $\Sigma_{\rm SFR}$. On the other hand, Region 1 clearly deviates from trends found in all line ratio plots against $\Sigma_{\rm SFR}$, suggesting the presence of another mechanisms to boost the observed line ratios (i.e., AGN).

We note that Figure 5.15 and 5.16 can be also regarded as luminosity ratio plots against FIR luminosity because all data points have the (almost) same distance,

aperture size, and filling factor.

5.5.5 Radiative Transfer Modeling under LTE

Here we derive excitation temperature ($T_{\rm rot}$) and column density ($N_{\rm tot}$) at each aperture position in VV 114 using single component rotation diagram method, assuming optically-thin gas and LTE conditions. Recent multiple CO transitions have revealed that nearby IR-bright galaxies (e.g., Downes & Solomon 1998; Zhu et al. 2003; Iono et al. 2007; Zhu et al. 2007; Sliwa et al. 2012; Saito et al. 2015) show CO (1–0) emission with moderate optical depth ($\sim$ 1). Considering 1-2 orders of magnitude weaker HCN (1–0) and HCO^+ (1–0) emission relative to CO (1–0) in such IR-bright galaxies (Gao & Solomon 2004a,b; Privon et al. 2015), it is reasonable to assume optically-thin HCN (1–0) and HCO^+ (1–0) lines in VV 114 (but this is not the case with higher J transitions).

Rotation Diagram Analysis

We fitted the observed flux densities by using the following equation (e.g., Goldsmith & Langer 1999; Watanabe et al. 2014; Mangum & Shirley 2015),

$$W_\nu = \frac{8\pi^3 S\mu_0^2\nu N_{\rm tot}}{3kQ_{\rm rot}}\left\{1-\frac{\exp(h\nu/kT_{\rm rot})-1}{\exp(h\nu/kT_{\rm bg})-1}\right\} \times \exp\left(-\frac{E_{\rm u}}{kT_{\rm rot}}\right), \quad (5.5)$$

where W_ν is the flux density (proportional to the upper state column density, $N_{\rm u}$), S is the line strength, μ_0 is the dipole moment, ν is the frequency of the transition, $Q_{\rm rot}$ is the rotational partition function, k is the Boltzmann constant, h is the Planck constant, $T_{\rm bg}$ is the cosmic microwave background temperature (= 2.73 K), and $E_{\rm u}$ is the upper state energy. The molecular line database Splatalogue[4] and the Cologne Database for Molecular Spectroscopy (CDMS[5]; Müller et al. 2001, 2005) were used to get the transition parameters necessary for calculation. When no or single transition

[4]http://www.splatalogue.net/
[5]http://www.astro.uni-koeln.de/cdms/catalog#partition

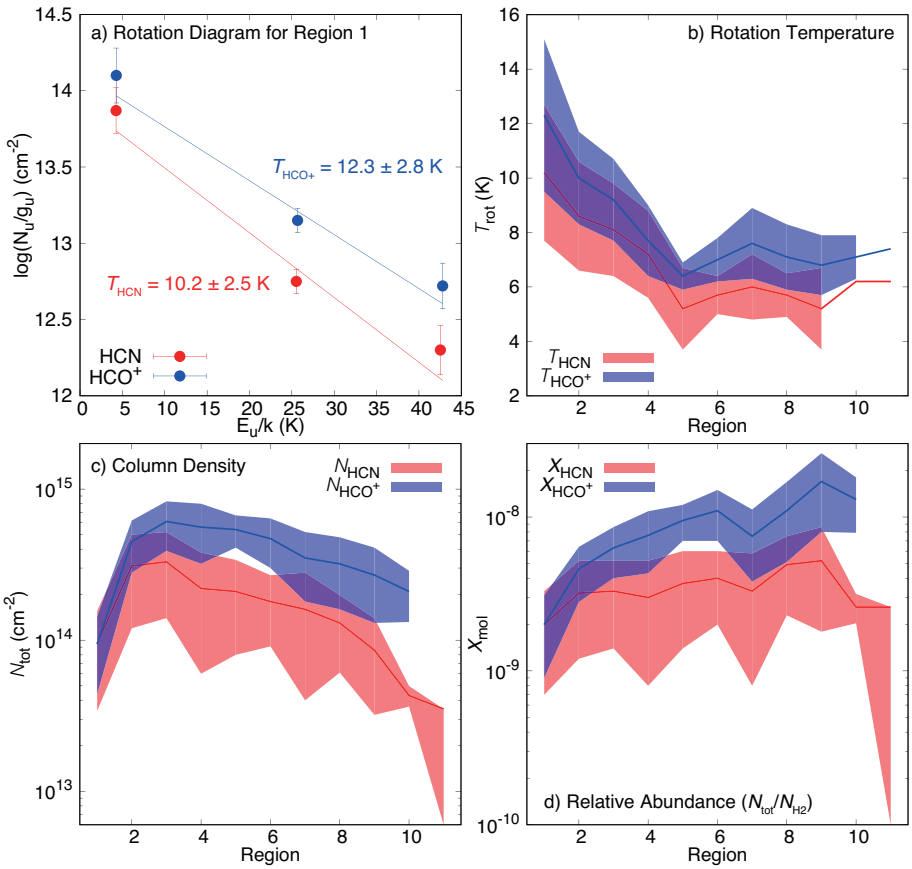

Figure 5.17. (a) Rotation diagrams of HCN and HCO^+ for Region 1. The lines show the best fitted linear function. The derived $T_{\rm rot}$ values are also shown. (b) $T_{\rm rot}$ along the filament of VV 114. 1σ error ranges of the fitting are shown as colorized areas. Values without error indicate the adopted $T_{\rm rot}$. See text. (c) $N_{\rm tot}$ along the filament of VV 114. (d) $X_{\rm mol}$ along the filament of VV 114.

is available, we used an averaged $T_{\rm rot}$ between Region 3 and 9 where show two detected lines, and are not contaminated by the AGN.

Figure 5.17a shows an example of the fitting for Region 1. The data appear to be well fitted by a single component, although all regions show the same trend that J = 3–2 (J = 1–0 and 4–3) flux is overestimated (underestimated). Some possibilities to explain this trend will be discussed in Section 5.5.5. Derived $T_{\rm rot}$ and $N_{\rm tot}$ for HCN ($T_{\rm HCN}$ and $N_{\rm HCN}$) and HCO^+ ($T_{\rm HCO+}$ and $N_{\rm HCO+}$) are listed in Table 5.5 and shown in Figure 5.17b and 5.17c. Both $T_{\rm HCN}$ and $T_{\rm HCO+}$ peak at Region 1 (10.2 ± 2.5 K and 12.3 ± 2.8 K, respectively) and decrease as going to the western side

of the filament (i.e., Region 11). The derived temperature of 5-8 K at Overlap is consistent with $T_{\rm rot}$ derived from rotational transitions of methanol ($T_{\rm CH_3OH}$ = 6-9 K; see Section 4). We compare the derived $T_{\rm HCN}$ and $T_{\rm HCO^+}$ with $\Sigma_{\rm SFR}$ in Figure 5.18. This figure is more straightforward relative to the excitation ratio plots (Figure 5.15) to understand energetics of dense gas, because some effects controlling observed line ratios (e.g., optical depth, column density, and fractional abundance) are decomposed. As already seen in Figure 5.15, both $T_{\rm HCN}$ and $T_{\rm HCO^+}$ correlate with $\Sigma_{\rm SFR}$, except for that for Region 1. The correlation coefficients are 0.71 and 0.63 for $T_{\rm HCN}$ and $T_{\rm HCO^+}$, respectively, whereas, without Region 1 data, those are 0.96 and 0.94, respectively. Those correlations clearly show that HCN and HCO^+ molecules are excited by star-forming activities (i.e., FUV heating) in the filament of VV 114, and Region 1 needs additional efficient heating mechanisms (i.e., radiative and/or mechanical heating from the putative AGN). This explanation is consistent with that for CO excitation (Greve et al. 2014; Kamenetzky et al. 2016), indicating that, in general, both diffuse and dense molecular ISM are excited by the same mechanisms (but see, e.g., Sakamoto et al. 2013; Aalto et al. 2015b; Imanishi et al. 2016b, which show the importance of radiative (IR) pumping for higher-J HCN and HNC).

The derived column densities (Figure 5.17c) peak at Region 3 and slightly decrease as going to the western side, that is, the eastern nucleus contains warmer and more massive dense gas relative to the Overlap region. However, when we see their fractional abundances relative to H_2 (e.g., $X_{\rm HCN} = N_{\rm HCN}/N_{\rm H_2}$), the trend changes. $X_{\rm HCN}$ shows a remarkably flat distribution along the filament, whereas $X_{\rm HCO^+}$ shows a slightly increasing trend toward west. The average $X_{\rm HCN}$ and $X_{\rm HCO^+}$ are $(3.5 \pm 0.7) \times 10^{-9}$ and $(8.9 \pm 1.4) \times 10^{-9}$, respectively, which are the first measurements of the spatially-resolved $X_{\rm HCN}$ and $X_{\rm HCO^+}$ for a LIRG. This is roughly consistent with other measurements for Galactic star-forming regions and nearby bright galaxies (e.g., Blake et al. 1987; Krips et al. 2008). Next, we divide $N_{\rm HCN}$ by $N_{\rm HCO^+}$ to see the spatial distribution of the HCN/HCO^+ abundance ratio, $X_{\rm HCN}/X_{\rm HCO^+}$, as shown in Figure 5.19. Although the errors are too large, the abundance ratio tends to peak at Region 1. Also, HCN (1–0)/HCO^+ (1–0) flux ratio shows a similar trend (Figure 5.10) from 1 (Region 1) to 0.2 (Region 10), indicating that optically-thin

Table 5.5. Results of rotations diagram

ID[a]	$T_{\rm HCN}$ (K)	$N_{\rm HCN}$ (10^{14} cm^{-2})	$X_{\rm HCN}$ (10^{-9})	$T_{\rm HCO+}$ (K)	$N_{\rm HCO+}$ (10^{14} cm^{-2})	$X_{\rm HCO+}$ (10^{-9})	$X_{\rm HCN}/X_{\rm HCO+}$[b]
1	10.2 ± 2.5	1.0 ± 0.6	2.0 ± 1.3	12.3 ± 2.8	0.9 ± 0.5	2.0 ± 1.1	1.0 ± 0.9
2	8.6 ± 2.0	3.1 ± 1.9	3.2 ± 2.0	10.0 ± 1.7	4.5 ± 1.7	4.6 ± 1.8	0.7 ± 0.5
3	8.1 ± 1.7	3.3 ± 1.9	3.3 ± 1.9	9.2 ± 1.5	6.1 ± 2.2	6.3 ± 2.3	0.5 ± 0.4
4	7.2 ± 1.6	2.2 ± 1.6	3.0 ± 2.2	7.7 ± 1.3	5.6 ± 2.4	7.6 ± 3.3	0.4 ± 0.3
5	5.2 ± 1.5	2.1 ± 1.3	3.7 ± 2.3	6.4 ± 0.5	5.4 ± 1.3	9.5 ± 2.5	0.4 ± 0.3
6	5.7 ± 0.7	1.8 ± 0.9	4.0 ± 2.0	7.0 ± 0.8	4.7 ± 1.7	10.5 ± 4.0	0.4 ± 0.2
7	6.0 ± 1.2	1.6 ± 1.2	3.3 ± 2.5	7.6 ± 1.3	3.5 ± 1.7	7.5 ± 3.7	0.4 ± 0.4
8	5.7 ± 0.8	1.3 ± 0.7	4.9 ± 2.6	7.1 ± 1.2	3.2 ± 1.6	11.5 ± 5.9	0.4 ± 0.3
9	5.2 ± 1.5	0.9 ± 0.5	5.2 ± 3.4	6.8 ± 1.1	2.7 ± 1.4	16.5 ± 9.0	0.3 ± 0.3
10	6.2[c]	0.4 ± 0.1	2.6 ± 5.6	7.1 ± 0.8	2.1 ± 0.8	1.3 ± 5.1	0.2 ± 0.1
11	6.2[c]	<0.4	< 2.6	7.4[c]	0.02 ± 0.01	< 0.1	< 20.6
E0	9.8 ± 1.6	8.0 ± 3.9	···	10.9 ± 2.4	5.0 ± 3.0	···	1.5 ± 1.2

[a]Aperture ID defined by Saito et al. (2016b). E0 is the AGN position at the eastern nucleus defined by Iono, Saito et al. (2013).

[b]This is derived by $N_{\rm HCN}/N_{\rm HCO+}$ in practice.

[c]In the case of non-detection or single transition detection, we apply the average $T_{\rm rot}$ between Region 3 and 9 to derive $N_{\rm tot}$. See text.

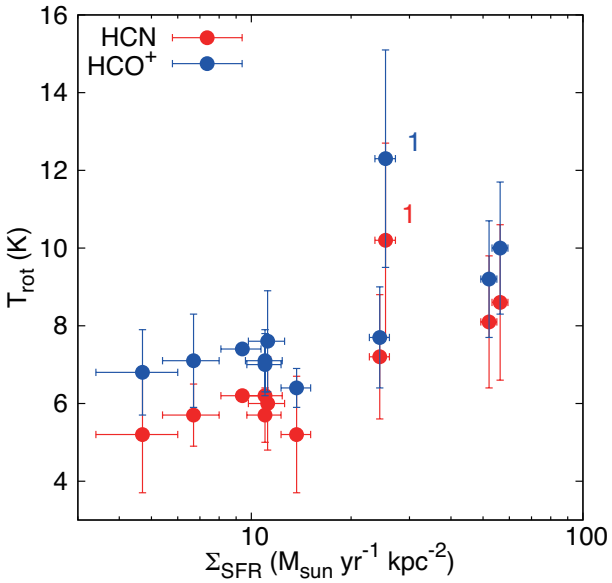

Figure 5.18. $T_{\rm rot}$ plots against $\Sigma_{\rm SFR}$. Data point at the AGN position is denoted as 1.

approximation for HCN (1–0) and HCO^+ (1–0) lines is an applicable assumption for the VV 114 data.

The same analysis for the AGN position (E0) shows that $T_{\rm HCN} = 9.8 \pm 1.6$ K, $N_{\rm HCN} = (8.0 \pm 3.8) \times 10^{13}$ cm^{-2}, $T_{\rm HCO^+} = 10.9 \pm 2.4$ K, $N_{\rm HCO^+} = (5.4 \pm 3.3) \times 10^{13}$ cm^{-2}, and $X_{\rm HCN}/X_{\rm HCO^+} = 1.5 \pm 1.2$ (Table 5.5). The putative AGN position of VV 114 shows a relatively high $X_{\rm HCN}/X_{\rm HCO^+}$, resulting in observed high HCN (1–0)/HCO^+ (1–0) flux ratio. Higher HCN/HCO^+ ratios in higher-J seen at the AGN position is due to the combination effect of the high $X_{\rm HCN}/X_{\rm HCO^+}$ and comparably high rotation temperatures between both molecules ($T_{\rm HCN} \sim T_{\rm HCO^+}$). Similar slopes in the rotation diagram (i.e., similar rotation temperatures) keep the ratio between the upper state column densities of HCN and HCO^+ at given J, so the observed HCN/HCO^+ ratio SLED seems to be flat for the AGN position (Figure 5.10). Other regions along the filament show relatively low $X_{\rm HCN}/X_{\rm HCO^+}$ (≤ 0.7) and low rotation temperatures (≤ 10 K). Lower HCN temperatures ($T_{\rm HCN} < T_{\rm HCO^+}$) result in the decreasing trends seen in the HCN/HCO^+ ratio SLED.

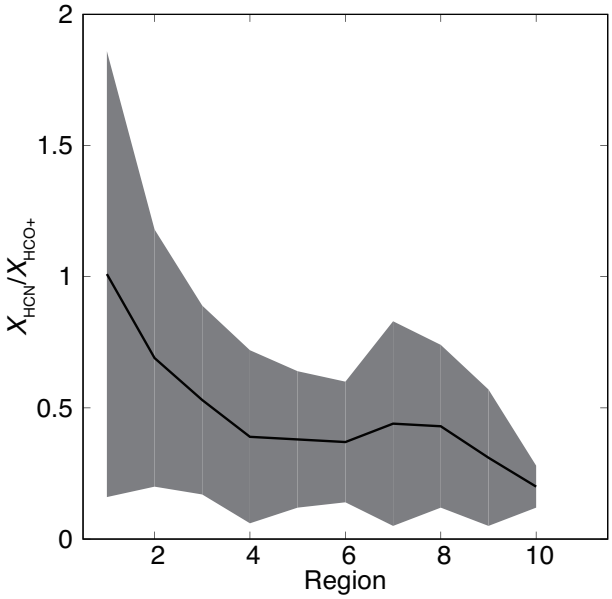

Figure 5.19. $X_{\rm HCN}/X_{\rm HCO^+}$ along the filament of VV 114. Practically, $X_{\rm HCN}/X_{\rm HCO^+}$ is derived by calculating $N_{\rm HCN}/N_{\rm HCO^+}$.

Two-component ISM?

Here, we discuss the effect of optical depth for the rotation diagram analysis. For the sake of simplicity, we ignore the background radiation term because the discussion does not change even if this term is included. According to the LTE radiative transfer calculation for a given linear molecule described by Goldsmith & Langer (1999), the transition of maximum opacity can be written as,

$$J_{\rm max\tau} = 4.6\sqrt{T/B_0}, \tag{5.6}$$

where T is the cloud temperature in Kelvin and B_0 is the rotation constant in GHz. For HCN molecule (B_0 = 44.31597 GHz) with T = 10-20 K, $J_{\rm max\tau}$ = 2-3. In the limit $hB_0/kT < 1$ (i.e., $0.048B_0 < T$), the ratio of the optical depth of the most thick transition ($\tau_{\rm max}$) to that of the J = 1–0 transition ($\tau_{1,0}$) can be expressed as,

$$\frac{\tau_{\rm max}}{\tau_{1,0}} = \frac{T}{0.048eB_0}. \tag{5.7}$$

This indicates that, for HCN molecule with T = 10-20 K, optical depth at $J_{\rm upp} \sim 3$ is 1.7-3.5 times larger than that at $J_{\rm upp} = 1$.

On the rotation diagram (Figure 5.17a), data points should be aligned with a single straight line when the observed transitions are optically-thin under LTE. The expected deviation of the apparent upper state column density at $J_{\max\tau}$ from the optically-thin straight line can be estimated using the equation below.

$$N_{\rm u} = \frac{\tau_{\rm max}}{1 - e^{-\tau_{\rm max}}} N_{\rm u}^{\rm thin}, \tag{5.8}$$

where $N_{\rm u}^{\rm thin}$ is the apparent upper state column density attenuated by line opacity ($\tau_{\rm max}$) and $N_{\rm u}$ is the opacity-corrected (true) upper state column density. When $\tau \rightarrow 0$ (i.e., optically-thin limit), $N_{\rm u}^{\rm thin}$ becomes $N_{\rm u}$. The apparent deviation at J = 3–2 from the straight line through J = 1–0 and 4–3 is $N_{\rm u}/N_{\rm u}^{\rm thin} \sim 10^{13.0}/10^{12.75} \sim 1.78$ (Figure 5.17a), which corresponds to $\tau_{\rm max} \sim 1.3$. This $\tau_{\rm max}$ is a lower limit because here we assumed optically-thin J = 1–0 and 4–3 emissions to derive $N_{\rm u} = 10^{13.0}$ cm^{-2}. Using $\tau_{\rm max}/\tau_{1,0}$ = 1.7-3.5, $\tau_{1,0}$ is $\geq$ 0.4-0.8. Although this is a rough estimate, it is consistent with $\tau_{1,0}$ = 0.3-1.4 derived by the non-LTE modeling for HCN and HCO$^+$ transitions (Krips et al. 2008), indicating that the moderate optical depth at J = 3–2 ($\tau_{\rm max} \geq 1.3$) may drive the apparent two-component seen along the filament of VV 114. Those discussion can expand to HCO$^+$, which has similar excitation parameters to HCN. We conclude the apparent two-component excitation condition seen in the rotation diagrams of HCN and HCO$^+$ for VV 114 data can be explained by moderate optical depth effects, which peaks at $J_{\rm upp} \sim 3$. For much higher-J HCN ($J_{\rm upp} \sim 15$), radiative pumping rather than collision becomes more important to explain the level population, resulting in a two-component ISM (e.g., Rangwala et al. 2011). Observations of other rotational transitions are essential to investigate the appropriateness for other assumptions (e.g., non-LTE excitation). We note that the finite optical depths for observed transitions nonlinearly lead to column density underestimations, which can be addressed by non-LTE approaches (e.g., RADEX).

5.6 Summary of This Section

We present new high-resolution images of multiple HCN and HCO$^+$ transitions (J = 1–0, 3–2, and 4–3), HNC J = 1–0, CS J = 7–6, and continuum emissions toward

the nearby luminous infrared galaxy VV 114 with ALMA Band 3, 6, and 7. We map the spatial distribution of three HCN and HCO^+ transitions for a LIRG for the first time. We summarize the main results of this Section as follows:

1. All line and continuum images, except for HCN (1–0) and CS (7–6) lines, show an extended clumpy filament ($\sim$ 6 kpc length) across the progenitor's galaxy disks of VV 114, which is previously reported by many molecular and ionized gas tracers. High-resolution Band 7 images ($\sim$ 80 pc resolution) found that the filament has an extremely narrow width ($\leq$ 200 pc). Such a filamentary structure was predicted by recent numerical simulations of major mergers.

2. Both excitation ratios (e.g., HCN (3–2)/HCN (1–0)) and HCN/HCO^+ ratios (e.g., HCN (1-0)/HCO^+ (1–0)) show higher values at the eastern nucleus, relative to the Overlap region where is located between the progenitor's disks. We plot spatially-resolved HCN and HCO^+ SLEDs for the first time, which clearly shows the peaks are located at $J_{\rm upp} \leq 3$ for the Overlap region whereas $J_{\rm upp} \geq 3$ for the eastern nucleus. HCO^+ SLEDs are generally larger than HCN SLEDs. HCN/HCO^+ ratio SLED shows a remarkably high, flat shape at the AGN position, while a decreasing trend with increasing $J_{\rm upp}$ is seen in other regions.

3. Fluxes - $\Sigma_{\rm SFR}$ ($= L'_{\rm dense}$ - $L_{\rm IR}$) and flux ratios - $\Sigma_{\rm SFR}$ ($= L'_{\rm dense}/L'_{1,0}$ - $L_{\rm IR}$) plots show positive trends when excluding the putative AGN, indicating that star formation activity is closely related to surface densities and excitations of dense gas tracers in the filament of VV 114. For both HCN and HCO^+, we found that the slope of the log $L'_{\rm dense}$ - log $L_{\rm IR}$ plots decreases as J increases. This is explained by subthermalized gas excitation at the lower $\Sigma_{\rm SFR}$ regime ($L_{\rm IR}$) and/or the presence of additional heating source(s) rather than radiation from star formation at the higher $\Sigma_{\rm SFR}$ regime.

4. Furthermore, we estimate the surface densities of total H_2 mass and dense gas mass, and then $\rm SFE_{H_2}$ ($= \Sigma_{\rm SFR}/\Sigma_{\rm H_2}$), $\rm SFE_{dense}$ ($= \Sigma_{\rm SFR}/\Sigma_{\rm dense}$), and $f_{\rm dense}$ ($= \Sigma_{\rm dense}/\Sigma_{\rm H_2}$), assuming contant conversion factors. Although both SFEs peaks

at the eastern nucleus and are lower at the Overlap region, $f_{\rm dense}$ shows different trend peaking at the Overlap. This trend becomes clearer when we adopt appropriate conversion factors. A simple so-called density threshold star formation model cannot reproduce those behaviors found in VV 114.

5. We examine a turbulence-regulated star formation model, and find that the Overlap region has diffuser and more turbulent dense gas properties relative to dense gas at the eastern nucleus. Combined with the fact that methanol abundance in gas-phase at the Overlap region is elevated due to large-scale shocks, we suggest that collision between the progenitors of VV 114 has produced the filamentary structure and violent gas inflow toward the eastern nucleus triggering starburst and AGN activities. Merger-induced shocks, which can enhance the intracloud turbulence, were dominated at the Overlap region, and have started to be dissipated to form new massive star-forming regions.

6. Radiative transfer analysis under LTE and optically-thin assumptions revealed that the rotation temperatures and column densities are higher at the eastern nucleus. Except for the AGN position, the rotation temperatures are clearly correlated to $\Sigma_{\rm SFR}$, indicating that dense gas excitation in the filament is dominantly governed by star formation activity. The fractional abundance of HCN relative to H_2 is remarkably flat along the filament, showing that the HCN abundance might be insensitive to environmental effects (i.e., AGN, starbursts, and shocked Overlap region). The average fractional abundances of HCN and HCO^+ are $(3.5 \pm 0.7) \times 10^{-9}$ and $(8.9 \pm 1.4) \times 10^{-9}$, respectively.

7. The observed high HCN/HCO^+ ratios at the eastern nucleus may be due to a high HCN/HCO^+ abundnace ratio, and the high excitation ratios are due to efficient heating by the possible AGN activity.

Chapter 6

Conclusions

6.1 Summary

In this Thesis, we investigated physical conditions of molecular gas in two nearby luminous infrared galaxies, NGC 1614 and VV 114, through high angular resolution and high sensitivity ALMA observations of bright rotational transitions of CO, HCN, HCO^+, and CH_3OH supplemented with other lines and continuum emission. Spatially-resolved data of multiple transitions for given molecule allow us to characterize spatial variations of heating sources of cold molecular gas ISM within a LIRG, which has not been studied yet because of instrumental limitations at the submillimeter wavelength. We list the summary in a simple table (Table 6.1). VV 114 is mainly powered by AGN, star formation, and shocks, although NGC 1614 is dominantly powered by star formation. We found different characteristics for these three energetic activities as shown in Table 6.1. Here we summarize our main conclusions.

1. Although our main aim is molecular line imaging, continuum images, which can be always observed simultaneously with molecular lines, can have better quality (i.e., S/N) than molecular line images, taking advantage of the ALMA wideband correlators. There is another advantage that assigned antenna configuration must be same between line and continuum data, making it easier to deal with the missing flux effects. Thus, we investigated the usage of submillimeter continuum emission. For the sake of simplicity, we observed a well-studied

Table 6.1. A summary table for (sub-)millimeter diagnostics of nearby U/LIRGs

Diagnostics	Target	AGN	Star Formation	Shock/Overlap	Section
SED	NGC 1614	N/A	synchrotron, free-free, dust	N/A	2
CO SLED	NGC 1614	N/A	FUV heating (PDR)	stellar feedback	3
CH_3OH	VV 114	dissociation, CO desorption	dissociation, CO desorption	galaxy collision	4
HCN/HCO^+ SLEDs	VV 114	HCN-rich, warm, massive	HCO^+-rich, warm	HCO^+-rich, cold	5
SFE, $f_{\rm dense}$	VV 114	N/A	dense, star-forming	diffuse, turbulent	5

starburst-dominated LIRG NGC 1614. Combined with similar resolution VLA data, we made spatially-resolved ($\sim$ 330 pc) SED from 4.81 GHz to 691 GHz with the same maximum recoverable scale. A starburst SED template successfully explained the observed radial variations by a combination of non-thermal synchrotron, thermal free-free, and thermal dust emission, and derived some physical quantities: e.g., surface density of star formation rate and dust opacity.

2. High-resolution, high-sensitivity, and *uv*-matched ALMA observations of CO (1–0), CO (2–1), CO (3–2), and CO (6–5) lines toward NGC 1614 mapped CO SLED for a LIRG for the first time. The CO (6–5) emission is confined within the central starburst ring, although lower-J CO lines spread over the entire disk. Non-LTE radiative transfer modeling yielded that the starburst ring has two-phase molecular gas ISM ($>$ 70 K and $\sim$ 19 K). This is consistent with observed two-phase dust SED ($\sim$ 110 K and $\sim$ 35 K) assuming a concomitant gas and dust ISM. At the starburst ring the cold ISM is heated by UV from star-forming regions, while star formation is not enough to heat the warm ISM. We suggested mechanical heating from supernovae and stellar winds as an alternative power source for the warm ISM at the starburst ring. The outer disk is dominated by moderately FUV-illuminated cold PDR ($\sim$ 22 K and $G_0 \sim 10^{0.9}$).

3. We observed thermal rotational transitions of CH_3OH toward the nearby IR-bright mid-stager merger VV 114 in order to test kpc-scale shocks in molecular gas ISM driven by a gas-rich galaxy-galaxy collision for the first time. Applying a LTE radiative transfer calculation, we found that the CH_3OH abundance is almost an order of magnitude larger at the Overlap region than the nuclear regions. This trend can be explained by two mechanisms: (1) at the nuclear regions, the presence of AGN and starburst activities suppress the CH_3OH abundance by strong photodissociation (i.e., efficient destruction of CH_3OH) or desorption of the precursor molecule CO (i.e., inefficient production of CH_3OH) on dust grains. (2) merger-induced shocks enhance the CH_3OH abundance at

the kpc-scale Overlap region. The observed properties of CH_3OH in VV 114 cannot be explained by hot-core chemistry.

4. We also observed thermal rotational transitions of HCN and HCO^+ toward VV 114 to study dense gas excitation and its relation to star formation and AGN activities. All dense gas tracers distribute along the clumpy filament between the progenitor's disks of VV 114. We found that all fluxes and flux ratios (e.g.., HCN (3–2)/HCN (1–0), HCN (1–0)/HCO^+ (1–0)) are strongly correlated with $\Sigma_{\rm SFR}$, except for the data at the putative AGN position, indicating that star formation activity dominantly affects dense gas physics at the filament of VV 114. By comparing SFE_{H_2} and $SFE_{\rm dense}$ with $f_{\rm dense}$, we found that the simple density threshold star formation model (i.e., $\Sigma_{\rm SFR} \propto \Sigma_{\rm dense} = f_{\rm dense}\Sigma_{H_2}$ $\Longleftrightarrow$ $SFE_{H_2} \propto f_{\rm dense}$) doesn't fit to our VV 114 data (i.e., SFE_{H_2} decrease as $f_{\rm dense}$ increases). Alternatively, the turbulence-regulated star formation model can explain the observed trend; i.e., the Overlap region has diffuser and more turbulent dense gas properties relative to dense gas at the eastern nucleus. We suggest that collision between the progenitors of VV 114 has produced the filamentary structure and violent gas inflow toward the eastern nucleus triggered starburst and AGN activities. Merger-induced shocks, which can enhance the intracloud turbulence, were dominated at the Overlap region (i.e., the origin of the CH_3OH enhancement), and have started to be dissipated to form new massive star-forming regions.

As summarized above, our case studies have established that spatially-resolved observations of molecular gas tracers can be used to understand the physical properties of the origin of molecular gas excitation in LIRGs.

6.2 Future Work

Studies shown in this Thesis are focused on testing the usage of spatially-resolved molecular line data. As next steps, we have planed the following studies.

1. Spatially-resolved Radio-to-FIR SED and CO SLED

   Increase sample size Recent multiple J CO studies by *Herschel* have revealed that nearby U/LIRGs are generally classified into 3 categories; warm gas excess ($J_{\rm upp} > 6$), cold gas excess ($J_{\rm upp} < 6$), and moderate ($J_{\rm upp} \sim 6$) (Rosenberg et al. 2015). As a pilot survey we have observed lower-J CO SLED during the Cycle 3 ALMA period toward a representative LIRG in each category, NGC 1614 (cold), VV 114 (moderate), and NGC 6240 (warm). Combining with the ALMA archive, high-resolution, high-sensitivity, and uv-matched CO SLED data up to $J_{\rm upp} = 6$ are already available for all three galaxies. I will clarify differences of spatial/spectral/energy characteristics of the spatially-resolved CO SLEDs, as well as spatially-resolved radio-to-FIR SEDs using the VLA archive, as We did for NGC 1614 (Section 2 and 3).

   Toward higher-J for mid-redshift HyLIRGs In order to expand CO SLED knowledge obtained from local studies, and in order to bridge studies between local U/LIRGs and high-z SMGs in the context of galaxy evolution, I will employ mid-z Hyperluminous IR galaxies (HyLIRGs). HyLIRGs (10^{13} $L_\odot$ < $L_{\rm IR}$ < 10^{14} $L_\odot$; Rowan-Robinson 2000) are thought to be the most appropriate targets as a local analogue of SMGs in terms of their $L_{\rm IR}$. In fact, most of mid-z HyLIRGs (z $\sim$ 0.5) can be classified as SMGs if they lay at higher-z (Farrah et al. 2002). Such mid-z HyLIRGs allow us to (1) increase the sample size, (2) observe redshifted higher-J CO lines using lower frequency bands (e.g., CO (6–5) at $\sim$345 GHz when observing at z $\sim$ 1), so we can go up to $J_{\rm upp} \sim 16$ by ALMA, and (3) expand our understandings of CO SLED to 1-3 orders of magnitude larger luminosities. Also, such intermediate redshift still give us a chance to spatially resolve them by using high resolution facilities.

2. Spatially-resolved Dense Gas Chemistry

   Test other shock tracers and molecules The Band 3 and Band 4 data used

for Section 4 and 5 were observed as a part of the 54 GHz-wide spectral scan project toward VV 114 with ALMA. In Appendix B, we briefly summarize the observation design and preliminary spectra toward the position of AGN (Region 1), SB (Region 3), and Overlap (Region 5-7) (Figure B.1). The spectra clearly shows differences among three specific regions, indicating that different energy sources can affect kpc-scale molecular gas chemistry, and those can be distinguished by molecular line diagnostics as we did (Section 4 and 5).

Spatially-resolved CS SLED Combined data from the spectral scan and the pilot CO SLED survey, we can collect high-sensitivity data of CS (2–1), CS (3–2), CS (5–4), and CS (7–6) lines (i.e., CS SLED) for VV 114 with a comparable resolution to the HCN and HCO^+ SLEDs shown in Section 5. CS lines are known as another dense gas tracers (e.g., Bayet et al. 2009), so the spatially-resolved CS SLED will provide new insight into dense gas excitation along the filament of VV 114.

Bibliography

Aalto, S., Johansson, L. E. B., Booth, R. S., & Black, J. H. 1991, A&A, 249, 323

Aalto, S., Polatidis, A. G., Hüttemeister, S., & Curran, S. J. 2002, A&A, 381, 783

Aalto, S., Spaans, M., Wiedner, M. C., & Hüttemeister, S. 2007, A&A, 464, 193

Aalto, S. 2013, IAU Symposium, 292, 199

Aalto, S., Garcia-Burillo, S., Muller, S., et al. 2015, A&A, 574, A85

Aalto, S., Martín, S., Costagliola, F., et al. 2015, A&A, 584, A42

Aladro, R., Martín, S., Martín-Pintado, J., et al. 2011, A&A, 535, A84

Aladro, R., Martín, S., Riquelme, D., et al. 2015, A&A, 579, A101

Albrecht, M., Krügel, E., & Chini, R. 2007, A&A, 462, 575

Alonso-Herrero, A., Engelbracht, C. W., Rieke, M. J., Rieke, G. H., & Quillen, A. C. 2001, ApJ, 546, 952

Armus, L., Mazzarella, J. M., Evans, A. S., et al. 2009, PASP, 121, 559

Bally, J., Cunningham, N. J., Moeckel, N., et al. 2011, ApJ, 727, 113

Barnes, J. E. 2004, MNRAS, 350, 798

Barnes, J. E., & Hernquist, L. E. 1991, ApJ, 370, L65

Bayet, E., Aladro, R., Martín, S., Viti, S., & Martín-Pintado, J. 2009, ApJ, 707, 126

Bayet, E., Williams, D. A., Hartquist, T. W., & Viti, S. 2011, MNRAS, 414, 1583

Bellocchi, E., Arribas, S., & Colina, L. 2012, A&A, 542, A54

Bellocchi, E., Arribas, S., Colina, L., & Miralles-Caballero, D. 2013, A&A, 557, A59

Bicay, M. D., Kojoian, G., Seal, J., Dickinson, D. F., & Malkan, M. A. 1995, ApJS, 98, 369

Bigiel, F., Leroy, A., Walter, F., et al. 2008, AJ, 136, 2846

Blake, G. A., Sutton, E. C., Masson, C. R., & Phillips, T. G. 1987, ApJ, 315, 621

Bolatto, A. D., Warren, S. R., Leroy, A. K., et al. 2013, Nature, 499, 450

Bolatto, A. D., Wolfire, M., & Leroy, A. K. 2013, ARA&A, 51, 207

Bournaud, F., Powell, L. C., Chapon, D., & Teyssier, R. 2011, IAU Symposium, 271, 160

Brinchmann, J., Charlot, S., White, S. D. M., et al. 2004, MNRAS, 351, 1151

Chien, L.-H., & Barnes, J. E. 2010, MNRAS, 407, 43

Combes, F., García-Burillo, S., Casasola, V., et al. 2013, A&A, 558, A124

Condon, J. J., Helou, G., Sanders, D. B., & Soifer, B. T. 1990, ApJS, 73, 359

Condon, J. J. 1992, ARA&A, 30, 575

Costagliola, F., Aalto, S., Rodriguez, M. I., et al. 2011, A&A, 528, A30

Costagliola, F., Aalto, S., Sakamoto, K., et al. 2013, A&A, 556, A66

Costagliola, F., Sakamoto, K., Muller, S., et al. 2015, A&A, 582, A91

Cox, T. J., Jonsson, P., Somerville, R. S., Primack, J. R., & Dekel, A. 2008, MNRAS, 384, 386

Daddi, E., Dickinson, M., Morrison, G., et al. 2007, ApJ, 670, 156

Daddi, E., Elbaz, D., Walter, F., et al. 2010, ApJ, 714, L118

Davis, T. A., Heiderman, A., Evans, N. J., & Iono, D. 2013, MNRAS, 436, 570

Downes, D., & Solomon, P. M. 1998, ApJ, 507, 615

Duc, P.-A., Brinks, E., Wink, J. E., & Mirabel, I. F. 1997, A&A, 326, 537

Dunne, L., Eales, S., Edmunds, M., et al. 2000, MNRAS, 315, 115

Dunne, L., & Eales, S. A. 2001, MNRAS, 327, 697

Eales, S., Dunne, L., Clements, D., et al. 2010, PASP, 122, 499

Elbaz, D., Dickinson, M., Hwang, H. S., et al. 2011, A&A, 533, A119

Espada, D., Matsushita, S., Peck, A. B., et al. 2012, ApJ, 756, L10

Falstad, N., González-Alfonso, E., Aalto, S., et al. 2015, A&A, 580, A52

Farrah, D., Verma, A., Oliver, S., Rowan-Robinson, M., & McMahon, R. 2002, MNRAS, 329, 605

Frayer, D. T., Ivison, R. J., Smail, I., Yun, M. S., & Armus, L. 1999, AJ, 118, 139

Galametz, M., Zhang, Z.-Y., Immer, K., et al. 2016, arXiv:1606.06225

Gao, Y., & Solomon, P. M. 2004, ApJ, 606, 271

Gao, Y., & Solomon, P. M. 2004, ApJS, 152, 63

García-Burillo, S., Usero, A., Fuente, A., et al. 2010, A&A, 519, A2

García-Burillo, S., Usero, A., Alonso-Herrero, A., et al. 2012, A&A, 539, A8

García-Burillo, S., Combes, F., Usero, A., et al. 2014, A&A, 567, A125

García-Burillo, S., Combes, F., Usero, A., et al. 2015, A&A, 580, A35

Garrod, R. T., Widicus Weaver, S. L., & Herbst, E. 2008, ApJ, 682, 283-302

Goldsmith, P. F., & Langer, W. D. 1999, ApJ, 517, 209

Goldader, J. D., Meurer, G., Heckman, T. M., et al. 2002, ApJ, 568, 651

Goto, T., Takagi, T., Matsuhara, H., et al. 2010, A&A, 514, A6

Graciá-Carpio, J., García-Burillo, S., Planesas, P., & Colina, L. 2006, ApJ, 640, L135

Graciá-Carpio, J., García-Burillo, S., Planesas, P., Fuente, A., & Usero, A. 2008, A&A, 479, 703

Greve, T. R., Leonidaki, I., Xilouris, E. M., et al. 2014, ApJ, 794, 142

Grimes, J. P., Heckman, T., Hoopes, C., et al. 2006, ApJ, 648, 310

Gruppioni, C., Pozzi, F., Rodighiero, G., et al. 2013, MNRAS, 432, 23

Hatsukade, B., Tamura, Y., Iono, D., et al. 2015, arXiv:1503.07997

Henkel, C., Jacq, T., Mauersberger, R., Menten, K. M., & Steppe, H. 1987, A&A, 188, L1

Herrera, C. N., Boulanger, F., Nesvadba, N. P. H., & Falgarone, E. 2012, A&A, 538, L9

Herrero-Illana, R., Pérez-Torres, M. Á., Alonso-Herrero, A., et al. 2014, ApJ, 786, 156

Hibbard, J. E., & Yun, M. S. 1996, Cold Gas at High Redshift, 206, 47

Hodge, J. A., Riechers, D., Decarli, R., et al. 2015, ApJ, 798, L18

Hopkins, P. F., Hernquist, L., Cox, T. J., & Kereš, D. 2008, ApJS, 175, 356-389

Hollenbach, D. J., & Tielens, A. G. G. M. 1999, Reviews of Modern Physics, 71, 173

Hsieh, P.-Y., Ho, P. T. P., Kohno, K., Hwang, C.-Y., & Matsushita, S. 2012, ApJ, 747, 90

Huettemeister, S., Henkel, C., Mauersberger, R., et al. 1995, A&A, 295, 571

Ichikawa, K., Imanishi, M., Ueda, Y., et al. 2014, ApJ, 794, 139

Iguchi, S., Morita, K.-I., Sugimoto, M., et al. 2009, PASJ, 61, 1

Ikarashi, S., Ivison, R. J., Caputi, K. I., et al. 2015, ApJ, 810, 133

Ilbert, O., Salvato, M., Le Floc'h, E., et al. 2010, ApJ, 709, 644

Imanishi, M., Nakanishi, K., Tamura, Y., Oi, N., & Kohno, K. 2007, AJ, 134, 2366

Imanishi, M., & Nakanishi, K. 2013, AJ, 146, 47

Imanishi, M., & Nakanishi, K. 2013, AJ, 146, 91

Imanishi, M., & Nakanishi, K. 2014, AJ, 148, 9

Imanishi, M., Nakanishi, K., & Izumi, T. 2016, ApJ, 822, L10

Imanishi, M., Nakanishi, K., & Izumi, T. 2016, ApJ, 825, 44

Imanishi, M., Nakanishi, K., & Izumi, T. 2016, arXiv:1609.01291

Iono, D., Yun, M. S., & Mihos, J. C. 2004, ApJ, 616, 199

Iono, D., Ho, P. T. P., Yun, M. S., et al. 2004, ApJ, 616, L63

Iono, D., Yun, M. S., & Ho, P. T. P. 2005, ApJS, 158, 1

Iono, D., Wilson, C. D., Takakuwa, S., et al. 2007, ApJ, 659, 283

Iono, D., Wilson, C. D., Yun, M. S., et al. 2009, ApJ, 695, 1537

Iono, D., Saito, T., Yun, M. S., et al. 2013, PASJ, 65, L7

Ishibashi, W., & Fabian, A. C. 2016, MNRAS, 463, 1291

Izumi, T., Kohno, K., Martín, S., et al. 2013, PASJ, 65, 100

Izumi, T., Kohno, K., Aalto, S., et al. 2015, ApJ, 811, 39

Izumi, T., Kohno, K., Aalto, S., et al. 2016, ApJ, 818, 42

Jones, P. A., Burton, M. G., Cunningham, M. R., et al. 2008, MNRAS, 386, 117

Kalnajs, A. J. 1978, Structure and Properties of Nearby Galaxies, 77, 113

Kamenetzky, J., Rangwala, N., Glenn, J., Maloney, P. R., & Conley, A. 2014, ApJ, 795, 174

Kamenetzky, J., Rangwala, N., Glenn, J., Maloney, P. R., & Conley, A. 2016, ApJ, 829, 93

Kaneko, H., Kuno, N., Iono, D., et al. 2014, arXiv:1411.2660

Karim, A., Schinnerer, E., Martínez-Sansigre, A., et al. 2011, ApJ, 730, 61

Kartaltepe, J. S., Sanders, D. B., Le Floc'h, E., et al. 2010, ApJ, 721, 98

Kaufman, M. J., Wolfire, M. G., & Hollenbach, D. J. 2006, ApJ, 644, 283

Kawakatu, N., Anabuki, N., Nagao, T., Umemura, M., & Nakagawa, T. 2006, ApJ, 637, 104

Kazandjian, M. V., Meijerink, R., Pelupessy, I., Israel, F. P., & Spaans, M. 2015, A&A, 574, A127

Kennicutt, R. C., & Evans, N. J. 2012, ARA&A, 50, 531

Knudsen, K. K., Walter, F., Weiss, A., et al. 2007, ApJ, 666, 156

König, S., Aalto, S., Muller, S., Beswick, R. J., & Gallagher, J. S. 2013, A&A, 553, A72

Kohno, K., Matsushita, S., Vila-Vilaró, B., et al. 2001, The Central Kiloparsec of Starbursts and AGN: The La Palma Connection, 249, 672

Kohno, K. 2005, The Evolution of Starbursts, 783, 203

König, S., Aalto, S., Muller, S., et al. 2016, arXiv:1603.05405

Kormendy, J., & Ho, L. C. 2013, ARA&A, 51, 511

Kotilainen, J. K., Reunanen, J., Laine, S., & Ryder, S. D. 2001, A&A, 366, 439

Krips, M., Neri, R., García-Burillo, S., et al. 2008, ApJ, 677, 262-275

Krumholz, M. R., & McKee, C. F. 2005, ApJ, 630, 250

Krumholz, M. R., & Thompson, T. A. 2007, ApJ, 669, 289

Lada, C. J., Forbrich, J., Lombardi, M., & Alves, J. F. 2012, ApJ, 745, 190

Lee, H.-H., Bettens, R. P. A., & Herbst, E. 1996, A&AS, 119, 111

Leech, J., Isaak, K. G., Papadopoulos, P. P., Gao, Y., & Davis, G. R. 2010, MNRAS, 406, 1364

Le Floc'h, E., Papovich, C., Dole, H., et al. 2005, ApJ, 632, 169

Li, A., & Draine, B. T. 2001, ApJ, 554, 778

Lin, L.-H., Wang, H.-H., Hsieh, P.-Y., et al. 2013, ApJ, 771, 8

Lis, D. C., Goldsmith, P. F., Carlstrom, J. E., & Scoville, N. Z. 1993, ApJ, 402, 238

Loenen, A. F., Spaans, M., Baan, W. A., & Meijerink, R. 2008, A&A, 488, L5

Lotz, J. M., Jonsson, P., Cox, T. J., et al. 2011, ApJ, 742, 103

Lu, N., Zhao, Y., Xu, C. K., et al. 2014, ApJ, 787, L23

A. Lundgren, 2013, ALMA Cycle 2 Technical Handbook Version 1.1, ALMA

Madau, P., & Dickinson, M. 2014, ARA&A, 52, 415

Maloney, P. R. 1999, Ap&SS, 266, 207

Man, A. W. S., Zirm, A. W., & Toft, S. 2016, ApJ, 830, 89

Mangum, J. G., & Shirley, Y. L. 2015, PASP, 127, 266

Mao, R.-Q., Schulz, A., Henkel, C., et al. 2010, ApJ, 724, 1336

Martín, S., Mauersberger, R., Martín-Pintado, J., Henkel, C., & García-Burillo, S. 2006, ApJS, 164, 450

Martín, S., Martín-Pintado, J., & Mauersberger, R. 2006, A&A, 450, L13

Martín, S., Martín-Pintado, J., & Viti, S. 2009, ApJ, 706, 1323

Martín, S., Krips, M., Martín-Pintado, J., et al. 2011, A&A, 527, A36

Martín, S., Kohno, K., Izumi, T., et al. 2015, A&A, 573, A116

Mashian, N., Sturm, E., Sternberg, A., et al. 2015, ApJ, 802, 81

Mathys, G., 2013, ALMA Cycle 2 Proposer's Guide, Version 1.8, ALMA

Matsui, H., Saitoh, T. R., Makino, J., et al. 2012, ApJ, 746, 26

Matsushita, S., Iono, D., Petitpas, G. R., et al. 2009, ApJ, 693, 56

McCray, R., & Kafatos, M. 1987, ApJ, 317, 190

McMullin, J. P., Waters, B., Schiebel, D., Young, W., & Golap, K. 2007, Astronomical Data Analysis Software and Systems XVI, 376, 127

Meier, D. S., & Turner, J. L. 2005, ApJ, 618, 259

Meier, D. S., & Turner, J. L. 2012, ApJ, 755, 104

Meier, D. S., Turner, J. L., & Beck, S. C. 2014, ApJ, 795, 107

Meijerink, R., Kristensen, L. E., Weiß, A., et al. 2013, ApJ, 762, LL16

Meixner, M., & Tielens, A. G. G. M. 1993, ApJ, 405, 216

Michiyama, T., Iono, D., Nakanishi, K., et al. 2016, PASJ,

Mihos, J. C., & Hernquist, L. 1996, ApJ, 464, 641

Müller, H. S. P., Thorwirth, S., Roth, D. A., & Winnewisser, G. 2001, A&A, 370, L49

Müller, H. S. P., Schlöder, F., Stutzki, J., & Winnewisser, G. 2005, Journal of Molecular Structure, 742, 215

Murphy, E. J., Condon, J. J., Schinnerer, E., et al. 2011, ApJ, 737, 67

Nakajima, T., Takano, S., Kohno, K., et al. 2015, PASJ, 67, 8

Nakagawa, T., Kii, T., Fujimoto, R., et al. 1999, Ap&SS, 266, 43

Narayanan, D., Cox, T. J., Shirley, Y., et al. 2008, ApJ, 684, 996-1008

Narayanan, D., & Krumholz, M. R. 2014, MNRAS, 442, 1411

Nishimura, Y., Shimonishi, T., Watanabe, Y., et al. 2016, arXiv:1608.01099

Olsson, E., Aalto, S., Thomasson, M., & Beswick, R. 2010, A&A, 513, A11

Papadopoulos, P. P. 2007, ApJ, 656, 792

Papadopoulos, P. P. 2010, ApJ, 720, 226

Papadopoulos, P. P., van der Werf, P. P., Xilouris, E. M., et al. 2012, MNRAS, 426, 2601

Papadopoulos, P. P., Zhang, Z.-Y., Xilouris, E. M., et al. 2014, ApJ, 788, 153

Pellegrini, E. W., Smith, J. D., Wolfire, M. G., et al. 2013, ApJ, 779, L19

Pereira-Santaella, M., Colina, L., Alonso-Herrero, A., et al. 2015, arXiv:1509.07765

Pérez-Beaupuits, J. P., Aalto, S., & Gerebro, H. 2007, A&A, 476, 177

Privon, G. C., Herrero-Illana, R., Evans, A. S., et al. 2015, ApJ, 814, 39

Privon, G. C., Aalto, S., Falstad, N., et al. 2016, arXiv:1612.04401

Querejeta, M., Schinnerer, E., García-Burillo, S., et al. 2016, arXiv:1607.00010

Rabli, D., & Flower, D. R. 2010, MNRAS, 406, 95

Rangwala, N., Maloney, P. R., Glenn, J., et al. 2011, ApJ, 743, 94

Rangwala, N., Maloney, P. R., Wilson, C. D., et al. 2015, ApJ, 806, 17

Rich, J. A., Kewley, L. J., & Dopita, M. A. 2011, ApJ, 734, 87

Rich, J. A., Kewley, L. J., & Dopita, M. A. 2015, ApJS, 221, 28

Riechers, D. A., Weiß, A., Walter, F., & Wagg, J. 2010, ApJ, 725, 1032

Rodighiero, G., Daddi, E., Baronchelli, I., et al. 2011, ApJ, 739, L40

Rosenberg, M. J. F., van der Werf, P. P., & Israel, F. P. 2012, A&A, 540, A116

Rosenberg, M. J. F., van der Werf, P. P., Aalto, S., et al. 2015, ApJ, 801, 72

Rothberg, B., & Joseph, R. D. 2004, AJ, 128, 2098

Rowan-Robinson, M. 2000, MNRAS, 316, 885

Saito, T., Iono, D., Yun, M. S., et al. 2015, ApJ, 803, 60

Saito, T., Iono, D., Xu, C. K., et al. 2016, PASJ, 68, 20

Saito, T., Iono, D., Espada, D., et al. 2016, arXiv:1611.01156

Saitoh, T. R., Daisaka, H., Kokubo, E., et al. 2009, PASJ, 61, 481

Sakamoto, S., Handa, T., Sofue, Y., Honma, M., & Sorai, K. 1997, ApJ, 475, 134

Sakamoto, K., Wang, J., Wiedner, M. C., et al. 2008, ApJ, 684, 957-977

Sakamoto, K., Aalto, S., Costagliola, F., et al. 2013, ApJ, 764, 42

Sakamoto, K., Aalto, S., Combes, F., Evans, A., & Peck, A. 2014, ApJ, 797, 90

Salim, S., Rich, R. M., Charlot, S., et al. 2007, ApJS, 173, 267

Sanders, D. B., Soifer, B. T., Scoville, N. Z., & Sargent, A. I. 1988, ApJL, 324, L55

Sanders, D. B., Scoville, N. Z., & Soifer, B. T. 1991, ApJ, 370, 158

Sandstrom, K. M., Leroy, A. K., Walter, F., et al. 2013, ApJ, 777, 5

Schirm, M. R. P., Wilson, C. D., Parkin, T. J., et al. 2014, ApJ, 781, 101

Schirm, M. R. P., Wilson, C. D., Madden, S. C., & Clements, D. L. 2016, ApJ, 823, 87

Schmitt, H. R., Calzetti, D., Armus, L., et al. 2006, ApJS, 164, 52

Schöier, F. L., van der Tak, F. F. S., van Dishoeck, E. F., & Black, J. H. 2005, A&A, 432, 369

Schutte, W. A., Tielens, A. G. G., & Sandford, S. A. 1991, ApJ, 382, 523

Scoville, N. Z., Evans, A. S., Thompson, R., et al. 2000, AJ, 119, 991

Scoville, N., Sheth, K., Aussel, H., et al. 2016, ApJ, 824, 63

Shirley, Y. L. 2015, PASP, 127, 299

Simpson, J. M., Smail, I., Swinbank, A. M., et al. 2015, ApJ, 807, 128

Sliwa, K., Wilson, C. D., Petitpas, G. R., et al. 2012, ApJ, 753, 46

Sliwa, K., Wilson, C. D., Krips, M., et al. 2013, ApJ, 777, 126

Sliwa, K., Wilson, C. D., Iono, D., Peck, A., & Matsushita, S. 2014, ApJ, 796, L15

Soifer, B. T., Neugebauer, G., Helou, G., et al. 1984, ApJL, 283, L1

Soifer, B. T., Sanders, D. B., Madore, B. F., et al. 1987, ApJ, 320, 238

Solomon, P. M., & Vanden Bout, P. A. 2005, ARA&A, 43, 677

Sparre, M., Hayward, C. C., Springel, V., et al. 2015, MNRAS, 447, 3548

Spilker, J. S., Marrone, D. P., Aguirre, J. E., et al. 2014, ApJ, 785, 149

Stephens, I. W., Jackson, J. M., Whitaker, J. S., et al. 2016, ApJ, 824, 29

Stewart, K. R., Bullock, J. S., Barton, E. J., & Wechsler, R. H. 2009, ApJ, 702, 1005

Stierwalt, S., Armus, L., Charmandaris, V., et al. 2014, ApJ, 790, 124

Sugai, H., Davies, R. I., Malkan, M. A., et al. 1999, ApJ, 527, 778

Takano, S., Nakajima, T., Kohno, K., et al. 2014, PASJ, 66, 75

Takeuchi, T. T., Buat, V., & Burgarella, D. 2005, A&A, 440, L17

Tamura, Y., Saito, T., Tsuru, T. G., et al. 2014, ApJ, 781, L39

Tasca, L. A. M., Le Fèvre, O., Hathi, N. P., et al. 2015, A&A, 581, A54

Tateuchi, K., Konishi, M., Motohara, K., et al. 2015, ApJS, 217, 1

Tacconi, L. J., Genzel, R., Neri, R., et al. 2010, Nature, 463, 781

Teyssier, R., Chapon, D., & Bournaud, F. 2010, ApJ, 720, L149

Toomre, A., & Toomre, J. 1972, ApJ, 178, 623

Toomre, A. 1977, Evolution of Galaxies and Stellar Populations, 401

Tsai, M., Hwang, C.-Y., Matsushita, S., Baker, A. J., & Espada, D. 2012, ApJ, 746, 129

Tunnard, R., Greve, T. R., Garcia-Burillo, S., et al. 2015, ApJ, 815, 114

U, V., Sanders, D. B., Mazzarella, J. M., et al. 2012, ApJS, 203, 9

Ueda, J., Iono, D., Yun, M. S., et al. 2014, ApJS, 214, 1

Ueda, J., Watanabe, Y., Iono, D., et al. 2016, arXiv:1611.00002

Urrutia, T., Lacy, M., & Becker, R. H. 2008, ApJ, 674, 80-96

Usero, A., García-Burillo, S., Martín-Pintado, J., Fuente, A., & Neri, R. 2006, A&A, 448, 457

Usero, A., Leroy, A. K., Walter, F., et al. 2015, AJ, 150, 115

Väisänen, P., Rajpaul, V., Zijlstra, A. A., Reunanen, J., & Kotilainen, J. 2012, MNRAS, 420, 2209

van der Tak, F. F. S., Black, J. H., Schöier, F. L., Jansen, D. J., & van Dishoeck, E. F. 2007, A&A, 468, 627

van der Werf, P. P., Isaak, K. G., Meijerink, R., et al. 2010, A&A, 518, LL42

Viti, S., Jimenez-Serra, I., Yates, J. A., et al. 2011, ApJ, 740, L3

Viti, S., García-Burillo, S., Fuente, A., et al. 2014, A&A, 570, A28

Wang, Z., Fazio, G. G., Ashby, M. L. N., et al. 2004, ApJS, 154, 193

Wang, J., Zhang, J., Gao, Y., et al. 2014, Nature Communications, 5, 5449

Watanabe, N., Shiraki, T., & Kouchi, A. 2003, ApJ, 588, L121

Watanabe, Y., Sakai, N., Sorai, K., & Yamamoto, S. 2014, ApJ, 788, 4

Watanabe, Y., Sakai, N., López-Sepulcre, A., et al. 2015, ApJ, 809, 162

Whitaker, K. E., van Dokkum, P. G., Brammer, G., & Franx, M. 2012, ApJ, 754, L29

Wilson, C. D., Petitpas, G. R., Iono, D., et al. 2008, ApJS, 178, 189

Wilson, C. D., Warren, B. E., Israel, F. P., et al. 2012, MNRAS, 424, 3050

Wilson, C. D., Rangwala, N., Glenn, J., et al. 2014, ApJ, 789, L36

Wuyts, S., Förster Schreiber, N. M., van der Wel, A., et al. 2011, ApJ, 742, 96

Xu, C. K., Shupe, D. L., Béthermin, M., et al. 2012, ApJ, 760, 72

Xu, C. K., Cao, C., Lu, N., et al. 2014, ApJ, 787, 48

Xu, C. K., Cao, C., Lu, N., et al. 2015, ApJ, 799, 11

Yun, M. S., Scoville, N. Z., & Knop, R. A. 1994, ApJ, 430, L109

Yun, M. S., & Carilli, C. L. 2002, ApJ, 568, 88

Zaragoza-Cardiel, J., Beckman, J., Font, J., et al. 2016, arXiv:1611.03863

Zhang, Z.-Y., Gao, Y., Henkel, C., et al. 2014, ApJ, 784, L31

Zhao, Y., Lu, N., Xu, C. K., et al. 2016, arXiv:1602.07070

Zhu, M., Seaquist, E. R., & Kuno, N. 2003, ApJ, 588, 243

Zhu, M., Gao, Y., Seaquist, E. R., & Dunne, L. 2007, AJ, 134, 118

Appendix A

Channel Maps of the CO SLED of NGC 1614

We show the channel map of the *uv*-matched CO (1–0), CO (2–1), CO (3–2), and CO (6–5), and ACA-combined CO (1–0) in Figure A.1, A.2, and A.3. These maps have the same angular resolution of $1\farcs0 \times 1\farcs0$, the same velocity resolution of 30 km s^{-1}, and the same MRS of 45 kλ ($\simeq 4\farcs6$), except for the ACA-combined CO (1–0) image. The lower-J three transitions show almost same structures although the CO (6–5) is only restricted within the central $2\farcs3$ radius.

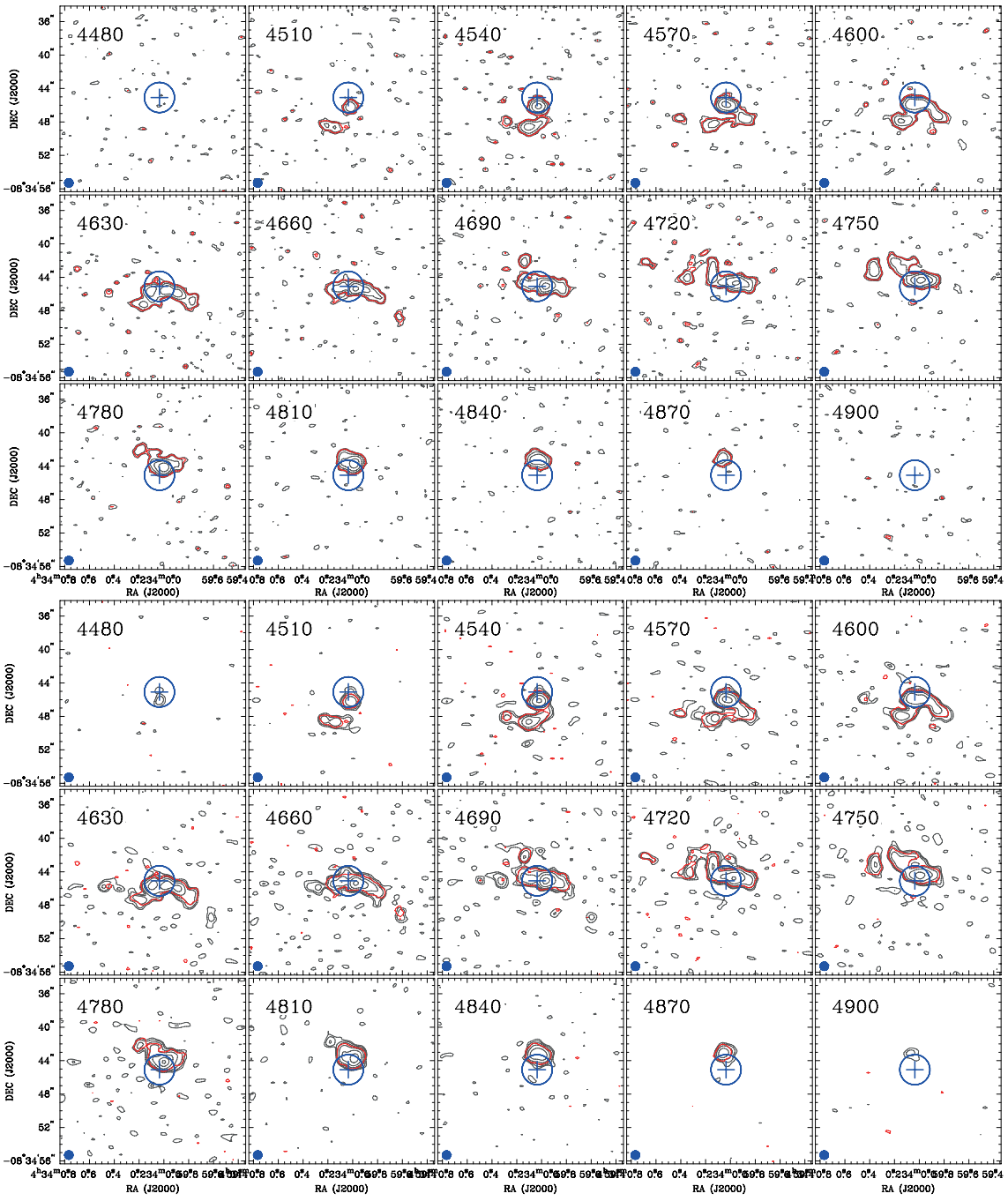

Figure A.1. Channel maps (black contours) of CO (1–0) [top] and CO (2–1) [bottom] in NGC 1614. The nth contours are at $2^n\sigma$ ($n = 1, 2, 3$ ...). σ is the noise rms listed in Table 5.1. The red contours show the 4σ level of the CO (1–0) as a comparison. The blue cross indicates the nucleus which is detected in Pa α and the radio continuum emission (Olsson et al. 2010; Herrero-Illana et al. 2014). The blue circle indicates the approximate outer edge of the nuclear ring (Herrero-Illana et al. 2014; Xu et al. 2015; Saito et al. 2016a).

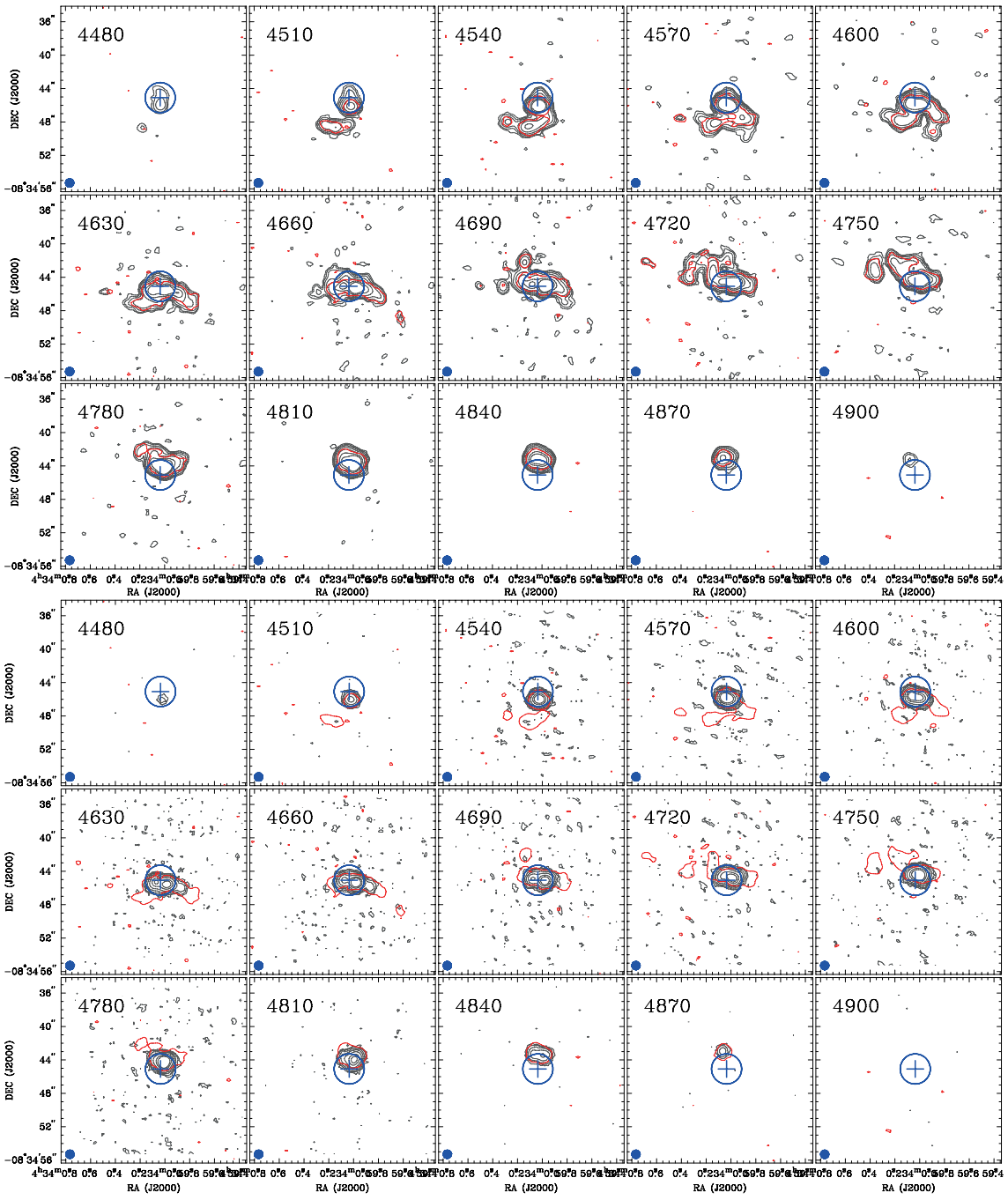

Figure A.2. Same as Figure A.1 but for CO (3–2) (top) and CO (6–5) (bottom).

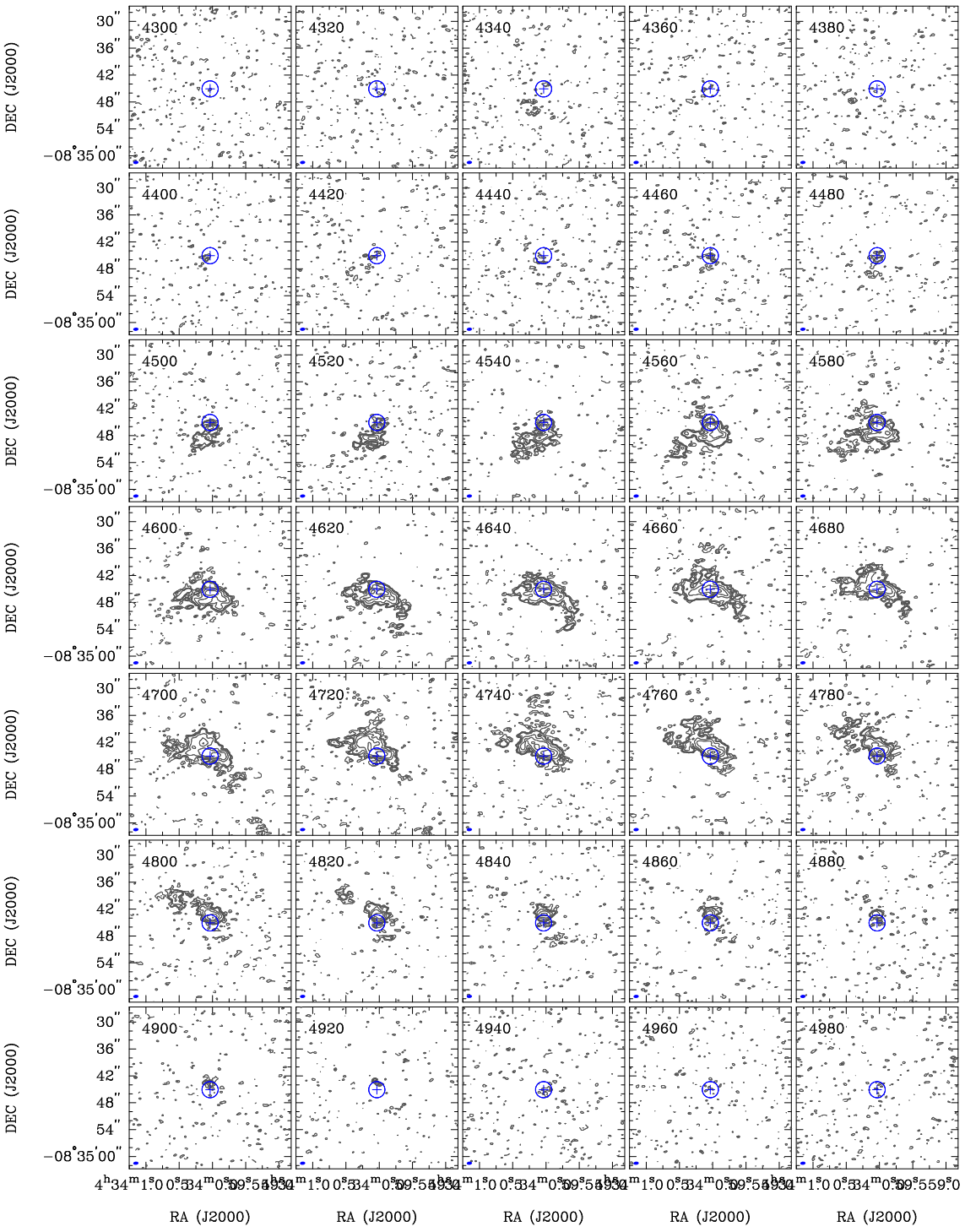

Figure A.3. Same as Figure A.1 but for the ACA-combined CO (1–0). The contours are 1σ × (-2, 2, 3, 4, 8, 16, and 32) mJy beam^{-1}.

Appendix B

Preliminary Results of the Spectral Scan toward VV 114

Here we briefly summarize observation properties of the spectral scan project toward VV 114, a part of which are used in Section 4 and 5.

Table B.1 shows a list of ALMA observation properties including observing date, frequency setups, $T_{\rm sys}$, antenna configuration, observed calibrators, and on-source time.

In Table B.2, we show nominal relative flux uncertainty of the bandpass ($\sigma_{\rm bp}$) and phase calibrator ($\sigma_{\rm ph}$) for each sideband in each tuning. The nominal flux uncertainties correspond to the S/N ratio of the calibrators. The S/N ratios were calculated by integrating data over time and frequency per SPW. Each sideband consists of two SPWs, and each SPW has 1.875 GHz bandwidth, so each sideband has 3.75 GHz. We calculated the resultant total flux uncertainty of a data ($\sigma_{\rm sys}$) as $\sqrt{\sigma_{\rm bp}^2 + \sigma_{\rm ph}^2 + \sigma_{\rm fl}^2}$, where $\sigma_{\rm fl}$ is the absolute flux uncertainty determined by flux calibration. For all data in this project, two solar-system objects, Uranus and Neptune, are used for the flux calibrations, and the uncertainties are nominally known as 5% at Band 3 and Band 4 (Lundgren 2013, see also ALMA memo #594[1]). Those flux uncertainties were applied for discussion in Section 4 and 5.

Table B.3 lists the spectral index of the bandpass ($\alpha_{\rm bp}$) and phase calibrator ($\alpha_{\rm ph}$)

[1]https://library.nrao.edu/public/memos/alma/memo594.pdf

for each sideband in each tuning. This was estimated by fitting all four SPW fluxes using $S_\nu \propto \nu^\alpha$, where S_ν is the flux density, ν is the observed frequency, and α is the spectral index. Considering the relatively narrow frequency range ($\sim$ 12 GHz) for the fitting, α is consistent with each other. For the purpose of checking data quality, the Band 4 calibrators were also observed for a part of the Band 3 observations (e.g., B3-1 tuning consists of totally six individual observations, three of which assigned calibrators same as the Band 4 observations). As a result, we don't see any systematic differences between the Band 3 and Band 4 data, verifying uniform, high data quality after calibrations.

In Figure B.1, preliminary continuum-unsubtracted spectra toward the position of AGN (Region 1), SB (Region 3), and Overlap (Region 6-8) of VV 114 are shown. We list preliminarily detected lines at each region below:

AGN Band 3 CCH ($1_{3/2}$–$0_{1/2}$), CCH ($1_{1/2}$–$0_{1/2}$), HCN (1–0), HCO^+ (1–0), HNC (1–0), CS (2–1), CH_3CCH (6_K–5_K), $C^{18}O$ (1–0), ^{13}CO (1–0), CN ($1_{1/2}$–$0_{1/2}$)

SB Band 3 CCH ($1_{3/2}$–$0_{1/2}$), CCH ($1_{1/2}$–$0_{1/2}$), HCN (1–0), HCO^+ (1–0), HNC (1–0), CS (2–1), HC_3N (11-10), CH_3CCH (6_K–5_K), $C^{18}O$ (1–0), ^{13}CO (1–0), CN ($1_{1/2}$–$0_{1/2}$)

Overlap Band 3 CCH ($1_{3/2}$–$0_{1/2}$), CCH ($1_{1/2}$–$0_{1/2}$), HNCO (4–3), HCN (1–0), HCO^+ (1–0), CH_3OH (2_K–1_K), OCS (8–7), CS (2–1), SO (3–2), HNCO (5–4), OCS (9–8), ^{13}CO (1–0), ($C^{17}O$ (1–0)), CN ($1_{1/2}$–$0_{1/2}$)

AGN Band 4 H_2CS (4–3), CH_3CCH (8_K–7_K), H_2CO (2–1), CS (3–2), CH_3CCH (9_K–8_K)

SB Band 4 H_2CS (4–3), CH_3CCH (8_K–7_K), H_2CO (2–1), ($C^{34}S$ (3–2)), CH_3OH (3_K–2_K), CS (3–2), H_2CO (2–1), multiple c-C_3H_2, CH_3CCH (9_K–8_K), HNCO (7–6)

Overlap Band 4 HNCO (6–5), SO (4–3), H_2CO (2–1), CH_3CCH (9_K–8_K), HNCO (7–6)

Table B.1. Log of ALMA Observations

EB	Scan	Date	Central freq.		$T_{\rm sys}$	Configuration		Calibrator			$t_{\rm int}$
			USB	LSB		$N_{\rm ant}$	$L_{\rm baseline}$	Flux	Bandpass	Phase	
			(GHz)	(GHz)	(K)		(m)				(min.)
X85c183_X1c2d	B3-1	140702	97.941	85.939	39 - 71	30	20 - 626	Uranus	J0137-2430	J0116-2052	7.9
X847097_X153c	B3-1	140617	97.941	85.939	40 - 89	30	20 - 606	Uranus	J0137-2430	J0116-2052	7.9
X847097_X1855	B3-1	140617	97.941	85.939	38 - 79	30	20 - 641	Uranus	J0137-2430	J0116-2052	7.9
Xa2300a_X26c7	B3-1	150604	97.941	85.939	40 - 85	38	20 - 778	Uranus	J2258-2758	J0110-0741	7.9
Xa2300a_X2229	B3-1	150604	97.941	85.939	45 - 90	38	18 - 780	Neptune	J2258-2758	J0110-0741	7.9
Xa24618_X29f5	B3-1	150605	97.941	85.939	40 - 83	37	20 - 778	Neptune	J2258-2758	J0110-0741	7.9
X85dcf7_X142a	B3-2	140703	101.689	89.687	34 - 78	31	19 - 650	Uranus	J0137-2430	J0116-2052	7.9
X85dcf7_X16ad	B3-2	140703	101.689	89.687	33 - 77	31	19 - 650	Uranus	J0137-2430	J0116-2052	7.9
X85dcf7_X185d	B3-2	140703	101.689	89.687	34 - 76	31	19 - 650	Uranus	J0137-2430	J0116-2052	7.9
X85dcf7_X1d8b	B3-3	140703	105.439	93.437	42 - 72	31	19 - 621	Uranus	J0137-2430	J0116-2052	7.9
X85dcf7_X15c6	B3-3	140703	105.439	93.437	44 - 72	31	19 - 621	Uranus	J0137-2430	J0116-2052	7.9
X85f3e3_X7d6	B3-3	140704	105.439	93.437	39 - 77	32	39 - 649	Neptune	J0137-2430	J0116-2052	7.9
Xa2300a_X2447	B3-3	140704	105.439	93.437	41 - 102	38	19 - 589	Neptune	J2258-2758	J0110-0741	7.9
Xa309c2_X388e	B3-3	150611	105.439	93.437	40 - 101	34	20 - 778	Uranus	J2258-2758	J0110-0741	7.9
Xa309c2_X3556	B3-3	150611	105.439	93.437	40 - 103	34	20 - 778	Uranus	J2258-2758	J0110-0741	7.9
X85f3e3_X8c9	B3-4	140704	109.189	97.187	40 - 81	32	19 - 649	Uranus	J0137-2430	J0116-2052	23.3
Xa18feb_X22b0	B4-1	150525	140.876	128.875	47 - 124	36	21 - 539	Neptune	J2258-2758	J0110-0741	20.0
Xa18feb_X2551	B4-2	150525	144.626	132.624	45 - 111	36	21 - 539	Neptune	J2258-2758	J0110-0741	20.0
Xa16f89_X26dc	B4-3	150525	148.376	136.374	40 - 102	34	21 - 539	Uranus	J2258-2758	J0110-0741	20.0
Xa16f89_X2404	B4-4	150524	152.126	140.124	40 - 96	34	19 - 537	Neptune	J2258-2758	J0110-0741	20.0

Note. — Column 1: Execution Block. Column 3: Observed date. Column 4-5: Central frequency of USB and LSB. Both sidebands have two spectral windows (spw) to cover 3.75 GHz width. Column 6: DSB system temperature toward VV 114 after data flagging. Column 7: Number of available antenna. Column 8: Projected length of assigned baseline for VV 114. Column 8: Maximum recoverable scale at the central frequency of USB and LSB, respectively. Column 10: Observed flux calibrator. Column 11: Observed bandpass calibrator. Column 12: Total integration time on VV 114. Column 13: Averaged noise rms per channel of 50 km s^{-1} for data which all same scans are combined using `natural` weighting.

Table B.2. Flux uncertainties of the calibrations

Scan	Sideband	Central freq. (GHz)	$\sigma_{\rm bp}$ (%)	$\sigma_{\rm ph}$ (%)	$\sigma_{\rm sys}$ (%)
B3-1	LSB	85.939	1.9	0.1	5.4
B3-2	LSB	89.687	7.6	0.1	9.1
B3-3	LSB	93.437	1.5	0.2	5.2
B3-4	LSB	97.187	2.9	0.3	5.8
B3-1	USB	97.941	2.6	0.1	5.7
B3-2	USB	101.689	9.9	0.2	11.1
B3-3	USB	105.439	2.5	0.1	5.6
B3-4	USB	109.189	4.9	0.4	7.0
B4-1	LSB	128.875	0.8	0.2	5.1
B4-2	LSB	132.624	0.6	0.3	5.0
B4-3	LSB	136.374	0.4	0.2	5.0
B4-4	LSB	140.124	0.5	0.6	5.1
B4-1	USB	140.876	1.4	0.6	5.2
B4-2	USB	144.626	0.5	0.3	5.0
B4-3	USB	148.376	0.5	0.3	5.0
B4-4	USB	152.126	0.7	0.4	5.1

Table B.3. Spectral indices of the calibrators

Scan	$\alpha_{\rm bp}$		$\alpha_{\rm ph}$	
	J0137-2430	J2258-2758	J0116-2052	J0110-0741
B3-1	−0.74	−0.68	−1.78	−0.76
B3-2	−0.68	···	−1.68	···
B3-3	−0.55	−0.72	−1.26	−0.77
B3-4	−0.65	···	−1.43	···
B4-1	···	−0.63	···	−0.73
B4-2	···	−0.58	···	−0.63
B4-3	···	−0.69	···	−0.72
B4-4	···	−0.60	···	−0.52

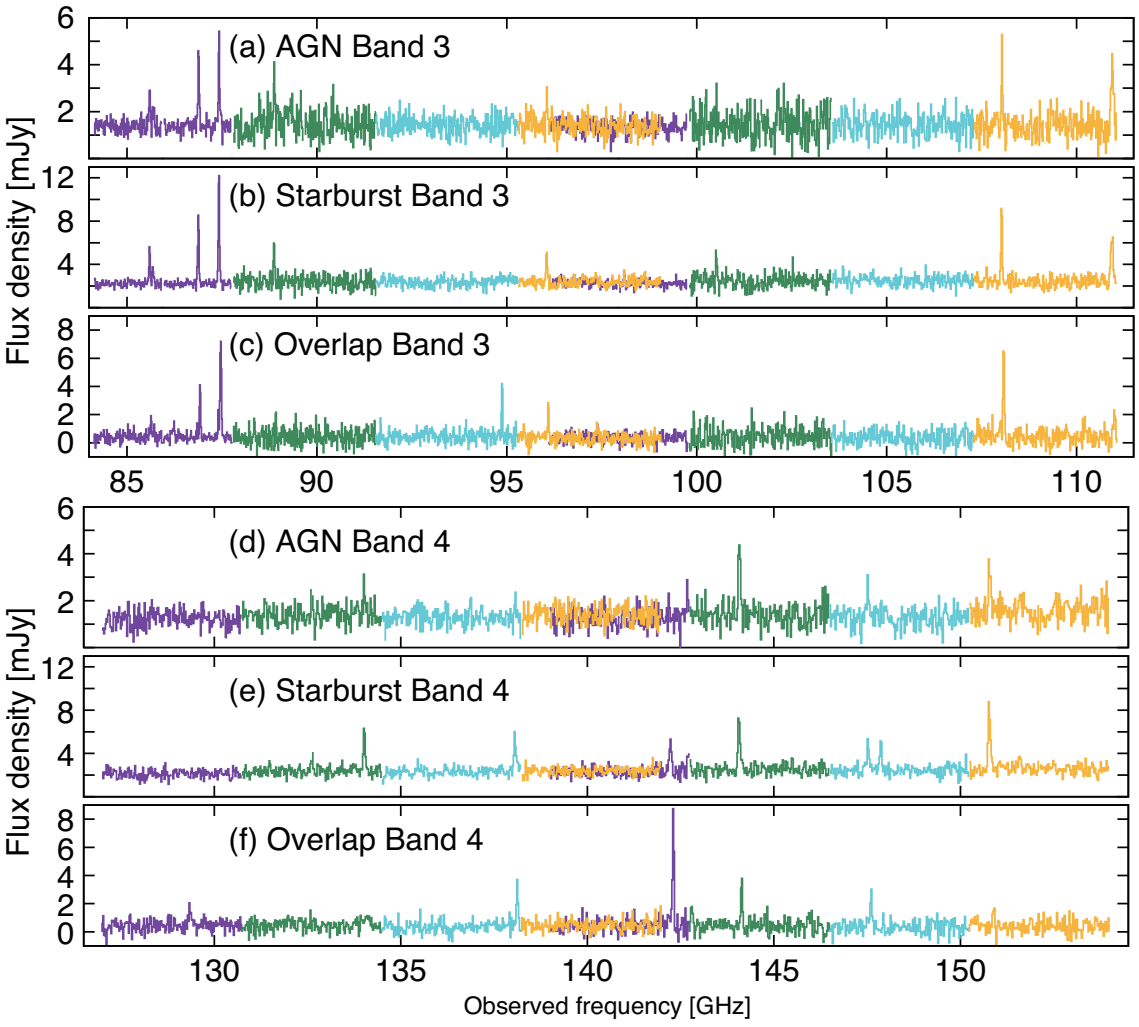

Figure B.1. 54 GHz-wide spectra (84-111 GHz and 127-154 GHz) toward the position of AGN (Region 1), SB (Region 3), and Overlap (Region 6-8) of VV 114. Each tuning is colorized.

Appendix C

Unexpected Discovery of z ∼ 2.5 SMGs behind VV 114

C.1 Continuum Overview

We detected a compact 140.5 GHz continuum emission (Figure C.1b and C.1e) from two positions: SMG-E and $(\alpha, \delta)_{\rm J2000}$ = ($01^{\rm h}07^{\rm m}47.0$, -17°30′09.″8) (hereafter SMG-N). Both are marginally detected in the 97.6 GHz continuum (Figure C.1a and C.1d). The positions coincide with the 338.2 GHz peak positions (Figure C.2; Tamura, Saito et al. 2014; Saito et al. 2015). In this Appendix we used apertures of 4.″0 and 3.″0 to measure the flux densities of SMG-E and SMG-N, respectively. In order to achieve the highest S/N for all line and continuum emission, we chose the smallest aperture size that contains all flux from each SMG with varying the aperture radius from 0.″2 to 4.″5 (i.e., curve-of-growth correction). The central filamentary structure detected in all the continuum is a dense gas filament of the nearby LIRG VV 114 (Iono, Saito et al. 2013; Saito et al. 2015).

The 0.″2 resolution (∼ 1.6 kpc at z = 2.5) 338.2 GHz continuum images toward SMG-N and SMG-E are shown in Figure C.1c and C.1f, respectively. We find extended clumpy structures toward the positions of SMG-E and SMG-N. These structures have the circularized effective (i.e., half-light) radius of $R_{\rm c,e} = 4.2^{+1.0}_{-0.7}$ kpc for SMG-E and $3.7^{+0.4}_{-0.3}$ kpc for SMG-N, showing comparable sizes to GN20 (Hodge et al.

2015), but $\sim$ 4 times larger values compared with other SMGs ($\sim$ 1 kpc; Ikarashi et al. 2015; Simpson et al. 2015). Both SMGs are clearly resolved into a few peaks with the strongest peak of 1.0 $\pm$ 0.1 mJy beam^{-1} for SMG-E and 0.5 $\pm$ 0.1 mJy beam^{-1} for SMG-N. The projected separation of the two strongest peaks of SMG-E (SMG-N) is $\sim$ 2.1 kpc ($\sim$ 6.4 kpc).

The submillimeter spectral energy distribution (SED) of SMG-E is shown in Figure C.3. The Band 4-to-Band 7 continuum are dominated by thermal dust emission (spectral index $\alpha^{338.2\mathrm{GHz}}_{147.1\mathrm{GHz}} \sim 3.38 \pm 0.18$ for SMG-E and $\alpha^{338.2\mathrm{GHz}}_{134.0\mathrm{GHz}} > 4.4$ for SMG-N). A part of the Band 3 continuum of SMG-E ($\alpha^{134.0\mathrm{GHz}}_{97.6\mathrm{GHz}} = 1.46 \pm 0.91$) may be affected by other shallower components (i.e., non-thermal synchrotron and/or thermal free-free emission), although the VLA 3 cm continuum was not detected (< 0.3 mJy; Tamura, Saito et al. 2014). The possible radio excess in SMG-E is consistent with the hard X-ray detection (Tamura, Saito et al. 2014), indicating an intense AGN activity. We need deeper millimeter-to-submilimeter observations enough to estimate the non-thermal and thermal radio contributions to the 97.6 GHz continuum.

C.2 Line Overview

We detected CO (3–2), CO (4–3), and C_I (1–0) lines from both SMG positions (Figure C.4), determining the unique redshift for SMG-E (z = 2.4664 $\pm$ 0.0002) and SMG-N (z = 2.3098 $\pm$ 0.0007). This is consistent with previous photo-z prediction (Tamura, Saito et al. 2014). Unfortunately, since the CO (3–2) line from SMG-E fell between two tunings of the spectral scan, we use the cycle 0 data (Tamura, Saito et al. 2014). The all detected lines have narrow velocity widths (FWHM $\sim$ 180 km s^{-1}), whereas the velocity fields are spatially-resolved by $\sim 1\farcs0$ resolution (Figure C.5). According to the 2D Gaussian fittings using `CASA imfit`, the deconvolved size FWHM are $\sim$ 9 kpc $\times$ $\sim$ 4 kpc and $\sim$ 4 kpc $\times$ $\sim$ 1 kpc for SMG-E and SMG-N, respectively. These are comparable to apparent 338.2 GHz sizes (Figure C.2d and C.2e), indicating concomitant gas and dust ISM. We derived the dynamical mass by $M_{\mathrm{dyn}} = r\sigma^2(\sin i)^{-2}/G$. Adopting r as the deconvolved major axis FWHM and $\sigma \sim 180$ km s^{-1}, $M_{\mathrm{dyn}} \sim 3.7 \times 10^{10}\ (\sin i)^{-2}\ M_\odot$ for SMG-E and $\sim 1.5 \times 10^{10}\ (\sin i)^{-2}\ M_\odot$

for SMG-N.

C.3 Stacking Analysis for Weak Lines

Our frequency coverage of the Band 3 and Band 4 spectral scan can include some weak lines, which allow us to understand the nature of warmer/denser molecular gas in high-redshift galaxies. According to CASAguides[1], we performed image stacking analyses for multiple ^{13}CO ($J_{\rm upp}$ = 3, 4), HCN ($J_{\rm upp}$ = 4, 5, 6), and HCO$^+$ ($J_{\rm upp}$ = 4, 5) transitions in order to increase line sensitivity. The spectra and image of the stacked ^{13}CO, HCN, and HCO$^+$ are shown in Figure C.6. We detected HCN with S/N $\sim$ 4 (peak) and $\sim$ 7 (integrated), while remaining molecules were non-detection. The imaging properties are listed in Table C.1. Assuming HCN (4–3) is the brightest HCN transition for SMG-E and SMG-N, we can estimate $L'_{\rm HCN(4-3)}/L'_{\rm CO(3-2)}$ of 0.25 $\pm$ 0.05 for SMG-E and $<$ 0.36 for SMG-N.

[1]https://casaguides.nrao.edu/index.php/Stacking_Multiple_Spectral_Lines_at_Same_Position

Table C.1. Line and continuum properties of SMG-E and SGM-N

Source	Emission	$\nu_{\rm rest}$ (GHz)	$\nu_{\rm obs}$ (GHz)	Beam size ($''$, $^\circ$)	rms (mJy b^{-1})	$S_{\rm peak}$ or S_ν (mJy)	FWHM (km s^{-1})	$S_{\rm line}dv$ (Jy km s^{-1})	$L'_{\rm line}$ (K km s^{-1} pc^2)
SMG-E	CO (3–2)	345.796	99.757	2.37 × 1.57 (+94)	1.2 (20)	14.1 ± 1.2	186 ± 16	2.78 ± 0.34	(8.8 ± 1.1) × 10^{10}
	CO (4–3)	461.041	133.003	1.50 × 1.11 (+64)	1.2 (10)	18.8 ± 1.2	187 ± 9	3.74 ± 0.31	(6.6 ± 0.6) × 10^{10}
	C_I (1–0)	492.161	141.980	1.60 × 1.05 (+68)	0.8 (30)	5.5 ± 0.7	177 ± 25	1.04 ± 0.21	(1.6 ± 0.3) × 10^{10}
	HCN	···	···	1.27 × 1.15 (+16)	0.25 (100)	2.2 ± 0.5	···	0.69 ± 0.10	···
	HCO^+	···	···	1.26 × 1.14 (+16)	0.35 (100)	< 2.2	···	< 0.44	···
	^{13}CO	···	···	1.42 × 1.23 (+65)	0.35 (100)	< 2.0	···	< 0.40	···
	97.6 GHz	338.3	97.6	1.31 × 1.19 (+16)	0.037	0.34 ± 0.08	···	···	···
	134.0 GHz	464.5	134.0	1.49 × 1.08 (+64)	0.025	0.54 ± 0.09	···	···	···
	147.1 GHz	509.9	147.1	1.31 × 0.98 (+63)	0.031	0.84 ± 0.09	···	···	···
	338.2 GHz	1172.3	338.2	0.21 × 0.17 (+82)	0.094	∼ 14.0	···	···	···
SMG-N	CO (3–2)	345.796	104.476	1.31 × 1.02 (+90)	0.4 (50)	4.8 ± 0.7	179 ± 27	0.92 ± 0.19	(2.6 ± 0.5) × 10^{10}
	CO (4–3)	461.041	139.296	1.53 × 1.04 (+65)	0.5 (20)	5.2 ± 0.4	174 ± 13	0.97 ± 0.11	(1.5 ± 0.2) × 10^{10}
	C_I (1–0)	492.161	148.698	1.19 × 0.95 (+59)	0.4 (50)	2.9 ± 0.9	147 ± 54	0.45 ± 0.22	(1.6 ± 0.3) × 10^{10}
	HCN	···	···	1.29 × 0.99 (−88)	0.25 (100)	< 1.7	···	< 0.33	···
	HCO^+	···	···	1.30 × 1.05 (+64)	0.15 (100)	< 1.0	···	< 0.19	···
	^{13}CO	···	···	···	···	···	···	···	···
	97.6 GHz	323.0	97.6	1.31 × 1.19 (+16)	0.037	< 0.26	···	···	···
	140.5 GHz	465.0	134.0	1.40 × 1.03 (+63)	0.021	< 0.13	···	···	···
	338.2 GHz	1119.4	338.2	0.21 × 0.17 (+82)	0.097	∼ 6.2	···	···	···

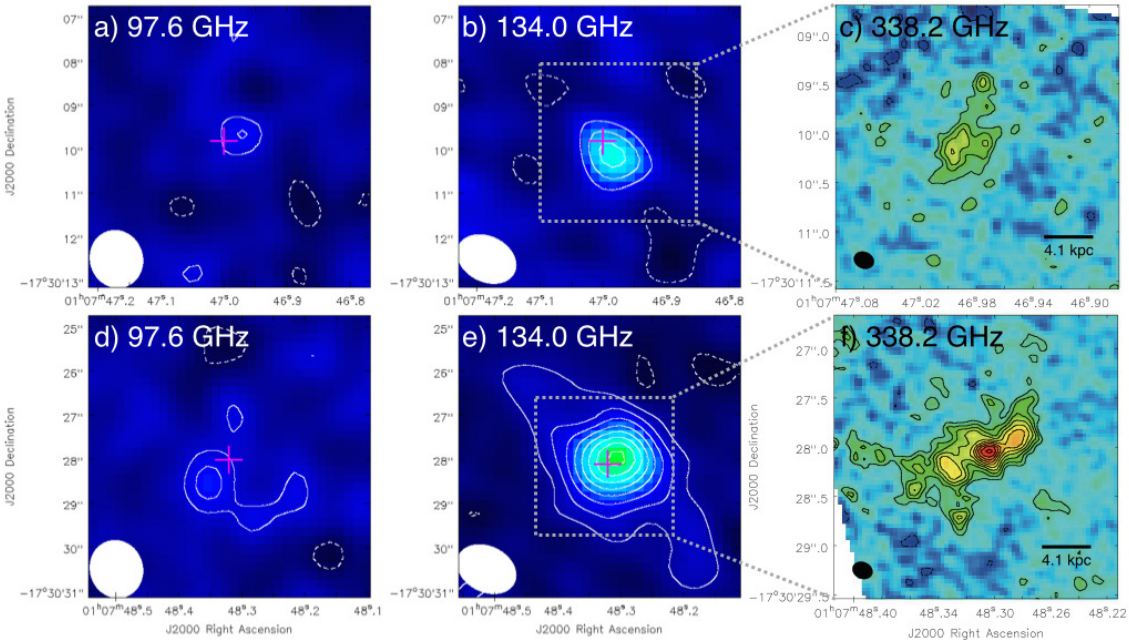

Figure C.1. (a) 97.6 GHz, (b) 140.5 GHz, and (c) 338.2 GHz images of SMG-N. The contours are $1\sigma \times$ (-2, 2, 3, 4, ...) for Figure C.1a and Figure C.1c, whereas $1\sigma \times$ (-2, 2, 4, 6, ...) for Figure C.1b. The 1σ levels are 37, 13, and 110 μJy beam^{-1} for Figure C.1a, C.1b, and C.1c, respectively. The cross shows the peak position of the cycle 0 338.2 GHz image (Figure C.2). The synthesized beam is shown in the bottom left corner. (d/e/f) The same as (a/b/c) but for SMG-E.

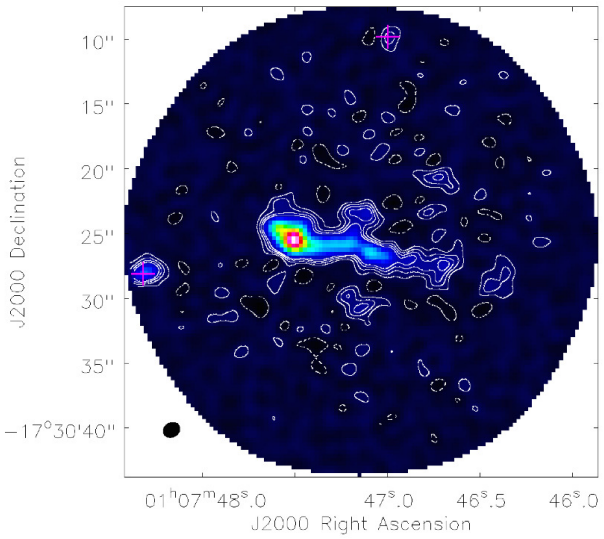

Figure C.2. 338.2 GHz images of VV 114 obtained by cycle 0 ALMA (Saito et al. 2015). The contours are 110 × (-2, 2, 3, 4, and 5) μJy beam^{-1}. The crosses show the peak position of SMG-E (Tamura, Saito et al. 2014) and SMG-N.

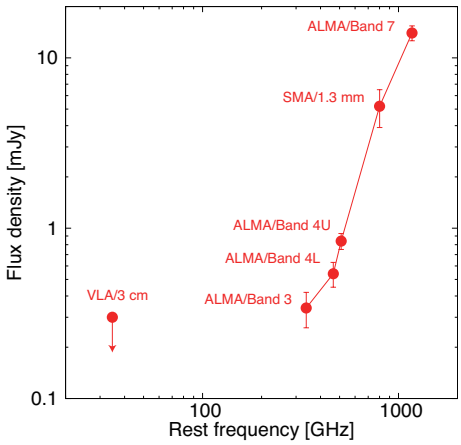

Figure C.3. Millimeter-to-submillimeter SED for SMG-E. The arrows show the 3 σ upper limits (Tamura, Saito et al. 2014).

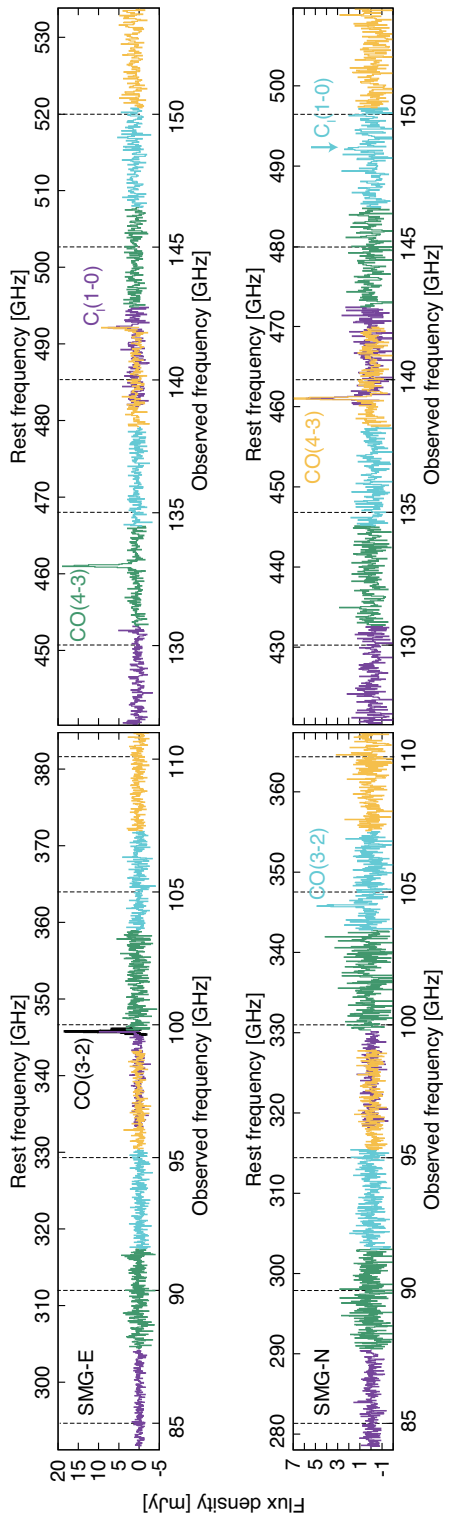

Figure C.4. 84 - 111 GHz (Band 3) and 127 - 154 GHz (Band 4) spectra for SMG-E (top) and SMG-N (bottom) with the velocity resolution of 50 km s^{-1}. We adopt aperture sizes of 4″for SMG-E and 3″for SMG-N.

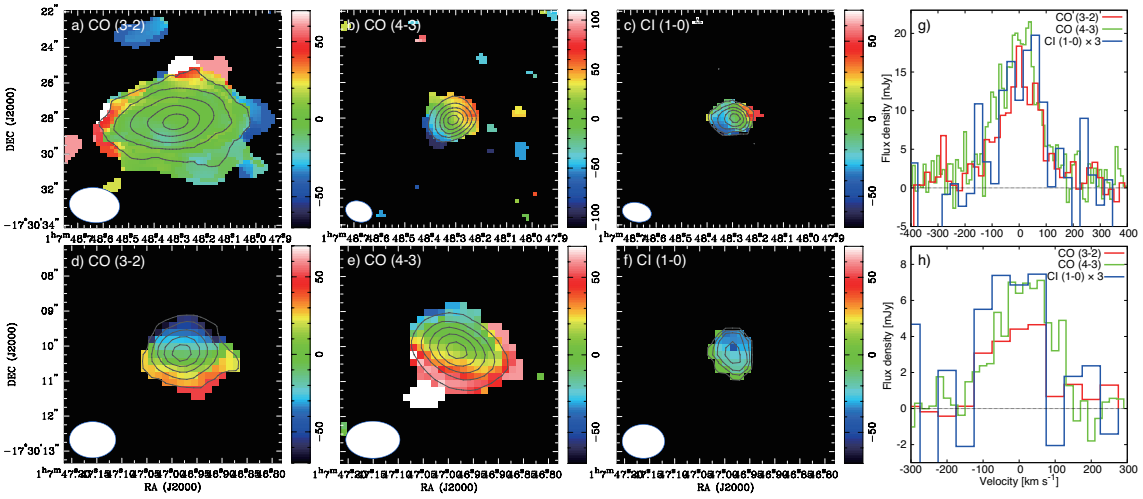

Figure C.5. The integrated intensity contour images overlaid on the velocity field of (a) CO (3–2), (b) CO (4–3), and (c) C_I (1–0) lines for SMG-E. (d/e/f) The same as (a/b/c) but for SMG-N. The contours are 0.08, 0.16, 0.32, 0.64, and 0.96 × S_{peak} mJy beam^{-1}. (g/h) CO (3–2) (red), CO (4–3) (green), and C_I (1–0) × 3 (blue) spectra for SMG-E and SMG-N. The systemic velocities are estimated by a single Gaussian fitting. We adopt aperture sizes of 4″for SMG-E and 3″for SMG-N.

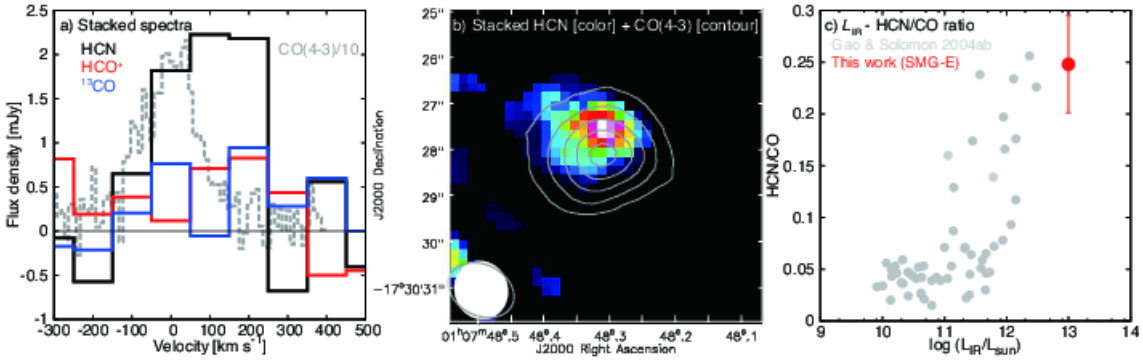

Figure C.6. (a) Stacked spectrum of HCN, HCO^+, and ^{13}CO toward SMG-E. The dashed line shows the CO (4–3) spectrum divided by 10. (b) Stacked HCN integrated intensity image. The contour shows the CO (4–3) integrated intensity. The synthesized beams for the stacked HCN and the CO (4–3) are shown as the while filled and grey contour ellipses, respectively.